

Magnetization, Anomalous Hall Effect and Single Pulse Partial All-optical Switching in Amorphous Rare-earth Transition-metal Thin Films

Zexiang Hu

Supervisor: Prof. J.M.D. Coey

Cosupervisor: Prof. Plamen Stamenov



2024

A dissertation submitted in partial fulfilment
of the requirements for the degree of
Doctor of Philosophy

Declaration

I declare that this thesis has not been submitted as an exercise for a degree at this or any other university and it is entirely my own work.

I agree to deposit this thesis in the University's open access institutional repository or allow the Library to do so on my behalf, subject to Irish Copyright Legislation and Trinity College Library conditions of use and acknowledgement.

I consent to the examiner retaining a copy of the thesis beyond the examining period, should they so wish (EU GDPR May 2018).

Signed: _____

Date: _____

Summary

Research on rare-earth (R) transition-metal (T) thin films has a long history. A revival of interest in this field was sparked by the discovery of single pulse all-optical switching (SP-AOS) in a-GdFeCo¹ alloy thin films by sub-picosecond laser pulses without the presence of a magnetic field, approximately a decade ago. This reopens some questions about amorphous metals that were not perfectly resolved in the last century:

- How do Co moments in the a-R-Co system change with composition and temperature? Will the Co orbital moment be quenched in amorphous materials?
- How will the noncollinear magnetic structure a-Dy_xCo_{1-x} and a-Tb_xCo_{1-x} evolve with temperature?
- Will the noncollinear magnetic structure on the R sites in a-Dy_xCo_{1-x} and a-Tb_xCo_{1-x} contribute to the anomalous Hall effect (AHE)?
- Does the noncollinear magnetic structure on the R sites in a-Dy_xCo_{1-x} and a-Tb_xCo_{1-x} influence the SP-AOS?

Driven by the non-magnetic properties of Y and its similar metallic radius to the other rare earths like Gd, Dy and Tb, the binary a-Y_xCo_{1-x} was chosen to answer the first question listed above. The work on sputtered thin films of binary a-Y_xCo_{1-x} with $0 \leq x \leq 0.54$ and thickness ≈ 15 nm provides a basis for understanding the ferromagnetism of cobalt in other amorphous R-Co alloy thin films. All compositions below the critical value $x_c = 0.5$ are very soft ferromagnets with almost no coercivity at room temperature. Above x_c , the Co moment vanishes. In these thin films, the ferromagnetic easy axis is in-plane when $x < 0.45$. The average total moment is $1.63 \mu_B$ in a-YCo₃, consisting of $1.31 \mu_B$ spin moment and $0.32 \mu_B$ orbital moment, deduced from X-ray magnetic circular dichroism measurements. Because the orbital moment is similar to that in crystalline YCo₅ with a big uniaxial anisotropy constant, the local anisotropy of a-YCo₃ is expected to be similar. The strong ferromagnetic exchange ensures that deviations from collinear ferromagnetism due to random anisotropy are negligible because of exchange averaging. The Co moments are almost temperature-independent when $x < 0.4$ due to large exchange interaction.

Based on the research conducted on a-Y_xCo_{1-x}, the temperature dependence of the averaged magnetic moment of the noncollinear R subnetwork is deduced in the a-Dy_xCo_{1-x} and a-Tb_xCo_{1-x} sputtered thin films. For Dy, the z -component of magnetic moment changes from $7.3 \mu_B$ (4 K) to $3.6 \mu_B$ (300 K); For Tb, the z -component of magnetic moment changes from $7.0 \mu_B$ (4 K) to $4.0 \mu_B$ (300 K). The cone angle also decreases from $\sim 50^\circ$ with increasing temperature. A spin-flop transition near compensation temperature, with a spin-flop field of approximately 2 T, was observed in the anomalous Hall effect measurement of a-DyCo₃ in 14 T field. The temperature dependence of the Hall voltage of a-DyCo₃ is used to infer that the Co subnetwork dominates the AHE.

In order to answer the final question listed above, the all-optical switching experiments were performed in a-Dy_xCo_{1-x} and a-Tb_xCo_{1-x} with $x \approx 0.25$, irradiated with single 200 fs pulses of

¹a- is used to denote an amorphous alloy.

800 nm laser light. A new type of partial and random SP-AOS, non-uniform on a length scale of about 150 nm, as measured by XMCD-PEEM, is found in $a\text{-Dy}_x\text{Co}_{1-x}$ for temperatures both below and above magnetization compensation temperature. This switching behavior is distinct from that in $a\text{-GdFeCo}$ (with a complete switching and a well-defined switching boundary). Ringlike switched domain patterns appear at higher fluence, but below the fluence at which the anisotropy begins to change towards in-plane. Optical control of coercivity is demonstrated with a possible application in magnetic logic.

These three main parts of the work help to obtain a better understanding of the behavior of Co magnetic moments in binary amorphous metals $a\text{-R}_x\text{Co}_{1-x}$ and to further clarify the influence of the noncollinear magnetic structure of the Dy and Tb ions on the magnetization, the AHE and the partial and random SP-AOS in $a\text{-Dy}_x\text{Co}_{1-x}$ and $a\text{-Tb}_x\text{Co}_{1-x}$.

To my parents, sister, and grandparents.

Acknowledgement

First, I really would like to thank my family for their continued support, which enables me to dedicate myself to my research abroad.

I have resided in Dublin for over four and a half years, beginning with my final-year undergraduate project in 2019. Time has passed swiftly, yet I still vividly recall the day when I first met Prof. Coey in Beijing. Without that meeting, I wouldn't be in Dublin today, and this entire thesis would not exist. One of the most remarkable aspects of Prof. Coey is his continuous pursuit of knowledge. He consistently posed the most questions during our Tuesday group meetings, leaving a lasting influence on every student. Over the course of my PhD journey, I had the opportunity to attend nearly ten international conferences and advanced schools. I made a conscious effort to engage with people as much as possible. During a month-long HERCULES school, I contributed close to 20% of the questions.

Our research group is quite extensive, typically comprising around 20 members. I've had the privilege of learning and benefiting from nearly everyone in our group, and I'm genuinely grateful to each one of them. I still vividly remember the day when I entered Trinity College Dublin, guided by Rui. During my whole PhD study, her advice was invaluable, not only pertaining to research but also in navigating daily life. Venky and Anup were among the first members I met in the lab. Initially, I faced difficulty finding accommodation, and it was Anup who generously offered his room for me to stay.

My journey commenced with the creation of bulk samples, a skill I acquired from Venky. Venky played a pivotal role in guiding my PhD study. Given my limited English proficiency at the beginning, I often struggled to follow discussions during subgroup meetings. Venky would help to take notes, outlining my tasks for the following week. His guidance helped me recognize the significance of pacing myself instead of rushing through assignments. Throughout these years, whenever unexpected challenges arose, Venky was consistently the first person to answer my call and provide assistance. With my family far away, his unwavering support made me feel less alone. I approached him with numerous scientific inquiries and gained a wealth of knowledge. However, the most profound lesson I learned from him was how to navigate the difficult phases of life. Words cannot adequately convey my gratitude towards him.

Most of my work on thin films was conducted at CRANN, where I collaborated closely with several colleagues. I worked extensively with Gwenael (thin films growth), Niclas (MOKE), and Jean (single-pulse all-optical switching), all of whom are highly experienced postdocs. My knowledge and expertise in these areas are largely attributed to their guidance. It's worth noting that they come from different European countries, providing me with valuable insights into their diverse cultures. Interactions with fellow postdocs like Karsten, Hwachol, Chandrima, and Yangkun greatly enriched my understanding. The exchange of ideas and discussions with them proved invaluable. I also had the unforgettable hiking experiences and engaging in diverse conversations with Yangkun and Rui during our hikes.

Furthermore, I had extensive interactions with other PhD students in our group, including Lucy, Brian, Simon, Ross, Jack, Ajay, Kat, and Hasen. Lucy's assistance was pivotal in improving my English proficiency during my initial days. Brian's guidance was instrumental in mastering the use of Shamrock. Simon adeptly maintained our various electrical transport

setups. Ross provided invaluable assistance for the XMCD data fitting of amorphous YCo. Ajay guided me through the process of creating Hall bars, while Kat played a crucial role in conducting XMCD measurements on amorphous YCo and DyCo thin film samples. It's important to underscore that I learned almost as much from my fellow students as I did from our supervisors and senior postdocs.

Additionally, I received invaluable assistance from various staff members at Trinity College Dublin. Professors Paschalis, Bradley, Stefano, and Mauro generously allowed me to attend undergraduate courses, which I found truly enjoyable. Marie, from the financial office, provided much-needed support with the financial system, even extending a helping hand during a challenging period when my credit card encountered issues, allowing me to sustain myself in Dublin. James, from the teaching lab, made my time there memorable with fascinating demonstrations and even encouraged and helped me to apply for the teaching fellow position at Durham University. My gratitude extends to David and Patrick in the workshop, who crafted essential components for my research. Niamh played a pivotal role in assisting me with GNIB renewals, UK and Schengen visa applications. Her support enabled me to obtain the UK visa, ultimately leading me to discover postdoc opportunities in the UK. During the later stages of my journey, when accommodation became a concern, I received tremendous support from the staff at Trinity Hall (particularly Martin) and Peter Gleeson (Intel Components Research, Researcher in Residence at CRANN). Their assistance ensured a peaceful final month leading up to the completion of my PhD study. Eva in the finance office and Rashima in the school office always greeted me warmly, providing much-needed moments of relaxation. Lastly, I found my brain power was significantly boosted in daily swimming, made possible by the dedicated staff at the sports center, who ensured the smooth operation of the swimming pool.

Throughout my entire PhD journey, I had the privilege of working closely with Prof. Plamen, from whom I learnt a wealth of knowledge and skills. Particularly during the challenging times of the COVID-19 pandemic, he guided me in becoming proficient with various experimental setups. I firmly believe that the skills I acquired from him will greatly benefit my future work. In the pursuit of experimental data, our discussions sometimes extended late into the night, with conversations continuing until 11 pm. During an especially demanding period when the LEGEND laser faced technical difficulties, we spent weekends to make the most of the limited laser time. I distinctly remember those moments when I successfully managed to collect magnetic domain images after single pulse all-optical switching experiments. I am at a loss for words to adequately express my gratitude to Prof. Plamen. I am well aware that I took a significant portion of his precious free time away from his family. Nevertheless, his unwavering support and guidance have been invaluable to my academic journey.

Finally, I really would like to express my deep gratitude and admiration for Mrs. Wong May Coey, who provided continued assistance to me in both direct and indirect ways. Although she is not affiliated with a university, her invaluable translation work of Tang poems serves as a vital bridge between the East and West. I hope that one day I can undertake similar efforts to enhance mutual understanding between these two important cultures.

List of Publications

1. **Zexiang Hu**, Jean Besbas, Ross Smith, Niclas Teichert, Gwenael Atcheson, Karsten Rode, Plamen Stamenov, and J. M. D. Coey.
Single-pulse all-optical partial switching in amorphous Dy_xCo_{1-x} and Tb_xCo_{1-x} with random anisotropy.
Applied Physics Letters, **120** (11), 2022.
2. **Zexiang Hu**, Jean Besbas, Katarzyna Siewierska, Ross Smith, Plamen Stamenov, and J. M. D. Coey.
Magnetism, transport and atomic structure of amorphous binary Y_xCo_{1-x} alloys.
arXiv preprint, arXiv:2309.16996 (2023).
3. **Zexiang Hu**, Ajay Jha, Katarzyna Siewierska, Simon Lenne, Ross Smith, Karsten Rode, Plamen Stamenov, and J. M. D. Coey.
Magnetism of noncolinear amorphous $TbCo_3$ and $DyCo_3$ thin films.
In preparation.

Contents

List of Figures	iv
List of Tables	viii
1 Introduction	1
1.1 Fundamentals of magnetism	1
1.1.1 Magnetic field	1
1.1.2 Magnetization	3
1.1.3 Anisotropy	4
1.1.4 Orbital and spin moment	7
1.2 Magnetism of cobalt and rare-earths	10
1.2.1 Localized moments	12
1.2.2 Delocalized moments	13
1.3 The theory of magnetic order	15
1.3.1 Exchange interaction	15
1.3.2 Mean field theory	17
1.3.3 Micromagnetism	19
1.4 Magnetotransport	24
1.4.1 Magnetoresistance	24
1.4.2 Ordinary Hall effect	27
1.4.3 Anomalous Hall effect	27
1.5 Ultrafast magnetism	28
1.5.1 Ferromagnets	28
1.5.2 Ferrimagnets	29
1.6 Amorphous materials and amorphous magnets	31
1.6.1 Amorphous materials	31
1.6.2 One network structure: such as YCo	33
1.6.3 Two network structure: such as DyCo	34
1.7 My PhD Project	34
References	36
2 Experimental methods	42
2.1 Magnetron Sputtering Thin Film Deposition	42
2.1.1 Direct Current Magnetron Sputtering	42
2.1.2 Radio Frequency Magnetron Sputtering	44
2.2 Crystallography	44
2.2.1 X-ray Diffraction	44
2.2.2 X-ray reflectivity	44
2.2.3 Different scan modes	45
2.3 Magneto-transport	46
2.3.1 Two and four points methods	47

2.3.2	Van der Pauw Method	47
2.3.3	Hall bars	48
2.4	Optical lithography	48
2.4.1	Mask design	49
2.4.2	Coating	49
2.4.3	Exposures	50
2.4.4	Development	51
2.5	Magnetometry	51
2.5.1	Vibrating-sample magnetometer	51
2.5.2	SQUID magnetometry	52
2.6	Magneto-optical Microscopy	53
2.6.1	Magneto-Optic Phenomena	53
2.6.2	Polar and longitudinal Kerr effect	56
2.7	Synchrotron X-ray radiation techniques	58
2.7.1	X-ray magnetic circular dichroism	58
2.7.2	X-ray photoemission electron microscopy	61
2.8	Ultrafast optics	62
2.8.1	Laser	63
2.8.2	Ultrafast laser	64
2.8.3	Optical layout	65
	References	68
3	Magnetism, transport and atomic structure of amorphous binary Y_xCo_{1-x} alloys	72
3.1	Background and motivation	72
3.2	Sample preparation	73
3.3	Results	73
3.3.1	XRD	73
3.3.2	XRR	74
3.3.3	Magnetization as a function of field and composition	78
3.3.4	Resistivity and Hall effect	80
3.3.5	Magnetization of a function of temperature	83
3.3.6	Magnetic moment vs x	84
3.3.7	X-ray magnetic circular dichroism	84
3.3.8	Binary amorphous structure	86
3.4	Discussion	87
3.4.1	Mass density	87
3.4.2	Anisotropy	88
3.4.3	Appearance of magnetism	91
3.4.4	Comaprision with a- Y_xFe_{1-x}	94
3.4.5	Electrical transport	95
3.5	Conclusion	95
	References	97
4	Magnetism of noncolinear amorphous $TbCo_3$ and $DyCo_3$ thin films.	103
4.1	Motivation and background	103
4.2	Methodology	104
4.3	Results	106
4.3.1	Dysprosium alloys	107
4.3.2	Terbium alloys	107

4.4	Discussion	107
4.4.1	Dispersed moments induced by local anisotropy	107
4.4.2	Effect of the underlayer	113
4.4.3	Anomalous Hall effect	114
4.4.4	Divergence of coercivity	116
4.4.5	Magnetically-ordered anhysteretic component silent in AHE and MOKE	117
4.5	Conclusions and outlook	119
References		120
5	Single pulse all-optical partial switching in amorphous Tb_xCo_{1-x} and Dy_xCo_{1-x}	124
5.1	Background and motivation	124
5.2	Methodology	125
5.3	Results	128
5.3.1	XRD, XRR and AFM	128
5.3.2	MOKE and AHE	128
5.3.3	Single pulse all-optical switching	128
5.3.4	XMCD-PEEM	132
5.3.5	Growth of magnetic domains with a swept pulsed laser beam	135
5.4	Discussion	138
5.4.1	Anisotropy	138
5.4.2	Optical control of coercivity	141
5.4.3	Single pulse partial switching	141
5.4.4	Ringlike-domain patterns	144
5.4.5	Growth of magnetic domains	146
5.4.6	Aging effects on the magnetic properties	146
5.5	Conclusions	147
References		149
6	Conclusions and outlook	153
6.1	Conclusions	153
6.2	Outlook	154
7	Appendix	155
7.1	B , H and M for a magnet	155
7.2	Self-energy	155
7.3	Adiabatic approximation	157
7.4	Deposition rate calculation	158
7.5	Fast Fourier transform	159
7.6	Resistivity and conductivity tensor	160
7.7	Make Hall bar	162
7.8	XMCD-PEEM image process	164
7.9	Phase diagram of Y-Co, Tb-Co and Dy-Co	164
7.10	Additional data for Chapter 5	165
References		169

List of Figures

1.1	Effects of shape anisotropy on magnetization equilibrium states.	6
1.2	Level scheme of the carbon atom $(1s)^2(2s)^2(2p)^2$	10
1.3	Illustration of the composition of the atomic magnetic moment \mathbf{m}	11
1.4	A schematic representation of density of states of 3d and 4s bands.	14
1.5	Energy bands with balanced and unbalanced spins.	14
1.6	Coordinates for hydrogen molecules represented diagrammatically.	16
1.7	The Zeeman splitting of the magnetic energy levels in the field.	18
1.8	Comparison of Brillouin functions for $J = 1/2$ and $J = 2$ with Langevin function.	19
1.9	Graphical solution of the mean-field state equations.	19
1.10	Schematic of domain wall structures.	20
1.11	Dependence of the dimensionless critical field h_c on the orientation of applied field.	23
1.12	The Stoner-Wohlfarth model for single domain particles.	23
1.13	Macrospin dynamics simulation using the Landau-Lifshitz-Gilbert (LLG) model.	25
1.14	Timeline of the main Hall related effects.	28
1.15	Transient remanent longitudinal MOKE signal of a Ni(20 nm)/MgF ₂ (100 nm) film.	29
1.16	SP-AOS in a-GdFeCo alloy thin films	30
1.17	Features of the radial distribution function.	32
1.18	Illustration of Atomic arrangements in ordered and disorder systems.	32
1.19	Schematic representation of one-subnetwork magnetic structures in amorphous solids.	33
1.20	Schematic representation of two-subnetwork magnetic structures in amorphous solids.	34
1.21	Relative spin orientations in the rare-earth-transition metal compounds.	35
2.1	Shamrock sputtering system	43
2.2	Erosion profile of a circular target.	43
2.3	X-ray reflectivity of two pure metallic elements Co and yttrium.	45
2.4	The Phillips Panalytical X'Pert Pro.	46
2.5	Definition of different angles in Phillips Panalytical X'Pert Pro machine.	46
2.6	The geometry of in-plane and out-of plane magnetoresistance measurement.	47
2.7	2 T GMW setup.	48
2.8	5.5 T Cryomagnet setup.	49
2.9	Optical micrograph of Hall bar	50
2.10	Schematic of lift-off process.	50
2.11	Setup components for a Hall bar device fabrication.	51
2.12	Schematic of the whole VSM system.	52
2.13	Schematic of SQUID and its raw measured data.	53
2.14	The Quantum Design MPMS-XL5.	54
2.15	Three configurations of MOKE.	57
2.16	Polar magneto-optical Kerr effect and Evico Magnetics wide-field Kerr microscope.	58
2.17	Schematic of the rotation angle in Kerr microscope without motor-driven analyzer.	59

2.18	The principle of XMCD.	60
2.19	The working principle of XPEEM.	62
2.20	Single pulse all-optical switching setup.	63
2.21	Schematic of basic laser action.	63
2.22	Simplified diagram of a laser.	64
2.23	Operating principle of chirped pulse amplification.	65
2.24	Schematic of single pulse all-optical switching experiment.	66
2.25	Laser fluence calibration.	66
3.1	XRD data of a bare $\langle 001 \rangle$ silicon wafer, an arbitrarily selected a- Y_xCo_{1-x} with a nominal chemical formula a- YCo_4 and a pure Co thin films on all silicon wafer substrates.	75
3.2	XRR of the number 18 a- Y_xCo_{1-x} sample with $x = 0.4$	76
3.3	Density of amorphous Y_xCo_{1-x} , crystalline Y_xCo_{1-x} and Y-Co model.	76
3.4	Thickness vs x of a- Y_xCo_{1-x}	77
3.5	Film thickness effect on density of a- Y_xCo_{1-x} with $x = 0.185$	77
3.6	Example showing the data after geometrical correction and diamagnetic correction.	79
3.7	Workflow illustrating the sequential steps involved in the $M(H)$ data analysis process.	79
3.8	Magnetisation versus applied field, perpendicular and parallel to the surface of the number 10 a- Y_xCo_{1-x} sample with $x = 0.1$	80
3.9	Magnetisation versus applied field, perpendicular and parallel to the surface of the number 17 a- Y_xCo_{1-x} sample with $x = 0.29$	80
3.11	Magnetisation versus applied field, perpendicular and parallel to the surface of the number 5 a- Y_xCo_{1-x} sample with $x = 0.54$	81
3.12	Magnetization vs x , where the magnetization is measured at room temperature for both OOP (black dots) and IP (red dots) configurations.	82
3.13	Composition dependence of resistivity of a- Y_xCo_{1-x}	83
3.14	Magnetoresistance of a- $Y_{0.155}Co_{0.845}$	84
3.15	Magnetoresistance and Hall effect of four a- Y_xCo_{1-x} thin films, measured at room temperature.	85
3.16	Magnetization as a function of temperature for a- Y_xCo_{1-x} with $x = 0.4, 0.46$ and 0.485	86
3.17	The average magnetic moment per cobalt in amorphous Y_xCo_{1-x} and crystalline Y_nCo_m intermetallic compounds.	86
3.18	Spectra of X-ray Absorption Spectroscopy (XAS) and X-ray Magnetic Circular Dichroism (XMCD) for a- $Y_{0.25}Co_{0.75}$	87
3.19	Average numbers of Y and Co neighbours around an Y atom, and Y and Co neighbours around a Co atom in the binary random dense-packed amorphous model.	88
3.20	Plot of saturation magnetization versus saturation field of a- Y_xCo_{1-x}	89
3.21	Ratio of average orbital to spin moment to spin moment plotted against spin moment in crystalline Y-Co compounds.	92
3.22	Concentration dependence of the saturation moment per Co atom in a- Y_xCo_{1-x}	93
3.23	Co magnetic moment vs x for crystalline Y-Co compounds.	94
4.1	Room-temperature in-plane and out-of-plane magnetization curves of a- $Dy_{0.25}Co_{0.75}$ with different thicknesses.	105
4.2	Some representative hysteresis loops of a- $Dy_{0.25}Co_{0.75}$ (sample number 2) and a- $Tb_{0.25}Co_{0.75}$ (the number 5 sample) alloys.	106
4.3	Coercivity for a- $Dy_{0.25}Co_{0.75}$ (sample number 2) showing a divergence at the compensation temperature of 180 K.	108

4.4	Magnetic moment per DyCo_3 formula unit in $\text{a-Dy}_{0.25}\text{Co}_{0.75}$ (sample number 2).	109
4.5	Room-temperature hysteresis loops by SQUID, anomalous Hall effect and polar MOKE in blue light of $\text{a-Tb}_{0.25}\text{Co}_{0.75}$ (the number 5 sample).	109
4.6	Coercivity for $\text{a-Tb}_{0.25}\text{Co}_{0.75}$ (sample number 4) showing a divergence at the compensation temperature of 180 K.	110
4.7	Temperature dependence of magnetization in both anhysteretic and hysteretic phases of $\text{a-Tb}_{0.25}\text{Co}_{0.75}$ (sample number 4).	111
4.8	Magnetic moment per TbCo_3 formula unit in $\text{a-Tb}_{0.25}\text{Co}_{0.75}$ (sample number 4).	112
4.9	Temperature dependence of Hall voltage of a-DyCo_3 (sample number 2) measured at 14 T.	114
4.10	Sequence of magnetic structures are found with increasing temperature in a-DyCo_3 under a high field	115
4.11	Temperature dependence of Hall voltage of a-DyCo_3 (sample number 2) extracted from the Hall loops at zero magnetic field.	116
4.12	Room-temperature hysteresis loops measured by SQUID, anomalous Hall effect and polar MOKE in blue light of $\text{a-Y}_{0.25}\text{Co}_{0.75}$ (sample number 7).	117
4.13	Room-temperature magnetization loops of $\text{a-Dy}_{0.25}\text{Co}_{0.75}$ (the number 3 sample) measured by SQUID magnetometry before and after polishing the substrate sides.	118
5.1	Two types of optical switching experiments.	126
5.3	Liu method used for calibrating the laser beam spot size.	127
5.4	X-ray diffraction, x-ray reflectivity and AFM characterization of the $\text{Tb}_{0.25}\text{Co}_{0.75}$ (sample number 1) film.	128
5.5	Room-temperature hysteresis loops measured for $\text{a-Tb}_{0.25}\text{Co}_{0.75}$ (the number 1 sample) and $\text{a-Dy}_{0.25}\text{Co}_{0.75}$ (the number 4 sample) by polar MOKE in blue light and anomalous Hall effect.	129
5.6	Four responses to different laser pulse fluences.	129
5.7	Polar MOKE images of films of $\text{Dy}_{0.25}\text{Co}_{0.75}$ after a sequence of 200 fs laser pulses with a fluence of 3.2 mJ/cm^2 .	130
5.8	Polar MOKE images of films of $\text{Dy}_{0.25}\text{Co}_{0.75}$ (the number 5 sample) after a sequence of 200 fs laser pulses with a fluence of 7.0 mJ/cm^2 .	130
5.9	Polar MOKE images of films of $\text{Dy}_{0.25}\text{Co}_{0.75}$ (the number 5 sample) after a sequence of 200 fs laser pulses with a fluence of 9.3 mJ/cm^2 .	130
5.10	Polar MOKE images of films of $\text{Dy}_{0.25}\text{Co}_{0.75}$ (the number 5 sample) after a sequence of 200 fs laser pulses with fluences of 11.9 and 14.6 mJ/cm^2 .	131
5.11	Polar MOKE images of films of (a) $\text{a-Tb}_{0.25}\text{Co}_{0.75}$ (the number 1 sample) and (b) $\text{Dy}_{0.25}\text{Co}_{0.75}$ (the number 4 sample) after a sequence of 200 fs laser pulses.	131
5.12	Detailed analysis of higher-magnification MOKE images of $\text{a-Tb}_{0.25}\text{Co}_{0.75}$ (the number 1 sample) and $\text{a-Dy}_{0.25}\text{Co}_{0.75}$ (the number 4 sample) films obtained after a sequence of 200 fs laser pulses.	132
5.13	Room temperature X-ray absorption spectroscopy (XAS) of $\text{a-Dy}_{0.25}\text{Co}_{0.75}$ (the number 3 sample) film recorded at the Co $L_{2,3}$ edge (left) and Dy $M_{4,5}$ (right) edge respectively.	132
5.14	XMCD-PEEM images of $\text{a-Dy}_{0.25}\text{Co}_{0.75}$ (the number 3 sample) film showing single pulse partial all-optical switching at 300 K.	133
5.15	Room-temperature magnetization hysteresis measured for the $\text{a-Dy}_{0.25}\text{Co}_{0.75}$ (the number 3 sample) film used for XMCD-PEEM experiment.	134
5.16	XMCD-PEEM image of $\text{a-Dy}_{0.25}\text{Co}_{0.75}$ (the number 3 sample) film showing single pulse partial all-optical switching at 180 K.	135
5.17	XMCD-PEEM image of $\text{a-Dy}_{0.25}\text{Co}_{0.75}$ (the number 3 sample) film showing single pulse partial all-optical switching at 120 K.	136

5.18	The nucleation and growth of magnetic domains was observed by sweeping a 1 kHz pulsed laser beam along the yellow dashed line across the surface of the Dy _{0.33} Co _{0.66} (the number 5 sample) thin film.	137
5.19	A 1 kHz pulsed laser beam with a fluence of 14.6 mJ/cm ² was scanned from left to right of the Dy _{0.33} Co _{0.66} (the number 5 sample) thin film.	137
5.20	Fourier analysis of the binary magnetic domain images of the Dy _{0.33} Co _{0.66} (the number 5 sample) thin film.	138
5.21	Typical magnetic arrangements of dipoles.	139
5.22	Optical microscope images of a-Dy _{0.25} Co _{0.75} (sample number 3) thin film after SP-AOS experiment.	140
5.23	Room-temperature hysteresis loops measured by MOKE for the unirradiated and irradiated regions of an a-DyCo ₃ (the number 5 sample) thin film sample.	140
5.24	Room-temperature longitudinal MOKE hysteresis loop of irradiated spot center of the a-DyCo ₃ (the number 3 sample) thin film along with simultaneous recordings of magnetic domain structure evolution during the hysteresis loop.	141
5.25	Comparison of room-temperature longitudinal MOKE hysteresis loops between irradiated and unirradiated regions after the first pulse of the a-DyCo ₃ (the number 3 sample) thin film.	142
5.26	A strip with in-plane anisotropy within a surroundings that still exhibits perpendicular magnetic anisotropy in the a-DyCo ₃ (the number 4 sample) thin film.	142
5.27	Histogram of intensity of the spot center of 1 and 2 pulses, measured by polar MOKE in blue light. The greylevel is normalized.	144
5.28	Schematics for explaining of ringlike-domain patterns.	147
7.1	B , H and M for a cube magnet.	155
7.2	Calculation of magnetic field inside a solid.	156
7.3	Sketch of Hall bar layout.	160
7.4	Three images showing key steps in the fabrication Hall bars in the cleanroom.	164
7.5	Phase diagram of Y-Co.	165
7.6	Phase diagram of Tb-Co.	166
7.7	Phase diagram of Dy-Co.	166
7.8	Difference XMCD-PEEM images of a-Dy _{0.25} Co _{0.75} (the number 3 sample in Chapter 5) film were generated by subtracting the image captured after pulse N-1 from the image after pulse N, with the XMCD-PEEM images collected at 300 K.	167
7.9	Difference XMCD-PEEM images of a-Dy _{0.25} Co _{0.75} (the number 3 sample in Chapter 5) film were generated by subtracting the image captured after pulse N-1 from the image after pulse N, with the XMCD-PEEM images collected at 180 K.	167
7.10	Difference XMCD-PEEM images of a-Dy _{0.25} Co _{0.75} (the number 3 sample in Chapter 5) film were generated by subtracting the image captured after pulse N-1 from the image after pulse N, with the XMCD-PEEM images collected at 120 K.	168

List of Tables

1.1	Anisotropy constants for cobalt, iron, nickel at room temperature.	5
1.2	Crystal anisotropy energies for various directions in a cubic crystal.	5
1.3	Total orbital quantum number L in spectroscopic notation.	9
1.4	Magnetic ground states for 4f ions using Hund's rules.	12
2.1	Binding energies for L_3 and L_3 edges of Fe, Co and Ni are expressed in electron volts (eV).	59
3.1	Summary of data for 20 a- Y_xCo_{1-x} thin film samples.	74
3.2	Mass magnetic susceptibility of a bare Si <100> substrate measured OOP and IP.	78
3.3	Resistivity measurement of a- Y_xCo_{1-x} thin films by van der Pauw method.	82
3.4	Comparison of sheet resistance R_s , thickness d , resistivity ρ , and composition ratio x for some samples.	83
3.5	Atomic distance in the crystalline and amorphous states for Co-Co, Co-Y and Y-Y in YCo_2	94
4.1	Structural and magnetic data on amorphous $Dy_{0.25}Co_{0.75}$ and $Tb_{0.25}Co_{0.75}$ thin films.	106
5.1	Characteristics of the representative a- Tb_xCo_{1-x} and a- Dy_xCo_{1-x} samples.	125
5.2	Pulse fluence vs total area within the contour of switched domains.	127
5.3	Meaning of colorbar in the difference images.	134
5.4	Comparisons between our results and those in the case of the citation [38] on the a-TbCo system.	146
7.1	Symbol definitions for deposition rate calculation.	158

1 Introduction

It is of great advantage to the students of any subject to read the original memoirs on that subject, for science is always most completely assimilated when it is in the nascent state.

James Clerk Maxwell

1.1 Fundamentals of magnetism

1.1.1 Magnetic field

Central to experimental magnetic research is the generation and detection of magnetic field [1]. There are two physical quantities, referred as magnetic field, which are denoted as \mathbf{B} field and \mathbf{H} field. The names generally used for \mathbf{B} and \mathbf{H} are extremely confusing. A few of the better authorities use better names [2]. In particular Sommerfeld uses the names \mathbf{B} magnetic field strength and \mathbf{H} magnetic excitation¹.

Historically, the magnetostatics was build on a magnetic charge model first and then Ampèrian molecular current model was brought up. For the former model, there is indeed a Coulomb's law for the \mathbf{H} field, just like the more famous Coulomb's law for \mathbf{E} field. This approach is still widely used for \mathbf{H} field computation produced by magnetic materials such as hard magnets due to its computation convenience [3]. These magnetic chargers are called magnetic poles as well. People thought they were and made a complete analogy with electrostatics. But until now, we did not find any isolated magnetic charge or magnetic monopole. Therefore, poles should be understood as purely mathematical [4]. The molecular current model is widely used and taught in undergraduate courses [5, 6]. The molecular current approach is able to get some support from atomic physics, such as the orbital momentum concept for electrons, which will be discussed later. Based on these two different models, those two quantities \mathbf{B} field and \mathbf{H} field are both derivable. Although the \mathbf{B} and \mathbf{H} field have two different meanings in the two models, the physical laws governing them are the same as demonstrated by the equations presented below where $d\mathbf{S}$ is the surface element of the arbitrary enclosed surface, $d\mathbf{l}$ is the line element of the arbitrary enclosed loop and sum of I_{cond} is the total conduction current inside the loop:

$$\oint \mathbf{B} \cdot d\mathbf{S} = 0, \quad (1.1)$$

$$\oint \mathbf{H} \cdot d\mathbf{l} = \sum I_{cond}. \quad (1.2)$$

From this point of view, those two models are equivalent. The Ampèrian model will be introduced firstly and then magnetic charge model.

The long-sought relation between electricity and magnetism was discovered by the Danish physicist Hans Christian Oersted in July 1820. Later that year, Ampère submitted a paper to

¹He uses the names \mathbf{E} electric field strength and \mathbf{D} electric excitation. Those terminologies reflect the fact that \mathbf{B} and \mathbf{E} are physically fundamental fields, and \mathbf{H} and \mathbf{D} are derived quantities.

the French Academy and proposed that ferromagnetism in magnetic materials was due to an internal current. It is an equivalence between a magnet and a current loop of area A with a current I . Its magnitude is expressed as

$$m = IA, \quad (1.3)$$

where the magnetic moment has Am^2 as unit and its direction follows the right-hand rule. The magnetization \mathbf{M} is defined as average magnetic dipole moment per unit volume.

$$\mathbf{M} = \frac{\sum \mathbf{m}}{V}. \quad (1.4)$$

Based on the Ampèrian current model, it follows that equivalently there is an enormous surface current density on the order of 10^6 A/m at the curved surface of a commercial cylindrical hard magnets such as $\text{Nd}_2\text{Fe}_{14}\text{B}$. From the equivalence, we can derive $\mathbf{j}_{\text{mag}} = \nabla \times \mathbf{M}$. Magnetic moment is a vector and its direction is traditionally defined as that of the electric current by the right-hand rule. At the same time, the law of the relation between a current and the \mathbf{B} field was found by Jean-Baptiste Biot and Félix Savart:

$$d\mathbf{B} = \frac{\mu_0}{4\pi} \left(\frac{d\mathbf{l} \times \mathbf{r}}{r^2} \right). \quad (1.5)$$

Based on this law, it is possible to derive the divergence and curl of magnetostatic \mathbf{B} field:

$$\nabla \cdot \mathbf{B} = 0, \quad (1.6)$$

$$\nabla \times \mathbf{B} = \mu_0 \mathbf{j}, \quad (1.7)$$

where \mathbf{j} is the total current density and $\mu_0 = 4\pi \times 10^{-7}$ T mA⁻¹ is the permeability of free space. It is valid only when electric charge densities are constant and all currents are steady. The electric and magnetic fields have no time dependence. Now \mathbf{j} consists of conduction current \mathbf{j}_{cond} and magnetization current \mathbf{j}_{mag} . Experimentally, we only have full control of the former, such as changing the current sent to the wire from the power supply. Motivated by this, a new physical vector quantity \mathbf{H} can be defined as $\mathbf{H} = \left(\frac{\mathbf{B}}{\mu_0} - \mathbf{M} \right)$. After taking the curl of both sides and substituting the curl of \mathbf{B} and \mathbf{H} , we get

$$\nabla \times \mathbf{H} = \mathbf{j}_{\text{cond}}. \quad (1.8)$$

In the magnetic charge model, the idea and development of this magnetic charge is really similar to electric charge in the electrostatic case. There is a magnetic Coulomb's law $F = kq_{m1}q_{m2}/r^2$ where q_{m1} and q_{m2} represent magnetic charges and \mathbf{r} is the distance between those two charges. k is a constant and takes the value of $1/(4\pi\mu_0)$ in the SI system of units. Similar to the way how \mathbf{E} is defined, \mathbf{H} is defined as $\frac{q_{m1}}{4\pi\mu_0 r^2} \mathbf{e}_r$. The magnetic dipole $\mathbf{p}_m = q_m \mathbf{l}$ where \mathbf{l} is the displacement vector from the negative magnetic charge to the positive one. \mathbf{H} consists of two parts, \mathbf{H}_0 from conduction current I_{cond} and \mathbf{H}' from magnetic materials. \mathbf{H}_0 follows the Biot-Savart law as well, but without the μ_0 . From this, the two formulas can be derived, where the symbols $d\mathbf{S}$, $d\mathbf{l}$, and I_{cond} have the same meanings in equation 1.1:

$$\oiint \mathbf{H}_0 \cdot d\mathbf{S} = 0, \quad (1.9)$$

$$\oint \mathbf{H}_0 \cdot d\mathbf{l} = \sum I_{\text{cond}}. \quad (1.10)$$

\mathbf{H}' follows exactly the same laws as electric field \mathbf{E} except that there is no free magnetic charge here. So magnetic charge q_m corresponds to polarization charge. After substituting ϵ_0 by μ_0 , \mathbf{E} by \mathbf{H}' , q by q_m , the following two laws can be obtained:

$$\oiint \mathbf{H}' \cdot d\mathbf{S} = \frac{1}{\mu_0} \sum q_m, \quad (1.11)$$

$$\oint \mathbf{H}' \cdot d\mathbf{l} = 0. \quad (1.12)$$

If we combine them together, we get

$$\oiint \mathbf{H} \cdot d\mathbf{S} = \oiint (\mathbf{H}_0 + \mathbf{H}') \cdot d\mathbf{S} = \frac{1}{\mu_0} \sum q_m, \quad (1.13)$$

$$\oint \mathbf{H} \cdot d\mathbf{l} = \oint (\mathbf{H}_0 + \mathbf{H}') \cdot d\mathbf{l} = \sum I_{cond}. \quad (1.14)$$

Remember that electric polarization \mathbf{P} in electrostatics, like magnetic polarization \mathbf{J} can be defined as average magnetic dipole per unit volume:

$$\mathbf{J} = \frac{\sum \mathbf{p}_m}{V} \quad (1.15)$$

and similar to \mathbf{P} , \mathbf{J} has the following relation

$$\oiint \mathbf{J} \cdot d\mathbf{S} = -\sum q_m. \quad (1.16)$$

Combining equations 1.13 and 1.16, we can get

$$\oiint (\mu_0 \mathbf{H} + \mathbf{J}) d\mathbf{S} = \oiint \mathbf{B} d\mathbf{S} = 0, \quad (1.17)$$

where the auxiliary \mathbf{B} can be defined as $\mathbf{B} = \mu_0 \mathbf{H} + \mathbf{J}$. The surface integral of \mathbf{B} and the line integral of \mathbf{H} have the same formula in magnetic charge and Ampèrian molecular current model, although they have different physical meanings, respectively, in those two models. In the appendix an example is given for the flexible use of those two models to understand the field inside and outside a hard-magnetic cube.

1.1.2 Magnetization

In solid-state magnetism, there exist three distinct levels of description, ranging from the atomic scale to the mesoscopic scale and finally to the macroscopic scale. The atomic scale (mainly focusing on the spin and orbital motion of electron) will be discussed in section 1.1.4 and the mesoscopic (mainly the domain with a dimension μm) scale will be discussed in section 1.3.3. At the atomic scale, the magnetic moment associated with electron is usually denoted by \mathbf{m} . Even under the external applied field, the direction of \mathbf{m} is still dynamically changing due to thermal fluctuations. The competition between magnetic field energy tending to align the moments in the field direction and thermal energy tending to make them disorder can be described by the Boltzmann statistics. Therefore, it is helpful to define the physical quantities mesoscopic or local magnetization \mathbf{M} over a distance of order a few nanometers and times of order a few microseconds:

$$\mathbf{M} = \frac{\sum_i \mathbf{m}_i}{\delta V}, \quad (1.18)$$

where each \mathbf{m}_i represents a magnetic moment and the sum taken is over a mesoscopic volume δV . Since the unit of magnetic moment is Am^2 as will be discussed in section 1.1.4, the unit of

magnetization is A/m^2 . The representation of the magnetization \mathbf{M} which changes smoothly on a mesoscopic scale is the continuous medium approximation [1]. After building up the concept of mesoscopic magnetization, it is time to introduce the macroscopic average magnetization, which is defined as

$$\mathbf{M} = \sum_i \mathbf{M}_i V_i / \sum_i V_i, \quad (1.19)$$

where the sum is over all the domains having volume V_i . The sum $\sum_i V_i$ is the sample volume. The hysteresis loops are plots of the macroscopic average magnetization as a function of \mathbf{H} , which is measured directly by a magnetometer. It is usually highly nonlinear. We cannot write a functional relationship like $\mathbf{M} = f(\mathbf{H})$ because the value of \mathbf{M} at any instant depends not only on what \mathbf{H} field is at that time but on its whole past history. Hysteresis is at the heart of the behavior of magnetic materials [7].

1.1.3 Anisotropy

Magnetic anisotropy means the dependence of a magnetic material on the direction of magnetization with respect to its shape or crystal axis. For the magnetization curve, it means that the shape of magnetization curve depends on the magnetizing direction relative to the crystallographic orientation. This section is structured as follows, a phenomenology of magnetic anisotropy will be given firstly, followed by a discussion of anisotropy mechanisms encountered in practice.

The simplest crystal anisotropy is uniaxial anisotropy, observed in hexagonal cobalt where the easy axis aligns parallel to the c axis of the crystal at room temperature. when the magnetization rotates away from the c axis, the anisotropy energy increases with an increase of θ , the angle between c axis and magnetization³. The energy is in general invariant under the inversion of magnetization so the corresponding energy term will contain even powers only [7]. It can be expanded in a series of powers of $\sin^2 \theta$:

$$E_a = K_{u0} + K_{u1} \sin^2 \theta + K_{u2} \sin^4 \theta + \dots, \quad (1.20)$$

where the K_{ui} is the i -th anisotropy constant with a unit kJ/m^3 . The term K_{u0} is independent of angle and is usually ignored since only the change of energy is interested to us when magnetization rotates from the easy axis. K_{u1} is usually the leading term. When $K_{u1} > 0$, the magnetization is along the z axis (easy axis). When $K_{u1} < 0$, the energy is minimized for $\theta = 90^\circ$ (easy-plane anisotropy). The values of K_{u1} and K_{u2} for cobalt are 410 kJ/m^3 and 140 kJ/m^3 respectively [1]. For cubic crystals such as iron and nickel, based on the cubic symmetry, the anisotropy energy can be expressed in terms of direction cosines α_x , α_y and α_z [8]:

$$E_a = K_0 + K_1(\alpha_x^2 \alpha_y^2 + \alpha_x^2 \alpha_z^2 + \alpha_y^2 \alpha_z^2) + K_2(\alpha_x^2 \alpha_y^2 \alpha_z^2) + \dots, \quad (1.21)$$

where K_0 , K_1 and K_2 are the anisotropy constants⁴. The anisotropy constants for cobalt, iron, nickel at room temperature are summarized in Table 1.1. Using these anisotropy constants, it is possible to explain the magnetization behavior of Fe, Co, Ni for applied field in different directions. Table 1.1 gives the E_a when magnetization lies in a particular direction $[u \ v \ w]$. The sign and magnitude of K_1 and K_2 decide the easy axis direction.

²If it is a thin film sample, it is popular and convenient to define magnetization by using the volume. But in bulk samples, it is more convenient to use the mass of samples instead since the mass is easier to measure by using a mass balance.

³In the magnetism community, it is common for people to say energy but actually they are referring to energy density. E_a should be called anisotropy energy density. It is a convention and hard to change. Attention is needed when reading literature.

⁴The same argument for K_{u0} applies to K_0 here as well. The reason why those two terms are still written down will be clear later when talking about how to measure those anisotropy constants.

Substance	K_1 (kJ/m ³)	K_2 (kJ/m ³)
Fe	48.0	15.0
Ni	-5.0	5.0
Co	410.0	140.0

Table 1.1: Anisotropy constants for cobalt, iron, nickel at room temperature. For cobalt, the values for K_1 and K_2 should be thought as K_{u1} and K_{u2} respectively.

[u v w]	a	b	c	α_x	α_y	α_z	E
[1 0 0]	0°	90°	0°	1	0	0	K_1
[1 1 0]	45°	45°	45°	$1/\sqrt{2}$	$1/\sqrt{2}$	0	$K_1/4$
[1 1 1]	54.7°	54.7°	54.7°	$1/\sqrt{3}$	$1/\sqrt{3}$	$1/\sqrt{3}$	$K_1/3+K_2/27$

Table 1.2: Crystal anisotropy energies for various directions in a cubic crystal.

There are various methods for measuring magnetic anisotropy such as torque magnetometer, magnetization curve, ferromagnetic resonance [8, 9]. The second one magnetization curves will be discussed here since I mainly use this one. In 1926, the magnetization curves of single crystals of iron was first measured by Honda and Kaya [10]. There are two methods of determining anisotropy constants from magnetization curves of single crystals:

1. By fitting a calculated magnetization curve to an observed one.
2. By calculating the area enclosed by the magnetization curve, the ordinate axis and the line $M = M_s$.

For the first method, let's take an example of crystal cobalt with an uniaxial anisotropy. The field is applied at right angle to the c axis, i.e., the easy axis. The saturation magnetization M_s is tilted away from the easy axis by an angle θ . The total energy consists of anisotropy energy and Zeeman energy [9]:

$$E = K_{u0} + K_{u1} \sin^2 \theta + K_{u2} \sin^4 \theta - M_s \mu_0 H \cos(\pi/2 - \theta) \quad (1.22)$$

From the condition for energy minimum $\frac{dE}{d\theta} = 0$ and the definition of the component of magnetization along the field direction is given as $M = M_s \cos(\pi/2 - \theta)$, it is easy to obtain

$$H = \frac{2K_1}{M_s} \left(\frac{M}{M_s} \right) + 4 \frac{K_2}{M_s} \left(\frac{M}{M_s} \right)^3. \quad (1.23)$$

The relation between M and H is given by the above formula and used to fit the experimental data by changing K_1 and K_2 . By substituting $\frac{M}{M_s} = 1$ into equation 1.23, the saturation field can be expressed as

$$H_s = \frac{2K_1 + 4K_2}{\mu_0 M_s}. \quad (1.24)$$

A more convenient way for determining anisotropy constant is to calculate the area as mentioned already, which is based on the definition of anisotropy energy, namely, the energy stored in a crystal when it reaches its saturation magnetization in a non-easy direction. The work dW done by the magnetic field is $dW = \mu_0 H dM$ where dM is the increment of magnetization due to the applied field [9]. For a sample having a uniaxial anisotropy (assuming K_{u1} is the leading term), the magnetization is a linear function of field when the applied field is perpendicular to the c axis. If we denote W the area enclosed by the magnetization curve, the ordinate axis and

the line $M = M_s$ ⁵. From the equation 1.20, the increase of anisotropy energy E_a is

$$\Delta E_a = E_a(\theta = 90^\circ) - E_a(\theta = 0^\circ) = (K_{u0} + K_{u1}) - K_{u0} = K_{u1}. \quad (1.25)$$

The work done by the applied field is stored in the anisotropy energy and so $W = K_{u1}$.

There are mainly three sources of anisotropy which are related to sample shape, crystal structure and atomic or micro-scale texture [1].

- Shape anisotropy derives from the demagnetizing field discussed in the section 7.1. Obviously, this can not be an intrinsic property of the material, as it depends on the sample shape.
- Magnetocrystalline anisotropy is an intrinsic property. The magnetization process is different when the field is applied along different crystallographic directions and the anisotropy reflects the crystal symmetry. Single-ion anisotropy is the main source of anisotropy in hard ferromagnetic materials [11].
- Induced anisotropy arises when an easy direction of magnetization is created by applied stress or by growing a thin film in a magnetic field to imprint some atomic-scale structure.

Shape anisotropy and single-ion anisotropy will be discussed in detail here. The shape anisotropy is rooted in classical dipole-dipole interaction and it leads to a tendency of a magnetized sample to minimize its magnetostatic energy. For example, a long magnetic needle prefers to orient its magnetization along the long axis and a flat slab of ferromagnetic material tend to be magnetized in the plane of the slab, as shown in Figure 1.1 (a) and (b).

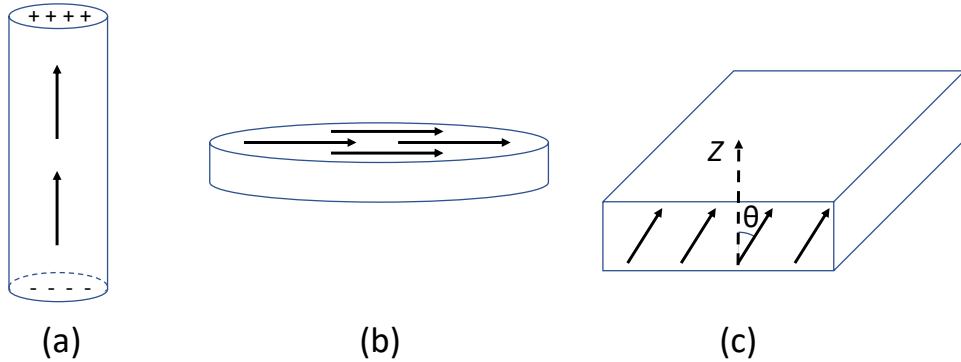


Figure 1.1: Effects of shape anisotropy on magnetization equilibrium states. (a) In a long needle, the magnetization points along the length of the needle. In the magnetic charge model, the positive and negative magnetic charges thus produced are well separated, lowering the magnetostatic energy; (b) A uniformly magnetized flat disk reduces the magnetostatic energy by orienting \mathbf{M} in the plane of the disk; (c) A thin film with uniform magnetization. The angle between \mathbf{M} and the normal is θ .

In reality, because of the competition between several energy terms, magnetic specimens usually contain magnetic domains, resulting in a complex magnetization distribution. For simplicity, we assume that the magnetization of the film is uniform and denoting by θ the angle between \mathbf{M} and the normal of sample as illustrated in Figure 1.1 (c), the demagnetizing field within the film is

$$\mathbf{H}_d = -|\mathbf{M}|\cos(\theta)\hat{z}. \quad (1.26)$$

⁵Note that, when plotting magnetization vs field, the x axis should be $\mu_0\mathbf{H}$ and y axis should be \mathbf{M} . So the area will represent the work done by the magnetic field.

The magnetostatic energy density is therefore given by

$$E = -\frac{1}{2}\mathbf{M} \cdot \mu_0\mathbf{H}_d = \frac{1}{2}\mu_0(M\cos(\theta))^2. \quad (1.27)$$

It indicates that the magnetostatic energy of a thin film with uniform \mathbf{M} has a minimum at $\theta = 90^\circ$ and a maximum at $\theta = 0^\circ$.

Single-ion anisotropy is essentially the electrostatic interaction of charges in orbitals of the magnetic ion with the potential created by the rest of the system. The electrostatic interaction tends to stabilize a particular orbital and via the spin-orbit interaction the magnetic moment is aligned along a particular axis, i.e., the local easy axis [1]. Steven demonstrated that the crystal field can be expressed in terms of the angular momentum operators via replacing x , y and z by J_x , J_y and J_z and allowing for the non-communication of J_x , J_y and J_z [12]. This method is called operator equivalents and has been explained in detail by Steven [13, 14, 15]. Therefore, the crystal field Hamiltonian can be expressed by

$$\mathcal{H}_{cf} = \sum_{nm} B_n^m \hat{O}_n^m, \quad (1.28)$$

where coefficients B_n^m determine the magnitude of the crystal field splitting [16] and \hat{O}_n^m are Steven operators⁶. It has been demonstrated by point charge calculation on amorphous model structure that the $B_2^0\hat{O}_2^0$ term dominates the crystal field and define a local easy axis at each site. Therefore, the crystal field Hamiltonian in amorphous magnets can be simplified to [17]:

$$\mathcal{H}_{cf} = B_2^0\hat{O}_2^0. \quad (1.29)$$

1.1.4 Orbital and spin moment

As late as the first quarter of the 20th century, the origin of the microscopic magnetic moments was not very clear. It was the appearance of quantum mechanics that helped to answer this question [18]. Within a single atom the distribution of magnetism is not smooth. For example, in an iron atom the magnetism is distributed in a more or less spherical shell, not too close to the nucleus and not too far away [19]. There are two contributions to atomic magnetic moment, orbital motion and spin of electron. Atomic magnetic moments occur whenever an atom or an ion contains a partially filled electron shell, which restricts the occurrence of paramagnetism to compounds to certain well-defined regions of the periodic table, known as the transition groups. Among the most well studied are the iron group (with 3d shell incomplete) and rare earth group (with 4d shell partially filled).

In the classical physics picture, the electron moves in a circular orbit of radius r at an angular frequency ω . The equivalent current I is $-\frac{e\omega}{2\pi}$, where e is the magnitude of the charge of the electron and the minus sign arises from the negative electronic charge. The orbital angular momentum is $\mathbf{l} = m_e\mathbf{r} \times \mathbf{v} = m_e\omega r^2$, where m_e is the electron mass. By using the above two formulae and $\mathbf{m} = I\mathbf{A}$, the magnetic moment is given by:

$$\mathbf{m} = -\frac{e}{2m_e}\mathbf{l}. \quad (1.30)$$

Here, the factor $-\frac{e}{2m_e}$ is known as the gyromagnetic ratio and denoted as γ . In quantum mechanics, it is required that the component of \mathbf{l} is quantized in some direction, such as the z -direction (usually the magnetic field direction). This quantization implies that the z -component of angular momentum, l_z , can only take on values that are integer multiples of \hbar . Therefore, the z -component of the magnetic moment m_z is also quantized as:

$$m_z = -\frac{e}{2m_e}m_l\hbar, \quad (1.31)$$

⁶ B_n^m are the parameters to be determined by experiments such as paramagnetic resonance; $\hat{O}_2^0 = 3\hat{J}_z^2 - J(J+1)$, corresponding to crystal field $3z^2 - r^2$ [3].

where $m_l = 0, \pm 1, \pm 2, \dots$. The natural unit for atomic magnetism is the Bohr magneton defined as⁷:

$$\mu_B = \frac{e\hbar}{2m_e}, \quad (1.32)$$

and $1\mu_B$ is equal to $9.274 \times 10^{-24} \text{ Am}^2$.

In the 1920s Stern-Gerlach experiment, the spin of the electron was experimentally confirmed by sending a beam of Ag atoms through a non-uniform magnetic field, resulting in only two spots detected on the detector screen. The magnetic moment related to spin is given by:

$$\mathbf{m} = -\frac{e}{m_e} \mathbf{s}. \quad (1.33)$$

The ratio of the magnitude of m_z in μ_B to the magnitude of l_z or s_z in \hbar is called the g -factor. Comparing the orbital and spin angular momentum contributions to the magnetic moment, the proportionality factors differ in the ratio $-\frac{e}{2m_e} : -\frac{e}{m_e} = 1 : 2$. Alternatively, the proportionality can be written as $g\left(-\frac{e}{2m_e}\right)$, where $g = 1$ for orbital motion and $g = 2$ for spin. This g -factor is commonly referred to as the g -factor [1]. The total magnetic moment of an electron is generally a vector sum of the spin and orbital magnetic moments:

$$\mathbf{m} = -\frac{\mu_B}{\hbar} (2\mathbf{s} + \mathbf{l}). \quad (1.34)$$

Here, the factor of 2 arises from the g -factor for the spin contribution.

Except for the hydrogen atom, there are more than two electrons in a single free atom, where each individual electron has its own orbital momentum \mathbf{l}_i and spin momentum \mathbf{s}_i . There are 3 types of interactions between angular momenta: spin-spin coupling, spin-orbit coupling, and orbit-orbit coupling. For the first-row transition series, which includes the three famous magnetic elements Fe, Co, and Ni, the interactions between \mathbf{s}_i and \mathbf{l}_i or those between \mathbf{s}_i and \mathbf{l}_i are small compared to the interaction between \mathbf{s}_i and \mathbf{s}_j and those between \mathbf{l}_i and \mathbf{l}_j [8].

The vectors that are strongly coupled with one another must always be added together first. Therefore, based on the vector model of magnetic atoms⁸, the spin vectors \mathbf{s}_i of individual electrons ($i = 1, 2, \dots, n$) are coupled via spin-spin coupling to produce the resultant spin vector:

$\mathbf{S} = \sum_{i=1}^n \mathbf{s}_i$. Similarly, the orbital vectors \mathbf{l}_i of electrons give rise to the resultant orbital vector: $\mathbf{L} = \sum_{i=1}^n \mathbf{l}_i$. The \mathbf{L} and \mathbf{S} , according to Russell-Saunders coupling, are then less strongly with one another and their resultant is \mathbf{J} :

$$\mathbf{J} = \mathbf{L} + \mathbf{S}. \quad (1.35)$$

Each allowable \mathbf{L} can be combined with each possible \mathbf{S} [21].

Based on spectroscopic observation, Hund gave empirical rules for determining the lowest energy state of a multielectron atom or ion, except the very heaviest elements. The rules are⁹:

- (1) The spin \mathbf{s}_i combines to give the maximum value of S consistent with the Pauli principle.
- (2) The orbital vectors \mathbf{l}_i combine to give the maximum values of L consistent with (1).
- (3) The resultant L and S combine to form J : $J = L - S$ if the shell is less than half full, and $J = L + S$ if the shell is more than half full¹⁰.

⁷All magnetic interactions involve the inverse of mass of particle. Here it is the mass of the electron. But for the nucleus, it is the nuclear mass, which is 1000 times bigger than electron mass. Therefore often the nuclear contribution to magnetism can be ignored.

⁸A good discussion of vector model can be found in the book by Cowan [20].

⁹Note that Hund's rules do not tell anything about the excited states.

¹⁰Here, S , J and L are quantum numbers and dimensionless. The third rule is the weakest one and might be violated in some cases [22, 23].

The first two rules are the result of electrostatic Coulomb interactions between electrons [24]. Rule (3) is mainly based on spin-orbit interaction between \mathbf{s}_i and \mathbf{l}_i of the same electron. As we discussed previously, there is a relation between angular momentum and magnetic moment in equations 1.30 and 1.33, as the energy when \mathbf{s}_i and \mathbf{l}_i are parallel is higher than that when \mathbf{s}_i and \mathbf{l}_i are antiparallel [25]. Therefore, if the shell is less than half full, the spin should be antiparallel to \mathbf{L} . But if the shell is more than half full, the spin of the electron in the unfilled half shell is opposite to \mathbf{S} . The orbit of the electrons is parallel to \mathbf{L} , the antiparallel of \mathbf{s}_i and \mathbf{l}_i results in the parallel of \mathbf{L} and \mathbf{S} . In summary, the energy of the coupling between \mathbf{L} and \mathbf{S} is expressed as

$$\mathcal{H}_{so} = \beta \mathbf{L} \cdot \mathbf{S}. \quad (1.36)$$

where β is a spin-orbit parameters for multielectron atom¹¹. β is positive for a less than half filled shell and negative for a more than half-filled shell [26].

From Hund's rules, we know the JLS triplet of numbers identifies the ground state of free atom (ions). Traditionally, the value of L is identified by the letters as listed in Table 1.3. The

$L =$	0	1	2	3	4	5	6	7
Symbol	S	P	D	F	G	H	I	K

Table 1.3: Total orbital quantum number L in spectroscopic notation.

spin is specified by the multiplicity $2S+1$ as a superscript, and total angular momentum quantum number J is shown in the subscript. The level of each term of a particular configuration can be summarized by a term symbol [27, 25]:

$$^{2S+1}L_J. \quad (1.37)$$

Take carbon with its six electrons as an example. There are 15 ways to accommodate two electrons in the 2p-orbitals [1]. The hierarchy of atomic structure of 2p configuration of carbon is plotted in Figure 1.2.

By analogy with 1.34 for single electron, the magnetic moment of an atom is represented by

$$\mathbf{m} = -\frac{\mu_B}{\hbar}(2\mathbf{S} + \mathbf{L}). \quad (1.38)$$

In many cases, \mathbf{S} and \mathbf{J} are not good quantum numbers, but \mathbf{J} is. Therefore, the component of magnetic moment \mathbf{m} parallel is a conserved quantity but the component perpendicular to \mathbf{J} will not be. The expression for the projected magnetic moment can be rewritten as follows [1]:

$$\mathbf{m} = -g \frac{\mu_B}{\hbar} \mathbf{J}, \quad (1.39)$$

where g is a constant to be determined. From the vector model of magnetic atoms as shown in Figure 1.3, it is possible to derive :

$$g = 1 + \frac{J(J+1) + S(S+1) - L(L+1)}{2J(J+1)}. \quad (1.40)$$

When $S = 0$, $J = L$, hence formula 1.40 gives $g = 1$. If $L = 0$, $J = S$, formula 1.40 gives $g = 2$ consistent with the discussion given previously [8]. When the atom is put in a magnetic field, vector \mathbf{J} is going to precess about the axis of the magnetic field. Due to the spatial quantization, the component of \mathbf{J} along the field axis, J_z , takes $2J + 1$ discrete values:

$$J_z = J\hbar, (J-1)\hbar, (J-2)\hbar, \dots, (-J+2)\hbar, (-J+1)\hbar, (-J)\hbar. \quad (1.41)$$

This will be important when we talk about mean field theory.

¹¹For a single electron, the spin-orbit coupling is expressed as $H_{so} = \lambda \mathbf{l} \cdot \mathbf{s}$, where λ is the spin-orbit coupling constant of single electron and λ is always positive. It is a measure of the magnetic interaction between momenta [25].

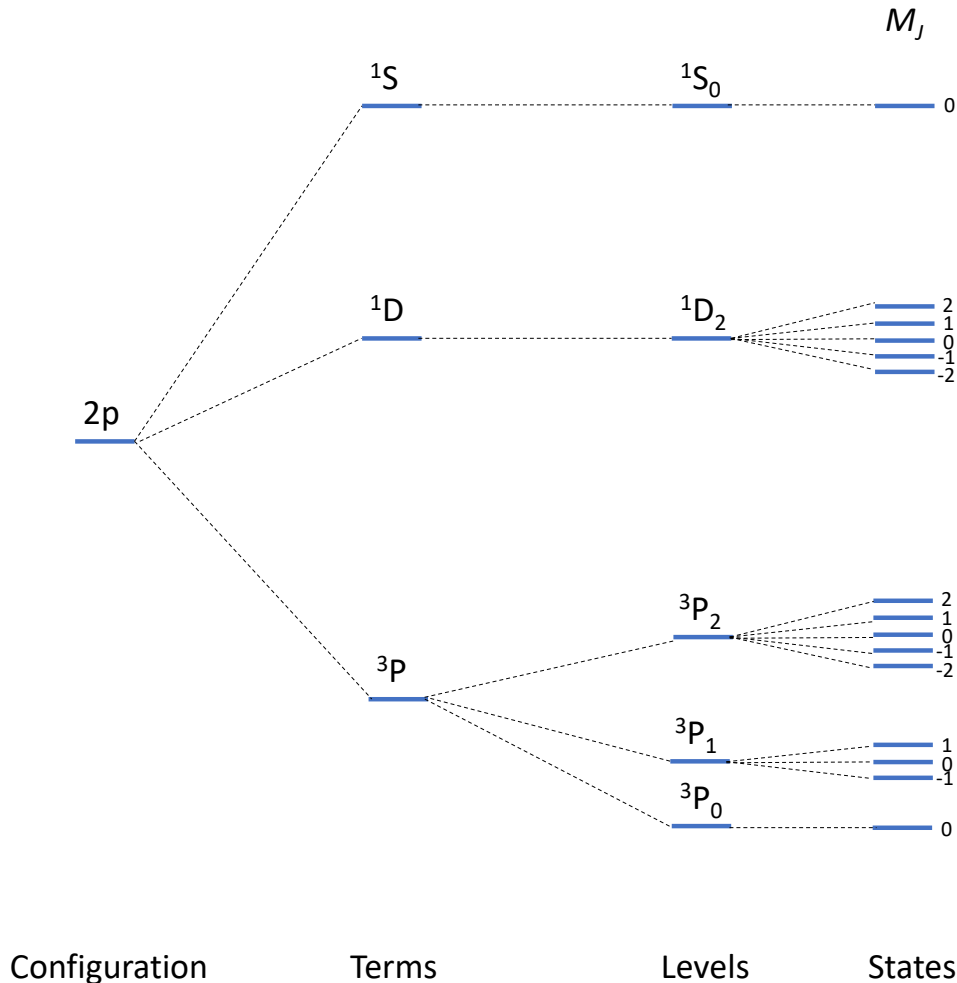


Figure 1.2: Level scheme of the carbon atom $(1s)^2(2s)^2(2p)^2$. Drawing is not to scale. The first column (**Configurations**): the energy without any two-particle interaction. The second column (**Terms**): three-fold energy splitting after switching on electrostatic electron-electron interaction (L and S are good quantum numbers). The third column (**Levels**): splitting after switching on first-order spin-orbit coupling (J is a good quantum number). For the 3P term, the separation between $J = 2({}^3P_2)$ and $J = 1({}^3P_1)$ is twice the one between $J = 1({}^3P_1)$ and $J = 0({}^3P_0)$. The spin-orbit coupling does not shift the mean energy. This must be the case for a perturbation that arises internally in the atom because the total energy can not be altered if the system is not interacting with the environment. Each of these levels have $2J + 1$ states, which are degenerate in the absence of external electric and magnetic field. The fourth column (**States**): Zeeman splitting in an external magnetic field.

1.2 Magnetism of cobalt and rare-earths

In the previous section 1.1.4, the origin of the magnetic moments of free atoms was discussed. In this section, it will be discussed how magnetic moments interact to give cooperative magnetic phenomena in situations such as solids. At or just below room temperature only four elements are found to have spontaneous ferromagnetic order (bcc Fe, hcp Co, fcc Ni and hcp Gd), despite the existence of thousands of compounds and alloys with substantial magnetic moments [28].

Two models are considered here: the band or itinerant electron model and the localized moment model. The former one works well for 3d transition metals and their alloys and the latter one is suitable for rare earth metals. Transition metals and rare earth metals are the two main magnetic groups. Cobalt (Co), iron (Fe) and nickel (Ni) belong to the transition metal

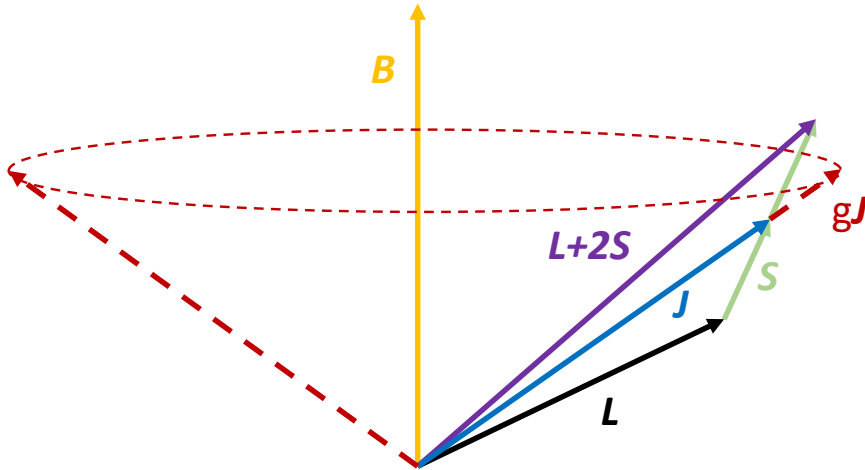


Figure 1.3: Illustration of the composition of the atomic magnetic moment m . Now S and L may not be good quantum numbers in many atoms but J is. Therefore the component of m parallel to J will be a conserved quantity. $L + 2S$ is precessing around J . gJ is the projection of $L + 2S$ onto the axis of J .

group. The outer-most 3d shell of is responsible for magnetism of transition metal. Because of being of this character, those electrons are easily influenced by the intense E -field created by the neighboring ions called crystal field, in alloys or compounds¹². The orbital moment is almost quenched in both insulators and metals¹³. As a result, the 3d ions in solids have $L \approx 0$, $J \approx S$ and $g \approx 2$, which disagrees with the predictions of Hund's rules. This makes it easy to estimate the moment of 3d electrons by spin counting. For example, ferrimagnetic magnetite Fe_3O_4 contains two Fe^{3+} with antiparallel ionic moments and one Fe^{2+} ion. The predicted value is $4 \mu_B$ per formula, which is very close to the observed value $4.1 \mu_B$. In 3d metals, where the number of 3d electrons per atom is non-integral, the orbital moment is only of the order of $0.1 \mu_B$ [29].

The rare earth metals are the fifteen elements ranging from lanthanum (La), atomic number 57, to lutetium (Lu), atomic number 71¹⁴. The small radius of rare-earth 4f shells results in a comparatively strong spin-orbit coupling, whereas the crystal field is largely screened by conduction electrons. The Hund's rules work very well for rare earth ions. They have similar chemical properties such as very vulnerable to oxygen since they have the same outer shell electron structure given by

$$(4f)^n(5s)^2(5p)^6(5d)^1(6s)^2$$

where n increases from 0 to 14 with increasing atomic number from 57 to 71. The incomplete 4f shell has a close relation to the magnetic properties. Even if the atoms are ionized by the loss of the 3 electron from $(5d)^1(6s)^2$ shell, the remaining electrons of $(5s)^2(5p)^6$ are still enclosing the 4f electrons. Therefore, the orbital angular momentum of 4f electrons remain unquenched by the crystal field even in the metallic state¹⁵, which is quite opposite to the case of transition

¹²The crystal field theory originated in the study of transition-metal complexes, which are also referred to as coordination complexes. An example was the distinction between yellow $\text{CoCl}_3 \cdot 6\text{NH}_3$ and purple $\text{CoCl}_3 \cdot 5\text{NH}_3$, which indicates the energy level differences of stereochemical origin. The quantitative crystal field theory dates back to Hans Bethe in 1929.

¹³For free atoms, those remain unquenched because of the lack of crystal field. The orbital moment quenching was first recognized by van Vleck in 1937.

¹⁴A comprehensive survey of its brief history of rare earth magnetism can be found in the book by Jen and Allan [30].

¹⁵The competition between spin-orbit coupling and crystal field decides whether the orbital moment is

metal [31]. Mathematically, the difference between quenched and unquenched wave functions is that between real and complex spherical harmonics. Those two sets of wave functions are linear combinations of each other, and both are solutions to the Schrödinger equation. But they are not equivalent when considering the orbital moment [3]. The total magnetic moment of a rare earth consists of spin and orbital magnetic moment. There is a good agreement between magnetic moments for the Lanthanide series in solids and isolated atoms [32].

1.2.1 Localized moments

The localized moment model assumes that the electrons in the unfilled shell¹⁶, which contribute to the magnetic moment, are localized in ionic sites in solids [32]. The root-mean-square radius of the 4f charge distribution is about 0.3 Å, of the order of 0.1 of the interatomic distance of about 3.6 Å, in the metallic state [33]. Hence, magnetic moments of rare earth magnets are very good representative examples of localized moments. Because of their large mass, spin-orbit coupling, which scales as Z^4 , dominates over all other magnetic energy scales. As a result, their magnetic moments are well predicted by the Hund's rules as shown in Table 1.4.

Ion	4f Shell	S	L	J	g	$m_{\text{eff}} = g\mu_B\sqrt{J(J+1)}$ (μ_B)	m_{exp} (μ_B)
Ce ³⁺	1	0.5	3	2.50	6/7	2.54	2.51
Pr ³⁺	2	1	5	4.00	4/5	3.58	3.56
Nd ³⁺	3	1.5	6	4.50	8/11	3.62	3.3-3.7
Pm ³⁺	4	2	6	4.00	3/5	2.68	*
Sm ³⁺	5	2.5	5	2.50	2/7	0.85	1.74
Eu ³⁺	6	3	3	0.00	-	0.00	3.40
Gd ³⁺	7	3.5	0	3.50	2	7.94	7.98
Tb ³⁺	8	3	3	6.00	3/2	9.72	9.77
Dy ³⁺	9	2.5	5	7.50	4/3	10.63	10.63
Ho ³⁺	10	2	6	8.00	5/4	10.60	10.40
Er ³⁺	11	1.5	6	7.50	6/5	9.59	9.50
Tm ³⁺	12	1	5	6.00	7/6	7.57	7.61
Yb ³⁺	13	0.5	3	3.50	8/7	4.53	4.50
Lu ³⁺	14	0	0	0.00	-	0.00	0.00

Table 1.4: Magnetic ground states for 4f ions using Hund's rules. The first column is the rare earth ions, almost always found in a trivalent state. The second column is the electron number in the 4f shell for each of them. From third to fifth, S , L and J are predicted based on Hund's rules. The sixth column g is calculated by formula 1.40. The final two columns are the calculated effective magnetic moments m_{eff} by using $g\mu_B\sqrt{J(J+1)}$ (For the derivation of effective magnetic moment formula, it can be introduced by considering the susceptibility of paramagnetic ions as discussed in Prof. J.M.D. Coey's book [1].) and experimentally measured m_{eff} respectively. The experimental values are obtained from measurements of the susceptibility of paramagnetic salts at temperature where $k_B T$ is much bigger than crystal field energy [34]. The symbol - means that the g value is not defined since it is divergent based on the formula 1.40. The symbol * means that the data is not available, because Pm³⁺ is radioactive.

The sign of the quadruple moment Q_2 reflects the shape of 4f electron cloud whether prolate (elongated, $Q_2 > 0$) or oblate (flattened, $Q_2 < 0$). It gives a measure of the charge distribution from a spherical shape. The unit of Q_2 is $C \cdot m^2$, where C is the coulomb - the standard unit of

quenched. In the 4f case, the spin-orbit coupling is large, the orbital motion of the electrons remains essentially unquenched by the crystal field. The opposite is true for 3d elements, where the spin-orbit coupling is smaller than the crystal field.

¹⁶For aluminium, zinc and silver, their ions have complete inner shells.

electric charge in the international System of Units (SI).

1.2.2 Delocalized moments

From the measurement of single crystal of transition metals, non-integral number of magnetic moments per atom are obtained, which are 2.17, 1.71, 0.60 μ_B for each Fe, Co, Ni atom [1]. Therefore, the localized model is not a realistic model to understand this non-integral values. Those 3d electrons are not closely bound, unlike 4f electron. They are further removed from the nucleus so are easily removed to form the conduction band. Those electrons, which are responsible for magnetism, are now itinerant and described by wave-like extended states forming the energy bands.

In addition, the value of paramagnetic susceptibility of most metals is much smaller than than would be expected from the Langevin model, essentially a localized model. The reason is that only those electron close to Fermi level are able to change spin direction and it is impossible for those well below Fermi level to change since there are no available state for them to occupy because of the Pauli exclusion principle. A net moment comes from the transfer of electrons at the Fermi level from the sub-band where spin moments are anti-parallel to the external magnetic field direction to the sub-band where spin moments are parallel to field direction. The energy shift is equal to $2\mu_B B$ where B is the magnitude of magnetic field. The associated spin contribution to susceptibility of conduction electrons is called Pauli paramagnetism.

After talking about paramagnetism based on band theory, it is time to discuss the band theory of ferromagnetism, which is an extension of the former one by the introduction of exchange coupling or interaction between the electrons. The band theory of ferromagnetism was first proposed by Stoner in 1933 and later by Slater in 1936 [8]. A rigid-band model will be used to show how band theory could explain the ferromagnetism of Fe, Co, Ni as shown in Figure 1.4. The rigid-band model assumes that the bands do not change much from one element to another, such as from the element Mn through to Zn. $N(E)$ curve shows the available levels. For different elements, the extent to which it is filled is indicated by the dashed lines. The topmost filled level for each element is called the Fermi level. As long as both bands 3d and 4s are partly filled, they must be filled to the same height. Ni has a total of 10 (3d+4s) electrons. The value of the magnetic moment of Ni metal indicates that 9.4 are in 3d band and 0.6 in 4s¹⁷. The Fermi level for Ni is just below the top of 3d band. Cu has one more electron so the 3d band is completely full¹⁸. Zn has 12 electrons, both 3d and 4s are full.

Fully occupied bands can't contribute a magnetic moment since two electrons in each level have opposite spin and thus cancel each other out. The exchange interaction is responsible for the imbalance in the spin up and spin down states instead of the electrons occupying the lowest state in a balanced pair. The decrement of energy due to the exchange effect with increase in the number of excess parallel spins outweighs the increase of energy due to the electrons close to Fermi level moving to states of higher energy state [37]. An example is given in Figure 1.5. In Figure 1.5 (a), those 10 electrons are in balanced pairs, without exchange interaction. When the exchange interaction is turned on, there is an imbalanced numbers of spin up and spin down electrons. Two of the spin down electrons are flipped to in the opposite direction as seen in Figure 1.5 (b). They occupy higher energy states but the reduction of energy due to exchange interaction favors this new state. Then this gives rise to a magnetic moment of 0.2 μ_B per atom. Therefore, the ferromagnetism of Fe, Co and Ni, is the result of a spin unbalance of 3d band. The 4s band is assumed to make no contribution to magnetism. Suppose one half of 3d is full. Let n and x represent the number of (3d+4s) and 4s electron respectively. Therefore, there are

¹⁷For comparison, in free Ni atom, 8 are in 3d and 2 are in 4s.

¹⁸ In 1936 Sir Nevil Mott proposed that in a scattering process, the s electrons can scatter into the many d states which available at Fermi level of d transition elements. Hence they experience a strong scattering, resulting in a considerable resistance. But for Cu, all 3d states are occupied and not available for scattering, which explains the high conductivity of Cu [35, 36].

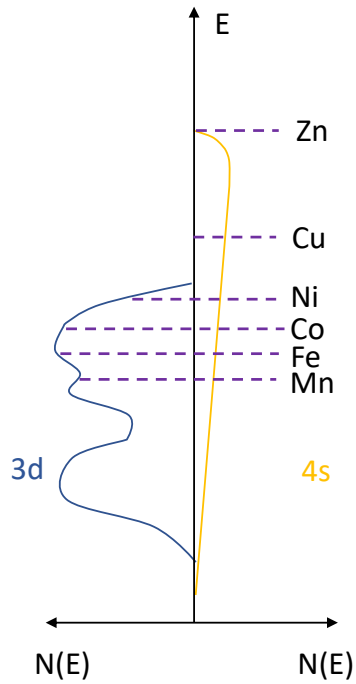


Figure 1.4: A schematic representation of density of states of 3d and 4s bands. $N(E)dE$ means the number of levels lying between the energies E and $E + dE$. The area under the $N(E)$ vs E curve is equal to the total number of levels in the band.

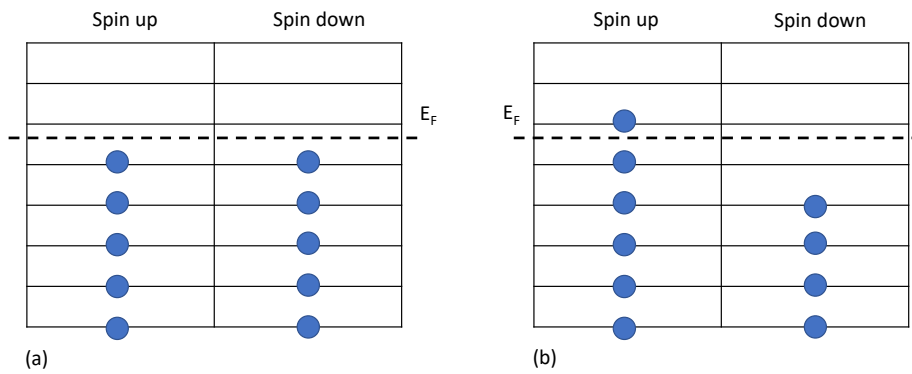


Figure 1.5: Energy bands with balanced and unbalanced spins: (a) balanced numbers of spin-up and spin-down electrons and (b) unbalanced numbers of spin-up and spin-down electrons due to the exchange interaction, leading to a net magnetic moment $0.2 \mu_B$ per atom. The dash line presents the Fermi energy level.

$n - x$ electron in 3d band. At saturation, five 3d electron have spin up and $n - x - 5$ spin down. The magnetic moment m per atom is

$$m = [5 - (n - x - 5)]\mu_B = [10 - (n - x)]\mu_B. \quad (1.42)$$

The n value for Fe, Co and Ni is 8, 9 and 10, respectively. Therefore, the calculated value of m for them are 2.60, 1.60, 0.60 μ_B respectively, which are not far away from the experimental values given before [9]. The difference comes from the use of rigid-band model. A better agreement can be reached by calculating the band structure of those pure metals individually.

1.3 The theory of magnetic order

1.3.1 Exchange interaction

Two basic mechanisms are at the roots of magnetic materials, exchange and anisotropy. Exchange arises from the combination of the electrostatic coupling between electron orbitals and the requirement to meet the Pauli exclusion principle. It can be thought as spin-spin interaction, favoring long-range spin ordering over macroscopic distances.

It might be thought the magnetic dipolar interaction plays an important role in magnetic materials. But it is not responsible for a high Curie temperature T_c of Fe, Co and Ni. The dipolar field sums to zero in Fe and Ni, because they are cubic, and the magnitude is only about 1 K in Co (hcp structure). The magnetic dipolar field \mathbf{B} created by a magnetic moment \mathbf{m} is:

$$\mathbf{B} = \frac{\mu_0}{4\pi} \left[3 \frac{(\mathbf{m} \cdot \mathbf{r}) \cdot \mathbf{r}}{r^5} - \frac{\mathbf{m}}{r^3} \right], \quad (1.43)$$

where the position vector \mathbf{r} goes from the magnetic moment \mathbf{m} to the point where field \mathbf{B} is measured¹⁹. Therefore, two magnetic moments \mathbf{m}_1 and \mathbf{m}_2 separated by \mathbf{r} have an energy given by:

$$E = \frac{\mu_0}{4\pi r^3} \left[\mathbf{m}_1 \cdot \mathbf{m}_2 - \frac{3}{r^2} (\mathbf{m}_1 \cdot \mathbf{r})(\mathbf{m}_2 \cdot \mathbf{r}) \right]. \quad (1.44)$$

By substituting the formula 1.43 into $E = -\mathbf{m} \cdot \mathbf{B}$ represents the energy of a magnetic moment in a magnetic field. It is very useful to make some order-of-magnitude estimate of this energy for two moments each of 1 μ_B separated by 0.1 nm. It is about 10^{-23} J which is equivalent to only about 1 K or 0.086 meV. So the magnetic dipolar interaction itself is quite unable to stabilize the magnetic order above room temperature like Co with a T_c of 1360 K.

The hydrogen molecule H_2 comprising two hydrogen nuclei fixed at a and b , and two electrons represented by symbol 1 and 2²⁰. The coordinates used for hydrogen molecule is shown in Figure 1.6. The wave equation for the two-hydrogen-atom reads

$$\mathcal{H}\Psi = E\Psi \quad (1.45)$$

with

$$\mathcal{H} = \left(\frac{p_1^2}{2m} - \frac{e^2}{4\pi\epsilon_0 r_{1a}} + \frac{p_2^2}{2m} - \frac{e^2}{4\pi\epsilon_0 r_{2b}} \right) + \left(\frac{e^2}{4\pi\epsilon_0 R_{ab}} + \frac{e^2}{4\pi\epsilon_0 r_{12}} - \frac{e^2}{4\pi\epsilon_0 r_{1b}} - \frac{e^2}{4\pi\epsilon_0 r_{2a}} \right) \quad (1.46)$$

For very large distance between R_{ab} , the normal state of the system consists of two normal hydrogen atoms. One electron is the one and the other electron on the other nucleus. Its wavefunctions (the state owning two-fold degeneracy) are $\Psi_I = \psi_a(\mathbf{r}_1)\psi_b(\mathbf{r}_2)$ and $\Psi_{II} = \psi_a(\mathbf{r}_2)\psi_b(\mathbf{r}_1)$

¹⁹The reason why it is called magnetic dipole field is that the field formula and the field pattern of \mathbf{m} are similar to those of electric dipoles [38]. But we do not have any evidence for the existence of magnetic charges.

²⁰The treatment is based on that given by Heitler and London in 1927 [39].

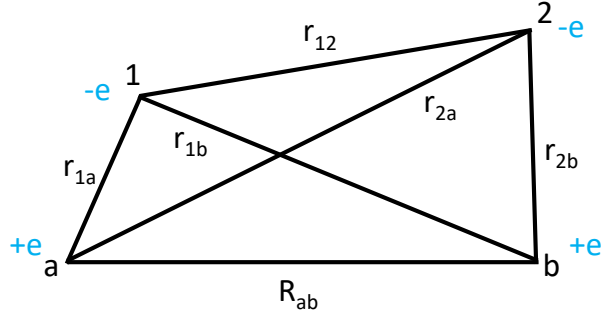


Figure 1.6: Coordinates for hydrogen molecules represented diagrammatically.

or any other two independent linear combinations of those two [40]. The $\psi_a(\mathbf{r}_2)$ represents that electron 2 about nucleus a . When the R_{ab} is getting smaller, a variational wavefunction can be taken as

$$\Psi = c_I \Psi_I + c_{II} \Psi_{II} \quad (1.47)$$

The solutions to this is better expressed in matrix notation where Ψ_I and Ψ_{II} are represented by vector (1,0) and (0,1) respectively. So Ψ is (c_I, c_{II}) . Since all wavefunctions under consideration are real (it was taken as 1s wavefunction of H atom in the original paper of Heitler and London), the equation can be expressed as an eigenvalue problem [39, 41]:

$$\begin{bmatrix} V & U \\ U & V \end{bmatrix} = (E - 2e_0) \begin{bmatrix} 1 & l^2 \\ l^2 & 1 \end{bmatrix} \begin{bmatrix} c_I \\ c_{II} \end{bmatrix} \quad (1.48)$$

where e_0 is the ground energy of one-particle Schrödinger equation and the various overlap integrals are defined as follows²¹:

$$\begin{aligned} 1 &= \int d^3r |\psi_a(\mathbf{r})|^2 = \int d^3r |\psi_b(\mathbf{r})|^2 \\ l &= \int d^3r \psi_a^*(\mathbf{r}) \psi_b(\mathbf{r}) \\ V &= \int \int d^3r_1 \int d^3r_2 |\Psi_I|^2 \left(\frac{e^2}{4\pi\epsilon_0 R_{ab}} + \frac{e^2}{4\pi\epsilon_0 r_{12}} - \frac{e^2}{4\pi\epsilon_0 r_{1b}} - \frac{e^2}{4\pi\epsilon_0 r_{2a}} \right) \\ &= \int \int d^3r_1 \int d^3r_2 |\Psi_{II}|^2 \left(\frac{e^2}{4\pi\epsilon_0 R_{ab}} + \frac{e^2}{4\pi\epsilon_0 r_{12}} - \frac{e^2}{4\pi\epsilon_0 r_{1a}} - \frac{e^2}{4\pi\epsilon_0 r_{2b}} \right) \end{aligned} \quad (1.49)$$

The solutions to it are the symmetric and antisymmetric orbital wavefunctions $\Psi_s = \Psi_I + \Psi_{II}$ and $\Psi_a = \Psi_I - \Psi_{II}$ respectively with the respective eigenvalues

$$E_{\pm} = 2e_0 + \frac{V \pm U}{1 \pm l^2} \quad (1.50)$$

where '+' represents the symmetric orbital wavefunction and '-' antisymmetric orbital wavefunction. Initially, when the two nuclei are far away, the total energy of the system is simply $2e_0$. But when two hydrogen atoms are getting close the degeneracy is lifted because of the nonzero overlap integral, which means that there exists a finite probability for the electron of a to belong to b [39].

So far, the spins of the electrons are not considered. The total wavefunction representing an actual state of a system having two or more electrons must be antisymmetric in the coordinates of the electrons, which means that when interchanging the coordinates of any two electrons, it must change its sign. This is the Pauli exclusion principle. Therefore, the symmetric orbital

²¹ $\mathcal{H}_{11} = 2e_0 + V$, $\mathcal{H}_{22} = 2e_0 + V$, $\mathcal{H}_{12} = 2el^2 + U$, $\mathcal{H}_{21} = 2el^2 + U$

wavefunctions must be multiplied by an antisymmetric spin function χ_a , and antisymmetric orbital wavefunctions must be multiplied by a symmetric spin function χ_s ²². So the total antisymmetric wavefunctions are $\Psi_s\chi_a$ and $\Psi_a\chi_s$. The energy separation between symmetric spin function and antisymmetric spin function is

$$\Delta E = E_- - E_+ = 2 \frac{Vl^2 - U}{1 - l^4} \quad (1.51)$$

and can be used to define an effective Hamiltonian by using dimensionless spin operators \mathbf{s}_1 and \mathbf{s}_2 for the two electrons

$$\mathcal{H} = -J_{12}\mathbf{s}_1 \cdot \mathbf{s}_2 \quad (1.52)$$

with energies given by

$$f(x) = \begin{cases} -\frac{J_{12}}{4}, & \text{if spin function is symmetric.} \\ +\frac{3J_{12}}{4}, & \text{if spin function is antisymmetric,} \end{cases} \quad (1.53)$$

where J_{12} is called the exchange constant. Compared with equation 1.51, the J_{12} is $-2\frac{Vl^2-U}{1-l^4}$. The sign of J_{12} depends on 'Coulomb integral' V , 'overlap integral' l and the 'exchange integral' U .

Heisenberg generalized equation 1.52 to many-electron atomic spins \mathbf{S}_1 and \mathbf{S}_2 , writing his famous Hamiltonian²³

$$\mathcal{H}_{Heis} = -\mathcal{J}\mathbf{S}_1 \cdot \mathbf{S}_2 \quad (1.54)$$

The exchange integral \mathcal{J} then has dimensions of energy. $J > 0$ indicates a ferromagnetic interaction, which tends to align the two spins parallel; $J < 0$ indicates an antiferromagnetic interaction, which tends to align the two spins antiparallel.

1.3.2 Mean field theory

There is a discrepancy of a factor of about 2600, since the Curie temperature of nickel is 627 K. Ferromagnetism was first explained phenomenologically by the molecular field theory of Pierre Weiss in 1906²⁴. It was based on the classical paramagnetism of Langevin by the application of Boltzmann's statistics. Although Langevin successfully explained Curie's law paramagnetism, the key question for ferromagnetism was unanswered. Why is the susceptibility of ferromagnets so much higher than that of paramagnets? In 1906, Weiss assumed the existence of a molecular field \mathbf{H}_m proportional to \mathbf{M} in addition to any external magnetic field \mathbf{H}

$$\mathbf{H}^i = \mathbf{H} + \mathbf{H}_m = \mathbf{H} + n_W \mathbf{M} \quad (1.55)$$

where \mathbf{H}^i is the internal molecular field and n_W is the Weiss coefficient (In practise, the Curie temperature is used to determine n_W).

The general expression for the thermodynamic average value of any quantity $\langle q \rangle$ is

$$\langle q \rangle = \frac{\sum_i q_i e^{(-\epsilon_i/k_B T)}}{\sum_i e^{(-\epsilon_i/k_B T)}} \quad (1.56)$$

where q_i is the value of q in the i^{th} one and ϵ_i is the energy of the i^{th} one.

The general quantum case of magnetism was treated by Léon Brillouin where $\mathbf{m} = -g\mu_B \mathbf{J}/\hbar$ as given previously in formula 1.39. The z-component magnetic moment m_{zi} is given by $-g\mu_B M_J$ where $M_J = J, J-1, J-2, \dots, -J$. An example of $J = 5/2$ is illustrated in Figure 1.7. The energy

²² $\chi_a = \frac{1}{\sqrt{2}} (|\uparrow\downarrow\rangle - |\downarrow\uparrow\rangle)$, $\chi_s = \frac{1}{\sqrt{2}} (|\uparrow\downarrow\rangle + |\downarrow\uparrow\rangle)$ and $|\uparrow\uparrow\rangle, |\downarrow\downarrow\rangle$ where the first arrow represents the electron 1 and second arrow for the electron 2. Each spin can point up or down.

²³Other conventions exist for exchange integral [24, 1].

²⁴The analogy between magnetization and fluids had been noticed by Pierre Curie. Weiss considered that the many aspects of paramagnetism are to ferromagnetism what ideal gases are to dense fluids. He invented the concept of a molecular field or mean field by stretching an analogy with van der Waals' theory of real gases [42, 43]

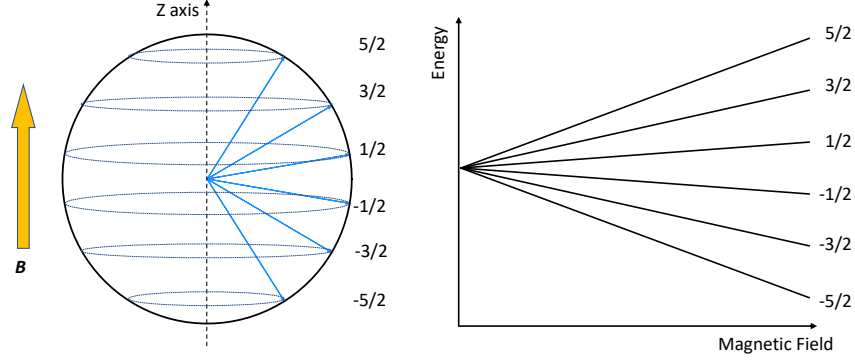


Figure 1.7: The Zeeman splitting of the magnetic energy levels in the field. A $J = 5/2$ quantum moment in an applied field whose direction is along the positive z -axis direction. The Zeeman shift is shown on the right where the energy spacing between neighboring state is $g\mu_B B$. The energy spacing increases with the applied field.

of a magnetic moment in a field is given by $-\mathbf{m} \cdot \mathbf{B} = -m_z B_z = -m_z B = g\mu_B M_J B$ here the direction of magnetic field is along the z -axis. The thermodynamics average $\langle m_z \rangle$ is given

$$\langle m_z \rangle = \frac{\sum_i m_{zi} e^{(-\epsilon_i/k_B T)}}{\sum_i e^{(-\epsilon_i/k_B T)}} \quad (1.57)$$

Setting $x = Jg\mu_B\mu_0 H/(k_B T) = m_0\mu_0 H/(k_B T)$, the equation can be expressed

$$\langle m_z \rangle = m_0 \left(\frac{2J+1}{2J} \coth \frac{2J+1}{2J} x - \frac{1}{2J} \coth \frac{x}{2J} \right) \quad (1.58)$$

where $m_0 = g\mu_B J$ is the maximum magnitude of the moment along the z axis, i.e., the field direction. The quantity in braces is called the Brillouin function $B_J(x)$:

$$\langle m_z \rangle = m_0 B_J(x) \quad (1.59)$$

The use of the above formula for fitting the paramagnetic salts, where magnetic moments do not interact with each other, gains a huge success. It reduces to the Langevin function $L(x) = (\coth(x) - 1/x)$ when J approaches infinity as illustrated in Figure 1.8. The generalization of this theory of paramagnetism to ferromagnetism is quite straight forward based on Weiss's idea as discussed already. The magnetization M along the field direction is given by the Brillouin function with $M_0 = nm_0 = ng\mu_B J$ where n is the number of magnetic atoms per unit volume,

$$M = M_0 B_J(x) \quad (1.60)$$

but now

$$x = \mu_0 m_0 (n_W M + H) / k_B T \quad (1.61)$$

Remember that $M_0 = nm_0$, we find

$$M/M_0 = (nk_B T / \mu_0 M_0^2 n_W) x - \frac{H}{n_W M_0} \quad (1.62)$$

The spontaneous magnetization can be found by letting $H = 0$ and solving equations 1.60 and 1.62 numerically or graphically. The graphical method is presented on the left of Figure 1.9. When the temperature is smaller than Curie temperature, there is an intersection point. It represents the reduced spontaneous magnetization M_s/M_0 at that temperature. On gradually increasing the temperature, M_s/M_0 is decreasing. It becomes 0 when the temperature reaches T_c , which is indicated by the blue line. Its slope is the same as that of the $B_{1/2}(x)$ at the origin. When the temperature is getting bigger, as shown by the green line, the origin is the only

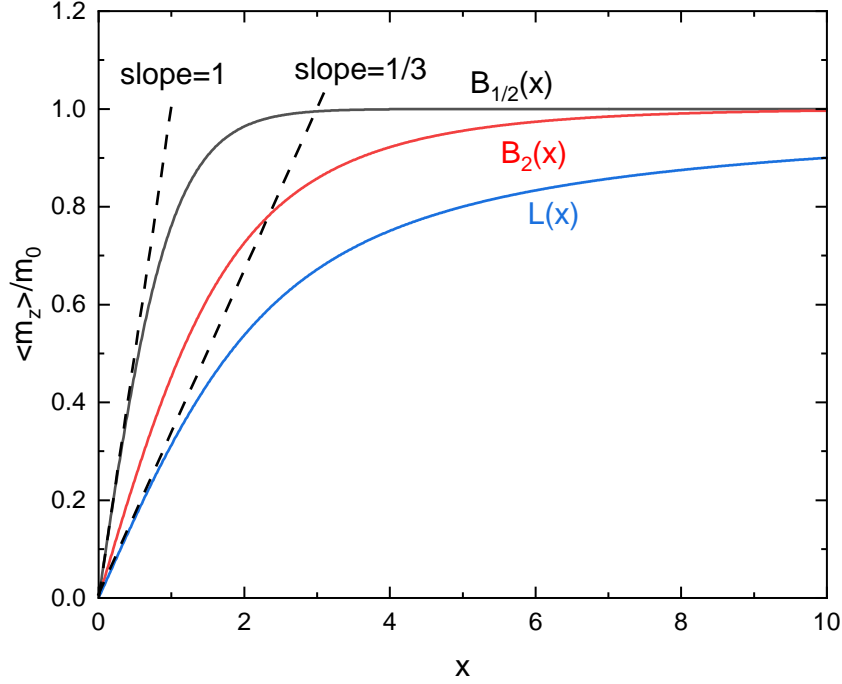


Figure 1.8: Comparison of Brillouin functions for $J = 1/2$ and $J = 2$ with Langevin function. The slopes at the origin of the Langevin and $B_{1/2}(x)$ are $1/3$ and 1 respectively.

intersection point, which means the magnetization is 0 and the sample does not have magnetic order. The thermal energy is dominant and the magnetic moment are pointing randomly in the system. Thermal disorder triumphs over magnetic order. The M_s/M_0 versus reduced temperature T/T_c is presented on the right of Figure 1.9 calculated using the numerical method, such as `scipy.optimize.fsolve` [44], to find the spontaneous magnetization for each temperature and then plot it.

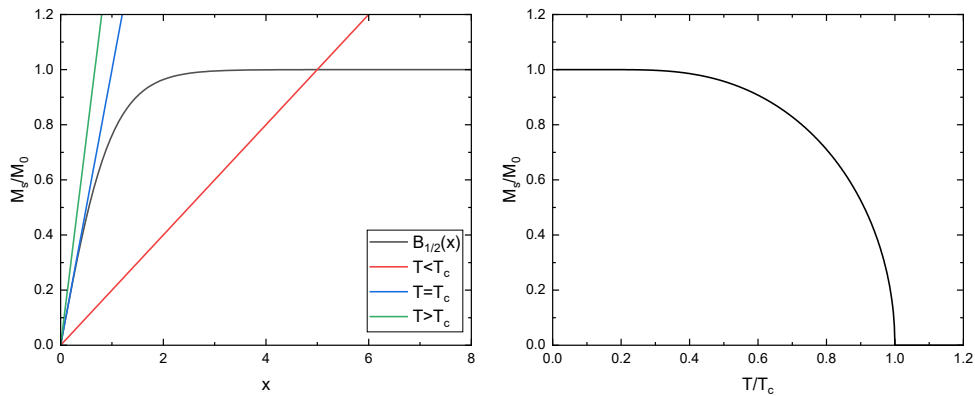


Figure 1.9: Graphical solution of the mean-field state equations: the left panel illustrates the graphical solution of equations 1.60 and 1.62 to find spontaneous magnetization. Here $J = 1/2$ and $g = 2$ are used. While the right panel displays the reduced spontaneous magnetization M_s/M_0 versus reduced temperature T/T_c .

1.3.3 Micromagnetism

In this section, domains, domain walls, the Stoner-Wohlfarth model for a single domain particle and micromagnetism governed by Landau-Lifshitz-Gilbert (LLG) equation will be discussed

sequentially [45].

Let's use a common phenomenon to introduce the domains. When an ingot of Co is made by some common methods like arc melting, the virgin sample typically does not show macroscopic magnetic property. The same piece of specimen however is attracted by a permanent magnet nearby. To explain those phenomena, it is necessary to take the dipolar interaction into consideration [46]. Micromagnetism is utilized to study magnetization phenomena on the intermediate scale between the atomic scale and macro scale. The very strong Heisenberg exchange interaction (falling off exponentially with spin separation in insulator) is still working at the atomic scale. But the long-range dipolar interaction (falling off only as the inverse cube of separation) does not favor that all magnetic moments point in the same direction in the bulk sample, which will build up a huge dipolar energy, also called magnetostatic energy. It is this long-range energy term that helps to form different region in the sample where moments point in one given direction. Those regions where magnetization is equal to saturation magnetization but the direction varies from place to place are known as magnetic domains. It was firstly predicted by P.Weiss in 1907 in his famous paper on the hypothesis of the molecular field. It was later observed by Barkhausen in 1919 by the indirect way of amplifying the voltage induced by changing magnetization and by Bitter in 1931 by applying a drop of ferromagnetic colloidal suspension to the polished surface of ferromagnetic specimen and observing the image of domain made visible by the fine ferromagnetic colloidal particles such as Fe_2O_3 [8]. The boundary of a domain, where magnetization changes direction, is known as domain wall.

From experiments, it is known that the domain walls have a dimension resulting from the balance between exchange interaction energy, which tends to increase the width of domain wall and anisotropy energy which tends to decrease it. There are two extreme cases as shown in Figure 1.10. When the anisotropy energy is bigger than exchange interaction energy, the spin must point up or down, i.e., a true Ising model as shown on the top of Figure 1.10. On the other hand, when anisotropy energy is smaller, it costs less for spins to point in the other directions and it is more important for them to point mostly in the directions of their neighbors [47], which causes the domain wall to be flat as presented on the bottom of Figure 1.10. The exchange

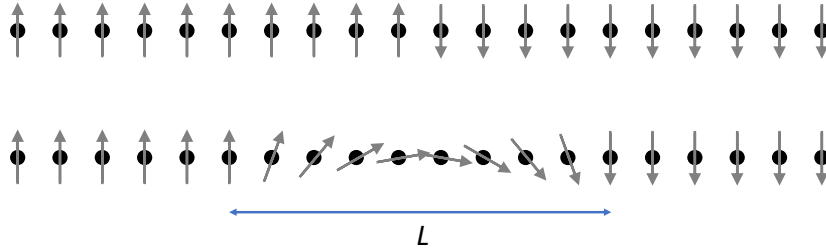


Figure 1.10: Schematic of domain wall structures. The top one is of a sharp domain wall. It happens when the anisotropy energy is very large, which dictates that the spin must point either up or down. The bottom one is of a *Néel* domain wall. The spin rotates continuously from up to down over a length L to save some cost of exchange interaction energy since the anisotropy energy is small.

energy between two neighboring spins can be written as

$$E = -\mathcal{J} \mathbf{S}_i \cdot \mathbf{S}_j = -\mathcal{J} S^2 \cos \theta_{ij} \approx -\mathcal{J} S^2 \left(1 - \frac{\theta_{ij}^2}{2} \right) \quad (1.63)$$

where \mathcal{J} is the exchange constant which has units of energy, θ_{ij} is the angle between neighboring spin vectors \mathbf{S}_i and \mathbf{S}_j and $\cos \theta_{ij}$ is expanded due to the smallness of θ_{ij} . When θ_{ij} is zero, the energy of exchange interaction is $-\mathcal{J} S^2$. When the θ_{ij} is not zero, the energy cost is $\mathcal{J} S^2 \frac{\theta_{ij}^2}{2}$. Let

us assume that the rotation angle between each pair of spins are equal to $\frac{\pi}{N}$ where N represents that the number of spins in the domain wall, which means that the spins rotates uniformly over the wall. Therefore, the total energy cost due to the N spins is $\frac{\mathcal{J}}{2}S^2\pi^2/N$. Until now, only one chain of spins in the wall is calculated and it has a length $L = Na$ where a is the lattice constant. In practise, the energy per unit area is more useful. In a square meter of wall, there are $\frac{1}{a^2}$ lines of spins. Therefore, the energy per unit area of domain wall σ_{DW} is

$$\sigma_{DW} = \frac{\mathcal{J}S^2\pi^2}{2Na^2} \quad (1.64)$$

From the above formula, it implies that the domain wall tends to grow in size through the whole sample if the anisotropy is negligible. However, this is not the case in reality. The anisotropy energy density with dimension $\frac{\mathcal{J}}{m^3}$. Let's assume a simple one, namely $K \sin^2 \alpha$ where K is an anisotropy constant with a unit of $\frac{\mathcal{J}}{m^3}$ and α is the angle between easy axis of anisotropy and the direction of local magnetization. If K is bigger than zero, the spins prefer to point along $\alpha = 0$ or $\alpha = \pi$. The anisotropy energy contribution from the N spins is

$$a^3 \sum_{i=1}^N K \sin^2 \alpha_i \approx a^3 \frac{N}{\pi} \int_0^\pi K \sin^2 \alpha d\alpha = a^3 \frac{NK}{2} \quad (1.65)$$

The energy contribution per unit area is $\frac{NKa}{2}$ by dividing the above energy term by a^2 . Combing those two formulas 1.64 and 1.65, the total energy per unit area of the domain wall is

$$\sigma_{DW} = \frac{\mathcal{J}S^2\pi^2}{2Na^2} + \frac{NKa}{2} \quad (1.66)$$

The first term tends to make the domain wall bigger, but the second tends to tighten it. The equilibrium state is achieved by using $\frac{d\sigma_{DW}}{dN} = 0$, which requires

$$N = \pi S \sqrt{\frac{\mathcal{J}}{Ka^3}} \quad (1.67)$$

Therefore, at the equilibrium state, the width of domain wall is

$$L = Na = \pi S \sqrt{\frac{\mathcal{J}}{Ka}} \quad (1.68)$$

and the σ_{DW} is

$$\sigma_{DW} = \pi S \sqrt{\frac{\mathcal{J}K}{a}} \quad (1.69)$$

When the particle size is small, it is possible to have a single domain particle. In this case, the Stoner-Wohlfarth model will be useful for modelling the magnetization behavior[24]. There are two ways to simulate quasi-static magnetization behavior. One is based on the energy equation, minimizing the total energy to reach the stable or meta-stable state²⁵. The alternative way is to use the dynamics equation, the LLG equation [48]. In the Stoner-Wohlfarth model for simulating magnetization behavior, the first one will be applied. For simplicity, only two energy terms are considered here, Zeeman energy and uniaxial anisotropy energy. The energy density of the system is

$$E = K \sin^2 (\theta - \phi) - \mu_0 H M_s \cos \phi \quad (1.70)$$

where θ is the angle between magnetic field \mathbf{H} and the easy axis of uniaxial anisotropy, ϕ is the angle between \mathbf{H} and magnetization \mathbf{M} , K is the anisotropy constant and M_s is the saturation

²⁵Magnetic hysteresis is essentially a metastable phenomenon.

magnetization²⁶. In this model, the magnitude of magnetization is assumed to be constant and only the direction of it is changing in order to obtain a local minimum energy. The equilibrium direction of magnetization is determined by satisfying the condition of local energy minimum:

$$\frac{\partial E}{\partial \phi} = -K \sin 2(\theta - \phi) + \mu_0 H M_s \sin \phi = 0 \quad (1.71)$$

This condition alone is not enough to determine the system completely [26]. In order to make the equilibrium stable, a second condition requires that

$$\frac{\partial^2 E}{\partial \phi^2} > 0 \quad (1.72)$$

It becomes unstable when

$$\frac{\partial^2 E}{\partial \phi^2} < 0 \quad (1.73)$$

The physical picture is that, when increasing the switching field gradually, the direction of magnetization is going to rotate to balance those two energy terms mentioned above. The coercivity field H_c for which the magnetization changes its direction is obtained when

$$\frac{\partial^2 E}{\partial \phi^2} = 2K \cos 2(\theta - \phi) + \mu_0 H M_s \cos \phi = 0 \quad (1.74)$$

At this critical point, the system is crossing from the metastable state to unstable state and immediately to a new metastable or stable state. Introducing a dimensionless quantity h given by

$$h = \frac{\mu_0 M_s H}{2K} \quad (1.75)$$

to simplify equations 1.71 and 1.74 and then solve them, the relation between θ and dimensionless critical field $h_c = \mu_0 M_s H_c / 2K$ where H_c is the critical field is

$$\sin 2\theta = \frac{1}{4h^2} \left(\frac{4 - 4h^2}{3} \right)^{\frac{3}{2}} \quad (1.76)$$

Figure 1.11 shows the h_c as a function of θ . The h_c reaches its minimum when $\theta = 45^\circ$, indicating that the switching of magnetization is most easy to happen. Being able to derive the analytical solution of the dependence of h_c on the angle θ between easy axis and field direction is nice. It is more useful to see directly energy surface as a function of θ and ϕ , which is illustrated in the Figure 1.12 (a) where θ is set to 45° . In this phase space, the order parameter magnetization follows the local minimum of energy. Figure 1.12 (b) shows the ϕ as a function of h which scans from $+2$ to -2 . When the field h is much bigger than 2 (not shown in the figure), the magnetization closely follows the field direction. With the decrease of h , the magnetization tilts a little bit away from the direction of field and points a direction between field direction and easy axis. When h equal to 0, the magnetization just simply follows the easy axis. When the field h reverses its direction as shown on the inserted schematic on the bottom left of Figure 1.12 (b), the magnetization tends to follow the field direction again. When the increase of the field reaches a critical point about 0.5, there is an abrupt change of ϕ , which means that the magnetization rotates to a state as shown on the top right schematic. A further enhancement of h tries to make the magnetization follow the field direction. At a field bigger than 2, the magnetization will essentially follow the field direction. Figure 1.12 (c) presents the magnetic hysteresis loop where \mathbf{M} is projected onto the field direction as measured usually in practise

$$M = M_s \cos \phi \quad (1.77)$$

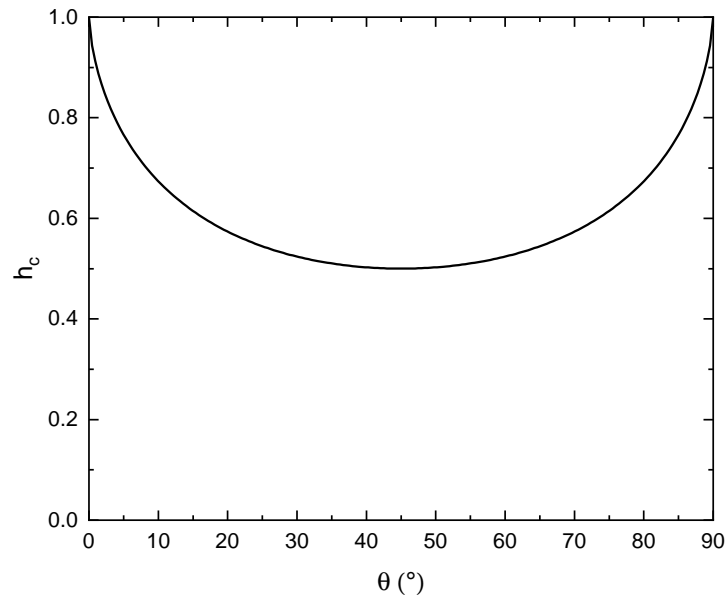


Figure 1.11: Dependence of the dimensionless critical field h_c on the θ angle between the applied field and the easy axis of uniaxial anisotropy.

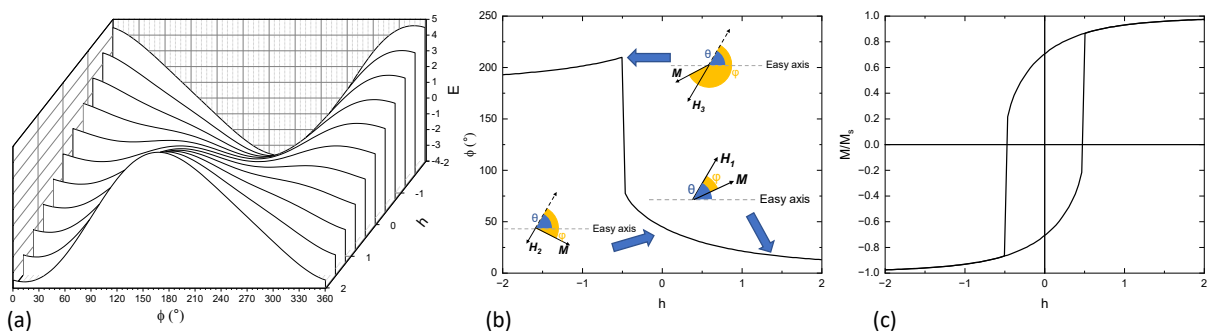


Figure 1.12: The Stoner-Wohlfarth model for single domain particles: (a) is the energy surface of function of ϕ and dimensionless field h when θ is 45° , (b) is the dependence of angle ϕ on h calculated the local minimum of energy from the energy surface by scanning field h from 2 to -2, (c) is the hysteresis loop made from the data in (b).

where M_s is the saturation magnetization.

Until now, the very important physical quantity of time does not appear in the process of magnetization. The dynamics of magnetization is essential in many spintronics applications determining how fast the magnetization switching can happen under the external stimulus such as applying pulsed magnetic field or injecting spin current, which can be answered or simulated in the micromagnetic framework. Within it, the magnetization is approximated by a continuous classical vector field with a constant magnitude whose dynamics is determined by the LLG equation [3]:

$$\frac{\partial \mathbf{m}}{\partial t} = -\frac{\gamma\mu_0}{1+\alpha^2}\mathbf{m} \times \mathbf{H}_{eff} - \frac{\gamma\mu_0\alpha}{1+\alpha^2}\mathbf{m} \times (\mathbf{m} \times \mathbf{H}_{eff}) \quad (1.78)$$

where the vector $\mathbf{m} = \frac{\mathbf{M}}{M_s}$ with unit 1, $\gamma = 1.76086 \times 10^{11} s^{-1} T^{-1}$ is the gyromagnetic ratio, α is the Gilbert damping constant and \mathbf{H}_{eff} is the effective field as discussed in the section 1.1.3. The first term on the right describes the precession of magnetization around the effective field and the second one describes the damping²⁷. The damping term causes the magnetization to spiral towards the effective field direction [49]. Damping is essential for any measurement in static magnetization where the hysteresis curves shows that above a certain value of applied field, the magnetization of a sample reaches its saturation value, i.e., all moments in the sample are aligned along the effective field direction. Without damping, the magnetization would just precess around the effective field direction forever and never align with it [1].

In Figure 1.13 a simulation of a macrospin is presented²⁸. The initial magnetic moment is pointing $1/\sqrt{3}(-1,-1,-1)$ direction in the Cartesian coordinate and the only effective magnetic field is the applied field 1.25 mT along the positive z axis. The dynamics of the macrospin is modelled by the LLG equation with damping constant $\alpha = 0.2$. Figure 1.13 (a) shows the time dependence of three components of the magnetic moment. The m_x and m_y show a damping oscillation behavior with a decreasing amplitude. The m_z is gradually switching to the field direction and reaches a saturation value 1. Figure 1.13 (b) is the 3-dimensional plot the vector of magnetic moment in real space. The color bar is utilized for showing the time sequence from 0 (corresponding to purple) to 1 (corresponding to red) with a time unit 120 ns. While the macrospin approximation is widely applicable, there are instances where incorporating a larger number of atoms becomes necessary, such as in the study of domain wall motion. This requirement can be fulfilled using various freely available software tools [48].

1.4 Magnetotransport

1.4.1 Magnetoresistance

Magnetoresistance (MR) is the change of resistance measured in the presence of magnetic field. Its magnitude is usually expressed by

$$MR = \frac{R(\mathbf{B}) - R(0)}{R(0)} \quad (1.79)$$

where $R(\mathbf{B})$ and $R(0)$ are electrical resistances in the presence and absence of a magnetic field²⁹, respectively [51]. Positive MR typically occurs in metals and semiconductors, while negative MR is observed in magnetic materials. MR is usually relatively weak effect in nonmagnetic compounds. In contrast, giant magnetoresistance (GMR) and colossal magnetoresistance (TMR)

²⁶Note the definitions for θ and ϕ here are different from previous ones when talking anisotropy section 1.1.3.

²⁷Actually, there are two forms of the equations, given by Landau and Lifschitz and Gilbert respectively. The equivalence of those two forms can be verified [7, 49].

²⁸The nonlinearity of LLG equation makes it hard to solve analytically and results in the use of numerical methods to solve. There are different numerical methods with their own strengths and weaknesses [50]

²⁹It can also be defined in terms of resistivity ρ .

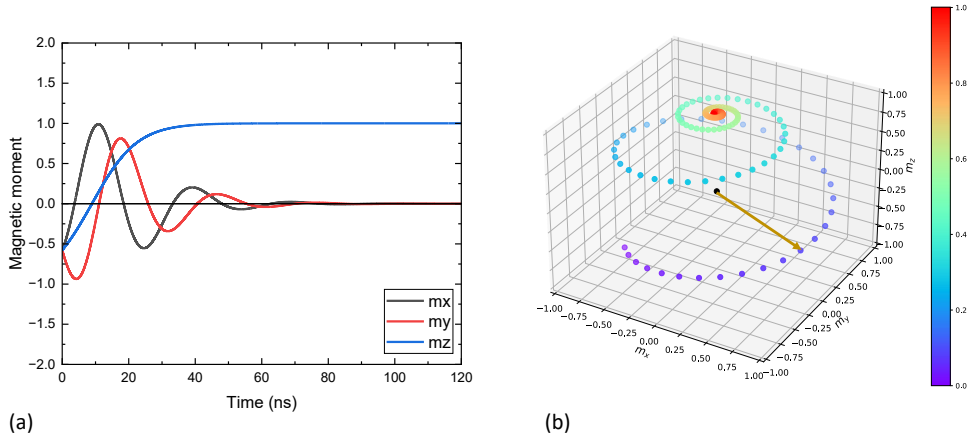


Figure 1.13: Macrospin dynamics simulation using the Landau-Lifshitz-Gilbert (LLG) model: (a) The figure illustrates the temporal changes in the three components of magnetization, namely m_x , m_y , and m_z , in response to an external magnetic field of 1.25 mT applied along the positive z-axis with a damping constant $\alpha = 0.2$ and a initial magnetic moment pointing $1/\sqrt{3}(-1, -1, -1)$ direction in the Cartesian coordinate, having a constant magnitude $|m| = 1$, (b) is the 3D plot of the magnetic moment as a function of time and the color bar is used for representing normalized time from 0 (corresponding to purple) to 1 (corresponding to red) with a time span of 120 ns. The arrows represent the magnetic moment which evolves with time.

occur in multilayers consisting of magnetic magnetic and nonmagnetic layers and in manganese-based perovskite oxides, respectively, showing values up to several orders of magnitude [52]. Materials with large MR have many applications such as data storage [1, 3].

Let us begin with a brief history of MR. More than one-and-half centuries ago, Lord Kelvin and Edwin Hall studied the electrical response of metals to magnetic fields [53, 54]. The first systematic study of MR is usually credited to Pyotr Kapitza, who reported high-field studies of MR in 37 different materials [55, 56]. His work contributed mainly two things. First, some materials were noticed to exhibit MR exceeding 100 % in a magnetic field of 30 T at room temperature, much higher than the others. Second, those materials studied showed a universal \mathbf{B} dependence. In small fields, it was always parabolic, consistent with the accepted understanding that cyclotron motion of electron should bend their paths and hence increase resistivity. However, in fields above several tesla, MR was found to increase linearly [57]. More recently, large MR effects at low temperature, different from GMR and TMR, have been reported for numerous materials, which have topological electronic phases [52].

Here, in this thesis, we focus on the MR in small fields in magnetic materials, which has a parabolic dependence of magnetic field. In the free electron theory, it predicts that the resistance of a sample perpendicular to a uniform magnetic field should not depend on the strength of the field. More specifically, the transverse Hall field is just enough to compensate for the deflection produced by the magnetic field, so that the path of each electron (or hole) is the same as if neither \mathbf{B} or transverse Hall field existed [58]. But, this does not apply to all cases, especially for the noble metals such as copper, silver and gold [46].

The two-band model is employed to derive the magnetoresistance's parabolic dependence on the magnetic field. First, let's solve a general vector equation:

$$\mathbf{E} = \mathbf{A} + a\mathbf{B} \times \mathbf{A} \quad (1.80)$$

where \mathbf{E} , \mathbf{A} , and \mathbf{B} are vectors without specific physical interpretations. From the elementary geometry, a solution can be found [58]:

$$\mathbf{A} = \frac{\mathbf{E} - a\mathbf{B} \times \mathbf{E}}{1 + a^2 B^2} \quad (1.81)$$

Suppose we have two kinds of carriers, for instance, electrons and holes. Now, the Drude model is going to be employed. The derivation of the below equation for electrons will be discussed in detail in the next section:

$$\mathbf{E} = \frac{\mathbf{J}_1 \times \mathbf{B}}{ne} + \frac{m}{ne^2\tau} \mathbf{J}_1 = -\frac{\mathbf{B} \times \mathbf{J}_1}{ne} + \frac{m}{ne^2\tau} \mathbf{J}_1 = R_{H1} \mathbf{B} \times \mathbf{J}_1 + \frac{\mathbf{J}_1}{\sigma_1} \quad (1.82)$$

Here, \mathbf{J}_1 represents the current density due to electrons having mass m_1 ; $\sigma_1 = \frac{ne^2\tau}{m_1}$ denotes the conductivity associated with electrons, and $R_{H1} = -\frac{1}{ne}$ represents the Hall coefficient of electrons. Similarly, for the holes, we have

$$\mathbf{E} = R_{H2} \mathbf{B} \times \mathbf{J}_2 + \frac{\mathbf{J}_2}{\sigma_2} \quad (1.83)$$

Here, \mathbf{J}_2 represents the current density contributed by holes having mass m_2 ; $\sigma_2 = \frac{ne^2\tau}{m_2}$ denotes the conductivity associated with holes, and $R_{H2} = \frac{1}{ne}$ represents the Hall coefficient of holes. The total current density is

$$\mathbf{J} = \mathbf{J}_1 + \mathbf{J}_2 \quad (1.84)$$

Using a solution of the form of equation 1.81 for each of 1.82 and 1.83 and introducing $\beta_1 = R_{H1}\sigma_1 = \frac{-e\tau}{m_1}$ and $\beta_2 = R_{H2}\sigma_2 = \frac{e\tau}{m_2}$, we get

$$\mathbf{J} = \left(\frac{\sigma_1}{1 + \beta_1^2 B^2} + \frac{\sigma_2}{1 + \beta_2^2 B^2} \right) \mathbf{E} - \left(\frac{\sigma_1 \beta_1}{1 + \beta_1^2 B^2} + \frac{\sigma_2 \beta_2}{1 + \beta_2^2 B^2} \right) \mathbf{B} \times \mathbf{E} \quad (1.85)$$

For MR, we need to compare \mathbf{J} with the component of \mathbf{E} along \mathbf{J} . Thus

$$\rho = (\mathbf{J} \cdot \mathbf{E})/J^2 = \frac{\left(\frac{\sigma_1}{1 + \beta_1^2 B^2} + \frac{\sigma_2}{1 + \beta_2^2 B^2} \right)}{\left(\frac{\sigma_1}{1 + \beta_1^2 B^2} + \frac{\sigma_2}{1 + \beta_2^2 B^2} \right)^2 + \left(\frac{\sigma_1 \beta_1 B}{1 + \beta_1^2 B^2} + \frac{\sigma_2 \beta_2 B}{1 + \beta_2^2 B^2} \right)^2} \quad (1.86)$$

The resistance in the absence of a magnetic field is

$$\rho_0 = \frac{1}{\sigma_1 + \sigma_2} \quad (1.87)$$

Based on the definition of MR, we get

$$MR = \frac{\Delta\rho}{\rho_0} = \frac{\rho - \rho_0}{\rho_0} = \frac{\sigma_1 \sigma_2 (\beta_1 - \beta_2)^2 B^2}{(\sigma_1 + \sigma_2)^2 + B^2 (\beta_1 \sigma_1 + \beta_2 \sigma_2)^2} \quad (1.88)$$

There are mainly three things we can learn from the formula above [58]:

- $\Delta\rho$ is proportional to B^2 for small fields and approaches to a saturation value at high fields.
- The MR vanishes if $\beta_1 = \beta_2$. The existence of MR in metals is a evidence for variation of β , i.e., different values of effective mass, or maybe a variation of β , over the Fermi surface since the transport property is mainly determined by those carriers around the Fermi surface.
- Suppose that both groups of carriers have the same value of τ . Then $\Delta\rho/\rho$ becomes a function of τB . But τ itself is inversely proportional to the ρ_0 , hence we can write $\frac{\Delta\rho}{\rho_0} = F\left(\frac{B}{\rho_0}\right)$ where F is a function, determined by the nature of the metal itself. This is known as *Kohler's Rule*.

1.4.2 Ordinary Hall effect

In 1879, Edwin Hall, working at John Hopkins university, noticed that a transverse voltage would appear when a current-carrying conductor is put in a perpendicular magnetic field. This effect, now called the ordinary Hall effect (OHE), arises from the reflection of conduction electrons by the Lorentz force [59, 60].

Drude model can be used to explain the ordinary Hall effect. Inside metals, there are many different kinds of collisions, which can be phenomenologically treated as a damping term $-\frac{\mathbf{p}(t)}{\tau}$ in the equation as shown in equation 1.89 where $\mathbf{f}(t)$ is the electric and/or magnetic fields and τ is the relaxation time or scattering time [46].

$$\frac{d\mathbf{p}(t)}{dt} = -\frac{\mathbf{p}(t)}{\tau} + \mathbf{f}(t) \quad (1.89)$$

After substituting Lorentz force for $\mathbf{f}(t)$, We now have equation [47]

$$\frac{d\mathbf{p}(t)}{dt} = -\frac{\mathbf{p}(t)}{\tau} - e(\mathbf{E} + \mathbf{v} \times \mathbf{B}). \quad (1.90)$$

In steady state, the left term becomes zero. And by using relations $\mathbf{p} = m\mathbf{v}$ and $\mathbf{E} = \frac{m}{e^2\tau n}\mathbf{J}$, the equation 1.90 becomes

$$0 = -e\mathbf{E} + \frac{\mathbf{J} \times \mathbf{B}}{n} + \frac{m}{ne\tau}\mathbf{J} \quad (1.91)$$

First, consider the case when only electric field is applied to bring out the relation between electric field \mathbf{E} and current density \mathbf{J} . Because $\mathbf{B} = 0$, $\mathbf{E} = \frac{m}{e^2\tau n}\mathbf{J}$ is obtained. From the material equation $\mathbf{E} = \tilde{\rho}\mathbf{J}$, we know

$$\rho_{xx} = \rho_{yy} = \frac{m}{n\tau e^2}. \quad (1.92)$$

Now magnetic field \mathbf{B} is turned on and oriented in the z direction. By writing out each component of equation 1.91, the equation 1.93 will be obtained.

$$\rho_{xy} = -\rho_{yx} = \frac{B}{ne}. \quad (1.93)$$

The Hall coefficient R_H is defined as $\frac{\rho_{yx}}{|\mathbf{B}|}$, which is $-\frac{1}{ne}$. In summary, when \mathbf{B} is applied along z axis, the general form of the resistivity tensor $\tilde{\rho}$ is

$$\begin{bmatrix} \frac{m}{n\tau e^2} & \frac{B}{ne} & 0 \\ -\frac{B}{ne} & \frac{m}{n\tau e^2} & 0 \\ 0 & 0 & \frac{m}{n\tau e^2} \end{bmatrix} \quad (1.94)$$

The discovery of ordinary Hall effect offered an elegant way to measure carriers' concentration more accurately in non-magnetic conductors and facilitated the development of semiconductor physics and solid-state electronics in the late 1940s.

1.4.3 Anomalous Hall effect

In 1880 and 1881, Hall found that in ferromagnetic materials such as nickel and iron the transverse voltage is an order of magnitude larger than that in normal metal like tin [54, 61]. This effect now is known as anomalous Hall effect (AHE). Despite the similarity between the OHE and AHE, the mechanism of AHE has remained controversial for decades. In 1954, Karplus and Luttinger performed the first serious calculation of the AHE. By introducing the spin-orbit

coupling in the energy bands, they proved that the Bloch electrons acquire an anomalous velocity which transverse to the applied electric current, resulting in a nonzero Hall current when summed over both components in a ferromagnet. Essentially, their model depends on the band structure and is independent of impurity scattering, which was questioned by others during that period. Shortly after that, Smit suggested that AHE can be explained by the asymmetric scattering amplitudes for spin-up and spin-down electrons in the presence of disorder and spin-orbit coupling (skew scattering). Later, Berger showed that the spin-orbit coupling could also result in a sudden transverse shift (side-jump) of the electron wave packet during the scattering event, contributing to the Hall current. Both skew scattering and side-jump are classified as extrinsic mechanisms. From the 1970s, debates surrounding the origin of AHE predominantly revolved around skew scattering and side-jump mechanisms, while the work of Karplus and Luttinger remained largely overlooked. It was until much later that the mechanism, proposed by Karplus and Luttinger, was interpreted as a Berry phase effect [60].

If the ordinary Hall effect and anomalous Hall effect were discovered at the macroscopic level, the other Hall related effects were found at the microscopic level over the years. One hundred year later, the spin Hall effect was reported in 1971 and integer quantum Hall effect in 1980. More recently observed, the quantum spin Hall effect in 2007 and the quantum anomalous Hall effect in 2013. Figure 1.14 shows the timeline of the discovered Hall-related effects [62]. For

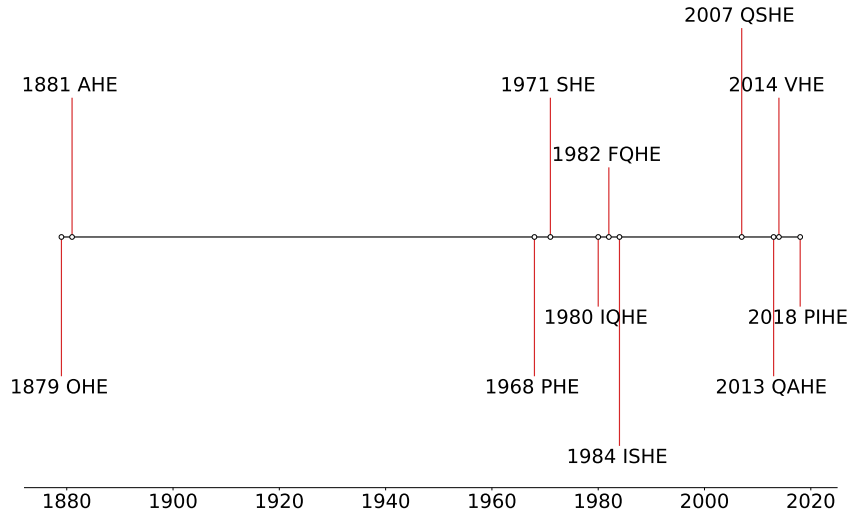


Figure 1.14: Timeline of the main Hall related effects. OHE—Ordinary Hall Effect; PHE—Planar Hall Effect; AHE—Anomalous Hall Effect; SHE—Spin Hall Effect; IQHE—Integer Quantum Hall Effect; FQHE—Fractional Quantum Hall Effect; ISHE—Inverse Spin Hall Effect; QSHE—Quantum Spin Hall Effect; QAHE—Quantum Anomalous Hall Effect; VHE—Valley Hall Effect; PIHE—Photo-induced Hall Effect.

a long time, anomalous Hall effect remained not-well understood. Only after the Berry phase approach was introduced, it became possible to gain a better understanding.

1.5 Ultrafast magnetism

1.5.1 Ferromagnets

In the 1980s, laser pulses of duration 10^{-11} and 10^{-8} second were used to address the time scale at which magnetic order of nickel can be quenched after sudden laser heating [63]. The first time-resolved experiments were performed by Vaterlaus and co-workers in the 1990s [64, 65]. After a rapid change of lattice temperature, a magnet needs time to establish its new equilibrium,

called the relaxation time of magnetization. The ferromagnet Gd, with a Curie temperature just below room temperature, was heated by 10 ns pump pulses. In order to determine the magnetic state of the heated ferromagnet Gd, the spin-polarization of the electrons emitted by 60 ps probe pulse was analysed. Based on this, the relaxation time of magnetization of Gd was found to be 100 ± 80 ps³⁰. In 1990's, an entirely new development was made possible by the commercial availability of fs pulsed laser sources. This development set the stage for the groundbreaking demonstration carried out by Eric Beaurepaire, Jean-Yves Bigot, and their colleagues in 1996. They were pioneers in the investigation of the demagnetization of nickel using 60 fs laser pulses [67]. They found that the magnetization in nickel thin films decreased rapidly within 2 ps followed by a relaxation to a long lived plateau as shown in Figure 1.15. The result was explained based on a 3-temperature model by assuming the existence of three thermalized reservoirs that exchange energy, namely, the electron system at temperature T_e , the spin system at temperature T_s and the lattice or phonons at temperature T_l . The time evolution of the system is described by a coupled differential equations with 3 interactions parameters, i.e., the electron-lattice, electron-spin and spin-lattice interaction constants³¹. This work initiated the development of research on ultrafast dynamics of magnetization [3]. Very recently, it was demonstrated that the polarized phonons carry angular momentum in ultrafast demagnetization [69].

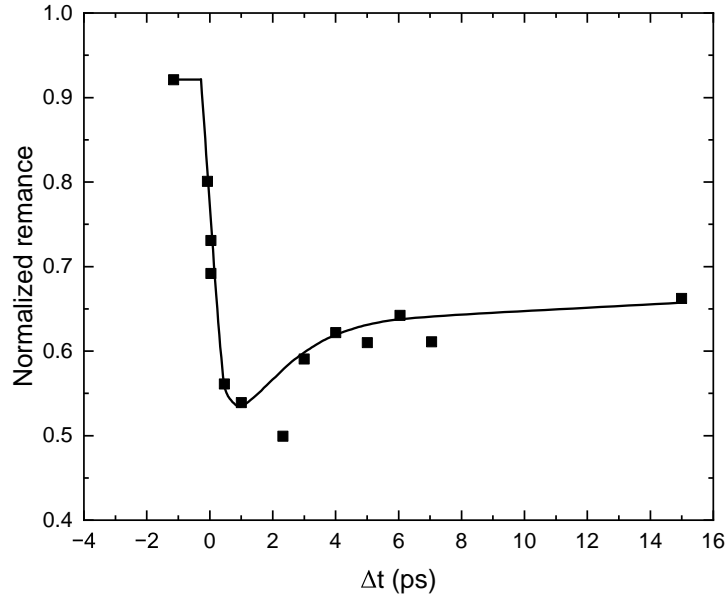


Figure 1.15: Transient remanent longitudinal MOKE signal of a Ni(20 nm)/MgF₂ (100 nm) film for 7 mJ cm⁻² pump fluence. The signal is normalized to the signal measured in the absence of pump beam. The line is a guide to the eye. Figure from [67].

1.5.2 Ferrimagnets

The field of ultrafast magnetism was boosted by the discovery of all-optical switching of magnetization. In 2007, the first demonstration of all-optical switching of magnetization was performed in a 20 nm amorphous ferrimagnetic GdFeCo thin film by using a single circularly polarized fs laser pulse as shown in Figure 1.16 (a). It is a rare-earth transition metal (RE-TM) alloy which has two different magnetic subnetworks which couple antiferromagnetically and a net

³⁰The ferromagnetism in Gd was discovered by G. Urbain, P. Weiss and F. Trombe in 1935 [66].

³¹The background of the 3-temperature model could be found in a paper in memory of Jean-Yves Bigot, Eric Beaurepaire, two pioneers of ultrafast magnetism, passed away on May 2, 2018 and April 24, 2018 [68]

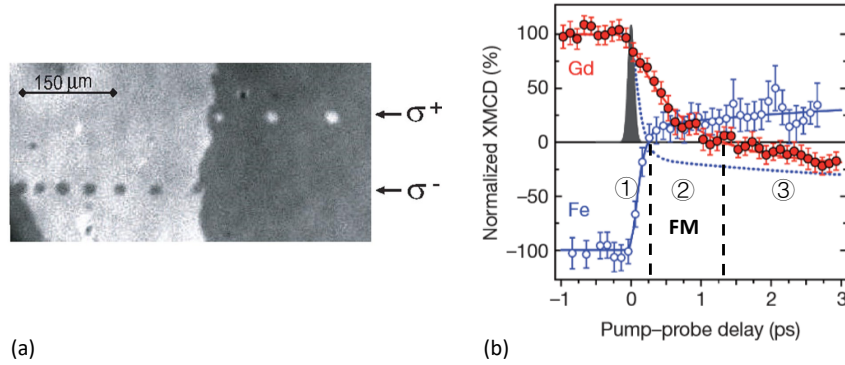


Figure 1.16: (a) Demonstration of SP-AOS in a-GdFeCo alloy thin films. The effect of a single 40-fs circularly polarized laser pulse on the magnetic domains in $\text{Gd}_{22}\text{Fe}_{74.6}\text{Co}_{3.4}$. The domain pattern was obtained by sweeping circularly polarized beams across the surface at high speed (≈ 50 mm/s), ensuring that each laser pulse landed at a different spot. The laser fluence was approximately 2.9 mJ/cm². The small variation in domain size is caused by the pulse-to-pulse fluctuation of the laser intensity. Figure extracted from [70]. (b) Time-resolved element-specific X-ray magnetic circular dichroism measurements on a GdFeCo thin film, showing the magnetization of Gd (filled circles) and Fe (open circles) over time following excitation by a linearly polarized 60-fs laser pulse. Figure extracted from [71].

magnetization is available since the unequal magnetization of those two subnetworks³². In 2012, a clearer demonstration was given when the magnetization in continuous a-GdFeCo film could be switched by using single linearly polarized laser pulse, which proves that single pulse all-optical switching (SP-AOS) is a purely thermal process [72]. In the same paper, the switching behavior was experimentally verified in isolated in-plane and out-of-plane microstructures of amorphous GdFeCo. The isolated microstructures excludes the possibility that the stray field from the unswitched surroundings medium plays a role for the SP-AOS. In the same year, the helicity dependence shown in Figure 1.16 (a) was attributed to the difference in absorption for left and right polarized light in magnetic materials [73], called magnetic circular dichroism.

A new insight to SP-AOS was actually observed earlier in 2011 using time-resolved element-specific X-ray magnetic circular dichroism measurement on the same system as shown in fig. 1.16 (b). The observed behavior is typically divided into 3 phases:

1. Different demagnetization rate of Gd and Fe. The magnetization of Fe reaches the zero earlier than that of Gd.
2. Fast Transfer angular momentum from Gd to the fully demagnetized Fe. It makes Fe builds up magnetization along the Gd magnetization direction. A transient ferromagnetic-like state appears.
3. The antiferromagnetic interaction between Gd (and Fe) recovers and pushes the Gd magnetic moment to switch after the system cools down. Eventually, the system completes the reversal of magnetization.

Later, the set of systems under study rapidly expanded, including various RE-TM alloys, multilayers and heterostructures [74]. For a quite long time, only in Gd-based amorphous ferrimagnetic films was it possible to observe the SP-AOS. In 2020, the crystal ferrimagnetic $\text{Mn}_2\text{Ru}_x\text{Ga}$ thin films was found by our group to show SP-AOS without Gd [75, 76].

³²Co and Fe are coupled together ferromagnetically, and they couple antiferromagnetically to Gd.

1.6 Amorphous materials and amorphous magnets

1.6.1 Amorphous materials

Since the discovery of the X-ray and X-ray diffraction in the early 1900s, extensive research has been conducted to investigate crystal structures. It was around the 1920s that scientists began delving into the realm of disordered crystals [77]. In 1960, in the lab Duwez demonstrated that it was possible to prepare certain alloys in an amorphous state by rapid cooling from the melt with sufficient celerity in order to prevent formation of the equilibrium crystalline structures [78]. The field of amorphous metals was born³³. In the general case amorphous metallic alloys are divided into two main groups: metal-metal and metal-metalloid [80]. Broadly speaking, the systems under study have progressively evolved toward greater disorder in accordance with the historical sequence as shown in Figure 1.18. It is not easy to obtain useful information by just looking at the distribution of N atomic centers (shown on the right side of Figure 1.18) when the N is very large number. The radial distribution function $G(r)$ is a useful representation of amorphous material structure. There are two equivalent definitions of $G(r)$:

$$G(r) = 4\pi r^2 \cdot \rho(r) = \frac{dN(r)}{dr}, \quad (1.95)$$

where $\rho(r)$ is the local density of atoms per unit volume and $N(r)$ is the number of atoms between r and $r + dr$ from an arbitrary central atom. What can we learn from $G(r)$? As may be seen in Figure 1.17 this has certain features which can be interpreted physically. It must be zero for a distance when r is small and then rises to a peak at some typical distance 3.2 Å, about the hard-core diameter of an atom. This is identified with the radius of the first coordination shell of atoms. By definition, the area under this first peak is the coordination number of the first coordination shell within the amorphous structure. Sometimes, it is convenient to define a normalized distribution function $g(r) = \frac{\rho(r)}{n}$ where n is the average density of atoms per unit volume, based on the assumption that the specimen is statistically homogeneous [81]. As the distance r increases, $g(r)$ approaches 1 because the atomic density becomes uniform when averaged over a large volume [1].

Glass³⁴ and other amorphous solids can consist of atoms, simple organic molecules, larger molecules such as polymers, or assemblies of colloidal particles. For many materials, making a glass is not difficult and a cooling rate about a few kelvin per minute is enough to avoid crystallization. However, for those having an efficient crystal nucleation, such as simple metals, glass formation can be challenging. In this case, extremely fast cooling is required with a cooling rate up to 10^9 K/s [82]. They have no crystal structure, which means there is no long range order and periodicity. The atoms are in a frozen, liquid-like state. Some basic thermal properties of amorphous materials can be measured via the thermal analysis techniques, such as differential scanning calorimetry in particular³⁵, which determine the glass transition temperature, crystallization temperature, melting temperature and so on [83]. Compared to crystals, the former two are unique to amorphous materials. The disorder introduces novel phenomena. For the thermal properties, there exists configurational specific heat as seen from the specific heat vs temperature curve. Notable among the electronic properties are localized state known as Anderson localization and the correlation between resistivity of disordered alloys containing transition metals and their negative temperature coefficients, known as the Mooij rule [84]. Important among the magnetic properties are random non-collinear magnetic structures and the influence of disorder on the magnetic moments and Curie temperature [85]. Sir Nevill

³³ A nice historical perspective of metallic glasses can be found in this review paper [79].

³⁴ As an ancient invention, colored glasses have been used for thousands years and can be observed in various places, including numerous churches. The Nobel Prize in Chemistry for 2023 has been awarded for groundbreaking work on quantum dots, a discovery that emerged within a glass matrix.

³⁵ The first known calorimeter was made Antoine Lavoisier and Pierre-Simon Laplace in the winter of 1782-83.

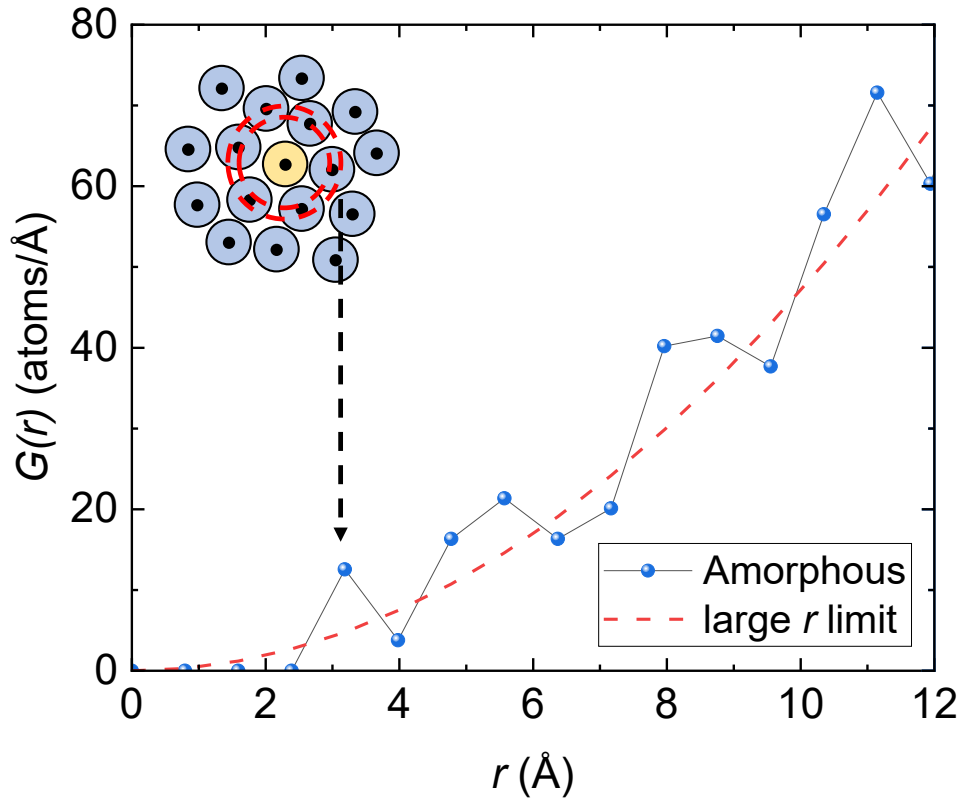


Figure 1.17: Features of the radial distribution function. The red dashed parabola is the large- r limit. At large distances, $G(r)$ tends to a parabola because the atomic density is uniform when averaged over a large volume, but at short distances the $G(r)$ shows a few peaks corresponding to different coordination shells.

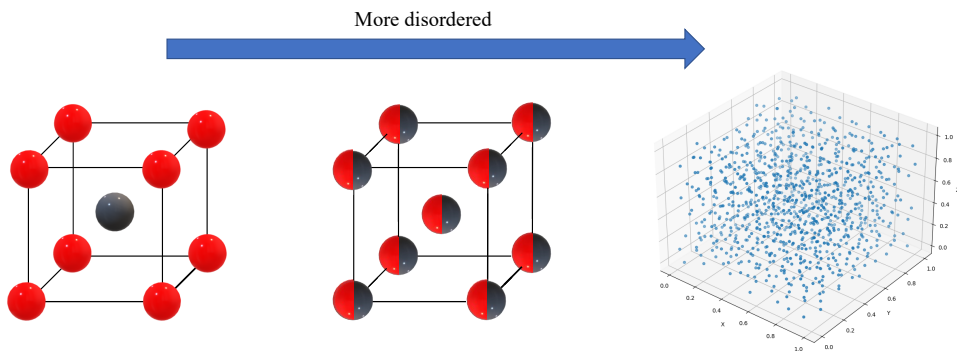


Figure 1.18: Illustration of Atomic arrangements in ordered and disorder systems. Two types of atoms represented by red and black circles. In the ordered crystal (left), each type of atom only occupies the certain sites. However, for the disordered crystal (middle), it still have a crystal structure but the atoms occupy the sites randomly. In amorphous materials (right), there is no crystal structure and atoms (only the centers of atoms are shown) arrange randomly. Moving from left to right, the system exhibits increasing disorder.

Francis Mott was awarded the 1977 Nobel Prize in Physics for his significant contributions to the field of amorphous materials [86].

For a long time, structural data obtainable from traditional experimental techniques, such as X-ray diffraction, were not enough to provide any information about the local structure of amorphous materials. Therefore, a different method is used, i.e., modeling. Models of those non-

crystalline structure were built in the laboratory or in the computer by using some algorithm. However, in recent years significant progress has been made experimentally for probing directly the local atomic structure of those amorphous systems, which is enabled by nano-beam electron diffraction and atomic electron tomography [87, 88, 89]. By applying Voronoi polyhedron analysis to those experimental results, a very detailed local atomic structure information can be obtained. The Voronoi polyhedron was defined by mathematician Georgy Voronoi firstly and then 'rediscovered' by physicists Eugene Wigner and Frederick Seitz³⁶. The name of Wigner-Seitz cells is very popular in condensed matter physics. Every polyhedron has enough information to describe uniquely the neighbourhood of the associated central point. The various types of Voronoi polyhedron are described by $(n_3n_4n_5\dots)$ for examining the local geometries or clusters found in amorphous systems where n_j refers to the number of faces with j edges that make up a given polyhedron [92, 93].

1.6.2 One network structure: such as YCo

These are the magnetic materials with a single magnetic network such as a-YCo₃ and a-Fe₈₀B₂₀. The reason why it is possible to have magnetism in amorphous materials goes back to exchange interaction, which is between the nearest atoms. Hence the periodicity of atoms is not essential [94]. Besides the exchange interaction (tending to align local moments with each other), there is another energy term, the local random anisotropy (coupling the individual moments to their local easy axes which are assumed to change from point to point) [95]. The competition between exchange interaction and local anisotropy enables many magnetic structures. When the exchange interaction is dominant, the magnetic moments are coupled strongly as shown in the left panel of Figure 1.19. The middle panel highlights the necessity of having at least two different elements in amorphous materials. When the local random anisotropy increases, it results in a cone angle in the distribution of magnetic moments as shown in right panel of Figure 1.19.

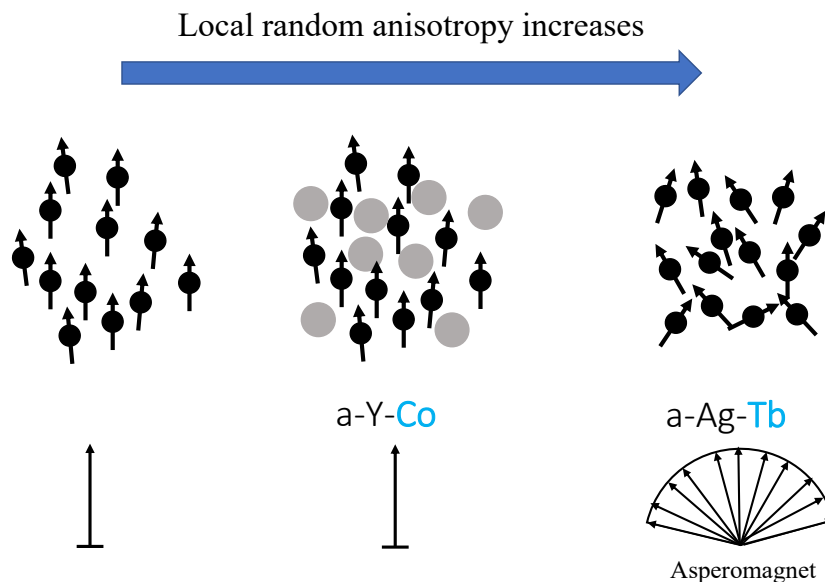


Figure 1.19: Schematic representation of one-subnetwork magnetic structures in amorphous solids. **Left:** Only magnetic atoms are shown with arrows representing the magnetic moments; **Middle:** As amorphous materials require at least two different elements, Y is used here; **Right:** The Tb moments distribution exhibits a cone angle, and Ag atoms are not plotted. The magnetic elements are highlighted in blue.

³⁶The Voronoi polyhedron has a lot of applications [90]. Very recently, it was applied in cosmology for measuring Hubble constant [91].

1.6.3 Two network structure: such as DyCo

It is possible to distinguish two magnetic subnetworks in amorphous solids based on the chemical basis. When the local random anisotropy is weak, we observe amorphous ferromagnet or amorphous ferrimagnet, as illustrated on the left side of Figure 1.20. However, as the anisotropy in one of the subnetworks strengthens, it results in a cone angle in the distribution of magnetic moments. The ferromagnet transitions to a speromagnet, and the ferrimagnet becomes a sperimagnet, as shown on the right side of Figure 1.20. Rare earth elements offer the flexibility to attain various magnetic structures by selecting different elements. Examples illustrating speromagnet (a-Nd-Co), ferrimagnet (a-Gd-Co), and sperimagnet (a-Dy-Co) configurations are provided in Figure 1.20.

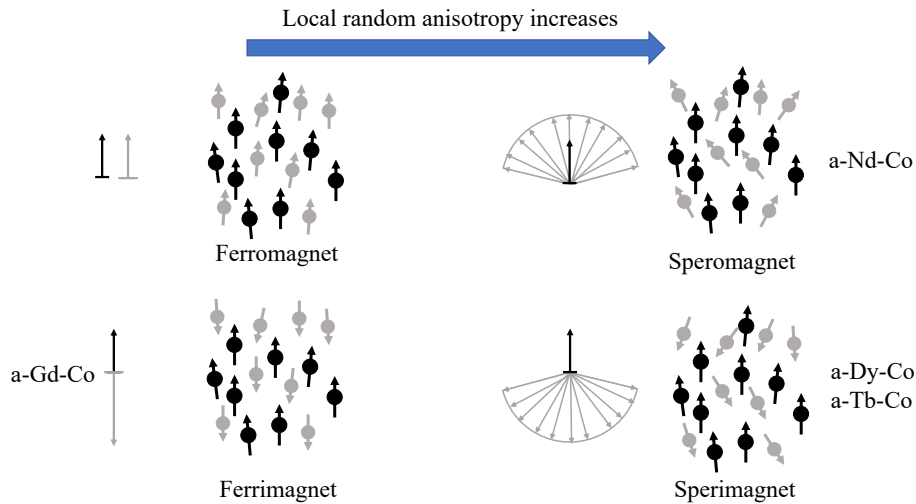


Figure 1.20: Schematic representation of two-subnetwork magnetic structures in amorphous solids. Please note that atomic sizes are not depicted to scale in this illustration. In the examples of a-Nd-Co, a-Gd-Co, a-Dy-Co and a-Tb-Co, a cobalt moment is depicted by a black arrow, while a rare earth moment is represented by a grey arrow.

Generally, they are the systems consisting of 3d and 4f atoms such as amorphous DyCo and TbFe system. Historically, the interest was speeded up by the experimental work of a-TbFe₂ which showed the existence of substantial magnetic anisotropy at a time when it was felt that anisotropy effects should be absent in non-crystalline solids [85]. It further stimulated Harris, Plischke, and Zuckermann to bring up their model for amorphous magnetism [96]. The magnetic moments of cobalt and light rare earths, such as Nd and Sm, are parallel but antiparallel for heavy rare earth and transition metals as seen in Figure 1.21. The reversal in the sign of coupling can be understood in terms of two facts [97]:

- An antiferromagnetic coupling of the spin angular momenta of the rare-earth and transition metals.
- $J = L + S$ and $J = L - S$ for heavy and light elements, respectively.

For a certain range of compositions, there might exist a compensation temperature where the net magnetization becomes zero, just like in crystalline ferrimagnets.

1.7 My PhD Project

My PhD project focuses on the nature of the noncrystalline structure and the noncollinear magnetism of amorphous R-T alloy thin films.

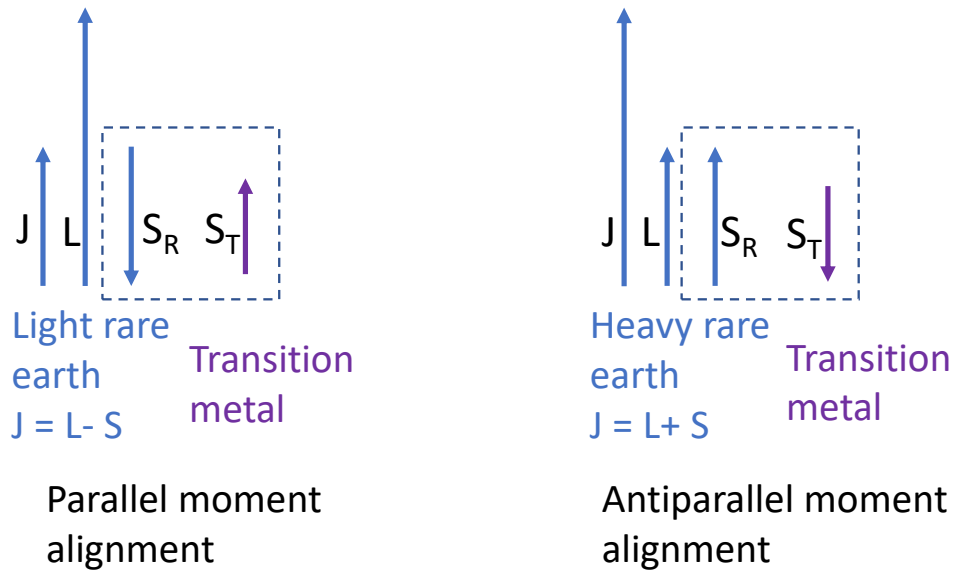


Figure 1.21: Relative spin orientations in the rare-earth-transition metal compounds.

First, magnetism, transport and atomic structure of binary $a\text{-Y}_x\text{Co}_{1-x}$ thin films with $0 \leq x \leq 0.54$ will be discussed in Chapter 3. This gives a basis for understanding the ferromagnetism of cobalt in other amorphous R-Co alloy thin films.

In chapter 4, it is found that replacing Y by Dy or Tb introduces a noncollinear magnetic structure in the amorphous $\text{Dy}_x\text{Co}_{1-x}$ and $\text{Tb}_x\text{Co}_{1-x}$ sputtered thin films, due to the strong local random uniaxial anisotropy at the rare earth sites.

Chapter 5 discusses a new type of single pulse partial all-optical switching, which is found in amorphous $\text{Dy}_x\text{Co}_{1-x}$ and $\text{Tb}_x\text{Co}_{1-x}$ with $x \approx 0.25$. Ringlike switched domain patterns show up at higher fluence, but below the fluence at which the anisotropy begins to change towards in-plane.

Finally, the thesis will end in Chapter 6 with the main conclusions arising from my work and outlook for future investigations.

References

- [1] J. M. D. Coey, *Magnetism and Magnetic Materials*. Cambridge university press, 2010. (Cited on page: [1](#), [4](#), [6](#), [7](#), [8](#), [9](#), [12](#), [13](#), [17](#), [24](#), [25](#), [31](#))
- [2] E. A. Guggenheim, *Thermodynamics-An Advanced Treatment for Chemists and Physicists*. North Holland, 1967. (Cited on page: [1](#))
- [3] J. M. D. Coey and S. S. Parkin, *Handbook of Magnetism and Magnetic Materials.*, vol. 1 and 2. Springer International Publishing, 2021. (Cited on page: [1](#), [7](#), [12](#), [24](#), [25](#), [29](#))
- [4] R. P. Feynman, R. B. Leighton, and M. Sands, *The Feynman Lectures on Physics; New millennium ed.* New York, NY: Basic Books, 2010. Originally published 1963-1965. (Cited on page: [1](#))
- [5] E. M. Purcell and D. J. Morin, *Electricity and Magnetism*. Cambridge University Press, 2013. (Cited on page: [1](#))
- [6] D. J. Griffiths, *Introduction to Electrodynamics*. Cambridge University Press, 4 ed., 2017. (Cited on page: [1](#))
- [7] G. Bertotti, *Hysteresis in magnetism: for physicists, materials scientists, and engineers*. Academic press, 1998. (Cited on page: [4](#), [24](#))
- [8] S. Chikazumi, *Physics of Magnetism*. Wiley, 1964. (Cited on page: [4](#), [5](#), [8](#), [9](#), [13](#), [20](#))
- [9] B. D. Cullity and C. D. Graham, *Introduction to Magnetic Materials*. John Wiley & Sons, 2011. (Cited on page: [5](#), [15](#))
- [10] K.Honda and S.Kaya, “On the magnetization of single crystals of iron,” *Science Reports*, vol. 15, pp. 721–752, 1926. (Cited on page: [5](#))
- [11] R. Skomski and D. Sellmyer, “Anisotropy of rare-earth magnets,” *Journal of Rare Earths*, vol. 27, no. 4, pp. 675–679, 2009. (Cited on page: [6](#))
- [12] K. Stevens, “Matrix elements and operator equivalents connected with the magnetic properties of rare earth ions,” *Proceedings of the Physical Society. Section A*, vol. 65, no. 3, p. 209, 1952. (Cited on page: [7](#))
- [13] B. Bleaney and K. Stevens, “Paramagnetic resonance,” *Reports on Progress in Physics*, vol. 16, no. 1, p. 108, 1953. (Cited on page: [7](#))
- [14] M. T. Hutchings, *Point-charge calculations of energy levels of magnetic ions in crystalline electric fields*, vol. 16. Elsevier, 1964. (Cited on page: [7](#))
- [15] V. Heine, *Group Theory in Quantum Mechanics: An Introduction to Its Present Usage*. Dover Publications, 2007. (Cited on page: [7](#))
- [16] B. Tomasello, C. Castelnovo, R. Moessner, and J. Quintanilla, “Single-ion anisotropy and magnetic field response in the spin-ice materials $\text{Ho}_2\text{Ti}_2\text{O}_7$ and $\text{Dy}_2\text{Ti}_2\text{O}_7$,” *Physical Review B*, vol. 92, no. 15, p. 155120, 2015. (Cited on page: [7](#))

- [17] J. M. D. Coey and S. Von Molnar, “Linear specific heat of an amorphous magnet due to single-ion excitations,” *Journal de Physique Lettres*, vol. 39, no. 18, pp. 327–330, 1978. (Cited on page: 7)
- [18] M. P. Marder, *Condensed Matter Physics*. John Wiley & Sons, 2010. (Cited on page: 7)
- [19] R. P. Feynman, R. B. Leighton, and M. Sands, *The Feynman Lectures on Physics; New millennium ed.* New York, NY: Basic Books, 2010. Originally published 1963-1965. (Cited on page: 7)
- [20] R. D. Cowan, *The Theory of Atomic Structure and Spectra*. Univ of California Press, 1981. (Cited on page: 8)
- [21] G. Herzberg and J. W. T. Spinks, *Atomic Spectra and Atomic Structure*. Dover Publications, 1944. (Cited on page: 8)
- [22] J. Herrero-Albillos, L. García, F. Bartolomé, and A. Young, “Breakdown of hund’s third rule for intrinsic magnetic moments,” *Europhysics Letters*, vol. 93, no. 1, p. 17006, 2011. (Cited on page: 8)
- [23] V. Kapaklis, P. T. Korelis, B. Hjörvarsson, A. Vlachos, I. Galanakis, P. Pouloupoulos, K. Özdoğan, M. Angelakeris, F. Wilhelm, and A. Rogalev, “Violation of hund’s third rule in structurally disordered ferromagnets,” *Physical Review B*, vol. 84, no. 2, p. 024411, 2011. (Cited on page: 8)
- [24] S. Blundell, *Magnetism in Condensed Matter*. Oxford University Press, 2001. (Cited on page: 9, 17, 21)
- [25] P. W. Atkins and R. S. Friedman, *Molecular Quantum Mechanics*. Oxford university press, 2011. (Cited on page: 9)
- [26] S. Chikazumi, *Physics of Magnetism*. Wiley, 1964. (Cited on page: 9, 22)
- [27] C. J. Foot, *Atomic Physics*. OUP Oxford, 2004. (Cited on page: 9)
- [28] A. Szilva, Y. Kvashnin, E. A. Stepanov, L. Nordström, O. Eriksson, A. I. Lichtenstein, and M. I. Katsnelson, “Quantitative theory of magnetic interactions in solids,” *Reviews of Modern Physics*, vol. 95, no. 3, p. 035004, 2023. (Cited on page: 10)
- [29] J. M. D. Coey, *Permanent Magnetism*. Institute of Physics Publishing, 1999. (Cited on page: 11)
- [30] J. Jensen and A. R. Mackintosh, *Rare Earth Magnetism*. Clarendon Press Oxford, 1991. (Cited on page: 11)
- [31] S. Mugiraneza and A. M. Hallas, “Tutorial: a beginner’s guide to interpreting magnetic susceptibility data with the curie-weiss law,” *Communications Physics*, vol. 5, no. 1, p. 95, 2022. (Cited on page: 12)
- [32] D. Jiles, *Introduction to Magnetism and Magnetic Materials*. CRC press, 2015. (Cited on page: 12)
- [33] W. C. Koehler and E. Wollan, “Paramagnetic scattering of neutrons by rare earth oxides,” *Physical Review*, vol. 92, no. 6, p. 1380, 1953. (Cited on page: 12)
- [34] G. H. Dieke, *Spectra and Energy Levels of Rare Earth Ions in Crystals*. John Wiley & Sons Inc, 1968. (Cited on page: 12)

- [35] K. Vetenskapsakademien, “The discovery of giant magnetoresistance, 2007,” *Scientific Background on the Nobel Prize in Physics*, p. 23, 2007. (Cited on page: 13)
- [36] N. F. Mott, “The electrical conductivity of transition metals,” *Proceedings of the Royal Society of London. Series A-Mathematical and Physical Sciences*, vol. 153, no. 880, pp. 699–717, 1936. (Cited on page: 13)
- [37] E. C. Stoner, “Collective electron ferromagnetism,” *Proceedings of the Royal Society of London. Series A. Mathematical and Physical Sciences*, vol. 165, no. 922, pp. 372–414, 1938. (Cited on page: 13)
- [38] E. M. Purcell and D. J. Morin, *Electricity and Magnetism*. Cambridge University Press, 2013. (Cited on page: 15)
- [39] W. Heitler and F. London, “Wechselwirkung neutraler atome und homöopolare bindung nach der quantenmechanik,” *Zeitschrift für Physik*, vol. 44, no. 6-7, pp. 455–472, 1927. (Cited on page: 15, 16)
- [40] L. Pauling and E. B. Wilson, *Introduction to Quantum Mechanics with Applications to Chemistry*. Dover Publications, New York, 1985. (Cited on page: 16)
- [41] D. C. Mattis, *The Theory of Magnetism I: Statics and Dynamics*, vol. 17. Springer Science & Business Media, 2012. (Cited on page: 16)
- [42] D. C. Mattis, *Theory Of Magnetism Made Simple, The: An Introduction To Physical Concepts And To Some Useful Mathematical Methods*. World Scientific Publishing Company, 2006. (Cited on page: 17)
- [43] J. Mehra, *The Solvay Conferences on Physics: Aspects of the Development of Physics since 1911*. Springer Science & Business Media, 2012. (Cited on page: 17)
- [44] P. Virtanen, R. Gommers, T. E. Oliphant, M. Haberland, T. Reddy, D. Cournapeau, E. Burovski, P. Peterson, W. Weckesser, J. Bright, S. J. van der Walt, M. Brett, J. Wilson, K. J. Millman, N. Mayorov, A. R. J. Nelson, E. Jones, R. Kern, E. Larson, C. J. Carey, Í. Polat, Y. Feng, E. W. Moore, J. VanderPlas, D. Laxalde, J. Perktold, R. Cimrman, I. Henriksen, E. A. Quintero, C. R. Harris, A. M. Archibald, A. H. Ribeiro, F. Pedregosa, P. van Mulbregt, and SciPy 1.0 Contributors, “SciPy 1.0: Fundamental Algorithms for Scientific Computing in Python,” *Nature Methods*, vol. 17, pp. 261–272, 2020. (Cited on page: 19)
- [45] J. Leliaert and J. Mulkers, “Tomorrow’s micromagnetic simulations,” *Journal of Applied Physics*, vol. 125, no. 18, p. 180901, 2019. (Cited on page: 20)
- [46] N. W. Ashcroft and N. D. Mermin, *Solid State Physics*. Brooks Cole, 1976. (Cited on page: 20, 25, 27)
- [47] S. H. Simon, *The Oxford Solid State Basics*. OUP Oxford, 2013. (Cited on page: 20, 27)
- [48] M. Beg, M. Lang, and H. Fangohr, “Ubermag: Toward more effective micromagnetic workflows,” *IEEE Transactions on Magnetics*, vol. 58, no. 2, pp. 1–5, 2022. (Cited on page: 21, 24)
- [49] T. L. Gilbert, “A phenomenological theory of damping in ferromagnetic materials,” *IEEE transactions on magnetics*, vol. 40, no. 6, pp. 3443–3449, 2004. (Cited on page: 24)
- [50] S. Wredh, A. Kroner, and T. Berg, “A comparison of three time-stepping methods for the llg equation in dynamic micromagnetics,” 2017. (Cited on page: 24)

- [51] A. B. Pippard, *Magnetoresistance in Metals*, vol. 2. Cambridge university press, 1989. (Cited on page: 24)
- [52] S. Zhang, Q. Wu, Y. Liu, and O. V. Yazyev, “Magnetoresistance from fermi surface topology,” *Physical Review B*, vol. 99, no. 3, p. 035142, 2019. (Cited on page: 25)
- [53] W. Thomson, “Xix. on the electro-dynamic qualities of metals:—effects of magnetization on the electric conductivity of nickel and of iron,” *Proceedings of the Royal Society of London*, no. 8, pp. 546–550, 1857. (Cited on page: 25)
- [54] E. H. Hall, “On the new action of magnetism on a permanent electric current,” *American Journal of Science*, vol. 3, no. 117, pp. 161–186, 1880. (Cited on page: 25, 27)
- [55] P. Kapitza, “The study of the specific resistance of bismuth crystals and its change in strong magnetic fields and some allied problems,” *Proceedings of the Royal Society of London. Series A, Containing Papers of a Mathematical and Physical Character*, vol. 119, no. 782, pp. 358–443, 1928. (Cited on page: 25)
- [56] P. Kapitza, “The change of electrical conductivity in strong magnetic fields. part i.—experimental results,” *Proceedings of the Royal Society of London. Series A, Containing Papers of a Mathematical and Physical Character*, vol. 123, no. 791, pp. 292–341, 1929. (Cited on page: 25)
- [57] N. Xin, J. Lourembam, P. Kumaravadivel, A. Kazantsev, Z. Wu, C. Mullan, J. Barrier, A. A. Geim, I. Grigorieva, A. Mishchenko, *et al.*, “Giant magnetoresistance of dirac plasma in high-mobility graphene,” *Nature*, vol. 616, no. 7956, pp. 270–274, 2023. (Cited on page: 25)
- [58] J. M. Ziman, *Principles of the Theory of Solids*. Cambridge university press, 1972. (Cited on page: 25, 26)
- [59] E. H. Hall *et al.*, “On a new action of the magnet on electric currents,” *American Journal of Mathematics*, vol. 2, no. 3, pp. 287–292, 1879. (Cited on page: 27)
- [60] Q. Niu, M.-C. Chang, B. Wu, D. Xiao, and R. Cheng, *Physical effects of geometric phases*. World Scientific, 2017. (Cited on page: 27, 28)
- [61] E. H. Hall, “On the "rotational coefficient" in nickel and cobalt,” *Proceedings of the Physical Society of London*, vol. 4, no. 1, p. 325, 1880. (Cited on page: 27)
- [62] A. Karsenty, “A comprehensive review of integrated hall effects in macro-, micro-, nanoscales, and quantum devices,” *Sensors*, vol. 20, no. 15, p. 4163, 2020. (Cited on page: 28)
- [63] M. Agranat, S. Ashitkov, A. Granovskii, and G. Rukman, “Interaction of picosecond laser pulses with the electron, spin, and phonon subsystems of nickel,” *Zh. Eksp. Teor. Fiz.*, vol. 86, no. 1376, p. 10, 1984. (Cited on page: 28)
- [64] A. Vaterlaus, T. Beutler, and F. Meier, “Spin-lattice relaxation time of ferromagnetic gadolinium determined with time-resolved spin-polarized photoemission,” *Physical review letters*, vol. 67, no. 23, p. 3314, 1991. (Cited on page: 28)
- [65] A. Vaterlaus, T. Beutler, D. Guarisco, M. Lutz, and F. Meier, “Spin-lattice relaxation in ferromagnets studied by time-resolved spin-polarized photoemission,” *Physical Review B*, vol. 46, no. 9, p. 5280, 1992. (Cited on page: 28)

- [66] K. Gschneider and L. Eyring, eds., *Handbook on the Physics and Chemistry of Rare Earths*, vol. 1: Metal. North Holland, 1979. (Cited on page: 29)
- [67] E. Beaupaire, J.-C. Merle, A. Daunois, and J.-Y. Bigot, “Ultrafast spin dynamics in ferromagnetic nickel,” *Physical review letters*, vol. 76, no. 22, p. 4250, 1996. (Cited on page: 29)
- [68] M. Agranat, S. Ashitkov, and A. Granovsky, “Two days in moscow by eric beaupaire and the background of the three-temperature model,” *Journal of Magnetism and Magnetic Materials*, vol. 502, p. 166474, 2020. (Cited on page: 29)
- [69] S. R. Tauchert, M. Volkov, D. Ehberger, D. Kazenwadel, M. Evers, H. Lange, A. Donges, A. Book, W. Kreuzpaintner, U. Nowak, and P. Baum, “Polarized phonons carry angular momentum in ultrafast demagnetization,” *Nature*, vol. 602, no. 7895, pp. 73–77, 2022. (Cited on page: 29)
- [70] C. D. Stanciu, F. Hansteen, A. V. Kimel, A. Kirilyuk, A. Tsukamoto, A. Itoh, and T. Rasing, “All-optical magnetic recording with circularly polarized light,” *Physical review letters*, vol. 99, no. 4, p. 047601, 2007. (Cited on page: 30)
- [71] I. Radu, K. Vahaplar, C. Stamm, T. Kachel, N. Pontius, H. Dürr, T. Ostler, J. Barker, R. Evans, R. Chantrell, *et al.*, “Transient ferromagnetic-like state mediating ultrafast reversal of antiferromagnetically coupled spins,” *Nature*, vol. 472, no. 7342, pp. 205–208, 2011. (Cited on page: 30)
- [72] T. Ostler, J. Barker, R. Evans, R. Chantrell, U. Atxitia, O. Chubykalo-Fesenko, S. El Mousaoui, L. Le Guyader, E. Mengotti, L. Heyderman, *et al.*, “Ultrafast heating as a sufficient stimulus for magnetization reversal in a ferrimagnet,” *Nature communications*, vol. 3, no. 1, p. 666, 2012. (Cited on page: 30)
- [73] A. Khorsand, M. Savoini, A. Kirilyuk, A. Kimel, A. Tsukamoto, A. Itoh, and T. Rasing, “Role of magnetic circular dichroism in all-optical magnetic recording,” *Physical review letters*, vol. 108, no. 12, p. 127205, 2012. (Cited on page: 30)
- [74] S. Mangin, M. Gottwald, C. Lambert, D. Steil, V. Uhlíř, L. Pang, M. Hehn, S. Alebrand, M. Cinchetti, G. Malinowski, *et al.*, “Engineered materials for all-optical helicity-dependent magnetic switching,” *Nature materials*, vol. 13, no. 3, pp. 286–292, 2014. (Cited on page: 30)
- [75] C. Banerjee, N. Teichert, K. Siewierska, Z. GerCSI, G. Atcheson, P. Stamenov, K. Rode, J. Coey, and J. Besbas, “Single pulse all-optical toggle switching of magnetization without gadolinium in the ferrimagnet $\text{Mn}_2\text{Ru}_x\text{Ga}$,” *Nature communications*, vol. 11, no. 1, p. 4444, 2020. (Cited on page: 30)
- [76] C. Banerjee, K. Rode, G. Atcheson, S. Lenne, P. Stamenov, J. Coey, and J. Besbas, “Ultrafast double pulse all-optical re-switching of a ferrimagnet,” *Physical Review Letters*, vol. 126, no. 17, p. 177202, 2021. (Cited on page: 30)
- [77] F. C. Nix and W. Shockley, “Order-disorder transformations in alloys,” *Reviews of Modern Physics*, vol. 10, no. 1, p. 1, 1938. (Cited on page: 31)
- [78] W. Klement, R. Willens, and P. Duwez, “Non-crystalline structure in solidified gold-silicon alloys,” *Nature*, vol. 187, no. 4740, pp. 869–870, 1960. (Cited on page: 31)
- [79] R. O’handley, “Physics of ferromagnetic amorphous alloys,” *Journal of applied physics*, vol. 62, no. 10, pp. R15–R49, 1987. (Cited on page: 31)

- [80] I. V. Zolotukhin and Y. E. Kalinin, “Amorphous metallic alloys,” *Soviet Physics Uspekhi*, vol. 33, no. 9, p. 720, 1990. (Cited on page: 31)
- [81] J. M. Ziman, *Models of disorder: the theoretical physics of homogeneously disordered systems*. Cambridge university press, 1979. (Cited on page: 31)
- [82] L. Berthier and M. D. Ediger, “Facets of glass physics,” *Physics today*, vol. 69, no. 1, pp. 40–46, 2016. (Cited on page: 31)
- [83] D. Janovszky, M. Sveda, A. Sycheva, F. Kristaly, F. Zámboorszky, T. Koziel, P. Bala, G. Czel, and G. Kaptay, “Amorphous alloys and differential scanning calorimetry (dsc),” *Journal of Thermal Analysis and Calorimetry*, pp. 1–17, 2021. (Cited on page: 31)
- [84] J. Mooij, “Electrical conduction in concentrated disordered transition metal alloys,” *physica status solidi (a)*, vol. 17, no. 2, pp. 521–530, 1973. (Cited on page: 31)
- [85] K. Moorjani and J. M. D. Coey, *Magnetic Glasses*. Elsevier, 1984. (Cited on page: 31, 34)
- [86] N. F. Mott, “Nobel lecture,” 1977. (Cited on page: 32)
- [87] A. Hirata, P. Guan, T. Fujita, Y. Hirotsu, A. Inoue, A. R. Yavari, T. Sakurai, and M. Chen, “Direct observation of local atomic order in a metallic glass,” *Nature materials*, vol. 10, no. 1, pp. 28–33, 2011. (Cited on page: 33)
- [88] Y. Yang, J. Zhou, F. Zhu, Y. Yuan, D. J. Chang, D. S. Kim, M. Pham, A. Rana, X. Tian, Y. Yao, *et al.*, “Determining the three-dimensional atomic structure of an amorphous solid,” *Nature*, vol. 592, no. 7852, pp. 60–64, 2021. (Cited on page: 33)
- [89] Y. Yuan, D. S. Kim, J. Zhou, D. J. Chang, F. Zhu, Y. Nagaoka, Y. Yang, M. Pham, S. J. Osher, O. Chen, *et al.*, “Three-dimensional atomic packing in amorphous solids with liquid-like structure,” *Nature materials*, vol. 21, no. 1, pp. 95–102, 2022. (Cited on page: 33)
- [90] W. Pokojski and P. Pokojska, “Voronoi diagrams—inventor, method, applications,” *Polish Cartographical Review*, vol. 50, no. 3, pp. 141–150, 2018. (Cited on page: 33)
- [91] S. Contarini, A. Pisani, N. Hamaus, F. Marulli, L. Moscardini, and M. Baldi, “Voids fill us in on rising cosmology tensions,” *arXiv preprint arXiv:2212.07438*, 2022. (Cited on page: 33)
- [92] J. Finney, “Random packings and the structure of simple liquids. I. the geometry of random close packing,” *Proceedings of the Royal Society of London. A. Mathematical and Physical Sciences*, vol. 319, no. 1539, pp. 479–493, 1970. (Cited on page: 33)
- [93] B. Gellatly and J. Finney, “Characterisation of models of multicomponent amorphous metals: The radical alternative to the voronoi polyhedron,” *Journal of Non-Crystalline Solids*, vol. 50, no. 3, pp. 313–329, 1982. (Cited on page: 33)
- [94] A. Gubanov, “Kvazi klassices kajateorija amorfnych ferromagnetikov,” *Fizika Tverdego Tela*, vol. 2, p. 502, 1960. (Cited on page: 33)
- [95] P. Hansen, “Magnetic amorphous alloys,” *Handbook of magnetic materials*, vol. 6, pp. 289–452, 1991. (Cited on page: 33)
- [96] R. Harris, M. Plischke, and M. Zuckermann, “New model for amorphous magnetism,” *Physical Review Letters*, vol. 31, no. 3, p. 160, 1973. (Cited on page: 34)
- [97] K. Taylor, “Intermetallic rare-earth compounds,” *Advances in Physics*, vol. 20, no. 87, pp. 551–660, 1971. (Cited on page: 34)

2 Experimental methods

Experiment is the only means of knowledge at our disposal. Everything else is poetry, imagination.

Max Planck

2.1 Magnetron Sputtering Thin Film Deposition

From the start of 1970s, the development in physics, chemistry and materials promoted new experimental techniques for manufacturing novel materials. Techniques that were introduced include for example sputtering, laser ablation, molecular epitaxy and chemical vapour deposition. The ability to grow multilayers and superlattices, facilitated the discovery and development of GMR [1]. During my PhD work, I mainly used magnetron sputtering.

It is a physical vapor deposition method like thermal evaporation. The verb *to sputter* originates from *sputare* (Latin, to emit saliva with noise). Sputtering is the ejection of atoms from the target caused by energetic atomic particles which typically are generated by an electrical discharge in a low-pressure gas. An electric field is built up between the target and the target holder shell or the substrate (depending on different system design). In order to increase the efficiency of ionization, a magnetic field is created by a set of permanent magnets. A magnetic field around the target enhances the possibility of collisions between electrons and neutral gas atoms by forcing the free electrons into helical paths around the magnetic field \mathbf{B} . Magnetron sputtering can be classified into two main types: direct current (DC) and radio frequency (RF) magnetron sputtering [2, 3]. The chamber B of Shamrock sputtering system in CRANN was used to grow samples during my PhD work as seen in Figure 2.1

2.1.1 Direct Current Magnetron Sputtering

In diode sputtering, the target always forms the cathode and the other parts of chamber acts as an anode. A high negative voltage is applied to the target. Under the right conditions of pressure and voltage, a plasma is generated because of electrons being accelerated away from the cathode leading to collisions with the sputter gas atoms, to create a cloud of ionized argon gas ions. The associated photon production emits light, hence the plasma typically has a very attractive visual effect. A range of parameters will influence the thin film samples quality, such as applied voltage, target current and sputter gas pressure. Compared with simple DC gas-discharge systems, DC magneton systems are more frequently used because they can be operated at lower pressure. This extends the electron path to the anode, thereby extending the time during which they can ionize the Argon atoms. This elongation of path and ionization time is more noticeable where the magnetic field is perpendicular to the electric field. However, the Ar^+ ions generated are almost not affected by the magnetic field because of their weight (thousands of times greater than the mass of electron) and so they only accelerate in the direction of target to strike the target and to remove material. A used targets exhibits a trench called an erosion profile as a consequence of ion bombardment from the plasma, as shown in the Figure 2.2. Another notable advantage of magnetron sputtering is the low chamber pressure so the mean free path will be in

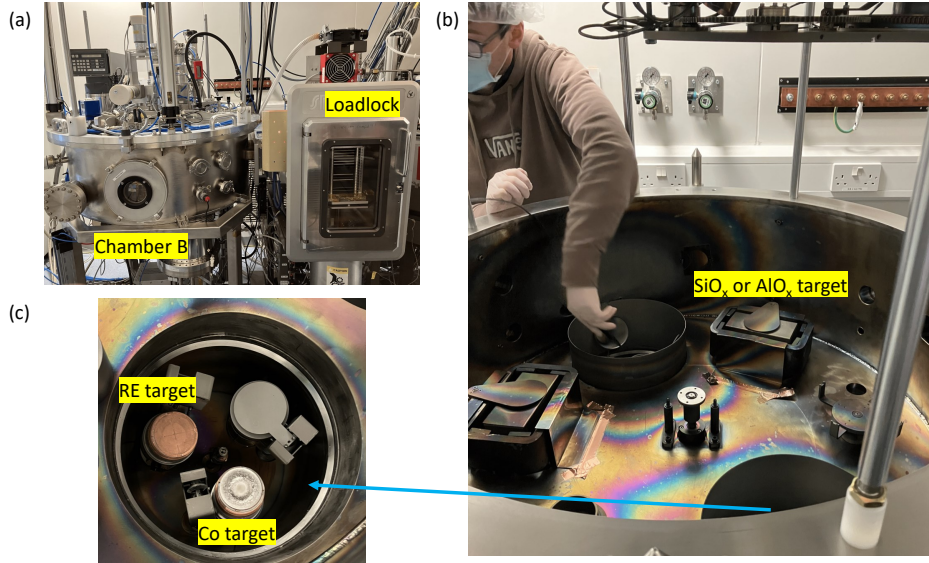


Figure 2.1: The Shamrock sputtering system consists of (a) a loadlock for loading samples, which are then transferred to Chamber B, (b) two clusters surrounded by cylinder shields for DC co-sputtering and three RF guns being used to deposit capping layers SiO_x or AlO_x , and (c) two DC guns for co-sputtering Co and RE targets respectively.

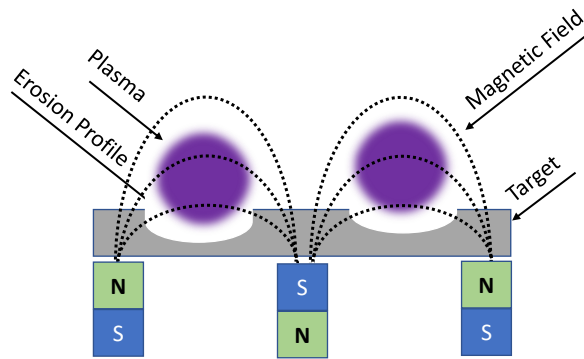


Figure 2.2: Erosion profile of a circular target.

the order of cm. Target atoms are less scattered in high vacuum than in rough vacuum. More dense films are obtained. The Shamrock sputtering system in CRANN used to make amorphous RE-Co has multiple targets so that alloys with different composition can be made flexibly from various pure metal targets by varying each individual target power and fixing the gas pressure. The Shamrock system uses the current to control the sputtering power. We usually fix the Co target current and adjust the RE targets to get the desired thin film samples with different compositions and thicknesses. Because of the lack of crystal structure, it is possible to get a series of samples with continuous composition ratio of RE without the limitation of the ordered compounds. All thin films studied during this PhD work were deposited by DC magnetron sputtering at room temperature on Si wafer substrates (n-doping with phosphorus) covered with 500 nm thermal oxide from Silicon Materials company. The large atomic size difference is the most important requirement for the growth of amorphous alloy films at room temperature [4]. In the Y-Co system, for instance, the relative difference of atomic radii of Y and Co is 33%.

During all depositions, no external magnetic field is applied¹. A good capping is necessary to protect samples from oxidation. For that, radio frequency magnetron sputtering is needed in order to deposit insulating protective coatings such as AlO_x and SiO_x .

2.1.2 Radio Frequency Magnetron Sputtering

The RF magnetron sputtering is very useful for depositing dielectric thin films such as capping layer SiO_x or AlO_x . The reason why it necessitates an RF power source is that those dielectric targets are not-conducting. Using DC power supply will end up with building electric charge there which hinders the bombardment process of ion in the target surface due to Column repulsion force between like charges. Therefore the power supply usually works at 13.56 MHz. For part of the cycle, the Ar^+ will bombard the target. For the rest of the cycle, the target has a negative bias so the electron is collected there to neutralize the positive charge built up on the dielectric target surface. What's more, an power supply, matching network module and tuner control module are also required. This right impedance matching is of huge practical significance, making the reflected energy to the power supply as small as possible. The mechanical analogy is that waves traveling along a string advance into the oil tank and disappear there [6]. The RF operation without a plasma will heat the source and damage it.

2.2 Crystallography

2.2.1 X-ray Diffraction

Because the interatomic distances in a solid are on the order of an Angstrom (10^{-10} m), X-rays, with a wavelength at the same order, are used to probe the spacing of the lattice plane of crystalline materials based on the Bragg's law:

$$n\lambda = 2d \sin \theta \quad (2.1)$$

where λ is the wavelength of the X-ray (e.g. Cu K_α is 0.154056 nm), n is a positive integer for the diffraction order, d is the atomic spacing and θ is the incident angle of X-ray. Since I work with amorphous materials, there is no peak from the amorphous samples. The only peak from X-ray diffraction is from the silicon substrate. The X-ray diffraction data will be presented in the following chapter.

2.2.2 X-ray reflectivity

X-ray reflectivity measures the reflected X-ray intensity as a function of the glancing incidence angle over a range of angles close to the critical angle θ_c for total external reflection which is due to materials with index of refraction n smaller than unity for X-rays [7]. It happens for X-ray because the frequency of X-ray is much higher than the resonant frequency of an electron bound in atom². In reality, the external reflection is only near-total due to the finite absorption of X-ray by the materials. Under lossless assumption, the critical angle θ_c is proportional to square root of electron density[8]. The electron density is equal to $\frac{\rho N_A}{M_r} Z$ where ρ is the mass density, N_A is the Avogadro constant, M_r is the molar mass and Z is the atomic number. Due to the fact that Co has almost twice the electron density of yttrium, Co has a bigger critical angle θ_c than yttrium (referring to the Figure 2.3).

X-ray reflectivity can be modeled and calculated exactly but the most intuitive and instructive view is the so-called Born approximation where multiple scattering effects are neglected. If

¹It is reported that, a uniaxial in-plane magnetic anisotropy is induced by applying 0.1 T field to the plane of film during growth of amorphous SmCo. [5]

²As derived in Feynman's lecture, $n - 1 \propto \frac{1}{(\omega_0^2 - \omega^2)}$

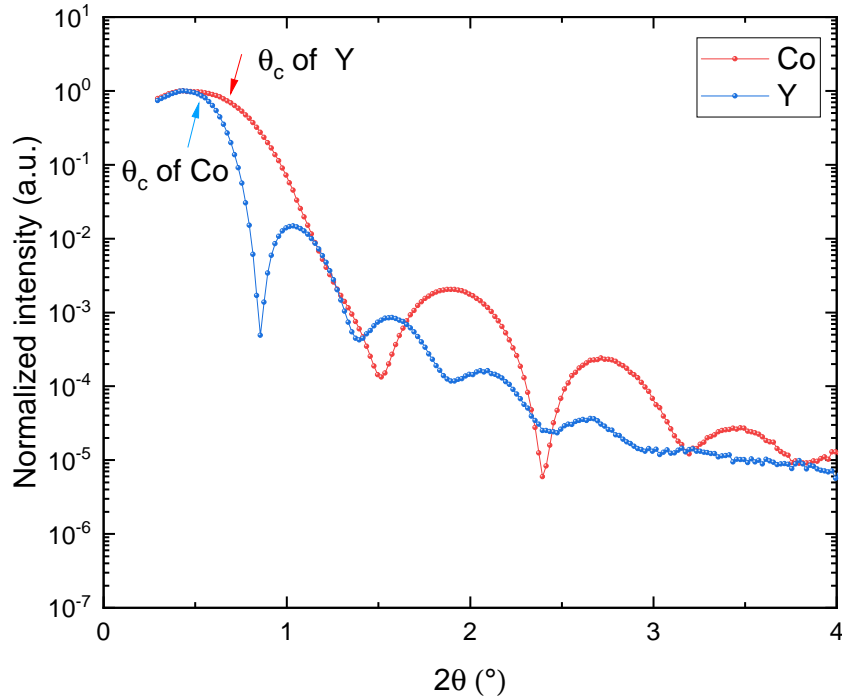


Figure 2.3: X-ray reflectivity of two pure metallic elements Co and yttrium.

momentum transfer Q is defined as $\mathbf{k}_i - \mathbf{k}_f$ where \mathbf{k}_i and \mathbf{k}_f are the wavevector of incident and scattered beam respectively, the reflectivity curve $R(Q)$ can be approximated by ³:

$$R(Q) \approx \frac{(16\pi^2)}{Q^4} \left| \int_{-\infty}^{\infty} \frac{d\beta}{dz} e^{-izQ} dz \right|^2 \quad (2.2)$$

where R is defined as the rate of specular reflective scattering divided by the rate of incidence and β is the scattering length density with unit m^{-2} [9]. β is proportional to the electron density for X-ray and the different layers of the sample can be defined by a piecewise function with corresponding thickness and scattering length density β . The above $R(Q)$ formula says that reflectivity is proportional to the absolute square of the Fourier transformation of the derivative of the scattering length profile and divided by Q^4 . For a sharp interface, a step function can be used for β , but for the more common rough interface, the error function $\text{erf}(x/\sigma)$ is preferred, using the σ parameter to take the interface roughness into consideration [10].

2.2.3 Different scan modes

The research presented in this PhD thesis primarily utilized the Phillips Panalytical X'Pert Pro machine. Its basic geometry is shown in Figure 2.4. It has a Cu-tube for producing X-ray radiation where the most intense emission line is K_α with wavelength 0.154056 nm. There are several scan modes, each having its own specific application [11]. The different angles are defined pictorially as shown in Figure 2.5.

Gonio Scan: The angle between incident beam and the sample surface is equal to that between the surface and the diffracted beam, i.e. $\omega = \theta$. That is why it is called symmetric scan as well. During this measurement, only the crystalline planes parallel to the surface are observed. It can be used for finding the critical angle of thin film samples for the X-ray reflectivity measurement based on the total external reflection discussed above.

³The relation between Q and grazing angle θ is that $Q = \frac{4\pi \sin\theta}{\lambda}$, so the curve can be converted to $R(\theta)$ which is closest to the experimental data.

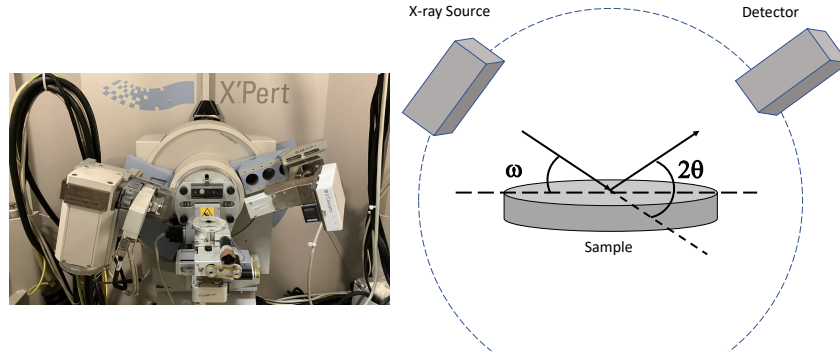


Figure 2.4: The Phillips Panalytical X'Pert Pro used for X-ray diffraction measurements. Essential features of X-ray diffractometer are a movable X-ray source and a detector on the diffractometer circle. Samples are mounted on the sample stage. The angle of incidence between the incident X-ray beam and sample surface is defined as ω . 2θ is the total angle by which the incident beam is deflected.

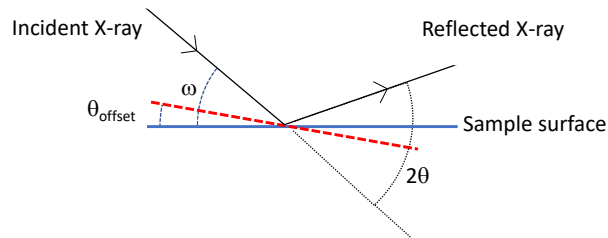


Figure 2.5: Definition of different angles in Phillips Panalytical X'Pert Pro machine.

$2\theta - \omega$ scan: It is similar to symmetric scan, but with an offset for the incident angle where it is zero for the Gonio scan, $\omega = \theta + \theta_{offset}$ where ω follows the half speed of the 2θ during scan.

2θ scan: The incidence angle is fixed but the detector moves so the 2θ is changing. It is used for aligning source and detector to make sure they are on the same straight line before loading sample onto the holder.

ω scan: X-ray source and detector are moved together while 2θ is kept at a fixed value. For 2θ fixed at 0 deg, ω scan is used for aligning the x-ray beam parallel to the sample surface.

The difference for set new zero and set the ω to half of the 2θ is the following:

- Set new zero: ω_{offset} becomes 0; current 2θ becomes 0.
- Set the ω to half of the 2θ : θ_{offset} becomes 0; current 2θ is still the same. The red dash line becomes the new axis. So the X-ray beam will travel along the red one when $\omega = 0$.

2.3 Magneto-transport

Magnetotransport provides a lot of information using transport-related phenomena such as magnetoresistance and Hall effect. Since the substrate has a thick thermal oxide layer on top, only the metallic thin film sample itself is measured, which is not the case for magnetometry measurements. Another advantage is the simplicity of the experimental setup and the relatively low cost. Most of magneto-transport measurements in this thesis were performed in 2 T GMW magnet and 5.5 T Cryomagnet located in the CRANN institute. The GMW machine operates

only at room temperature while the Cryomagnet is able to cool the sample environment down to 10 K.

2.3.1 Two and four points methods

Two points method uses a single source-measure unit to determine the resistance by the ratio of the voltage supplied to the current measured. It is a very convenient and quick way to check the conductivity of fresh thin films. But it is not accurate due to other contributions such as wire resistance and contact resistance. A better way to measure resistance is to use the four points method, by sourcing current across the outer most contacts and measuring voltage across the inner two contacts as presented in Figure 2.6 (a). The contact resistance between the sample and wire can be effectively removed since the current in the voltage meter is extremely small so the voltage across the contact can be negligible. There are some correction factors for the measurement of resistivity because of the geometry configuration of four contacts and finite thickness of thin film samples [12, 13]. A Keithley 2400 in 4-wire mode can be used to do four points measurement and is controlled by a LabVIEW program. In practise, it is able to measure in-plane and out-of plane magnetoresistance when the magnetic field is applied in-plane and out-of plane respectively as depicted in Figure 2.6. The longitudinal magnetoresistance is referred to (b). The transverse magnetoresistance also called planar Hall effect is referred to (c). It is called out-of plane magnetoresistance in (d). Ideally, the magnetic field should be big enough to saturate the in-plane and out-of plane magnetizations [14].

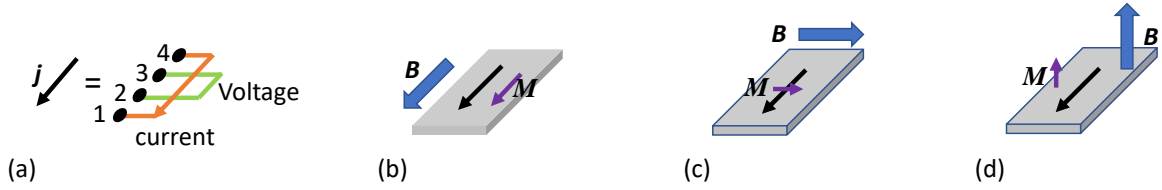


Figure 2.6: The geometry of in-plane and out-of plane magnetoresistance measurement via four points method. (a) the four points method as described in the context, (b) current density j parallel to magnetization M , (c) current density j transverse (in 90 degrees) to magnetization M and (d) magnetic field is applied out-of plane, current density j perpendicular to magnetization M

2.3.2 Van der Pauw Method

In 1958, Leo J. van der Pauw discovered a method of measuring the resistivity of flat samples of arbitrary shape if the contacts are small compared with sample size and located on the sample's periphery [15, 16]. The sample should be singly connected, i.e., the sample should not have isolated holes [17].

Numbering the contacts A, B, C and D in sequence around the boundary of sample, van der Pauw defines the resistance $R_{AB,CD}$ as the potential difference $V_D - V_C$ between contacts D and C per unit current through the contacts A and B. Similarly he defines the resistance $R_{BC,DA}$. As proved in his paper, there is a very useful formula for calculating the resistivity

$$e^{-\pi R_{AB,CD}d/\rho} + e^{-\pi R_{BC,DA}d/\rho} = 1 \quad (2.3)$$

where ρ is the resistivity and d is the thickness of sample. For the proof, a mathematical relation called Cauchy-Riemann is needed, which is a conformal mapping of two-dimensional field [7, 18].

The Hall coefficient R_H can be measured as well, by injecting current which enters at contact A and leaves at contract C measuring voltage between contact B and D.

$$R_H = \frac{d}{B} \Delta R_{AC,BD} \quad (2.4)$$

where $\Delta R_{AC,BD}$ represents the change of $R_{AC,BD}$ because of applying a uniform magnetic field perpendicular to sample surface. It is calculated by dividing $\Delta(V_B - V_D)$ by the injected current i_{AC} [16]. The Hall coefficient derivation does not rely on the conformal mapping.

The 2 T GMW setup is shown in Figure 2.7. The Keithley 2400 source meter is set to 4-wire mode. Through two co-axial cables, source meter is connected to the sample holder, to which the sample is secured by using silver wires that are fixed onto the sample surface by pressing indium metal. The 5.5 T Cryomagnet is illustrated in Figure 2.8. The sample holder is used to

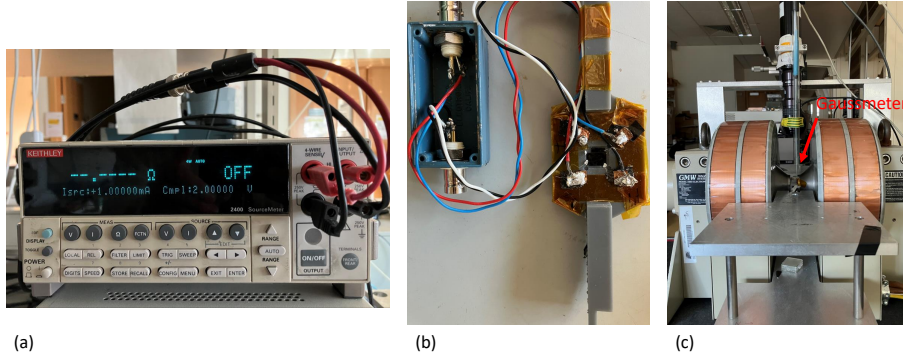


Figure 2.7: 2 T GMW setup. (a) the Keithley 2400 with current output and voltage measurement input, (b) sample holders with two co-axial cables for injecting current and measuring voltage and (c) the electromagnet with water cooling and a Gaussmeter for measuring the applied field.

mount the samples, which are then loaded into the large cylinder tube. The tube is connected to many cables for sending current, measuring voltage, monitoring temperature and communicating data and commands. The high field is provided by a superconducting magnet controlled by the power supply shown on the bottom. The pump system is used to pump the sample space into low pressure so that it allows to cool down to 10 K by the helium Joule-Thomson refrigerator [19].

2.3.3 Hall bars

Patterning a Hall bar onto the thin films is very important for precise electrical measurements since the dimensions of the bar could be measured accurately and the current direction is well-defined, which are very critical for Hall data analysis. Figure 2.9 illustrates the Hall bar geometry used for my transport work with a bridge width $W = 15 \mu m$ and $L = 50 \mu m$, and a current of no bigger than 1 mA is applied in order to reduce the heat generation. About how to convert the measured raw data into useful physical quantities such as ρ_{xx} and ρ_{yx} , it is shown in the Appendix section 7.6. More detail on how to make Hall bars of amorphous RE-Co thin films will be discussed in next section.

2.4 Optical lithography

Lithography is a method to print desired patterns on a smooth surface [20]. There are several different types of lithography used in nanotechnology, such as optical lithography and electron beam lithography. The latter one has no diffraction limitation because shorter wavelength of electron beam is possible when providing higher energy. Nevertheless, it is associated with

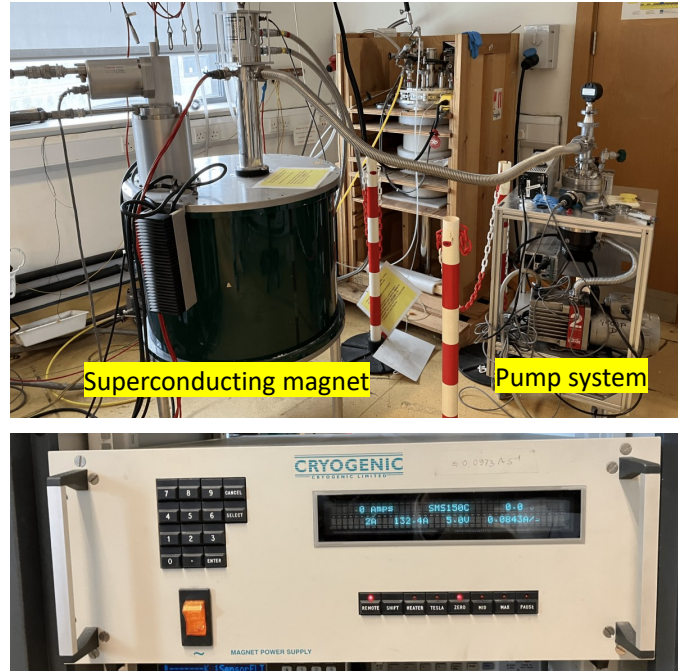


Figure 2.8: 5.5 T Cryomagnet setup.

certain drawbacks, including the high maintenance cost, forward scattering and back scattering problem and slow processing speed. For creating the Hall bar used in transport measurements, we primarily employed the lift-off method, a subset of optical lithography. Figure 2.10 illustrates the lift-off process [21]. The choice of the lift-off method over other techniques was primarily driven by its ability to bypass the step of milling amorphous sample, which will change the magnetic anisotropy from perpendicular to in-plane of the samples for some reasons. It mainly consists of four main steps: mask design, coating, exposure and development. All processes are done in the CRANN clean room with yellow light inside for protecting the resist, a radiation sensitive polymer. The OAI mask aligner and positive photoresist are used for patterning. The main setups used during the making of a Hall bar are shown in Figure 2.11. The recipe used is attached in the Appendix section 7.7.

2.4.1 Mask design

A mask is a glass or fused silica plate with chromium on top. The opaque material Cr is removed from some places based on the design so that light could reach and irradiate the resist on the sample.

2.4.2 Coating

A good surface condition is essential for successfully making good Hall bars. It is important to choose a suitable capping layer in order that photoresist will stick to it firmly and uniformly. I mainly use the positive photoresist where exposed layer zones are removed. In order to increase the resist adhesion, I used the SiO_x as the capping layer. Once having checked that the sample surface is clean, use a pipette to dispense a drop of resist onto the center of the surface. Using spin coating helps to get a uniform coating. Usually, the higher speed of spin, the thinner the resist layer. It is a balance between the centrifugal and viscous forces. Finally, soft bake solidifies the resist and removes solvent from resist.

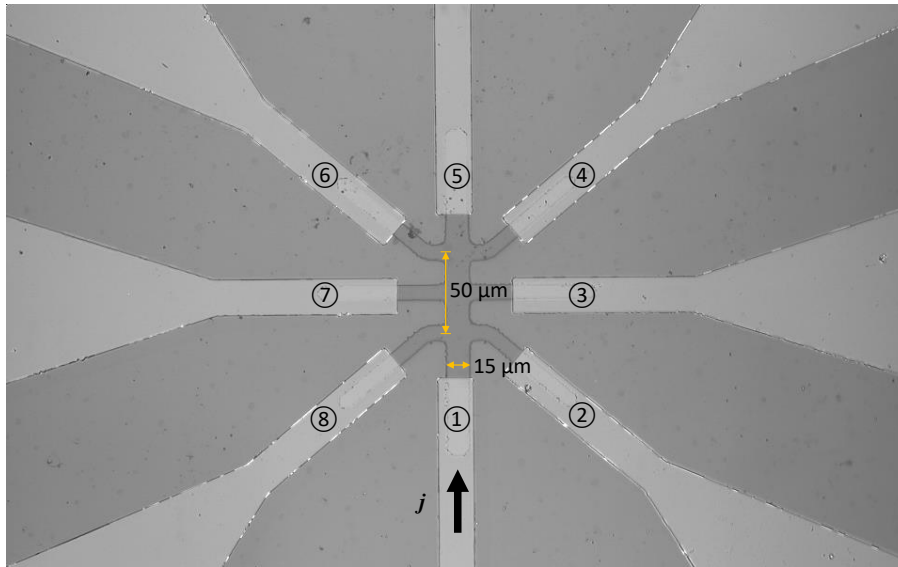


Figure 2.9: Optical micrograph of Hall bar with a bridge width $15\ \mu\text{m}$ and length $50\ \mu\text{m}$. A pair of connection pads 1 and 5 are for supplying current. A pair of pads 3 and 7 are for Hall voltage V_H measurement. A pair of pads 6 and 8 or 2 and 4 are used for magnetoresistance measurement.

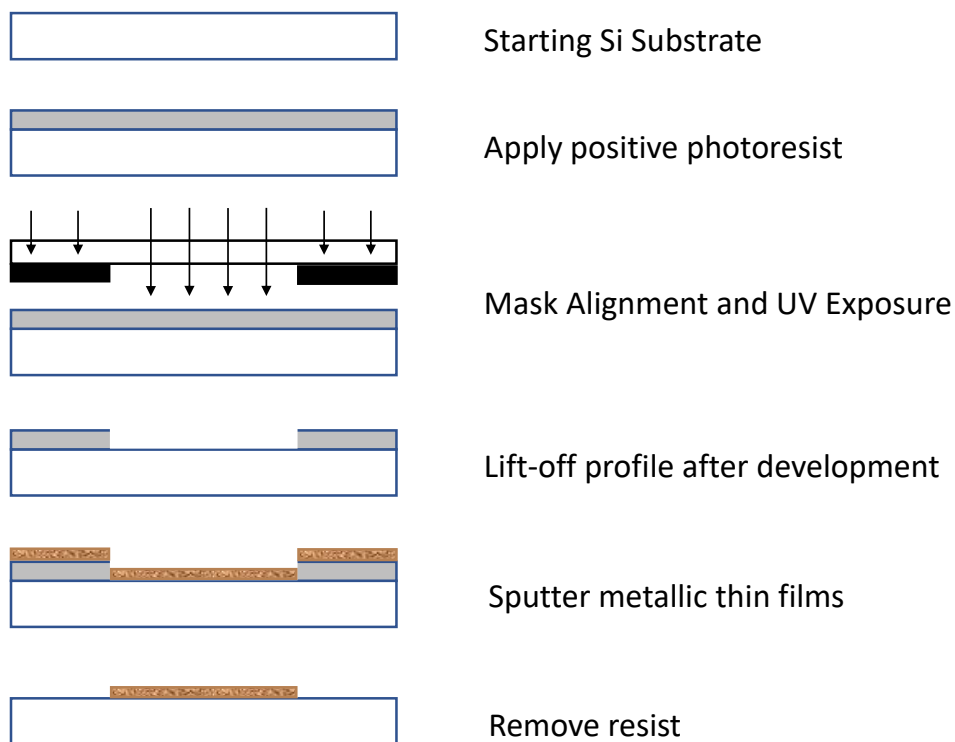


Figure 2.10: Schematic of lift-off process. The vertical lift-off profile offers the best pattern fidelity, albeit requiring significant effort to achieve.

2.4.3 Exposures

Aligning the sample as well as possible is very important for the corrected exposure. When the light contacts with the resist, some chemical reaction is going on, i.e., the reduction of average molecular weight for the positive resist. Good optical alignment between the sample and the

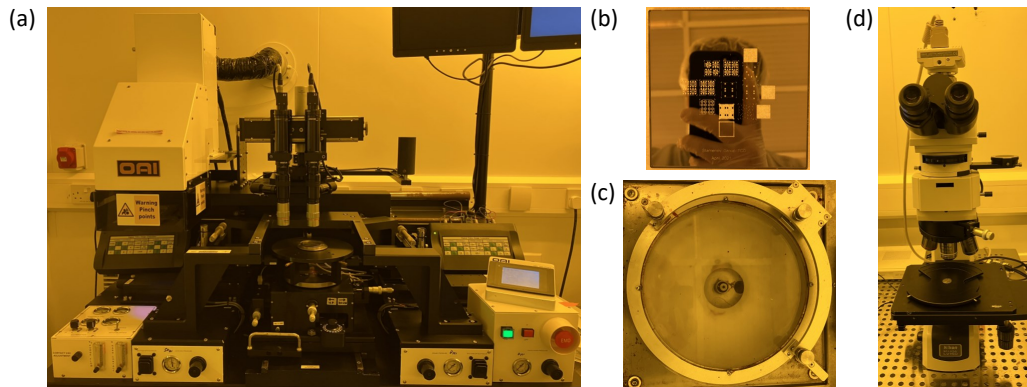


Figure 2.11: Setup components for a Hall bar device fabrication include: (a) the OAI mask aligner for precise patterning, (b) the Hall bar mask for defining the Hall bar geometry, (c) a photoresist spinner for achieving uniform photoresist coatings, and (d) a microscope for inspecting the Hall bar condition.

mask and the right exposure time are two key factors for getting a successful patterned sample.

2.4.4 Development

After the exposure step, sample is put into contact with a developer in order to remove the exposed parts of the resist. A reasonable reaction time is important here. If the time is too long, the sample will be over-developed and a undercut of the structure can be generated, while if it is too short, the reaction will not be completed.

2.5 Magnetometry

Magnetometry is used to determine magnetic hysteresis loops and magnetization as a function of temperature and magnetic field. During my PhD, a Quantum Design MPMS XL-5 magnetometer was mainly used for magnetometry measurements. Historically, vibrating-sample magnetometer was invented earlier and I also worked on building own high-temperature setup. So vibrating-sample magnetometer will be discussed firstly.

2.5.1 Vibrating-sample magnetometer

The vibrating-sample magnetometer (VSM) was first described by Foner [22], as shown in Figure 2.12. By vibrating the sample in a uniform magnetic field, the changing stray field coming from the sample will induce a voltage in the normal non-superconducting pick-up coils based on the Faraday's law [23]. The principle of reciprocity is used to design an optimum coil configuration and calculate its voltage output [24, 25]. And the voltage is proportional to the magnetic moment of the sample. Therefore, by calibrating with a sample of known magnetic moment, such as a standard Ni sphere, the relation between voltage and magnetic moment can be established.

Because only normal detection coils are used, the sensitivity of a VSM is not high. Also the VSM is usually equipped with an electromagnet to generate the applied field \mathbf{H} , whose maximum value usually is around 1 or 2 T. It is quite small compared with modern magnetometer with superconducting magnets. However, VSM has its own advantages. It is able to measure samples with a high Curie temperature T_c and it requires no expensive Helium. Furthermore, it takes less than an hour to measure the full loop $M(H)$ curve of sample with a big magnetic moment, which will be a issue for some modern magnetometers as discussed next.

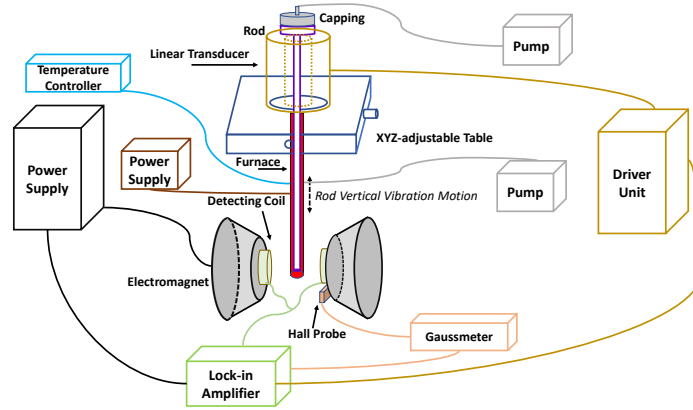


Figure 2.12: Schematic of the whole VSM system.

2.5.2 SQUID magnetometry

Superconducting QUantum Interference Device (SQUID) is a flux-to-voltage converter circuit which combines the physical phenomena that the flux threading through a superconducting ring enclosed by the Josephson junction. The flux of quantization says that the trapped flux by the closed superconducting ring is always an integer times Φ_0 where Φ_0 is the basic unit of flux called flux quantum with a value 2.068×10^{-15} Wb, as shown experimentally and explained theoretically in 1961 [26, 27, 28]. The Josephson junction consists of two superconductors separated by a barrier such as a thin insulator with only few nm thick. It was theoretically shown by Josephson in 1962 that the current flowing through this sandwich structure is given by

$$I = I_c \sin(\delta) \quad (2.5)$$

where δ is the phase difference between the two weakly coupled superconductors and I_c is the critical current, a characteristic of the junction [29, 7]. A radio frequency (RF) SQUID is made of a superconducting ring with single Josephson junction interrupting the ring and coupled to a LC circuit [30].

One of the issues of application SQUID as a magnetometer is the small inductance of the device. Therefore, a superconducting flux transformer is used to couple externally detected flux from sample to SQUID. The flux from the oscillation of the sample is detected by compensated superconducting pick-up coil systems, also called gradiometers. It can cancel the flux contribution from ambient magnetic noise as shown in (a) of Figure 2.13. Among the many different pick-up coil arrangements, second-order gradiometer is the most used one. It consists of two first-order gradiometers wound in opposite direction, which cancels zero-order and first-order field gradient [31]. These coils are electrically connected to SQUID which is kept magnetically shielded and far below T_c [32]. The SQUID in a magnetometer acts as an amplifier that amplifies the current from pick-up coils. The voltage across the SQUID is measured as a function of sample position in the illustration of (b) in Figure 2.13. The conversion between magnetic moment and voltage is done by calibrating a standard magnetic sample, similar to the VSM.

Thin film samples are usually measured in-plane and out-of-plane. Due to the finite size of the sample, there is a geometrical contribution to the measured magnetic moments. Therefore, a proper correction -4.08% and 2.09% for out-of-plane and in-plane measurements respectively is needed in order to extract the accurate magnetic moments of square thin film samples which are cut and fitted in a clear drinking straw with about 5 mm inner diameters [33, 34]. The magnetization can be obtained by dividing the magnetic moment by the sample volume. The lateral dimension can usually be measured by a combination of a ruler and phone camera and the film thickness can be fitted by the X-ray reflectivity data as introduced earlier. During my PhD work, Quantum Design MPMS-XL5 was used as illustrated to Figure 2.14.

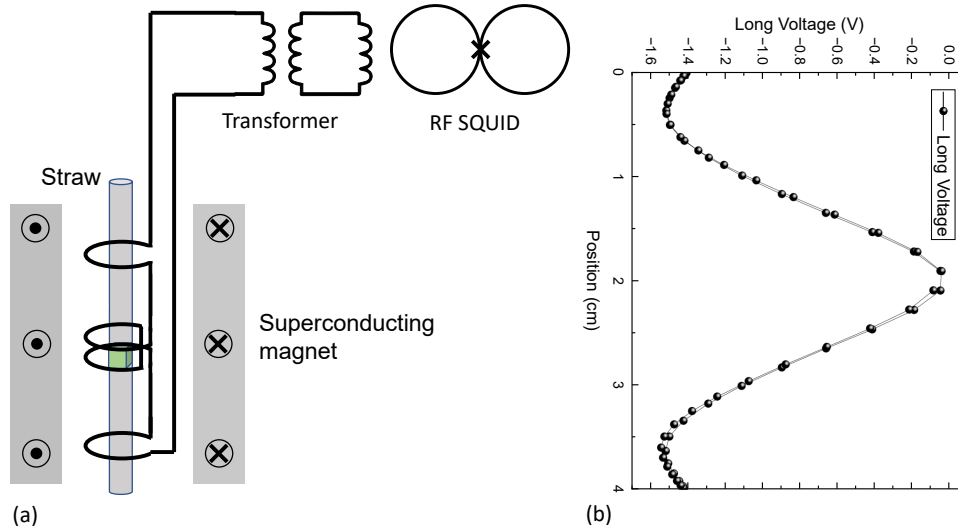


Figure 2.13: Schematic of SQUID and its raw measured data. (a) Four-turn pick-up detection coils inductively coupled to an RF SQUID via the flux transformer (b) the measured voltage vs sample position.

2.6 Magneto-optical Microscopy

Magneto-optical microscopy is widely used in spintronics as a magnetometry due to its spatial resolution allowing for domain imaging. Magneto-optics is concerned with the interaction of light with magnetized matter, causing a change in its intensity or polarization state. Faraday effect is seen with transmitted light and the magneto-optical Kerr effect (MOKE) is seen with reflected light [35, 36]. They are both based on small rotations of the polarization plane of light that become observable in a polarizing microscope [37]. The Faraday and Kerr effects first discovered by using visible light. Nowadays, with the developments of synchrotron radiation, these effects are also used in the X-ray such as the X-ray magnetic linear dichroism (XMLD) spectroscopy and X-Ray magnetic circular dichroism (XMCD) spectroscopy. Those are very powerful tools for providing information such as spin and orbital contributions to magnetic moments and element-specific domain imaging [3, 38].

2.6.1 Magneto-Optic Phenomena

There are several different magneto-optical effects involving polarized light but all of them share a single common character of somehow being externally controlled. It is more convenient to use left circularly polarization (LCP) and right circularly polarization (RCP) as a basis with some fundamental reasons from the Quantum Mechanics [39]. When looking at the direction of source, the polarization vector \mathbf{E} precesses anti-clockwisely and clock-wisely as a function of time at a fixed spatial position for LCP and RCP respectively. Related to circular polarization light, there are two important magneto-optical effects. One is called magnetic circular birefringence (MCB) and the other one is magnetic circular dichroism (MCD). The MCB is the magnetic field induced difference in refraction of LCP and RCP light. The MCD is about the differential absorption of LCP and RCP light, induced in a sample by a strong magnetic field. Faraday effect will be explained in detail. Since the Kerr effect shows many similarities it will be discussed briefly.

Many of the optical properties of solids can be understood based on the classical Maxwell electromagnetic theory. The microscopic origin of them can be treated classically on the basis of Newtonian equations or Quantum Mechanics⁴. In this thesis, Newtonian equations will be

⁴ It is the spin-orbit interaction that couples the electron spin to its motion, thus connecting the magnetic and optical properties of a ferromagnet [40].



Figure 2.14: The Quantum Design MPMS-XL5 is a versatile machine used for conducting magnetometry measurements. It offers a wide temperature range from 1.8 K to 700 K, and is capable of generating a magnetic field up to 5 T. The sample is loaded into the sample space, which is located in the center of the system, as shown in the figure on the right. The PC is utilized to control and record data, as depicted in the figure on the left.

used since this view is very instructive and gives good physical insight. The macroscopic theory consists of two parts: Maxwell's equations and material equations as shown below.

The response of the conduction electrons to the electric field \mathbf{E} is given by the current equation (Ohm's law)

$$\mathbf{J} = \sigma \mathbf{E} \quad (2.6)$$

where σ is the conductivity. The relation describing the response of the bound charges to \mathbf{E} is given by

$$\mathbf{D} = \epsilon \mathbf{E} \quad (2.7)$$

where ϵ is known as the dielectric constant. The corresponding magnetic relation is

$$\mathbf{B} = \mu \mathbf{H} \quad (2.8)$$

where μ is the magnetic permeability. For nonmagnetic, electrically neutral materials such as quartz, which means $\mathbf{M} = 0$ and $\rho = 0$. The Maxwell's equations can be reduced to the following form:

$$\nabla \times \mathbf{E} = -\mu_0 \frac{\partial \mathbf{H}}{\partial t} \quad (2.9)$$

$$\nabla \times \mathbf{H} = \epsilon_0 \frac{\partial \mathbf{E}}{\partial t} + \frac{\partial \mathbf{P}}{\partial t} + \mathbf{J} \quad (2.10)$$

$$\nabla \cdot \mathbf{E} = -\frac{1}{\epsilon_0} \nabla \cdot \mathbf{P} \quad (2.11)$$

$$\nabla \cdot \mathbf{H} = 0 \quad (2.12)$$

The general wave equations can be derived by taking the curl of equation (2.9) and time derivative of equation (2.10) and eliminating \mathbf{H} , as expressed below

$$\nabla \times \nabla \times \mathbf{E} + \frac{1}{c^2} \frac{\partial^2 \mathbf{E}}{\partial t^2} = -\mu_0 \frac{\partial^2 \mathbf{P}}{\partial t^2} - \mu_0 \frac{\partial \mathbf{J}}{\partial t} \quad (2.13)$$

where the two terms on the right part of equation are the source terms, which are important for nonconducting materials and metals respectively. Next, tensor is required to deal with general cases such as crystal optics(optical activity). The realtion between \mathbf{P} and \mathbf{E} is expressible as a tensor in the form:

$$\begin{bmatrix} P_x \\ P_y \\ P_z \end{bmatrix} = \epsilon_0 \begin{bmatrix} \chi_{11} & \chi_{12} & \chi_{13} \\ \chi_{21} & \chi_{22} & \chi_{23} \\ \chi_{31} & \chi_{32} & \chi_{33} \end{bmatrix} \begin{bmatrix} E_x \\ E_y \\ E_z \end{bmatrix} \quad (2.14)$$

By introducing susceptibility tensor $\tilde{\chi}$, it can be abbreviated:

$$\mathbf{P} = \epsilon_0 \tilde{\chi} \mathbf{E} \quad (2.15)$$

For a nonconducting medium with $\mathbf{J} = 0$ and by inserting plane waves of the usual form $e^{i(\mathbf{k}\cdot\mathbf{r}-\omega t)}$, the equation for propagation vector \mathbf{k} is

$$\mathbf{k} \times \mathbf{k} \times \mathbf{E} + \frac{\omega^2}{c^2} \mathbf{E} = -\frac{\omega^2}{c^2} \tilde{\chi} \mathbf{E} \quad (2.16)$$

For Faraday rotation in solids, the $\tilde{\chi}$ has conjugate imaginary off-diagonal elements, namely,

$$\tilde{\chi} = \begin{bmatrix} \chi_{11} & i\chi_{12} & 0 \\ -i\chi_{12} & \chi_{11} & 0 \\ 0 & 0 & \chi_{33} \end{bmatrix} \quad (2.17)$$

where χ_{12} is real number [41]. Assuming the wave is propagating in the z direction and inserting it in equation (2.16), we get finally an expression for indices of refraction of RCP and LCP

$$n_R = \sqrt{1 + \chi_{11} + \chi_{12}} \quad (2.18)$$

$$n_L = \sqrt{1 + \chi_{11} - \chi_{12}} \quad (2.19)$$

The difference of refractive indexes for them results their different propagation speed in a material. If d is the distance travelled by light, the travel time for RCP and LCP are $\frac{dn_R}{c}$ and $\frac{dn_L}{c}$ respectively. It causes an angle θ through which the direction of linearly polarized light turns with respect to the original direction of polarization, since the linearly polarized light can be thought as a combination of LCP and RCP. The rotation angle θ is

$$\theta = (n_R - n_L) \frac{\omega d}{2c} \quad (2.20)$$

When there is not difference between n_R and n_L , the θ will be 0, which makes sense.

Now, microscopic picture is needed for explaining Faraday effect by considering the motion of bound electrons in the presence of \mathbf{B} field and the oscillating \mathbf{E} field. By using Newton's second law and Lorentz force, the differential equation of motion is

$$m_e \frac{d^2 \mathbf{r}}{dt^2} = -k\mathbf{r} - e\mathbf{E} - e \frac{d\mathbf{r}}{dt} \times \mathbf{B} \quad (2.21)$$

where \mathbf{r} is the displacement of the electron from its equilibrium and k is the elastic-force constant [41, 7]. The \mathbf{P} has a simple relation with \mathbf{r} , namely $\mathbf{P} = -Ne\mathbf{r}$. Hence, the equation (2.21) implies that

$$(-m_e\omega^2 + k) \mathbf{P} = Ne^2 \mathbf{E} + i\omega \mathbf{P} \times \mathbf{B} \quad (2.22)$$

The equation (2.22) can be solved by writing it in component form and solving for the components of \mathbf{P} . The result has the same form as in equation (2.17).

$$\chi_{11} = \frac{Ne^2}{m\epsilon_0} \frac{\omega_0^2 - \omega^2}{(\omega_0^2 - \omega^2)^2 - \omega^2\omega_c^2} \quad (2.23)$$

$$\chi_{12} = \frac{Ne^2}{m\epsilon_0} \frac{\omega\omega_c}{(\omega_0^2 - \omega^2)^2 - \omega^2\omega_c^2} \quad (2.24)$$

$$\chi_{33} = \frac{Ne^2}{m\epsilon_0} \frac{1}{(\omega_0^2 - \omega^2)} \quad (2.25)$$

where \mathbf{B} is assumed along z direction and the definitions of resonance frequency ω_0 and cyclotron frequency ω_c are the following

$$\omega_0 = \sqrt{\frac{k}{m_e}} \quad (2.26)$$

$$\omega_c = \frac{eB}{m} \quad (2.27)$$

where B is the magnitude of \mathbf{B} field. Referring to equation (2.20), θ is approximately proportional to B under the assumption that $\omega\omega_c \ll |\omega_0^2 - \omega^2|$, which is the Faraday rotation in diamagnetic materials under the action of magnetic field. For isotropic medium without magnetic field ($\omega_c = 0$), the diagonal elements have the same values and the off-diagonal ones vanish [42]. For the Kerr effect, a Jones matrix introduced by C. Jones in 1941 will be used. The light electric polarization is described by a column complex vector with two components, which represent the s- and p-polarization respectively, i.e., field components perpendicular and parallel to the plane of incidence. Within this formalism, the optical operation can be represented by a two-by-two matrix. The matter and light interaction is just multiplying the related matrix with the incident light vector. A Jones matrix is introduced:

$$\begin{bmatrix} r_{ss} & r_{sp} \\ r_{ps} & r_{pp} \end{bmatrix} \quad (2.28)$$

where the diagonal entities represent the ordinary reflection coefficients for s- and p-polarization light and the off-diagonal terms are responsible for magneto-optical interactions. The subscript ps means that p-polarization component originates in the s-polarization light. The off-diagonal terms change sign when reversing \mathbf{M} and are much smaller than the diagonal ones. Take the case when s-polarization light is applied, the reflected light is

$$\begin{bmatrix} r_{ss} & r_{sp} \\ r_{ps} & r_{pp} \end{bmatrix} \begin{bmatrix} 1 \\ 0 \end{bmatrix} = r_{ss} \begin{bmatrix} 1 \\ r_{ps}/r_{ss} \end{bmatrix} = r_{ss} \quad (2.29)$$

The polarization has been rotated by an angle called Kerr angle $\pm r_{ps}/r_{ss}$ corresponding to magnetization in the $\pm z$ direction.

2.6.2 Polar and longitudinal Kerr effect

Maxwell summarized the Faraday effect based on Faraday's work on transparent diamagnetic media (The objective lens of a Kerr microscope belongs to this category.) in his treatise [43]. The angle through which the plane of the polarization is turned is proportional to (1) to the distance which the ray travels within the medium, (2) to the intensity of the resolved part of the magnetic force in the direction of the ray and (3) the amount of rotation depends on the nature of the medium. The angle θ_F through which the polarization vector \mathbf{E} rotates is given by the empirically expression:

$$\theta_F = \mathcal{V}Bd \quad (2.30)$$

where B is the magnitude of the \mathbf{B} field inside the medium, d is the length of the medium transversed and \mathcal{V} is a factor of proportionality known as Verdet constant.

In the MOKE microscopy, the Faraday effect is inevitable because the objective lens is in a magnetic field along the objective axis. A correction method is required. A non-magnetic mirror is used to correct the Faraday effect in the objective lens caused by the magnetic field from the electromagnet.

According to the relation between \mathbf{M} and the plane of incidence, there are three possible geometries for the magneto-optical Kerr effect [3], the polar geometry, the longitudinal geometry and the transverse geometry shown in Figure 2.15. The latter two are used to measure the in-plane component of magnetic moments.

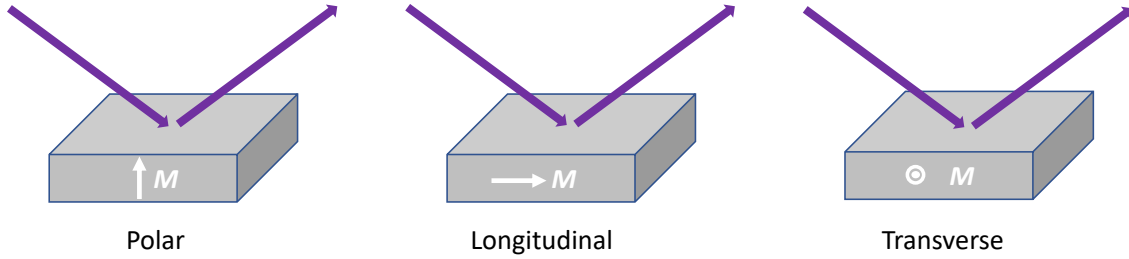


Figure 2.15: Three configurations of MOKE.

The polar geometry is most important for metallic magnetic thin film with strong perpendicular magnetic anisotropy, which favors magnetization points out-of plane. Upon reflection from the surface of a perpendicularly magnetized thin film, the polarization vector undergoes a rotation θ_k . The sense of rotation depends on the direction of the magnetization vector \mathbf{M} , and switches sign when \mathbf{M} is reversed, as shown in the (a) of Figure 2.16.

Polar MOKE was performed with an Evico Magnetics wide-field Kerr microscope, equipped with several different objective lenses. A cross-polarizer configuration is used with polarizer and analyzer set nearly 90° [3]. Usually, a 20x lens was first used to image the domains and the higher magnification if necessary. The main components of Polar MOKE setup I used is demonstrated in (b) to (e) in Figure 2.16. The spatial resolution is limited by the Rayleigh criterion:

$$s = \frac{\lambda}{NA} \quad (2.31)$$

where s is the smallest dimension that can be resolved, λ is the wavelength used and NA is the numerical aperture defined as $n \sin(\theta)$. The resolution can be increased by utilizing an immersion lens ($n > 1$).

Because the objective lens made of diamagnetic glass, is close to the magnetic field produced by perpendicular electromagnet, the Faraday effect is pronounced and inevitable. Hence a correction is needed. Firstly, a small piece of non-magnetic mirror is put onto the sample surface. Secondly, a motor-driven analyzer is applied instead of the conventional analyzer, helping to keep constant the average intensity of the selected region, which is some part of the mirror. The total rotation angle θ_{total} of the polarization plane can be decomposed to two parts. One part, from the lens is denoted by θ_{lens} (Faraday effect contribution), the other from sample itself, denoted by θ_{sample} . The total rotation angle expression is

$$\theta_{total} = \theta_{lens} + \theta_{sample} + \theta_{lens} = 2 \times \theta_{lens} + \theta_{sample}. \quad (2.32)$$

Polarized light goes through the lens, and then is reflected by the sample, and finally goes through the lens again so the rotation resulting from Faraday effect is doubled [43]. The motor-driven

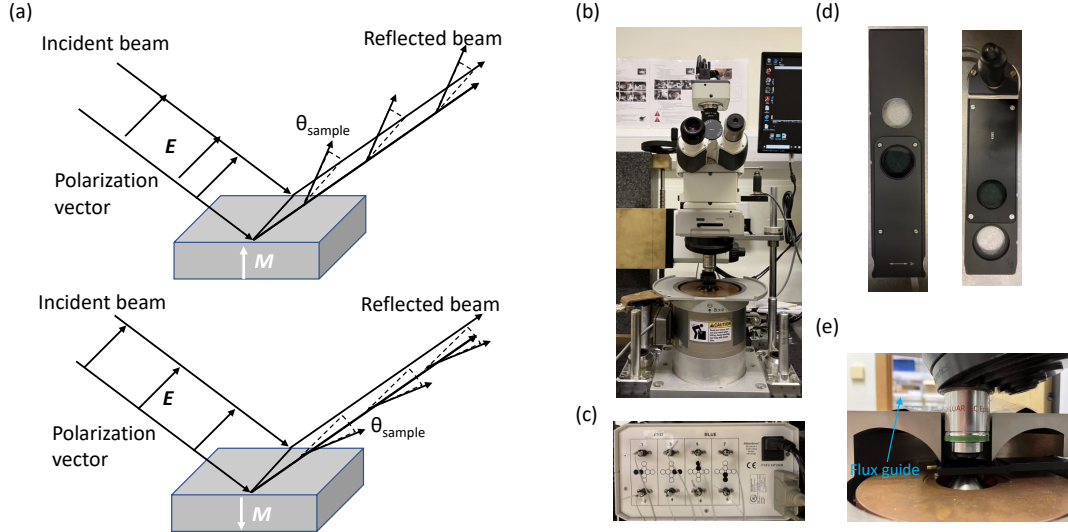


Figure 2.16: Polar magneto-optical Kerr effect and Evico Magnetics wide-field Kerr microscope. (a) upon reflection from the surface of a perpendicularly magnetized medium, the polarization vector undergoes a rotation and the sense of rotation depends on the direction of the magnetization vector \mathbf{M} which switches sign when \mathbf{M} is reversed, (b) shows the main components of Kerr microscope, the electromagnet, microscope and CCD camera, (c) red and blue LEDs as light source, (d) a manual analyzer and motor-driven analyzer, (e) 20x objective lens, flux guide and sample holder.

analyzer will make the $2\theta_{lens}$ effect become 0 so that the resulting rotation of the polarization is caused only by the Kerr effect of the thin film sample itself, as shown in Figure 2.17.

The hysteresis loops of thin film samples mapped out via Kerr microscope are very useful⁵ and can provide detailed magnetic information such as the nucleation and growth of magnetic domains. The \mathbf{B} field is scanned from positive saturation field $+\mathbf{B}_S$ to $-\mathbf{B}_S$ and then back to the initial field. A mirror and motor-driven analyser are used as explained previously.

2.7 Synchrotron X-ray radiation techniques

In comparison to optical measurements, widely used in magnetism, such as Kerr effect and Faraday effect, as discussed in the last section, Synchrotron X-ray radiation measurements provide significant advantages. Because excitations by X-ray are localized on atoms, X-ray offers unique sensitivity to each element and their chemical state. By use of the powerful sum rules, the spin and orbit magnetic moments can be determined separately from integrated peak intensities. Besides, thanks to the short wavelength of X-ray, it offers higher spatial resolution for imaging magnetic domains, down to the size of the X-ray wavelength [44].

2.7.1 X-ray magnetic circular dichroism

As analysers for X-rays are not available, X-ray spectroscopy has to rely on dichroic effects⁶ rather than polarization rotation effects as in optics, like Kerr effect or Faraday effect [37].

⁵Since most magnetic materials of interest are metals that absorb light, it is more convenient to measure the reflected light via Kerr effect [40]. But in astrophysics, the Faraday effect is more widely used.

⁶It might be helpful to list all major optical effects: birefringence, dichroism, optical activity and magneto-optical rotation. In modern theory, based on time-dependent perturbation theory and the quantum mechanical operator and matrix method, all interaction effects of polarized photons with matter can be described based on scattering theory.

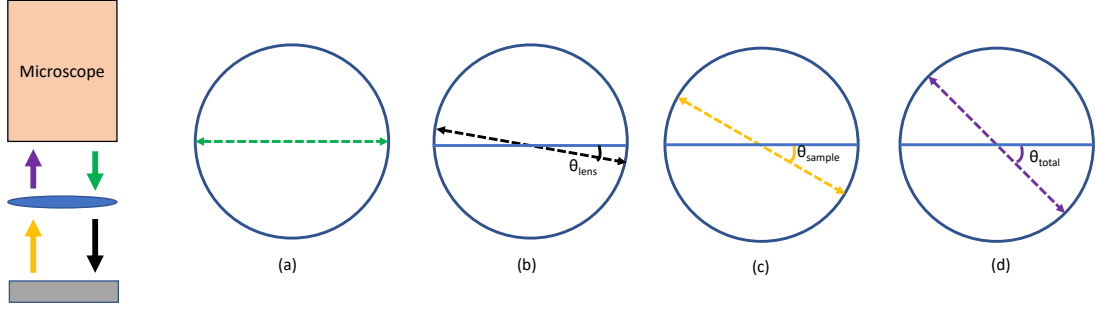


Figure 2.17: Schematic of the rotation angle in Kerr microscope without motor-driven analyzer. The four arrows with different colors represent the polarized light state at various stages along the light travel path, before or after interaction with the sample or lens. (a) is the polarized light after the polarizer. (b) is the light just passing through the lens. (c) is the light reflected from the sample surface. (d) is the light going through the lens again and finally is detected in the analyzer.

Circular dichroism is the difference in absorption of right and left handed circularly polarized light [45]. The first observation of a magnetically induced difference in absorption came with the Nobel prize-winning work of Zeeman. He observed magnetic circular dichroism effects on the absorption lines of Na vapor [46]. Soon after the discovery of X-rays by Röntgen in 1895, efforts were made to find magnetic effects on X-ray spectra. However, a successful experiment would have to wait another 80 years. The X-ray magnetic circular dichroism (XMCD) effect was observed in metallic Fe by Schütz *et al.* in 1987 [47].

XMCD experiments consist of measuring the difference in absorption of right and left handed circularly polarized X-rays in magnetic materials. These can be thought of as using polarized light to perform X-ray absorption (XAS) experiments. The inherent chemical sensitivity from XAS makes XMCD very suitable for studying multicomponent systems. The XMCD effect, as well as Kerr and Faraday effects, originate from electric dipole transitions driven by the electric field of the electromagnetic radiation [48]. The electric field \mathbf{E} does not act on the electron spin directly but only indirectly via the orbital momentum and the spin-orbit interaction⁷. For 3d elements Fe, Co and Ni, it is advantageous to excite the 2p shell for XMCD experiments since $L_{2,3}$ edges have much bigger jumps than 3p edges⁸. The largest splitting of the 2p shell is due to the spin-orbit interaction, which leads to the separation of L_3 ($2p_{3/2}$) and L_2 ($2p_{1/2}$) edges. The measured binding energies for these edges of 3d elements Fe, Co and Ni are listed in Table 2.1.

Element	L_3	L_2
Fe	707	720
Co	778	793
Ni	853	870

Table 2.1: Binding energies for L_3 and L_3 edges of Fe, Co and Ni are expressed in electron volts (eV).

In order to probe the magnetic properties of 3d magnetic elements, the dipole transition from 2p to 3d should be utilized, which is well described as a first-order transition. The selection rules

⁷By comparison, the nonresonant magnetic x-ray scattering arises from the direct interaction of \mathbf{B} with both the spin and the orbital moments.

⁸ L_2 and L_3 represent the transition from $2p_{1/2}$ to $3d$ and $2p_{3/2}$ to $3d$, respectively. By edge, it refers to the sharp rise in absorption that happens when a photon matches the energy needed to excite an electron.

for such dipole transitions requires

$$\Delta l = \pm 1, \Delta s = 0, \Delta m_l = \pm 1, \Delta m_s = 0 \quad (2.33)$$

where l is the orbital quantum number, m_l is the orbital magnetic quantum number, s is the spin quantum number and m_s is the spin magnetic quantum number [3]. The $\Delta l = \pm 1$ comes from the dipole selection rule. The $\Delta m_l = \pm 1$ requires a little more explanation. The circularly polarized photons possess a well-defined angular momentum $+\hbar$ and $-\hbar$ for right circularly polarized and left circularly polarized light, respectively. Since the annihilation of photon in the absorption process, the conservation of angular momentum requires that excited photoelectron must carry the angular momentum of the photon. In the absence of spin-orbit interaction, this can only be achieved by transferring the photon angular momentum to the orbital part. That is reason why the $\Delta m_l = \pm 1$. This is exactly the case for an atomic s core state, which has zero angular momentum and hence no spin-orbit interaction. The excited electron carries orbital momenta \hbar or $-\hbar$ and no spin polarization exists. For s and m_s , no operator changes them during electric dipole transition, they stay the same. It means that spin flips are forbidden, and spin up and down photoelectrons from $2p$ can only be excited to spin up and down unoccupied $3d$ state, respectively.

In the two-step dichroism model as illustrated in Figure 2.18, the core shell $2p$ can be viewed

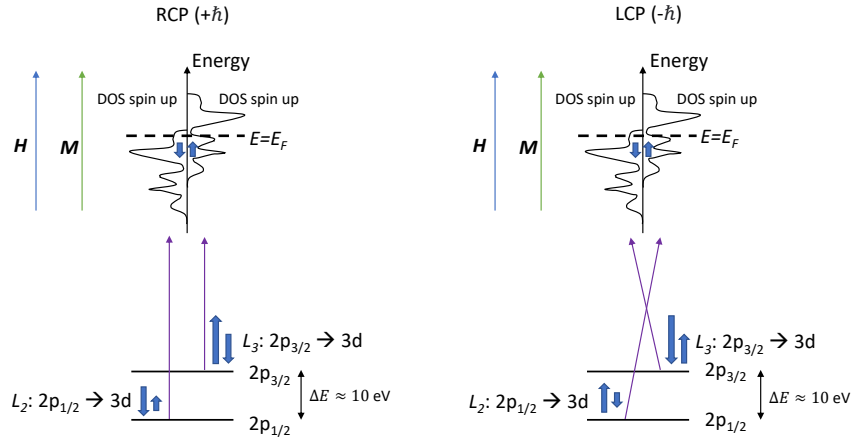


Figure 2.18: The principle of XMCD involves the excitation of spin-polarized electrons from the $2p_{1/2}$ and $2p_{3/2}$ core levels using circularly polarized X-rays. These core-level electrons exhibit opposite sign spin polarizations due to opposite-sign spin-orbit coupling. The spin orientations are represented by the direction of blue arrows, while the lengths of the blue arrows represent the populations of photoelectrons. By applying a magnetic field \mathbf{H} , the magnetization \mathbf{M} can be set and enhanced. **Left:** RCP X-ray carrying $+\hbar$ is used; **Right:** LCP carrying $-\hbar$ is used. In both cases, the magnetization \mathbf{M} aligns parallel to the incident X-ray beam's in-plane projection, with an angle of incidence less than 90° .

as an atom-specific, localized 'source' of spin-polarized electrons, which is the first step. For the second step, the spin-polarized electrons are analyzed by a 'spin-resolving detector' consisting of the vacant exchange-split d final state [48].

1. First step: Spin polarization. Because of conservation of angular momentum and spin-orbit interaction ($2p_{3/2}$ has positive spin-orbit interaction such that $J = L + S = 3/2$, $2p_{1/2}$ has negative spin-orbit interaction such that $J = L - S = 1/2$), excited electrons from $2p_{3/2}$ and $2p_{1/2}$ levels have net spin polarizations of opposite sign as indicated by blue arrows in Figure 2.18. For example, photons of RCP (LCP) transfer $+$ ($-$) \hbar angular momentum to $2p$ electrons, such that $2p_{3/2}$ ($2p_{1/2}$) electrons with L parallel (antiparallel) to S develop a net spin-up (spin-down) polarization.

2. Second step: *d*-band spin detector. The spin-dependent density of empty states near the Fermi energy determines the probability of the $2p \rightarrow 3d$ transitions and therefore the intensity of corresponding absorption peaks. Specially, for photons of RCP (LCP), the $2p_{3/2}$ electrons excited with a new spin-up (spin-down) polarization access less (more) unoccupied states near Fermi energy and so the intensity of the L_3 absorption peak is smaller (larger). For $2p_{1/2}$ electrons excited with a new spin-down (spin-up) access more (fewer) empty states near Fermi energy and so the intensity of L_2 absorption peak is larger (smaller).

At Helmholtz-Zentrum Berlin-Adlershof, the XMCD experimtn were performed on UE49 beamline of BESY II light source where the X-ray energy is in the soft X-ray energy region. The sensitivity of an XMCD experiment is greatly enhanced when the photon energy is in the vicinity of an absorption edge. While ideally one would like to measure transmission and directly relate it to transmission, which brings a big challenge for preparing a suitable sample thickness. Therefore, in our case, XMCD was measured by total electron yield (TEY) at the Co $L_{2,3}$ absorption edge, where signal is given by the sample drain current needed to replace the electrons ejected out of the materials due to X-ray absorption. And then it is normalized compared to a standard sample, such as a gold foil target. This TEY method has a better signal-to-noise ratio than the fluorescene detection method. However, the drawback is that the TEY is more surface sensitive. It is able to probe depths ranging from 2 nm to 10 nm, which means that capping layers should be around 2 nm thick, to ensure the probing of magnetic thin film materials.

One of the reasons that XMCD spectroscopy becomes popular is that it has been established that the orbital, m_{orb} and spin, m_{spin} , magnetic moments can be obtained from the sum rules, which relate integrals of the dichroic signal over the relevant absorption edges directly to m_{orb} and m_{spin} . The sum rules can be written in the case of 3d metals as [45]

$$m_{orb}[\mu_B/atom] = -\frac{4q(10 - n_{3d})}{r} \quad (2.34)$$

and

$$m_{spin}[\mu_B/atom] \approx -\frac{(6p - 4q)(10 - n_{3d})}{r} \quad (2.35)$$

where n_{3d} is the number of electrons in the 3d state, and p, q and r are given by

$$p = \int_{L_3} (\mu^+ - \mu^-) dE \quad (2.36)$$

$$q = \int_{L_3+L_2} (\mu^+ - \mu^-) dE \quad (2.37)$$

$$q = \int_{L_3+L_2} (\mu^+ + \mu^-) dE \quad (2.38)$$

2.7.2 X-ray photoemission electron microscopy

One of the most important applications of X-ray photoemission electron microscopy (XPEEM) is in polarization-dependent studies concerning magnetic materials [49, 50, 51]. The intensity changes with photon energy or X-ray polarization discussed earlier naturally offer themselves as contrast mechanisms for imaging in X-ray microscopy [44]. Hence, to be more precise, this measurement can be referred to as XMCD-PEEM.

It makes use of the fact that an electron excited by photon absorption can relax by transferring its energy to other electrons at the Fermi level. If this happens near the surface of the sample, some electrons receiving energy leave the sample into the vacuum. These free electrons

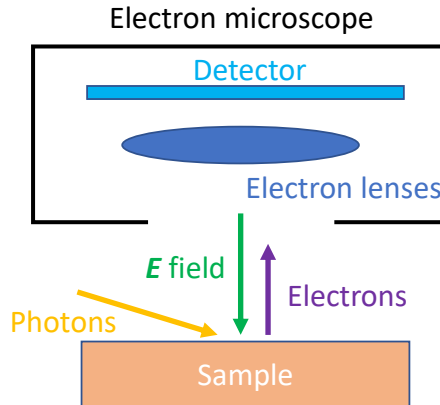


Figure 2.19: The working principle of XPEEM. The incident X-ray beam hits the sample under grazing incidence, hence being absorbed in the surface-near region. Some electrons receive enough energy to leave the sample into vacuum. They are accelerated by an electric field, and pass through magnetic and electrostatic lenses to form an intensity-absorption map on a detector screen.

are further accelerated by a high voltage and focused by a series of electromagnetic lens to a pixel detector, as depicted in Figure 2.19. Based on the XMCD effect, an image of the magnetization can be obtained [3]. If the sample contains magnetic domains with different magnetization orientations, the magnetic contrast will vary because of the dichroic absorption effect. The different signal strength can be used as a contrast mechanism for microscopy with contrasts up to 20-30 %. It is a very large contrast considering the fact that Kerr microscopy contrast is less than 1 % [44]. The XMCD intensity at a given absorption edge is proportional to the dot product $\mathbf{M} \cdot \mathbf{k}$ where \mathbf{M} is the magnetization and \mathbf{k} is the beam wavevector and the sign of the proportionality constant depends on the choice of absorption edge. By combining two XMCD-PEEM images obtained with orthogonal in-plane projections of the grazing-incidence beam, a vector map of in-plane magnetization is possible [52, 53].

The experiment on XPEEM, coupled with a 50 fs pulsed laser, variable temperature and modest magnetic fields, was done in UE49 SPEEM beamline of BESY II light source at Helmholtz-Zentrum Berlin-Adlershof. With X-rays, the instrument is capable of 30 nm spatial resolution [54]. It focused on the study Co $L_{2,3}$ edge and Dy, Tb $M_{4,5}$ edges (transition from 3d to 4f). The spectral range covered extends from 80 to 1800 eV. At typical working conditions of the microscope the field of view is about 3–10 μm .

2.8 Ultrafast optics

As the name ultrafast magnetism suggests, an ultrafast laser pulses of time duration in the femtosecond (fs) range up to few picoseocnds (ps) is required⁹ in order to resolve separately the effect of electron-spin and spin-lattice relaxation mechanism and achieve all-optical switching [55, 56, 57, 58]. During my PhD work, I mainly worked with a femtosecond titanium sapphire mode-locked pulsed laser from Coherent Inc¹⁰. It has a pulse duration about 200 fs and central wavelength of 800 nm. The setup used for single pulse all-optical switching is indicated in Figure 2.20. Some basic facts of laser will be reviewed firstly and then more detailed discussion on ultrafast pulsed lasers and different optical components are presented.

⁹1 fs is equal to 10^{-15} second, 1 ps to 10^{-12} second.

¹⁰In general, there are two types of lasers, continuous and pulsed ones. The one I used is a pulsed one.

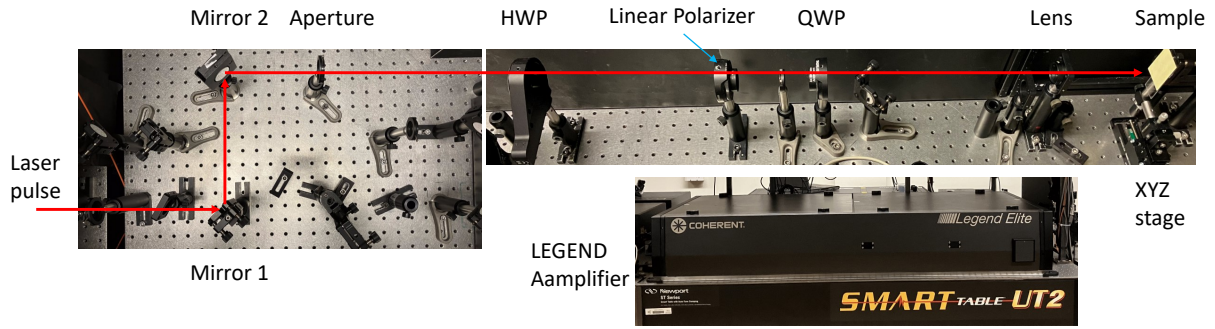


Figure 2.20: Single pulse all-optical switching setup. The laser pulse is obtained directly from a LEGEND amplifier as shown in the bottom right. Mirrors are used to change the beam direction. HWP, linear polarizer and QWP are used to change the laser pulse properties.

2.8.1 Laser

Laser is an acronym, representing for light amplification by stimulated emission radiation, which explains the working principle as shown in Figure 2.21. There are four different energy levels in

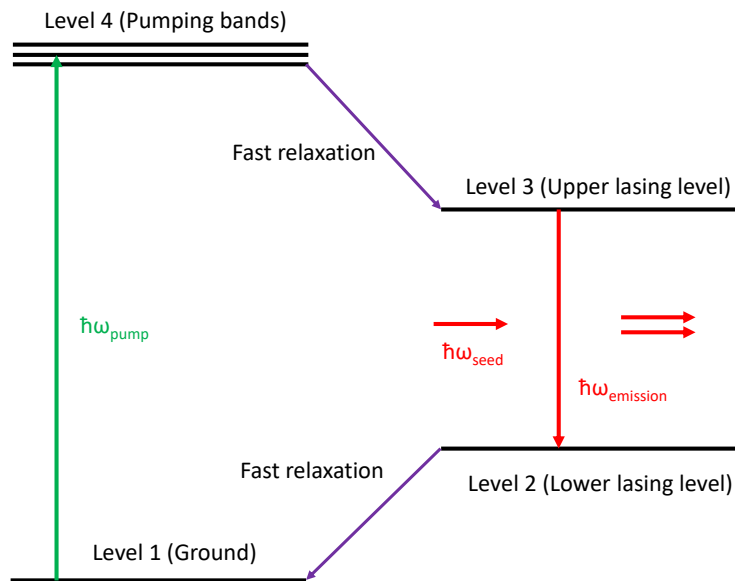


Figure 2.21: Schematic of basic laser action. Lasing is achieved between levels 2 and 3, via excitation from level 1 to level 4.

the system, which is how a titanium Sapphire laser works. A ground level is excited into level 4, under optical excitation with photon energy $\hbar\omega_{pump}$ provided by external light source such as pump laser. There is a broad band of levels (at level 4) instead of a single well-defined energy level, which is often the case in reality. A rapid relaxation from level 4 to level 3, a non-radiative transition, is essential for achieving population inversion between level 3 and level 2, which is a key for lasing. Stimulated emission from level 3 to level 2 then produces the laser radiation. Finally, another rapid relaxation from level 2 to 1 ensures that the population of level 2 remains low. The crystal sapphire makes the rapid relaxation possible by serving as a sink [59].

A real laser is mainly constructed from main three parts, gain medium, pump source, and mirrors. The gain medium is to provide the energy levels as shown in Figure 2.21 and determine the laser emission properties. In solid-state lasers, it is ions in crystals or glasses. The pump

serves as energy source for inverting the population, supplying at $\hbar\omega_{pump}$ such as eclectic discharge, arc lamp or another laser. Mirrors provide feedback mechanism for amplification and choose spectral and spatial properties of light, which together with the gain medium form an oscillator. The simplified diagram of a solid-state laser is displayed in Figure 2.22. It seems that there is no seed laser here, but actually, it can be spontaneous emission from level 3 to level 2.

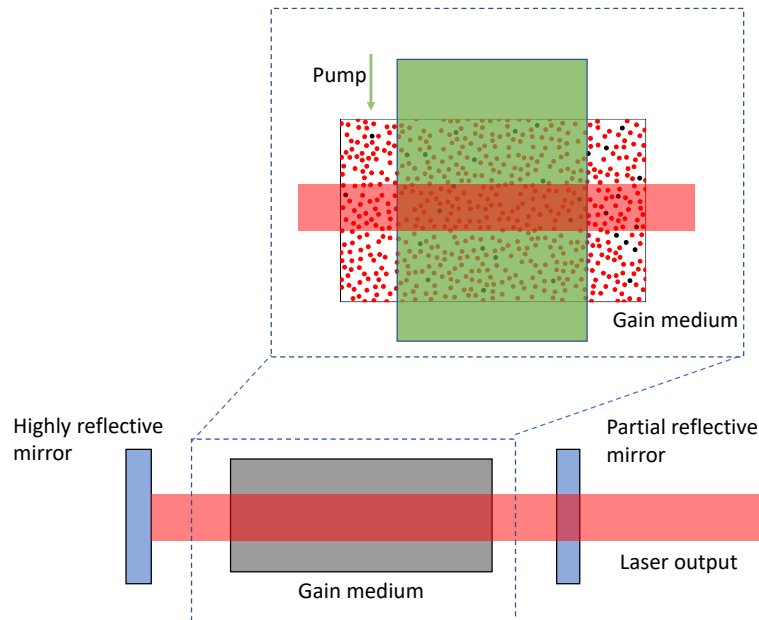


Figure 2.22: Simplified diagram of a laser, including the gain medium, pump source, and optical resonator mirrors with cavity length. Black dots inside the gain medium are representing the atoms in ground state. Red dots represents excited atoms under the action of pump laser shown in green color. One mirror is highly reflective and the other one is partially reflective so that the laser output beam can leave the laser system.

Technically, the gain medium could be thought of as an amplifier, which is a part of the laser system, responsible for amplifying an existing laser beam to a desired power level. The existing laser is the seed laser. The function of the amplifier is that energy of pump laser is reduced whereas the energy of the seed laser is increased as explained by Figure 2.21. The oscillator consists of amplifier and optical cavity as mentioned earlier. The optical cavity is the region enclosed by mirrors or by metallic coating on the two ends of laser rod.

Finally, an analogy is given of lasing and playing music. When a pair of earphone is connected to a mobile phone wirelessly, music is going to play under the amplification of power amplifier inside the earphone. Here, the mobile phone generating a weak signal is like an oscillator producing weak laser pulse. Laser amplifier is similar to power amplifier in the earphone for amplifying the music signal. The music heard by listener is equivalent to the desired laser beam with desired properties such as laser fluence.

2.8.2 Ultrafast laser

Soon after the first demonstration of laser in 1960 by Theodore Maiman, one of the ingredients of an ultrafast laser was developed in 1970s by the mode-locked technique. It enabled the simultaneous oscillations of many highly coherent laser modes which superpose into a very short pulse [60]. Actually, simplifications were made concerning sharp energy level 2 and 3 in the last section. The levels 2 and level 3 can easily be broad bands which in fact are necessary for picosecond laser pulse generation [61]. Obviously, there must be some gain media for those levels to exist. There are many various types of laser medium, such as the gas, solution and

solid ones. Solid-state gain medium is the most commonly used for ultrafast lasers because it has a broadband of laser emission which is necessary for ultrafast laser pulses. The laser we used has titanium-doped Sapphire as gain medium with a short name (Ti:Sa) following a standard nomenclature of ‘ion:host’. The pump wavelength is 400 – 600 nm and emission wavelength is 650 – 1100 nm with the broadest emission bandwidth of any solid-state lasers as desired for an ultrafast laser. For Ti:Sa, the absorption band peaks around 490 nm so a green pump laser is required for pumping. One more thing required for short pulse duration, which is the modelocking. With a large bandwidth but no phase relation between different frequency components, it is not possible to produce a short pulse based on the superposition principle. Therefore, each frequency in the cavity should have a specific relationship to all the others. In this case, the cavity is said to be in mode-locked. Pulses shorter than 100 fs is possible by mode-locked laser [62]. In ordinary laser systems, if red light with a wavelength of 800 nm is used, the shortest possible pulse of light is the length of a single period in the light wave, 2.66 fs¹¹.

In order to get higher pulse intensity without damaging the gain medium and other transmissive optical components, a new concept called chirped pulse amplification (CPA) is needed, which was developed by Strickland and Mourou in 1985 [63, 64]. A huge breakthrough came after that. There are 4 main components for CPA, mode-locked oscillator, stretcher, amplifier and compressor as shown in fig. 2.23.

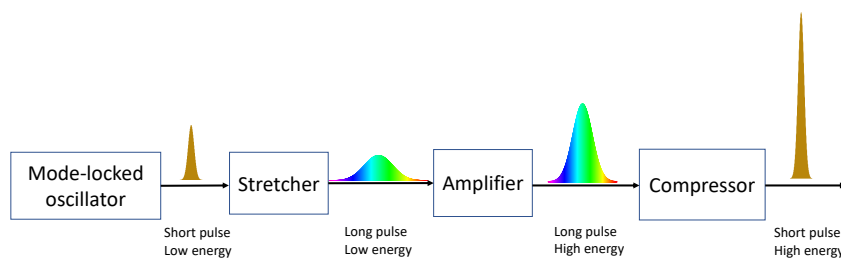


Figure 2.23: Operating principle of chirped pulse amplification.

A mode-locked oscillator or laser is utilized to produce femtosecond pulses, which are then temporally stretched by several orders of magnitude using a stretcher, which composed of a pair of gratings. Second, it is amplified in the gain medium without damaging since its pulse duration is longer and peak intensity is weaker. Finally, it is compressed in time back to original duration in the compressor consisting of a pair of grating, as is normally done nowadays.

2.8.3 Optical layout

The single pulse all-optical switching experiments are done by using the setup depicted in Figure 2.24. The polarizer is an optical component to allow light with a certain polarization direction through because of the various absorption coefficient along different crystal axis [39]. The wave plates are designed by applying the principle that the refractive index is different for linearly polarized light in different directions. Due to the difference of refractive index along fast and slow axis, half-wave plate (HWP) is utilized to introduce a π phase delay between two perpendicular components of polarized light along fast axis and slow axis [7]. Based on Malus’s law, the HWP is utilized to adjust the laser fluence through a combination with the downstream

¹¹In 1980s, this was thought as a hard limit for the shortest possible bursts of light. To surpass this limitation, a new idea called rescattering or three-step semiclassical model of high-harmonic generation was needed, going beyond Einstein’s stimulated emission theory. In recognition of this groundbreaking efforts in generating attosecond (10^{-18} s) pulses of light, the Nobel prize in Physics 2023 has been awarded to Pierre Agostini, Ferenc Krausz and Anne L’Huillier.

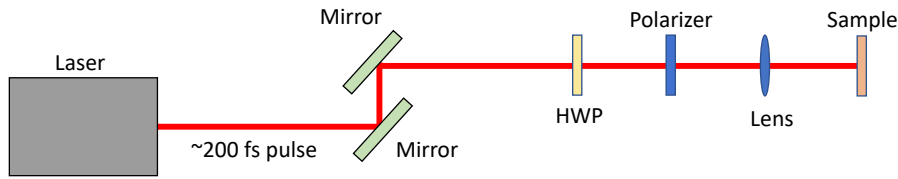


Figure 2.24: Schematic of single pulse all-optical switching experiment: using a lens to focus a single 800 nm laser pulse with time duration about 200 fs onto the sample surface. The polarisation of the laser beam as delivered is perpendicular to the table so there is only a need for a single polarizer.

polarizer by rotating the polarization plane of linearly polarized laser light with reference to the image in Figure 2.25. The HWP from EK SMA Optics is mounted on a motorized precision rotation stage from Thorlabs. The polarizer LPVIS100 from Thorlabs has an extinction ratio of $>10\,000:1$ over 550 - 1500 nm. This combination is used to study the influence of the laser fluence

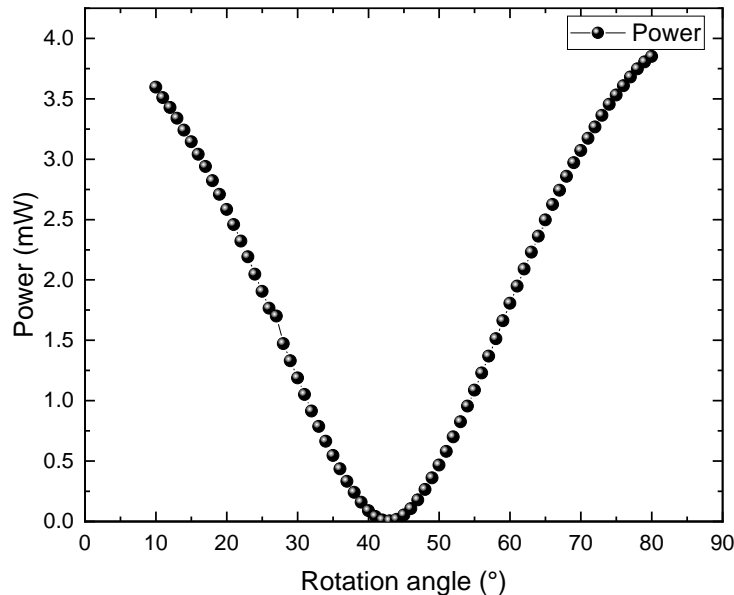


Figure 2.25: Laser fluence calibration. Rotation angle is the angle rotated by HWP. At 0° , the fluence should be at the maximum since the polarization direction of incident laser, the axis of HWP and that of polarizer are parallel. The particular measurement shown here begins with 10° . The angle between the output polarization and the input polarization will be twice the angle between the input polarization and the wave plate's axis, which explains the reason why the minimum of fluence happens occurs at 45° .

on the all-optical switching of magnetic thin films which will be discussed in detail later. The quarter-wave plate is used to obtain LCP and RCP from linearly polarized light by introducing a phase delay $\pi/2$ based on the same principle as HWP but with different phase delay. It can be added to the optical systems whenever study of effects of helicity of laser pulse on all-optical switching is needed. Finally, the laser is focused onto the magnetic thin film samples with a lens down to a spot size about $90\ \mu\text{m}$. Samples are mounted on a XYZ stage so that pulses can land at different positions for various pulse numbers. A cube of hard magnet with 0.5 T was utilized to saturate the sample with strong perpendicular magnetic anisotropy. This is not shown in the figure.

In order to gain higher resolution for domain imaging, which is very essential for image collection and data analysis, we used the commercial Evico Magnetics wide-field Kerr microscope to image the domains after pulses irradiation. The MOKE imaging configuration can be either in polar or longitudinal mode, with or without applied magnetic field, depending on the goals. But usually, I did imaging without field firstly so domains state were not disturbed and then did some field loop to see how the irradiated region behaved compared with non-irradiated ones.

The image recorded in greylevel has 1920×1242 pixels and 12 bits in depth. The sample during imaging is mounted on a 2-axis tilt so that a more uniform illumination background is accessible. High resolution and uniform background are both very important for domain imaging, since many isolated tiny domain are scattered around after laser pulses as will be discussed more in later chapters.

References

- [1] K. Vetenskapsakademien, “The discovery of giant magnetoresistance, 2007,” *Scientific Background on the Nobel Prize in Physics*, p. 23, 2007. (Cited on page: 42)
- [2] J. M. D. Coey, *Magnetism and Magnetic Materials*. Cambridge university press, 2010. (Cited on page: 42)
- [3] J. M. D. Coey and S. S. Parkin, *Handbook of Magnetism and Magnetic Materials.*, vol. 1 and 2. Springer International Publishing, 2021. (Cited on page: 42, 53, 57, 60, 62)
- [4] G. Weigang, H. Hecht, and G. Von Minnigerode, “Further investigations of cocondensation as a preparation method for amorphous states in transition metal alloys,” *Zeitschrift für Physik B Condensed Matter*, vol. 96, pp. 349–355, 1995. (Cited on page: 43)
- [5] F. Magnus, R. Moubah, A. H. Roos, A. Kruk, V. Kapaklis, T. Hase, B. Hjörvarsson, and G. Andersson, “Tunable giant magnetic anisotropy in amorphous SmCo thin films,” *Applied Physics Letters*, vol. 102, no. 16, 2013. (Cited on page: 44)
- [6] A. P. French, *Vibrations and Waves*. CRC Press, 2017. (Cited on page: 44)
- [7] R. P. Feynman, R. B. Leighton, and M. Sands, *The Feynman Lectures on Physics; New millennium ed.* New York, NY: Basic Books, 2010. Originally published 1963-1965. (Cited on page: 44, 47, 52, 55, 65)
- [8] D. Attwood, *Soft X-rays and Extreme Ultraviolet Radiation: Principles and Applications*. Cambridge university press, 2000. (Cited on page: 44)
- [9] D. S. Sivia, *Elementary Scattering Theory: for X-ray and Neutron Users*. Oxford University Press, 2011. (Cited on page: 45)
- [10] O. H. Seeck and B. Murphy, *X-ray Diffraction: Modern Experimental Techniques*. CRC Press, 2015. (Cited on page: 45)
- [11] M. Yasaka *et al.*, “X-ray thin-film measurement techniques,” *The Rigaku Journal*, vol. 26, no. 2, pp. 1–9, 2010. (Cited on page: 45)
- [12] F. Smits, “Measurement of sheet resistivities with the four-point probe,” *Bell System Technical Journal*, vol. 37, no. 3, pp. 711–718, 1958. (Cited on page: 47)
- [13] M. Urbaha, V. Vorohobovs, K. Savkovs, J. Fescuks, V. Feofanovs, and J. Korhs, “Electric current distribution in thin Ti–Cu base coatings,” in *IOP Conference Series: Materials Science and Engineering*, vol. 1140, p. 012053, IOP Publishing, 2021. (Cited on page: 47)
- [14] T. G. Rijks, S. Lenczowski, R. Coehoorn, and W. De Jonge, “In-plane and out-of-plane anisotropic magnetoresistance in Ni₈₀Fe₂₀ thin films,” *Physical Review B*, vol. 56, no. 1, p. 362, 1997. (Cited on page: 47)
- [15] L. J. van der Pauw, “A method of measuring specific resistivity and hall effect of discs of arbitrary shape,” *Philips Res. Rep.*, vol. 13, no. 1, pp. 1–9, 1958. (Cited on page: 47)

- [16] L. J. van der Pauw, “A method of measuring the resistivity and hall coefficient on lamellae of arbitrary shape,” *Philips technical review*, vol. 20, pp. 220–224, 1958. (Cited on page: 47, 48)
- [17] X. Hu, L. Zhu, K. Diao, W. Liu, X. Deng, and H. Wang, “Electrostatic derivation for the van der pauw formula and simulation using arbitrarily shaped resistive materials,” *AIP Advances*, vol. 12, no. 7, p. 075208, 2022. (Cited on page: 47)
- [18] D. De Vries and A. Wieck, “Potential distribution in the van der pauw technique,” *American Journal of Physics*, vol. 63, no. 12, pp. 1074–1078, 1995. (Cited on page: 47)
- [19] A. Alekseev, “Basics of low-temperature refrigeration,” *arXiv preprint arXiv:1501.07392*, 2015. (Cited on page: 48)
- [20] C. Mack, *Fundamental Principles of Optical Lithography: the Science of Microfabrication*. John Wiley & Sons, 2007. (Cited on page: 48)
- [21] R. Zaouk, B. Y. Park, and M. J. Madou, “Introduction to microfabrication techniques,” *Microfluidic Techniques: Reviews and Protocols*, pp. 5–15, 2006. (Cited on page: 49)
- [22] S. Foner, “Versatile and sensitive vibrating-sample magnetometer,” *Review of Scientific Instruments*, vol. 30, no. 7, pp. 548–557, 1959. (Cited on page: 51)
- [23] J. P. Phillips, S. Yazdani, W. Highland, and R. Cheng, “A high sensitivity custom-built vibrating sample magnetometer,” *Magnetochemistry*, vol. 8, no. 8, p. 84, 2022. (Cited on page: 51)
- [24] J. Mallinson, “Magnetometer coils and reciprocity,” *Journal of Applied Physics*, vol. 37, no. 6, pp. 2514–2515, 1966. (Cited on page: 51)
- [25] E. M. Purcell and D. J. Morin, *Electricity and Magnetism*. Cambridge University Press, 2013. (Cited on page: 51)
- [26] J. Bascom S. Deaver and W. M. Fairbank, “Experimental evidence for quantized flux in superconducting cylinders,” *Physical Review Letters*, vol. 7, no. 2, p. 43, 1961. (Cited on page: 52)
- [27] R. Doll and M. Näbauer, “Experimental proof of magnetic flux quantization in a superconducting ring,” *Physical Review Letters*, vol. 7, no. 2, p. 51, 1961. (Cited on page: 52)
- [28] N. Byers and C. Yang, “Theoretical considerations concerning quantized magnetic flux in superconducting cylinders,” *Physical review letters*, vol. 7, no. 2, p. 46, 1961. (Cited on page: 52)
- [29] B. D. Josephson, “Possible new effects in superconductive tunnelling,” *Physics letters*, vol. 1, no. 7, pp. 251–253, 1962. (Cited on page: 52)
- [30] J. Clarke and A. I. Braginski, *The SQUID Handbook*, vol. 1. Wiley Online Library, 2004. (Cited on page: 52)
- [31] R. Nagendran, N. Thirumurugan, N. Chinnasamy, and M. Janawadkar, “Development of advanced measuring instruments based on squid sensors for laboratory and industrial applications,” *Current Science*, vol. 101, no. 5, pp. 607–616, 2011. (Cited on page: 52)
- [32] A. Kraft, C. Rupprecht, and Y.-C. Yam, “Superconducting quantum interference device (SQUID),” *UBC Phys*, 2017. (Cited on page: 52)

- [33] P. Stamenov and J. M. D. Coey, “Sample size, position, and structure effects on magnetization measurements using second-order gradiometer pickup coils,” *Review of scientific instruments*, vol. 77, no. 1, p. 015106, 2006. (Cited on page: 52)
- [34] M. Buchner, K. Höfler, B. Henne, V. Ney, and A. Ney, “Tutorial: Basic principles, limits of detection, and pitfalls of highly sensitive squid magnetometry for nanomagnetism and spintronics,” *Journal of Applied Physics*, vol. 124, no. 16, p. 161101, 2018. (Cited on page: 52)
- [35] M. Faraday, “On the magnetization of light and the illumination of magnetic lines of force,” *Philosophical Transactions of the Royal Society of London*, vol. 136, pp. 1–20, 1846. (Cited on page: 53)
- [36] J. Kerr, “On rotation of the plane of polarization by reflection from a magnetic pole,” *The London, Edinburgh, and Dublin Philosophical Magazine and Journal of Science*, vol. 3, no. 19, pp. 321–343, 1877. (Cited on page: 53)
- [37] A. Hubert and R. Schäfer, *Magnetic Domains: the Analysis of Magnetic Microstructures*. Springer Science & Business Media, 2008. (Cited on page: 53, 58)
- [38] T. Lan, B. Ding, and B. Liu, “Magneto-optic effect of two-dimensional materials and related applications,” *Nano Select*, vol. 1, no. 3, pp. 298–310, 2020. (Cited on page: 53)
- [39] E. Hecht, *Optics*. Pearson Education India, 2012. (Cited on page: 53, 65)
- [40] Z. Qiu and S. D. Bader, “Surface magneto-optic kerr effect,” *Review of Scientific Instruments*, vol. 71, no. 3, pp. 1243–1255, 2000. (Cited on page: 53, 58)
- [41] G. R. Fowles, *Introduction to Modern Optics, 1989*. Dover Publications, New York. (Cited on page: 55)
- [42] M. Veis, *Optical interactions in thin films of selected magnetic oxides*. PhD thesis, 2009. (Cited on page: 56)
- [43] J. C. Maxwell, *A Treatise on Electricity and Magnetism*, vol. 1 and 2. Dover Publications, New York, 1954. (Cited on page: 56, 57)
- [44] J. Stöhr and H. C. Siegmann, *Magnetism*, vol. 5. Springer Berlin, Heidelberg, 2006. (Cited on page: 58, 61, 62)
- [45] J. Als-Nielsen and D. McMorrow, *Elements of Modern X-ray Physics*. John Wiley & Sons, 2011. (Cited on page: 59, 61)
- [46] P. Zeeman, “Nobel lecture,” 1902. (Cited on page: 59)
- [47] T. Funk, A. Deb, S. J. George, H. Wang, and S. P. Cramer, “X-ray magnetic circular dichroism—a high energy probe of magnetic properties,” *Coordination Chemistry Reviews*, vol. 249, no. 1-2, pp. 3–30, 2005. (Cited on page: 59)
- [48] J. Stöhr and Y. Wu, “X-ray magnetic circular dichroism: Basic concepts and theory for 3d transition metal atoms,” *New directions in research with third-generation soft x-ray synchrotron radiation sources*, pp. 221–250, 1994. (Cited on page: 59, 60)
- [49] F. Hippert, E. Geissler, J. L. Hodeau, E. Lelièvre-Berna, and J.-R. Regnard, *Neutron and X-ray Spectroscopy*. Springer Science & Business Media, 2006. (Cited on page: 61)

- [50] L. Gierster, A. Ünal, L. Pape, F. Radu, and F. Kronast, “Laser induced magnetization switching in a tbfeo ferrimagnetic thin film: discerning the impact of dipolar fields, laser heating and laser helicity by xpeem,” *Ultramicroscopy*, vol. 159, pp. 508–512, 2015. (Cited on page: 61)
- [51] A. Arora, M.-A. Mawass, O. Sandig, C. Luo, A. A. Ünal, F. Radu, S. Valencia, and F. Kronast, “Spatially resolved investigation of all optical magnetization switching in tbfe alloys,” *Scientific reports*, vol. 7, no. 1, p. 9456, 2017. (Cited on page: 61)
- [52] M. Ghidini, F. Maccherozzi, S. S. Dhesi, and N. D. Mathur, “Xpeem and mfm imaging of ferroic materials,” *Advanced Electronic Materials*, vol. 8, no. 6, p. 2200162, 2022. (Cited on page: 62)
- [53] A. Scholl, H. Ohldag, F. Nolting, J. Stöhr, and H. A. Padmore, “X-ray photoemission electron microscopy, a tool for the investigation of complex magnetic structures,” *Review of scientific instruments*, vol. 73, no. 3, pp. 1362–1366, 2002. (Cited on page: 62)
- [54] F. Kronast and S. V. Molina, “Speem: The photoemission microscope at the dedicated microfocus pgm beamline ue49-pgma at bessy ii,” *Journal of large-scale research facilities JLSRF*, vol. 2, pp. A90–A90, 2016. (Cited on page: 62)
- [55] E. Beaurepaire, J.-C. Merle, A. Daunois, and J.-Y. Bigot, “Ultrafast spin dynamics in ferromagnetic nickel,” *Physical review letters*, vol. 76, no. 22, p. 4250, 1996. (Cited on page: 62)
- [56] I. Radu, K. Vahaplar, C. Stamm, T. Kachel, N. Pontius, H. Dürr, T. Ostler, J. Barker, R. Evans, R. Chantrell, *et al.*, “Transient ferromagnetic-like state mediating ultrafast reversal of antiferromagnetically coupled spins,” *Nature*, vol. 472, no. 7342, pp. 205–208, 2011. (Cited on page: 62)
- [57] G. Kichin, M. Hehn, J. Gorchon, G. Malinowski, J. Hohlfeld, and S. Mangin, “From multiple-to single-pulse all-optical helicity-dependent switching in ferromagnetic Co/Pt multilayers,” *Physical Review Applied*, vol. 12, no. 2, p. 024019, 2019. (Cited on page: 62)
- [58] C. Davies, J. Mentink, A. Kimel, T. Rasing, and A. Kirilyuk, “Helicity-independent all-optical switching of magnetization in ferrimagnetic alloys,” *Journal of Magnetism and Magnetic Materials*, vol. 563, p. 169851, 2022. (Cited on page: 62)
- [59] P. F. Moulton, “Tunable solid-state lasers,” *Proceedings of the IEEE*, vol. 80, no. 3, pp. 348–364, 1992. (Cited on page: 63)
- [60] P. Fumagalli and J. Schoenes, “Magneto-optics,” in *Magneto-optics*, De Gruyter, 2021. (Cited on page: 64)
- [61] K. WALL and A. Sanchez, “Titanium sapphire lasers,” *The Lincoln laboratory journal*, vol. 3, no. 3, pp. 447–462, 1990. (Cited on page: 64)
- [62] J. D. Pickering, *Ultrafast Lasers and Optics for Experimentalists*. IOP Publishing, 2021. (Cited on page: 65)
- [63] G. Mourou, “Nobel lecture: Extreme light physics and application,” *Reviews of Modern Physics*, vol. 91, no. 3, p. 030501, 2019. (Cited on page: 65)
- [64] D. Strickland, “Nobel lecture: Generating high-intensity ultrashort optical pulses,” *Reviews of Modern Physics*, vol. 91, no. 3, p. 030502, 2019. (Cited on page: 65)

3 Magnetism, transport and atomic structure of amorphous binary Y_xCo_{1-x} alloys

In a Flight of Starlings.

Giorgio Parisi

3.1 Background and motivation

In the 1920s, a lot of effort were put into studying the order-disorder transformations based on previous work, such as the discovery of X-ray diffraction and the analysis of crystal structure by means of X-rays. One of the topics was the effect of order on magnetic properties [1]. In this case, the complexity induced by the disorder in a crystal was higher than that in an ordered crystal [2]. In 1960s, a further step towards more complex systems was made. Metallic glasses were experimentally discovered by quenching rapidly from the molten state by Duwez [3]. Since then they have been studied extensively for a lot of various interesting properties such as mechanical strength and magnetic coercivity. Due to its lack of long-range order, for a long time, there were no direct experimental methods able to determine three-dimensional structure of amorphous solids. Because of this, many models of amorphous materials were constructed in the laboratory or in the computer by using algorithms, hoping to simulate and reproduce some characters of the those complex systems, which were described by pairwise radial distribution function [4, 5].

However, in the last few years, a big advance was made in determining amorphous structures directly based on an experimental method named atomic electron tomography [6, 7]. It enables us to obtain a lot of information, such as the local atomic structure, coordination numbers, density and so on. The ability of being able to measure the local atomic structure and calculate coordination numbers might transform the understanding of amorphous materials and related properties in the future.

In the magnetic community, currently there are a lot of studies of amorphous magnets by focusing on magnetic properties such as spin-orbit torque and single pulse all-optical switching [8, 9, 10, 11]. One of the most studied systems is rare-earth transition metal system with two kinds of magnetic elements. However, there are few key questions which have been posed for a long time but not solved perfectly. For example, a- Dy_xCo_{1-x} and a- Tb_xCo_{1-x} have a very good perpendicular magnetic anisotropy for a certain range value of x around 0.25 [12, 13]. Where does the perpendicular anisotropy come from in amorphous systems? For 3d elements, such as Co, the orbital motion is very sensitive to the environment, such as the local electric field created by the other neighbors. Will the magnetic moment of Co be influenced by the amorphous structure? Will the orbital moment be quenched for Co in some structures? In order to try to answer those questions, a- Y_xCo_{1-x} is chosen because of several reasons. First, in this system Y is non-magnetic and Co is the only magnetic element. It is relatively easy to analyze, when compared with two magnetic elements system such as GdCo. Second, Y has a metallic radius of 1.80 Å, which is closest to that of trivalent magnetic rare-earths (1.75 - 1.83 Å)¹. Finally, Y has

¹The international Union for Pure and Applied Chemistry recommended in 1968 that the elements 58 through

the same outer electron structures and similar electronegativity as the magnetic rare earths²

With the availability of powerful computers and advanced experimental techniques for characterizing thin films, it is time to re-examine the magnetism of amorphous materials. In this work, we present a comprehensive study of a- Y_xCo_{1-x} alloy thin films, especially focusing on the appearance of magnetism, magnetic anisotropy and transport properties. We begin with the deposition and characterization of films, and then measure their magnetic and transport properties. Next, a relaxed model of binary atomic structure for a- Y_xCo_{1-x} is presented with 3:1 atomic volume ratio. Finally the discussion of those results will be made.

3.2 Sample preparation

All thin films were deposited by DC magnetron sputtering at room temperature on Si wafer substrates covered with 500 nm thermal oxide. The thin a- Y_xCo_{1-x} layers were deposited in a Shamrock system with a base pressure of 10^{-8} Torr. They were co-sputtered from separate 50 mm Y and Co targets. Composition was controlled by changing the Y target plasma power while fixing the Co power. Samples were capped with a layer of SiO_x or AlO_x 2-3 nm thick to protect them from further oxidation. In summary, the sample structure can be represented as Si/ SiO_x / Y_xCo_{1-x} /capping layer. For a systematic study, 20 samples with different yttrium ratio x were grown as shown in Table 3.1. Notation ' _ ' is used to separate different information in the sample code. Take the first sample code as an example. HZX20230130 means that this sample was made on 30th January 2023 by the author. YCo_3 means the nominal composition should be close to $x = 0.25$. 75 mA and 155 mA represent the target currents for Y target and Co target respectively, which follow the same sequence in the chemical formula Y_xCo_{1-x} . The last one represents the growth time 385 s for a specific thickness, usually close to 20 nm. The final point to be mentioned here is that there are two batches of samples. The first batch was made in January 2023 and the second batch was made in April 2023. Checking whether a sample is amorphous or not is made by X-ray diffraction. For the data such as thickness and density, from the third column to the final column, from fits to the X-ray reflectivity data.

3.3 Results

3.3.1 XRD

Examples of X-ray diffraction data on thin films sample are presented in Figure 3.1. They are measured using a Panalytical X'Pert Pro diffractometer. The top one is measured for a bare silicon wafer for a reference. The middle one, as a typical sample with a number 4 as listed in the Table 3.1, has a nominal chemical formula YCo_4 . The bottom one is just pure cobalt grown on a silicon wafer. For a- Y_xCo_{1-x} with a nonzero x , all peaks from the silicon wafer substrate are seen clearly from comparing the top and middle data patterns. Same or similar systems showing amorphous structures were reported before as well [16, 17, 18]. However for pure Co, a broadened diffraction pattern from nanocrystalline cubic close-packed cobalt. The peaks are labelled as explained in the caption. The reason for this appearance is that the single element is unable to form an amorphous structure, which requires at least two elements with different atomic size [3]. Based on the Scherrer equation, from the broadening of that peak it is possible to estimate the size of the nano-scale crystallites, with a value 8.6 nm. It was

71 be referred as *lanthanides* and that the name *rare earth* be reserved for the elements scandium, yttrium, lanthanum and the lanthanides [14].

²Similarly, in the inter-metallic compounds, yttrium transition metal compounds offer a good opportunity to study the nature of 3d-electron magnetism since the 3d atoms are fixed in a well-defined crystallographic positions. Very detailed information on 3d-electron magnetism can be obtained by using techniques such as nuclear magnetic resonance, the Mössbauer effect and diffraction with polarized neutrons [15].

Number	Sample code	Main layer thickness (nm)	Main layer roughness (nm)	Main layer density (g/cm ³)	Capping layer	Capping layer thickness (nm)	Y ratio based on calibration curve
1	HZX20230130_YCo3_75mA_155mA_385s	19.70	1.30	6.750	SiO ₂	3.21	0.25
2	HZX20230131_YCo4_75mA_205mA_326s	19.80	1.20	6.800	SiO ₂	3.10	0.185
3	HZX20230202A_YCo2_75mA_105mA_460s	17.50	1.50	6.700	SiO ₂	3.10	0.37
4	HZX20230202B_YCo1.5_75mA_80mA_518s	14.76	1.35	6.700	SiO ₂	3.78	0.46
5	HZX20230202C_YCo_75mA_60mA_586s	14.08	1.35	6.815	SiO ₂	3.76	0.54
6	HZX20230202D_YCo4_75mA_205mA_489s	30.20	1.25	6.600	SiO ₂	3.50	0.185
7	HZX20230202E_YCo4_75mA_205mA_163s	9.05	0.95	7.400	SiO ₂	4.38	0.185
8	HZX20230207B_YCo_75mA_65mA_586s	14.46	1.29	6.200	SiO ₂	4.11	0.53
9	HZX20230207A_YCo1p5_75mA_100mA_518s	17.55	1.72	6.400	SiO ₂	3.49	0.4
10	HZX20230209_YCo9_45mA_220mA_313s	16.46	1.16	7.000	SiO ₂	4.12	0.1
11	HZX20230208_YCo1.2_75mA_80mA_555s	15.60	1.75	6.700	SiO ₂	2.35	0.45
12	HZX20230130_Co_205mA_10mins	21.55	1.59	8.600	SiO ₂	4.56	0
13	HZX20230213_YCo0.8_75mA_55mA_616s	14.41	1.19	6.410	SiO ₂	4.14	0.55
14	HZX20230213_YCo1.35_75mA_90mA_536s	17.69	1.85	6.600	SiO ₂	3.59	0.425
15	HZX20230213_YCo1.1_75mA_70mA_570s	14.35	1.36	6.652	SiO ₂	3.87	0.485
16	HZX20230419C_YCo2_75mA_105mA_492s	19.62	1.85	6.446	Al ₂ O ₃	2.93	0.333
17	HZX20230419B_YCo2p45_75mA_125mA_453s	20.88	1.78	6.429	Al ₂ O ₃	2.90	0.29
18	HZX20230420_YCo1p5_75mA_80mA_554s	16.53	1.86	6.284	Al ₂ O ₃	3.14	0.4
19	HZX20230420_YCo5p7_75mA_220mA_280s	19.48	1.50	6.806	Al ₂ O ₃	3.18	0.155
20	HZX20230421_YCo1p2_75mA_60mA_593s	15.32	2.00	6.200	Al ₂ O ₃	3.10	0.45

Table 3.1: Summary of data for 20 a-Y_xCo_{1-x} thin film samples. The second column is the sample code given to each sample and written on the sample box. The letter 'p' is used to represent a dot in the code sometimes. The final column is the ratio x calculated from the calibration curves of the Co and Y targets. It is close to the nominal ratio given by the sample code but there are small deviations for some samples.

shown that films of pure Gd and Co have nanocrystalline structure and a rapid loss of crystal structure happens when the x is between 0.1 and 0.9 [19]. It has been reported that films of Y-Ni system, prepared by electron beam evaporation at room temperature in the concentration range of 10 and 80 atomic percentage of Y, show no indication of crystals found in the X-ray pattern [20]. However, in that instance, single crystalline sapphire was utilized as the substrate. It is reasonable to assume that the substrate may have an impact on the glass-forming ability. It is highly probable that the presence of a 500 nm amorphous silicon oxide layer aided in the formation of amorphous Y-Co thin films.

The strong Si (004) reflection at $2\theta = 69.1^\circ$ is accompanied by a shoulder at $2\theta = 66.5^\circ$. It might be thought to be a peak from the Si substrate or the thin film, but it is actually an aberration. This feature stems from the flat specimen error or equatorial divergence, which results in an asymmetric broadening on low 2θ . The magnitude of this effect is proportional to the divergent slit size [21]. The Si (002) peak is forbidden, however, its appearance is attributed to multiple diffraction which is essentially consecutive diffractions by different planes from $\langle 001 \rangle$ Si substrate [22].

3.3.2 XRR

The X-ray reflectivity data of a typical thin film a-Y_xCo_{1-x} is shown on the left panel in Figure 3.2 and it was measured by the same diffractometer as the X-ray diffraction. It is displayed on a logarithm scale, covering 7 orders of magnitude of intensity. The data is fitted by using the X'Pert Reflectivity software. It gives a film thickness of 16.53 nm, roughness of 1.86 nm, and 6.284 g/cm³ density of the main layer YCo with a 3.14 nm Al₂O₃ capping layer for protecting the sample from oxidation. The right panel of Figure 3.2 displays the fast Fourier transform of the same data, enabling a rough estimation of the layer thickness at approximately 20 nm and providing a reasonable set of starting parameters for proper fitting [23, 24, 25, 26].

The measured density of a-Y_xCo_{1-x} thin film samples is plotted in Figure 3.3, together with the densities of Y, Co and nine Y_nCo_m crystalline intermetallic compounds and the density of a 10,000 atom relaxed Y-Co binary atomic model. The black scatter points represent the experimental densities of a-Y_xCo_{1-x}, which are obtained by fitting XRR data. The blue scatter points represent the density of the inter-metallic compounds of Y_nCo_m. For example, when

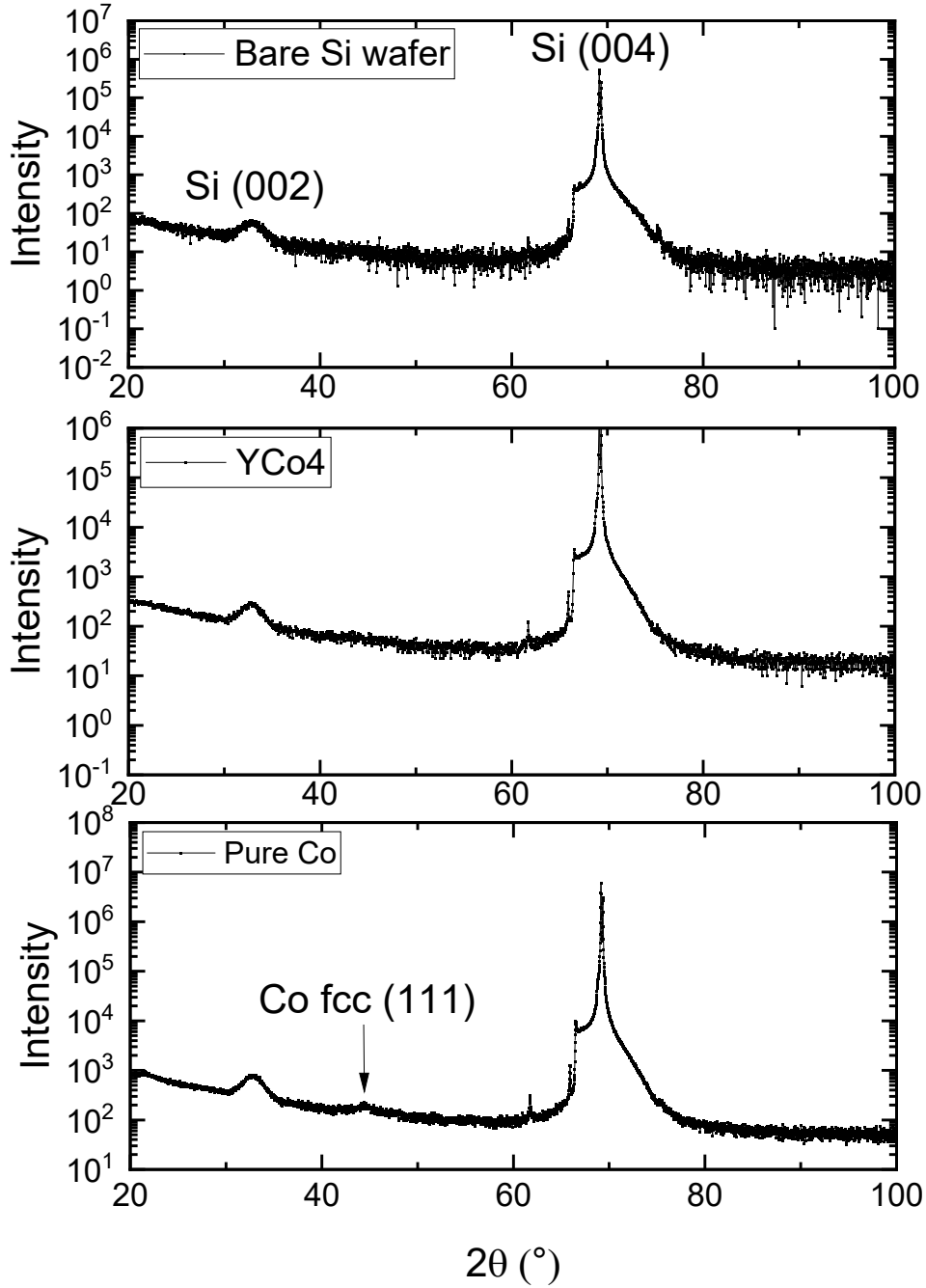


Figure 3.1: XRD data of a bare silicon wafer, a arbitrarily selected $a\text{-Y}_x\text{Co}_{1-x}$ with a nominal chemical formula $a\text{-YCo}_4$ and a pure Co thin films on all silicon wafer substrates. The Si (002), Si (004) and Co of face-centered cubic (fcc) structure (111) peaks are labelled.

$x = 0.25$, it corresponds to YCo_3 crystal. The red scatter points represent the density of 10,000 atoms relaxed Y-Co binary in the random close packing model. There are several things that need to be brought into attention. First, for the pure Co thin films, the density is only slightly lower compared to the crystalline form, with a difference of 2.6 %. It might be due to the fact that the Co thin films have many nano-crystals, as discussed already. Secondly, the densities of $a\text{-Y}_x\text{Co}_{1-x}$ are lower than those of inter-metallic compounds of Y-Co but higher than those of random close packed model.

Those data points in the Figure 3.4 include 18 samples with a thickness ranging from 14 nm to 22 nm. Despite our efforts to create a series of samples with a consistent thickness of 20 nm,

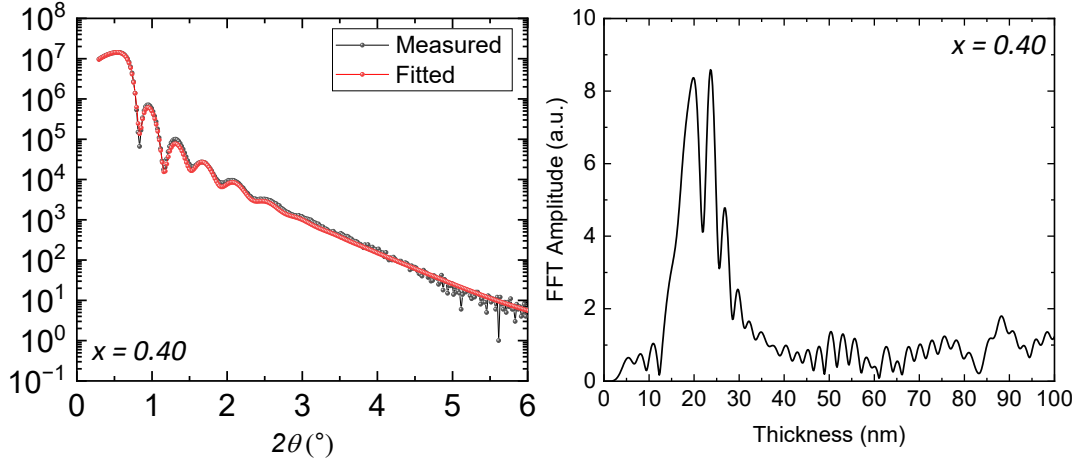


Figure 3.2: XRR of the number 18 a- Y_xCo_{1-x} sample with $x = 0.4$. **Left:** Fitting for a thickness of 16.53 nm, a density of 6.284 g cm^{-3} and a roughness of 1.86 nm for the main layer. The thickness for the capping layer Al_2O_3 is 3.14 nm. **Right:** Fast Fourier transform of the same experimental data from the left.

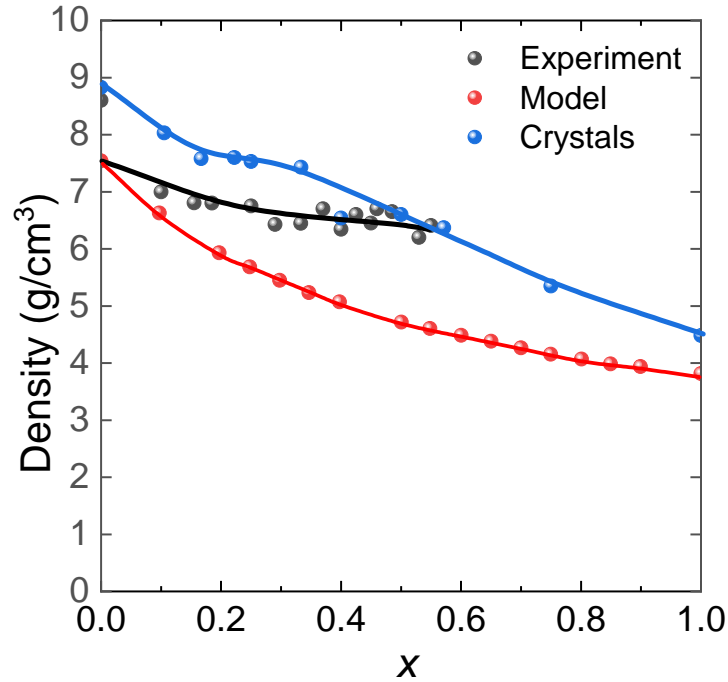


Figure 3.3: Density of amorphous Y_xCo_{1-x} , crystalline Y_xCo_{1-x} and Y-Co model. The black data points represent the experimental densities of a- Y_xCo_{1-x} , which are obtained by fitting XRR data. The blue data points represent the density of the inter-metallic compounds of Y-Co. For example, when $x = 0.25$, it corresponds to YCo_3 crystal. The red data points represent the density of 10,000 atoms relaxed Y-Co binary in the random close packing model. Those three lines serve as visual guides for the eyes.

we encountered fluctuations in thickness, particularly for high x values. Two samples, number 7 and 8, are not taken into consideration for this. Since they have thicknesses of 9 and 30 nm respectively and they were made for studying whether the thickness of thin film will influence its density as shown in Figure 3.5. The effect of thickness on magnetic properties will be discussed later. Those three samples with $x = 0.185$ were made by using the exactly same recipe and the

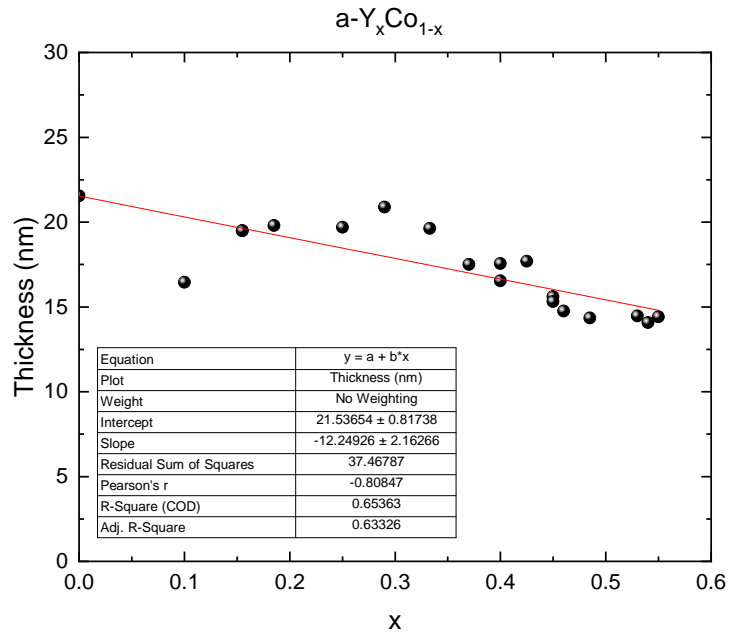


Figure 3.4: Thickness vs x of $a\text{-Y}_x\text{Co}_{1-x}$. A linear fitting of those data points is also shown.

only variable is the sputtering time. Since the growth rate is fixed, the thickness of thin film is proportional to the deposition time. The density decreases with increasing thickness, which is consistent with other similar systems such as Mg-Zn-Ca metallic glassy thin films [27]. This behavior is attributed to non-equilibrium growth mode for thin film with thickness typically below 400 nm. Those behavior applies to polymers as well, which also do not have a crystal structure [28, 29].

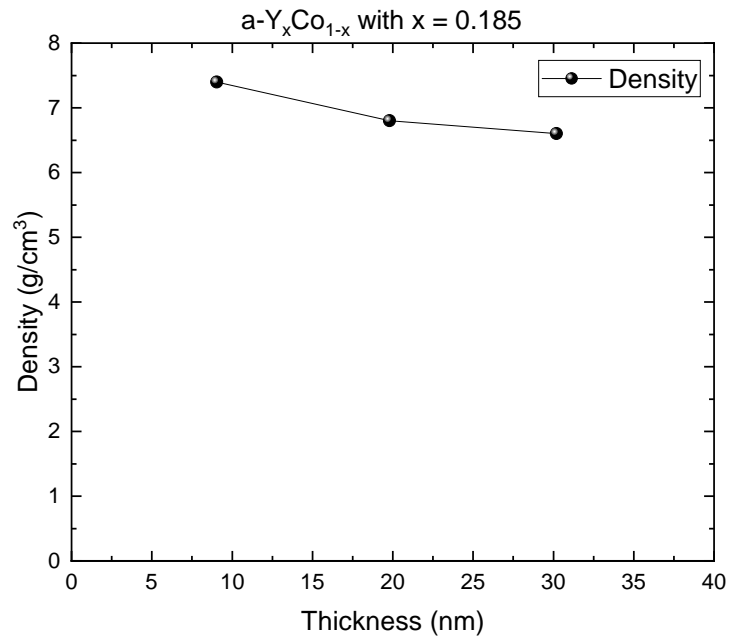


Figure 3.5: Film thickness effect on density of $a\text{-Y}_x\text{Co}_{1-x}$ with $x = 0.185$.

3.3.3 Magnetization as a function of field and composition

The magnetization as a function of field is measured in a 5 T Quantum Design SQUID Magnetometer at room temperature. The magnetic field was swept from 5 T to -5 T and then back to 5 T. Corrections must be made to get the real magnetization of the film itself. There are two main corrections. One is a geometrical correction for sample shape and orientation and the other one is a diamagnetic correction [30]. The geometrical correction is 4.08% and -2.23% for out-of-plane (OOP) measurement and in-plane measurement respectively. It means that, we need to multiply $(1 + 4.08\%)$ and $(1 - 2.23\%)$ respectively for the raw magnetic moment data of OOP and IP measurements. This is the first step before any further data processing. We need to perform the diamagnetic correction for the silicon substrate. The contribution from capping layer can be neglected since the mass is tiny compared with the Si substrate. A bare Si substrate should be measured in the SQUID for OOP and IP configurations, just like all the other $a\text{-Y}_x\text{Co}_{1-x}$ samples. Si substrate should be measured by a mass balance and calculate the mass magnetic susceptibility χ of it for OOP and IP configurations respectively. The χ is defined as

$$\chi = \frac{\text{magnetic moment}}{B \cdot \text{mass}} \quad (3.1)$$

The mass magnetic susceptibility of a bare Si substrate is tabulated in the Table 3.2.

	Mass (g)	Slope (Am ² /T)	Mass magnetic susceptibility (Am ² /T g)
OOP	0.0205	-2.42·10 ⁻⁸	-1.18·10 ⁻⁶
IP	0.0205	-2.59·10 ⁻⁸	-1.26·10 ⁻⁶

Table 3.2: Mass magnetic susceptibility of a bare Si <100> substrate measured OOP and IP.

We are now ready to process the data of $a\text{-Y}_x\text{Co}_{1-x}$ samples grown on Si substrates. We measure the mass of them as well and calculate the diamagnetic contributions based on the χ of the bare Si substrate. Subtract the diamagnetic signal from total magnetic moment and finally plot the magnetic moment from the main layer of $a\text{-Y}_x\text{Co}_{1-x}$ vs magnetic field. A plot including the raw data, data after only geometrical correction and data after both geometrical and diamagnetic corrections is shown in Figure 3.6. The workflow of this whole process is shown in Figure 3.7. It is applied to all samples. Among all samples listed in the Table 3.1, there are totally 4 different types of magnetization behavior when measured with the film parallel or perpendicular to the vertical field direction. This shows that the easy direction of magnetization lies in-plane for all the amorphous films that have a clear spontaneous magnetization.

When x is low with a value 0.1, the magnetization curves are depicted in Figure 3.8, which shows that the easy axis of magnetic anisotropy is in-plane. The saturation magnetization is 997 kA/m with saturation field 1.0 T. It shows a sharp transition of magnetization when the magnetic field is near 0 T. For the in-plane measurement, the sample behaves like a soft magnetic material with a step-like switching behavior.

With a bigger $x = 0.29$, as shown in Figure 3.9, both out-of-plane and in-plane magnetization measurement show single phase behavior with an easy axis of magnetic anisotropy lying in the plane. The saturation magnetization 340 kA/m is lower than the previous one since the Co percentage is lower. The saturation field 0.33 T is also smaller. A third type of magnetization curve is shown in Figure 3.10 with further increasing Co percentage. There is no big difference for in-plane and out-of-plane magnetization measurements, which indicates that there is no magnetic anisotropy. They behave like a paramagnet. The paraprocess³ is characterized by a nonlinear magnetization curve passing through the origin. It is superposed on a small in-plane ferromagnetic moment, yet no coercivity is measured with a field step of 24 mT. The fourth

³The high field leads to an increase of magnetization as a result of the paraprocess [31].

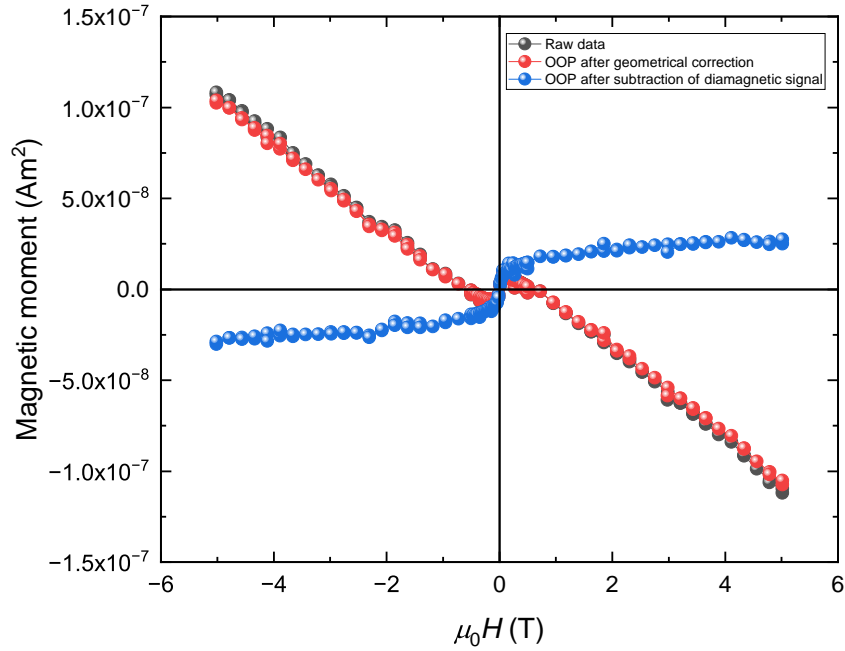


Figure 3.6: Example showing the data after geometrical correction and diamagnetic correction. The black curve represents the raw data for sample (number 20) measured OOP. The red one is the data after performing geometrical correction. The blue one is the data after a further diamagnetic correction and it represents the magnetic moment from the $a\text{-Y}_x\text{Co}_{1-x}$ with $x = 0.45$.

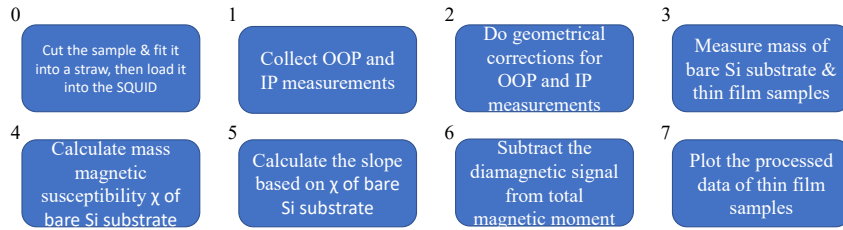


Figure 3.7: Workflow illustrating the sequential steps involved in the $M(H)$ data analysis process. The number in the top left corner denotes the sequence.

type of magnetization behavior is illustrated in Figure 3.11. The magnetization increases with increasing field without saturation up to 5 T magnetic field. It means the moment is induced by the applied field. The magnetization exhibits a para process⁴ with a broad maximum in the high-field susceptibility in the vicinity of x_0 shown in Figure 3.17 (c). The paraprocess is characterized by a nonlinear magnetization curve passing through the origin. It is consistent with what reported before that Co atoms lose their magnetic moment at Co concentration lower than a certain value [17, 18]. The magnetization measured at room temperature drops to zero when x is about 0.5, as seen from Figure 3.12. Besides that, the magnetization measured in-plane is always slightly bigger than that measured out-of-plane.

When $x = 0.33$, the crystalline YCo_2 does not have magnetic moment anymore, while the $a\text{-YCo}_2$ still has magnetization. For crystalline YCo_2 , $0.52 \mu_B$ per Co magnetic moment may be induced at 10 K by external large magnetic field up to 94 T [33].

⁴This is different from paramagnetism, where magnetization curve $M(H)$ response is linear, except in large fields or at very low temperatures [32].

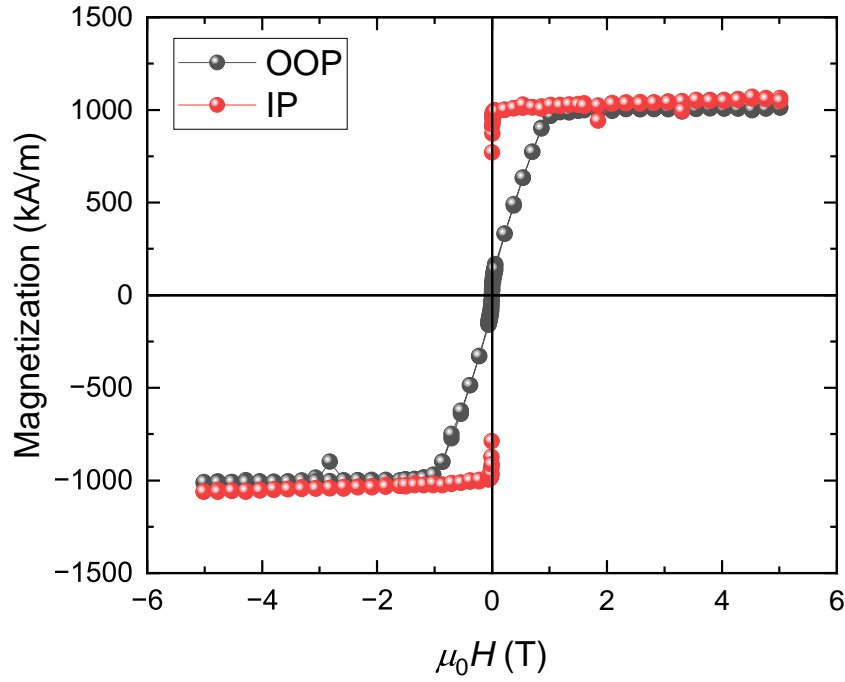


Figure 3.8: Magnetisation versus applied field, perpendicular and parallel to the surface of the number 10 $a\text{-Y}_x\text{Co}_{1-x}$ sample with $x = 0.1$.

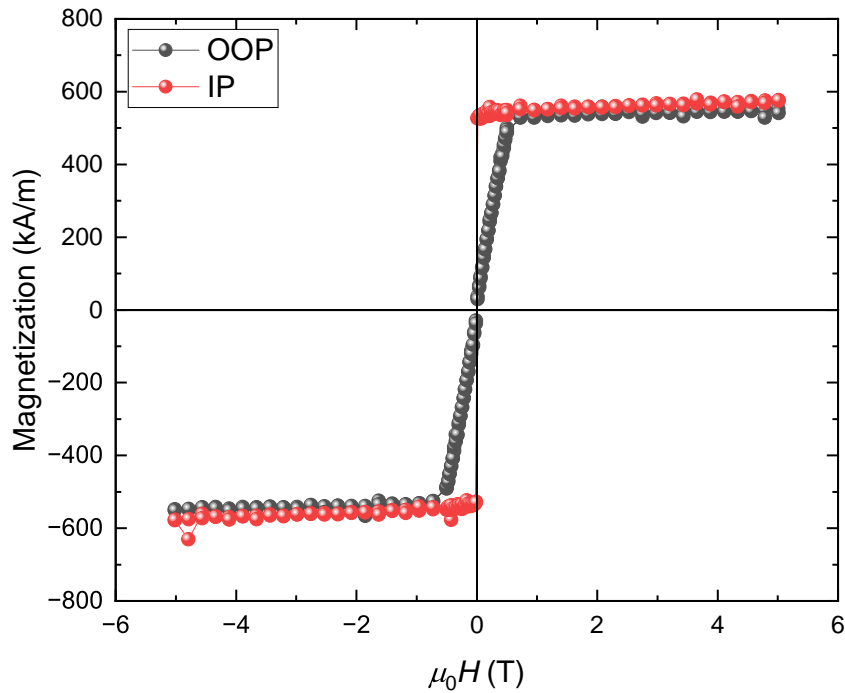


Figure 3.9: Magnetisation versus applied field, perpendicular and parallel to the surface of the number 17 $a\text{-Y}_x\text{Co}_{1-x}$ sample with $x = 0.29$.

3.3.4 Resistivity and Hall effect

The Van der Pauw method was used to measure the sheet resistivity at room temperature for a series of $a\text{-Y}_x\text{Co}_{1-x}$ with different x . The measurement configuration and results are shown in Table 3.3. Four measurements per sample were performed for each sample in order to reduce the measurement errors. The purple arrows represents the current direction in the thin film

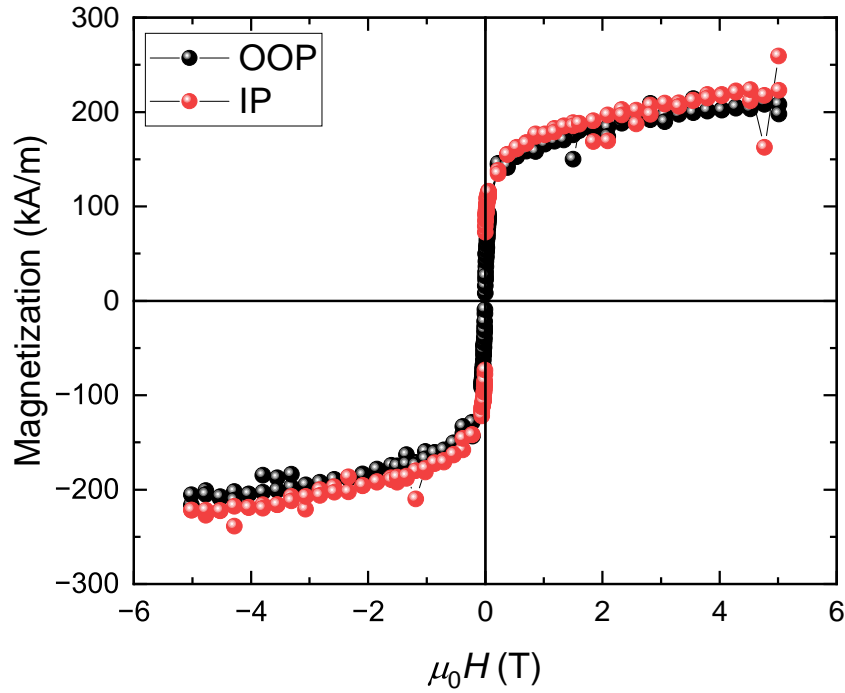


Figure 3.10: Magnetisation versus applied field, perpendicular and parallel to the surface of the number 11 a-Y_xCo_{1-x} sample with $x = 0.45$.

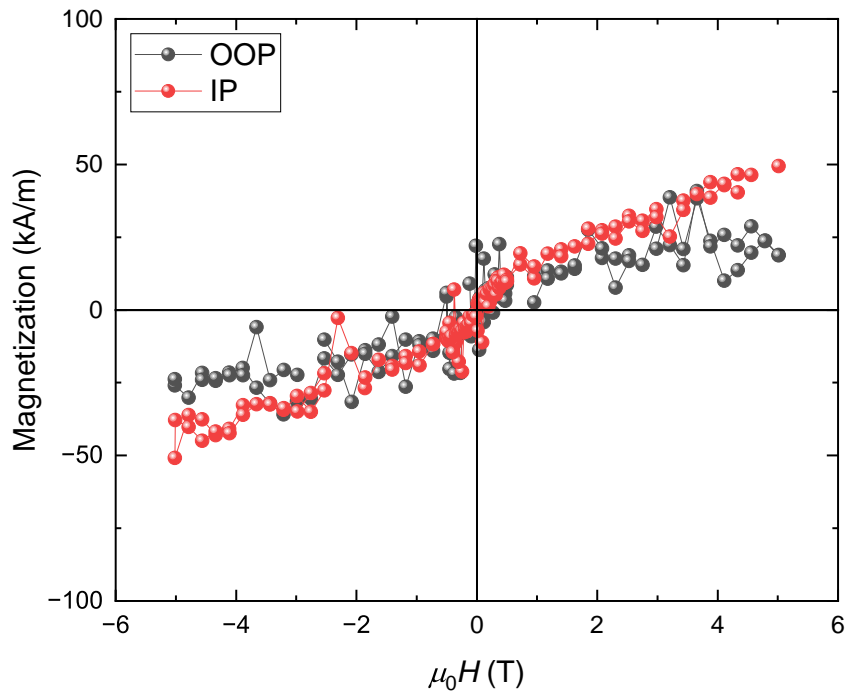


Figure 3.11: Magnetisation versus applied field, perpendicular and parallel to the surface of the number 5 a-Y_xCo_{1-x} sample with $x = 0.54$.

samples. The two red dots stand for the voltage measurement connections. The formula 2.3 is used to calculate the resistivity ρ . A function called `scipy.optimize.solve` from the SciPy is utilized to solve this non-linear equation. The sheet resistance R_S is defined as $\rho \times d$ where d is the thickness of thin films. The R_S and ρ are tabulated in Table 3.4. As seen from Figure 3.13, the resistivity of a-Y_xCo_{1-x} for $x > 0$ is higher than pure Co and has a value around $400 \mu\Omega\cdot\text{cm}$.

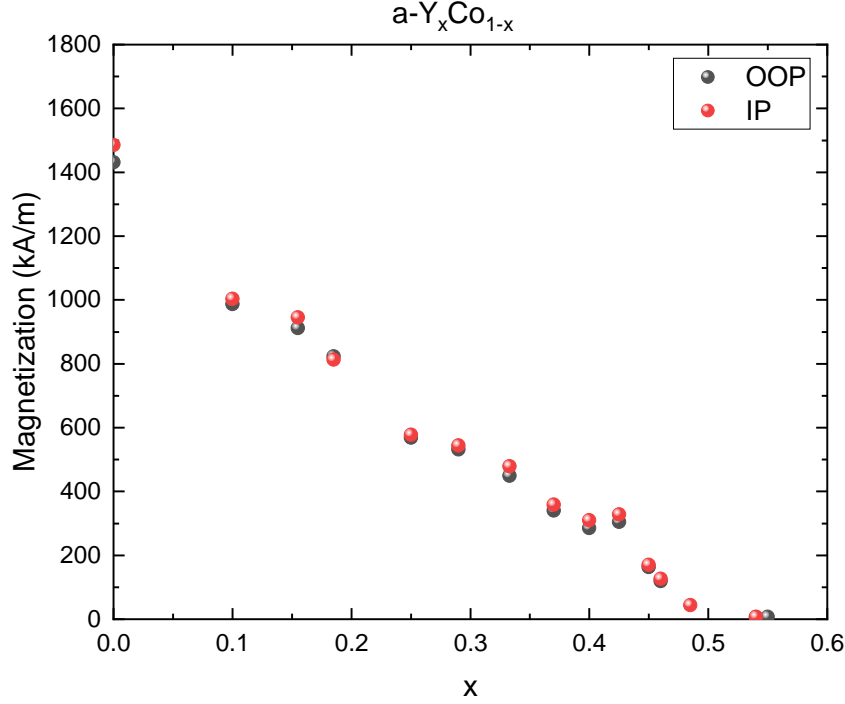


Figure 3.12: Magnetization vs x , where the magnetization is measured at room temperature for both OOP (black dots) and IP (red dots) configurations.

The maximum of ρ reaches a value $770.0 \mu\Omega\cdot\text{cm}$ when $x = 0.37$.

The four-point method, as illustrated in fig. 2.6 (a), was employed to measure the magnetoresistance when the magnetic field was applied perpendicular to the sample surface. The parabolic dependence of magnetoresistance on applied magnetic field can be seen in Figure 3.14. The antisymmetric behavior might be attributed to non-collinear positioning of the four connections (the outer twos for sending current and the inner ones for measuring voltage drop) and hence some signal from Hall effect was picked up.

The Van der Pauw method was applied to measure Hall effect at room temperature for most of the thin films with a current of 1 mA along the diagonal. A magnetic field of up to 2 T was applied out-of-plane using a electromagnet. In Figure 3.15, the out-of-plane magnetoresistance and Hall effect for different compositions are displayed. In each case, the Hall data as a function of perpendicular magnetic field is divided into two components: an asymmetric part representing the superposition of the anomalous and normal components of the Hall effect (plotted in red),





	Number 12	Number 10	Number 19	Number 2	Number 1	Number 17	Number 3	Number 9	Number 11	Number 13
Configuration 1 	3.60	40.68	38.48	60.27	36.08	60.04	122.80	33.80	48.82	43.32
Configuration 2 	3.59	41.36	40.32	60.28	41.89	62.84	123.20	39.84	48.93	46.70
Configuration 3 	2.62	65.11	24.58	37.34	69.55	48.16	71.13	80.80	61.96	48.24
Configuration 4 	2.62	64.40	23.91	38.13	57.82	46.56	79.30	80.40	60.60	42.20

Table 3.3: Resistivity measurement of $a\text{-Y}_x\text{Co}_{1-x}$ thin films by van der Pauw method: four different measurement configurations were used, and the resistance values are presented in ohm units. The purple arrows represents the current direction in the thin film samples. The two red dots stand for the voltage measurement connections. Each sample underwent four measurements, resulting in multiple data points. The measurements are tabulated and expressed in ohms.

	Number 12	Number 10	Number 19	Number 2	Number 1	Number 17	Number 3	Number 9	Number 11	Number 13
R_s (Ω)	13.97	235.46	141.32	217.98	227.92	245.12	440.00	252.76	248.53	204.70
d (nm)	21.55	16.46	19.48	15.32	19.70	20.88	17.50	17.55	15.60	14.41
ρ ($\mu\Omega$ cm)	30.11	387.57	275.29	333.94	449.00	511.81	770.00	443.59	387.71	294.97
x	0	0.1	0.155	0.185	0.25	0.29	0.37	0.4	0.45	0.55

Table 3.4: Comparison of sheet resistance R_s , thickness d , resistivity ρ , and composition ratio x for some samples. The table columns are organized based on the increasing x from left to right.

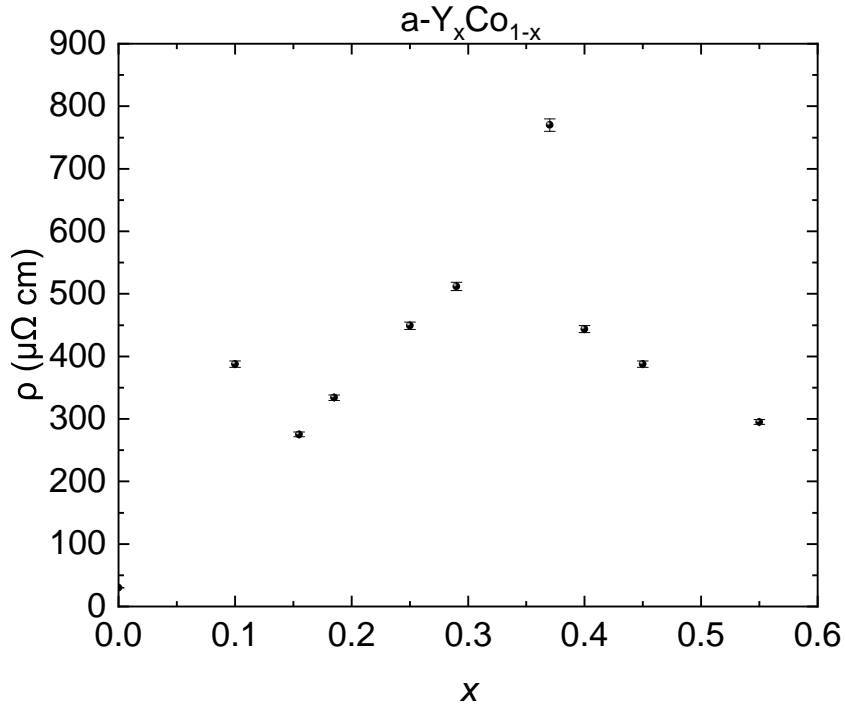


Figure 3.13: Composition dependence of resistivity of $a\text{-Y}_x\text{Co}_{1-x}$.

and a symmetric part representing the out-of-plane magnetoresistance (plotted in black). The magnetoresistance component consists of a band component varying as B^2 and saturating positive or negative component varying as M_z^2 . The polarity of the magnetoresistance can be either positive or negative due to variations in the equipotential offsets relative to the Hall contacts and an associated non-zero current component along the y-axis. For the samples measured, the leakage current through the silicon substrate, attributed to defects at the cleavage faces of the chips or some sample deposited at the substrate sides, amounts to smaller than 20% of the 1 mA current sent.

3.3.5 Magnetization of a function of temperature

Three samples with $x = 0.4, 0.46$ and 0.485 were selected and measured for the magnetization as a function of temperature from 100 K to 350 K with a perpendicularly applied 0.5 T or 0.6 T field to make sure the sample was saturated. The $M(T)$ curve is shown in Figure 3.16. These samples were chosen since their composition values x are close the critical value where the magnetic moment of Co disappears. As seen from the figure, when $x = 0.4$, the variation of magnetic moment of Co is very tiny, which indicates that the magnetic ordering temperature T_c is very high. The T_c was reported to be around 760 K when $x = 0.25$ [34]. Similar T_c is expected here. But when $x = 0.46$ and 0.485 , close the critical composition value x_c where the magnetic moment disappears, there is a big variation of the magnetic moment during the thermal scan.

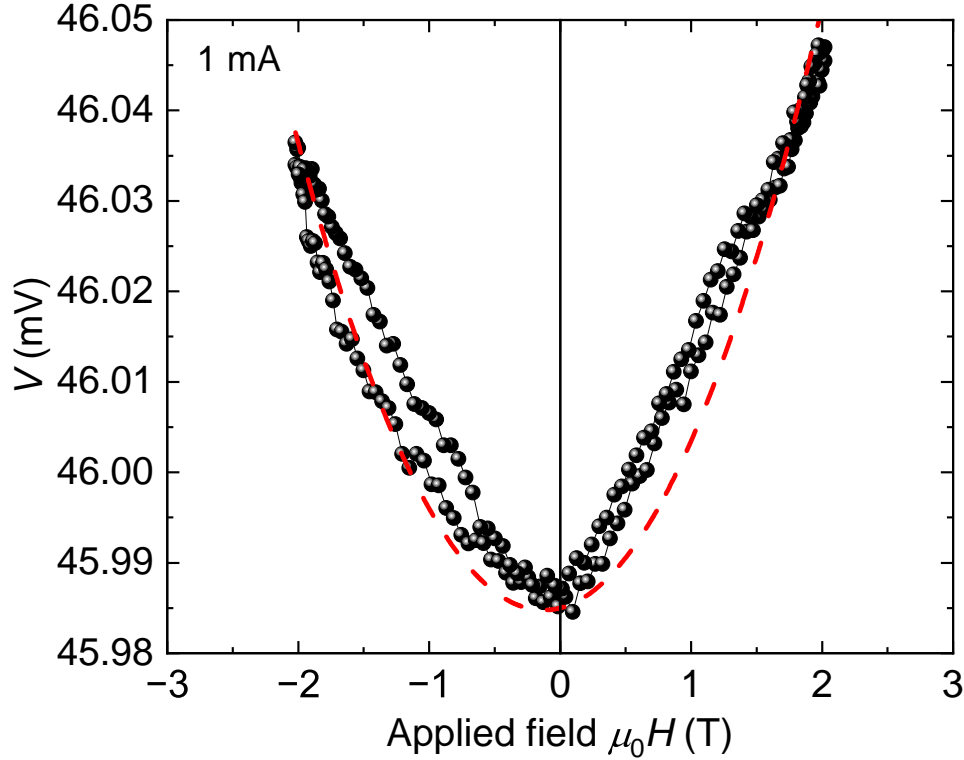


Figure 3.14: Magnetoresistance of a-Y_{0.155}Co_{0.845} by using the four-point method and magnetic field is perpendicular to the sample surface. The black dots are the experimental data points and the red dash line is the parabolic fitting curve.

3.3.6 Magnetic moment vs x

Since the Y has no contribution to the magnetic moment as measured at the Y $L_{2,3}$ edge in a-YCo₂ [35], a reasonable assumption could be made that the measured magnetic moment originates only from Co only for all samples with various compositions. Based on the density from XRR fitting and the sample composition from growth calibration, it is possible to know how many atoms in unit volume and therefore the magnetic moment per Co for the amorphous alloys is obtainable, as presented by data points in Figure 3.17 (a). All films are magnetically soft with a coercivity field less than 1 mT. The extracted magnetic moment from the published literature per Co for the crystalline intermetallic compounds is illustrated in Figure 3.17 (b).

There is a threshold x value about 0.53 for the appearance of intrinsic magnetic moment⁵. Above that value, there is only induced magnetic moment due to external magnetic field. When x is smaller than 0.2, the magnetic moment of Co is very high, about $1.79 \mu_B$ per Co atom. Those fitting curves will be discussed in the next section.

3.3.7 X-ray magnetic circular dichroism

A film of a-Y_{0.25}Co_{0.75} was measured on UE49 SGM beamline at the BESY II light source, Helmholtz-Zentrum Berlin-Adlershof. The X-ray beams were incident perpendicularly to the sample surface and X-ray magnetic circular dichroism was measured by total electron yield at the Co $L_{2,3}$ absorption edge. A well-defined difference spectrum was presented in Figure 3.18 for left and right circularly-polarized radiation. Data were analysed using the sum rule to obtain spin and orbital moments of $1.31 \mu_B/\text{Co}$ and $0.315 \mu_B/\text{Co}$ ⁶, respectively. Therefore, the total moment

⁵A similar threshold value of 0.5 for x is reported in a-La _{x} Co_{1- x} thin films [36].

⁶It has been reported that no magnetic moment was detected on Y $L_{2,3}$ edge in a-YCo₂ [35].

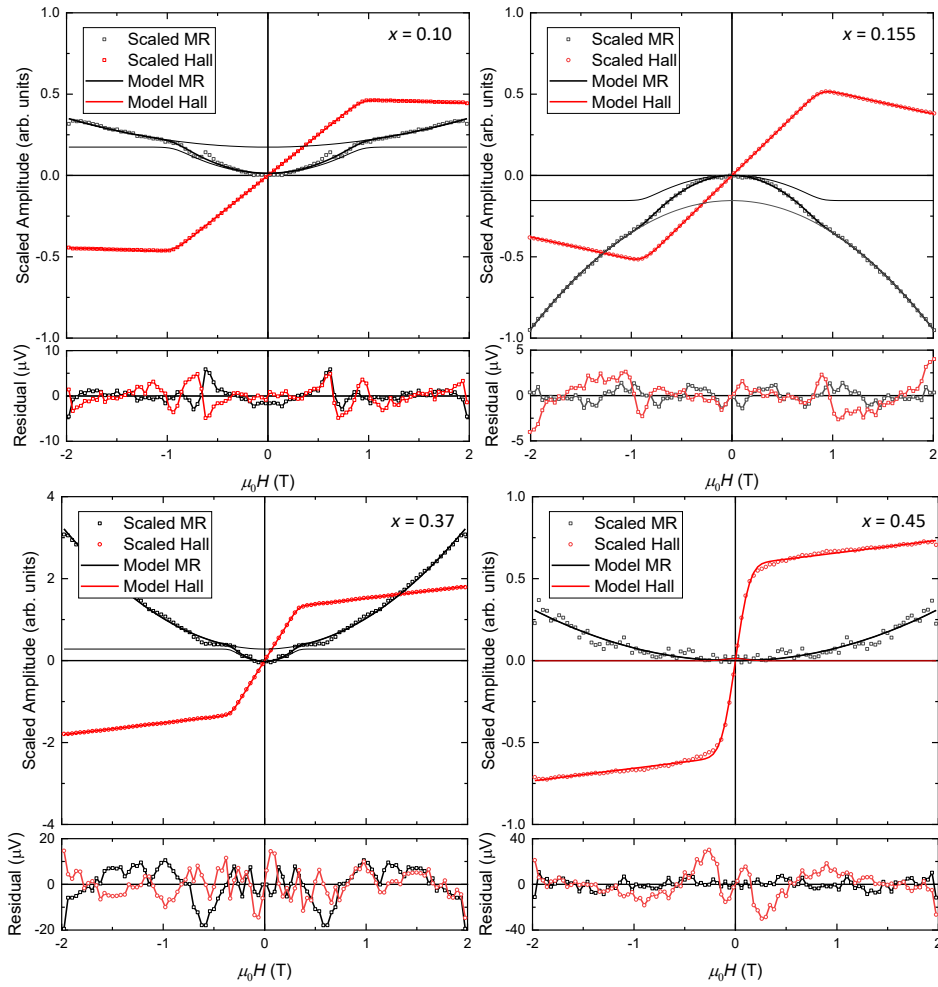


Figure 3.15: Magnetoresistance and Hall effect of four $a\text{-Y}_x\text{Co}_{1-x}$ thin films, measured at room temperature. The data are decomposed into symmetric and antisymmetric components in the applied field representing respectively the transverse magnetoresistance (black), and the normal and anomalous Hall effects (red) and in the top panels; The residuals from the simultaneous fits to a model of homogeneous rotation of the magnetization are shown below each panel

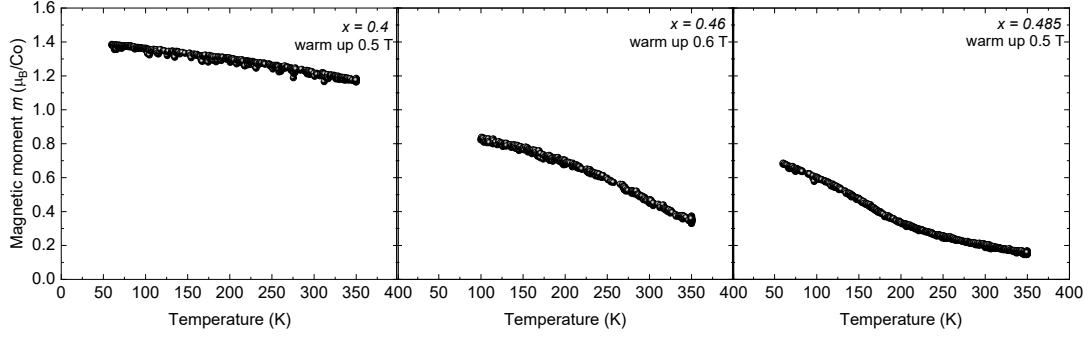


Figure 3.16: Magnetization as a function of temperature for a- Y_xCo_{1-x} with $x = 0.4$, 0.46 and 0.485 . It was measured with a 0.5 T or 0.6 T field applied perpendicularly to the thin film and data was recorded during warming up from 100 K to 350 K.

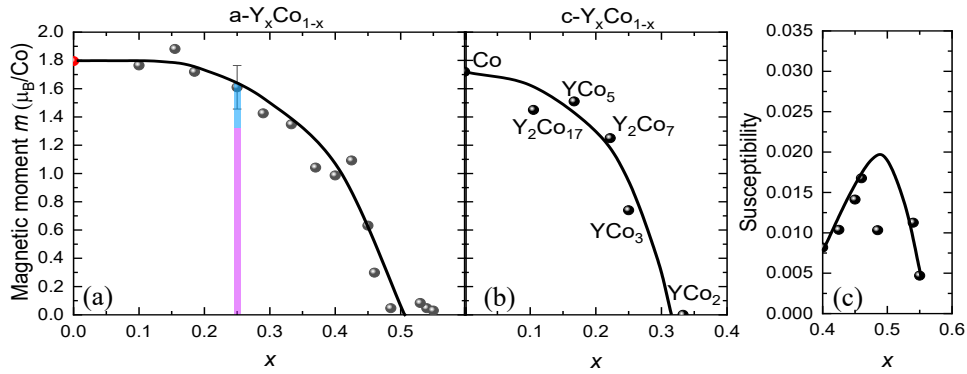


Figure 3.17: The average magnetic moment per cobalt in (a) amorphous Y_xCo_{1-x} alloys measured at room temperature and (b) crystalline Y_nCo_m intermetallic compounds (literature values). The vertical bar in (a) represents the spin moment (green) and orbital moment (blue) determined by X-ray magnetic circular dichroism (XMCD). (c) is a plot of the dimensionless high-field susceptibility in the vicinity of x_0 . Solid black lines are guides to the eye. The red data point in (a) represents pure Co, not in amorphous state as previously discussed. It is included to compare the Co moment at various x from 0 to 0.55 .

is $1.63 \mu_B$, compared with the value of 1.61 ± 0.18 measured from the SQUID magnetometry, where the error is the standard deviation of the mean of three different a- $Y_{0.25}Co_{0.75}$ samples.

3.3.8 Binary amorphous structure

To gain a better understanding of the local structure of the a- Y_xCo_{1-x} thin films, a $10,1000$ atom random close-packed model was constructed for a binary amorphous structure composed of hard sphere with a volume ratio $3:1$ to represent the Y and Co atoms. Following the procedure of Clark and Wiley, atoms were initially placed at random positions within a box with a periodic boundary conditions for a particular value of x , $0 \leq x \leq 1$. The method does not involve sequential addition of atoms to build the model, rather the whole array is defined at the beginning. The box is increased in size and atoms are moved to remove the overlap. Atoms are vibrated with small random displacements to eliminate jamming, allowing them to find higher density configurations as the box is again shrunk. Surprisingly, it is found from the simulation that the packing fraction for every composition is in the range from 0.629 - 0.637 . Information on the number of nearest-neighbors is derived from the resulting set of atomic positions. We designate the nearest-neighbors as A-B pairs, indicating the count of B atoms surrounding an A atom, where A and B can represent either Y or Co. For each x , the distributions are Gaussian and a fit

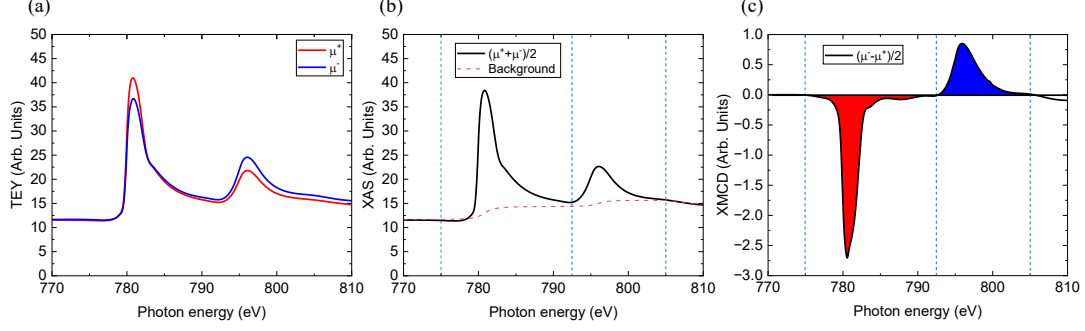


Figure 3.18: Spectra of X-ray Absorption Spectroscopy (XAS) and X-ray Magnetic Circular Dichroism (XMCD) for a-Y_{0.25}Co_{0.75}: (a) The polarization-dependent Co L-edge XAS of a magnetically saturated a-Y_{0.25}Co_{0.75} measured by total electron yield. The peaks at 780 eV and 796 eV are L₃ and L₂ absorption edges of Co, respectively. (b) The average XAS (black solid line) with background fit (red dash line). The background is removed before integration of the spectra. The three blue dash lines are used to denote the regions for calculating the integral r , p and q as introduced in the section 2.7.1. The integral r is calculated between the first and third blue dash lines. (c) XMCD spectrum. The three blue dash lines are used to denote the regions for calculating the integral p and q as introduced in the section 2.7.1. Areas under the x-axis will come out negative and areas above the x-axis will be positive. Therefore, integral p is equal to the area in red and integral q is equal to the sum of area in red and area in blue. This XAS and XMCD experiments were performed by Katarzyna Siewierska and the the data were analyzed by Ross Smith.

is used to extract their average values, shown in Figure 3.19. As we can see, at $x = 0.25$, the average Y and Co coordination numbers of a Co atom are 6.6 and 2.0, respectively. At $x = 0.5$, which represents the critical concentration for the appearance of the Co magnetic moment, the average coordination number for both Y and Co is approximately 3.2. This is analogous to the behavior observed in crystalline YCo₂, where just three neighboring atoms are sufficient to quench the Co magnetic moment.

3.4 Discussion

An aim of our study has been to establish the behaviour of the ferromagnetic cobalt subnetwork in a-Y_{*x*}Co_{1-*x*} and use it as a basis for analysing the magnetism of other a-R_{*x*}Co_{1-*x*} alloy systems, especially those exhibiting compensation and perpendicular magnetic anisotropy. This is often case for compositions lying between a-RCo₂ and a-RCo₃, $0.25 < x < 0.33$, when R = Gd [37, 38, 39, 40, 41], Tb [42, 43, 44], Dy [45, 44, 46, 47], Ho [38, 46], and Er [48, 37] for example. Our study mostly focused on properties at room temperature, which is appropriate because applications of these films in ultra-fast magneto-optics switching are likely to be at room temperature. The previous studies conclude that Curie temperature are well above room temperature when $x < 0.4$, and they are greater than the corresponding crystalline alloys. It extrapolates to 1850 K for amorphous cobalt. The R-Co exchange is antiferromagnetic for heavy rare earths and mediated by the rare earth 5d electrons. It prefers to couple heavy rare-earths atoms antiparallel to the strongly ferromagnetic cobalt subnetwork.

3.4.1 Mass density

We begin the discussion with mass density, one of the simplest but very important and useful physical quantities. Overall, the densities of a-Y_{*x*}Co_{1-*x*} thin films decrease with increasing x as

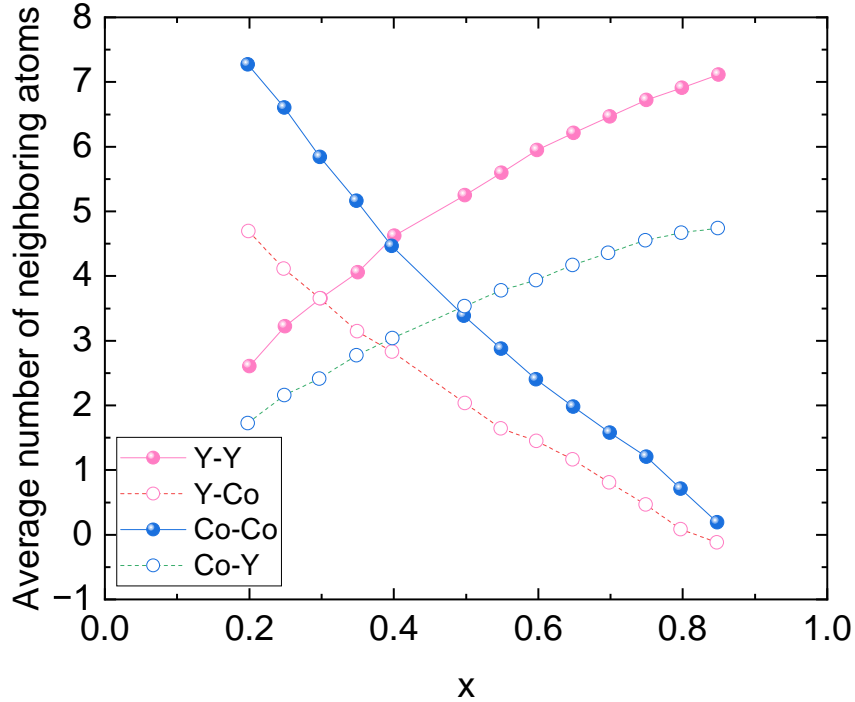


Figure 3.19: Average numbers of Y and Co neighbours around an Y atom, and Y and Co neighbours around a Co atom in the binary random dense-packed amorphous model, which was studied by Dr. Jean Besbas. The legend label A-B corresponds to the number of B atoms found around an A atom.

shown in Figure 3.3. It is consistent with what found in amorphous Cu-Zr system [49], where Cu and Zr have similar radius with Co and Y respectively. The densities of $a\text{-Y}_x\text{Co}_{1-x}$ is about 10 % smaller than those corresponding crystals when $0 < x < 0.4$. Amorphous metals typically are only 0.5% - 2% smaller than the corresponding crystals [50, 13]. There are several possible reasons for these. One possible explanation for this quite big difference is that the $a\text{-Y}_x\text{Co}_{1-x}$ thin films are all grown onto the substrate at room temperature. As reported already, there is a dependence of film density as a function of substrate temperature. The density of films increase continuously with the increase in the substrate temperature [51]. Argon gas pressure is also a possible reason. The higher argon pressure leads to films with a lower density. It can be attributed to the different energy of atoms forming the films during deposition. At high pressure, the deposited atoms are thermalized by argon gas during collision process. So the energy of the deposited atoms is too low to induce a sufficient atomic mobility to produce an energetically favorable configuration. It therefore leads to less-dense films. Decreasing the distance between the target and substrate has a similar effect, that is why some researchers define a quantity called pressure-distance product. Using that as a control parameter in order to get a desired density of thin films [52]. The difference between densities of simulation and those experimental densities might be due to the assumption of hard spheres. It is possible that atoms deform in such a way so as to fill space more efficiently than a random close packing of hard spheres [50].

3.4.2 Anisotropy

All thin films of $a\text{-Y}_x\text{Co}_{1-x}$ with x no bigger than 0.4 exhibit in-plane magnetization resulting from shape anisotropy, as seen from the four different types of magnetization data presented above. However, the saturation field H_s in the hard direction is less than the saturation magnetization M_s . The slope of the graph in Figure 3.20 is 1.18, which indicates that there is a intrinsic perpendicular anisotropy. When a magnetic field is applied perpendicularly to thin

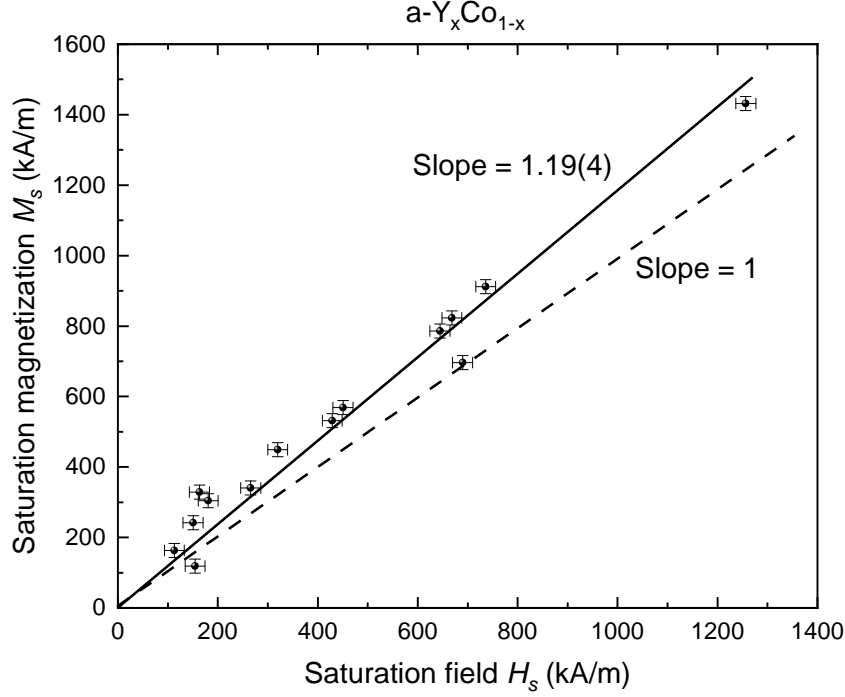


Figure 3.20: Plot of saturation magnetization versus saturation field of a-Y_xCo_{1-x}. The solid line, a fit to the data points, displays a slope >1, suggesting that there is an intrinsic perpendicular magnetic anisotropy that is overcome by shape anisotropy in the amorphous films. The dash line has a slope of 1, where H_s is equal to M_s .

films and the net magnetization is denoted by a vector \mathbf{M} that rotates and makes an angle θ with the normal to the film, the magnetostatic energy E comprises three terms:

$$E(\theta) = \frac{1}{2}\mu_0(M \cos \theta)^2 - \mu_0 H M \cos \theta + K_1 \sin^2 \theta \quad (3.2)$$

Equilibrium is found by minimizing $E(\theta)$:

$$\frac{dE}{d\theta} = -\mu_0 M^2 \cos \theta \sin \theta + \mu_0 H M \sin \theta + 2K_1 \sin \theta \cos \theta = 0 \quad (3.3)$$

Therefore

$$(M \sin \theta) \cdot \left(-\mu_0 M \cos \theta + \mu_0 H + \frac{2K_1}{M} \cos \theta \right) = 0 \quad (3.4)$$

If $K_1 = 0$, the magnetization curve is $H = M \cos \theta$, otherwise $H = \left(1 - \frac{K_1}{\mu_0 M^2}\right) M \cos \theta$. Because $H_s = 0.85M_s$, $\frac{2K_1}{\mu_0 M_s^2} = 0.15$. If $M_s = 500 \text{ kAm}^{-1}$, for example, $K_1 = 24 \text{ kJm}^{-3}$. Hence, this intrinsic Co contribution to the anisotropy will be enough to enable out-of-plane magnetization in a-R_xCo_{1-x} films near compensation temperature [19], when $M_s < 195 \text{ kA/m}$. The origin of the intrinsic contribution may come from the interface anisotropy in the thin cobalt films.

Figure 3.21 presents a comparison between the calculated average orbital moments for the crystalline Y-Co intermetallic compounds, including both spin-orbit interaction and orbital polarization term [53], with those measured for YCo₅ [54, 55] and hcp Co [32] and with that of a-YCo₃ deduced from XMCD. Since YCo₅ possesses a significant magnetocrystalline anisotropy of 6.5 MJm^{-3} , it is expected that the local anisotropy of cobalt in a-YCo₃ is of similar magnitude. Despite the large random anisotropy resulting from the disordered structure, it does not appear to suppress the ferromagnetism observed in a-Y_xCo_{1-x}, as evidenced by the magnetization data. In the HPZ model of an amorphous ferromagnet [56], the local anisotropy is represented by a

term $\mathbf{D}_i(\mathbf{S}_i \cdot \mathbf{e}_i)^2$ where the direction of local anisotropy parameter \mathbf{D}_i changes from site to site, \mathbf{e}_i is the local anisotropy direction and \mathbf{S}_i is the local spin angular momentum of the Co atom. The contributions of all Co atoms are summed to produce a set of macroscopic energy terms. The sum is straightforward if we assume that the local anisotropy axes of each site point in the same direction. If taking $S = 1$ for Co and the film density as 6.6 g/cm^3 and assuming that \mathbf{D}_i has the same magnitude at each site D , the D/k_B is 5.2 K, corresponding to $K_2 = 3.2 \text{ MJ/m}^3$, where K_2 is the local uniaxial anisotropy⁷. The value of K_2 is deduced from the fact that orbital moment of Co in a-YCo₃ is practically the same as that in crystalline YCo₅ and scaling by the number of Co atoms per unit volume. The Curie temperature of a-YCo₃ was estimated theoretically and measured experimentally to be 760 K. The corresponding Weiss coefficient $n_W = T_c/C$ where the Curie constant $C = \mu_0 n g^2 \mu_B^2 S(S+1)/3k_B$ [32]. Based on these, the molecular field $\mu_0 H_W$ is

$$\mu_0 H_W = \frac{3k_B T_c}{g\mu_B(S+1)}. \quad (3.5)$$

By assuming the $S = 1$ and $g = 2$, a molecular field $\mu_0 H_W$ of 848 T acts on the ferromagnetic Co⁸. The exchange energy is 1139 K/Co atom, and the ratio α , defined as $\frac{\text{anisotropy energy}}{\text{exchange energy}}$ per atom, is 0.005, significantly smaller than 1. Therefore, the exchange interaction predominates. In such case, a wandering ferromagnetic axis over a length scale can be identified. The ferromagnetic correlation length L can be estimated by minimizing the sum of anisotropy and exchange energy. Mathematically the problem reduces to evaluating two competing terms [57, 58, 32, 59]:

$$E = A[(\nabla m_x)^2 + (\nabla m_y)^2 + (\nabla m_z)^2] - K_2(\mathbf{m} \cdot \mathbf{e}_i)^2 \quad (3.6)$$

where A is the exchange interaction of stiffness, K_2 is strength of local uniaxial anisotropy, \mathbf{e}_i is a unit vector giving the local easy axis direction and $\mathbf{m}(r) = \mathbf{M}(r)/M_s$ is the local reduced magnetization.

The local anisotropy direction is assumed to change over a structural correlation length d . We first make an assumption that $L \gg d$ so that magnetization fluctuations average over many regions with different anisotropy directions. In a region of volume L^3 there will always be some easiest direction determined by statistical fluctuations in the way the random anisotropies add up [58]. The effective anisotropy affecting the magnetization process results from averaging over the $N = (\frac{L}{d})^3$ within the volume $V = L^3$, where N is the finite number of structural correlated regions⁹. Among the N regions, approximately \sqrt{N} regions have their local easy axes pointing in the easiest direction as discussed earlier, in contrast to the remaining $N - \sqrt{N}$ regions where the local easy axis is uniformly distributed, pointing in all directions in space. From this, it follows that, if the moment points along the easiest direction, the average anisotropy energy density is

$$E_a/V \approx -K_2 \sqrt{N}/N = -K_2/\sqrt{N} = -K_2/(d/L)^{3/2}. \quad (3.7)$$

The anisotropy energy of the $N - \sqrt{N}$ regions is a constant and does not depend on any variable like the angle between moments and the externally applied magnetic field. Therefore, in this case, only the anisotropy from the \sqrt{N} regions is considered.

The ferromagnetic axis changes its direction by $\pi/2$ on passing from one region with dimension L to the next, so the average exchange energy density is given by

$$E_{ex}/V \approx A/L^2 \quad (3.8)$$

⁷The notation K_2 is used, instead of using K_1 , in order to distinguish it from the macroscopic anisotropy K_1 previously discussed in equation 3.2.

⁸In principle, the equation 3.5 is valid when $L = 0$ and the central Co atom is touching 6 other Co atoms in the primitive unit cell, like in the hcp Co.

⁹Or it could be called the XRD coherent domain.

The value of L which gives the minimum total energy is

$$L \approx \frac{16A^2}{9K_2^2d^3}, \quad (3.9)$$

and the energy density relative to the fully aligned state is:

$$E/V \approx -0.1 \frac{K_2^4 d^6}{A^3}. \quad (3.10)$$

The field necessary to uniformly rotate the moments into alignment is approximately given by

$$\mu_0 H_s = -(E/V)/M_s. \quad (3.11)$$

From the computer simulation results, the coercivity $\mu_0 H_c \approx 0.5\mu_0 H_s$ [58]. At the end, the $\mu_0 H_c$ of a perfectly random amorphous materials is given by:

$$\mu_0 H_c \approx \frac{1}{20} \frac{K_2^4 d^6}{A^3 M_s}. \quad (3.12)$$

This applies when the magnetic scale length L is much larger than the structural length d . Therefore, we can deduce the d based on the information of the other magnetic parameters. For $x = 0.1$, the a-Y_xCo_{1-x} has a saturation magnetization M_s of 1000 kA/m. Taking K_2 as 3.2 MJ/m³ as previously explained and $\mu_0 H_c \approx 1$ mT¹⁰, and assuming A to be 31 pJ/m based on the value for hcp Co, the equation 3.12 gives the d of 1.3 nm, which closely aligns with the reported values for amorphous alloys [60].

The situation is different in a-R-Co alloys containing heavy rare earth elements Dy or Tb. In those materials, the anisotropy per rare-earth is more substantial in magnitude but the R-Co exchange is considerably weaker, resulting in a random, noncollinear component of the rare earth magnetic moment, especially at low temperature. These materials are discussed in Chapter 4.

3.4.3 Appearance of magnetism

As we seen from those fitting curves in Figure 3.22, all data points are contained by those green and red curves nicely. Those three curves, green, blue and blue curves in the figure are calculated based on the Jaccarino-Walker model [61]. Essentially, it is a model in terms of localized 3d electrons. They suggested that moment being either zero or having some maximum value. The apparently continuous change in moment is attributed to the probability that individual Co atoms have enough nearest neighbour Co atoms to have a magnetic moment for each x . Let Z to be the nearest neighbor coordination number and x to be the Y ratio as before. Suppose that cobalt requires a minimum of z cobalt atoms as its nearest neighbors to be coupled by exchange, and then write $P_Z(z, x)$ for the probability of this event. We have

$$P_Z(z, x) = \sum_{n=z}^Z \frac{Z!}{n!(Z-n)!} (1-x)^n (x)^{Z-n} \quad (3.13)$$

where the probability of finding Co atom is $1-x$ and that of finding Y atom is x . The probability of finding a Co atom near by is assumed to be proportional to the Co concentration. The same applies for Y atom as well. The physical meaning of probability of $P_Z(z, x)$ is that, it represents the average magnetic moment of Co normalized to value 1.79 μ_B at 0 K. By assuming that Z is 12, assigning 7, 8 and 9 to z , calculating $P_Z(z, x)$ by the formula 3.13 and finally multiplying it by the Co moment 1.79 μ_B , those fitting curves are obtained.

It indicates that the required minimum number of nearest neighbors for Co to have magnetic moment is dependent on composition ratio x . When x is low, the Co concentration is so high

¹⁰No coercivity was measured with a field step 24 mT.

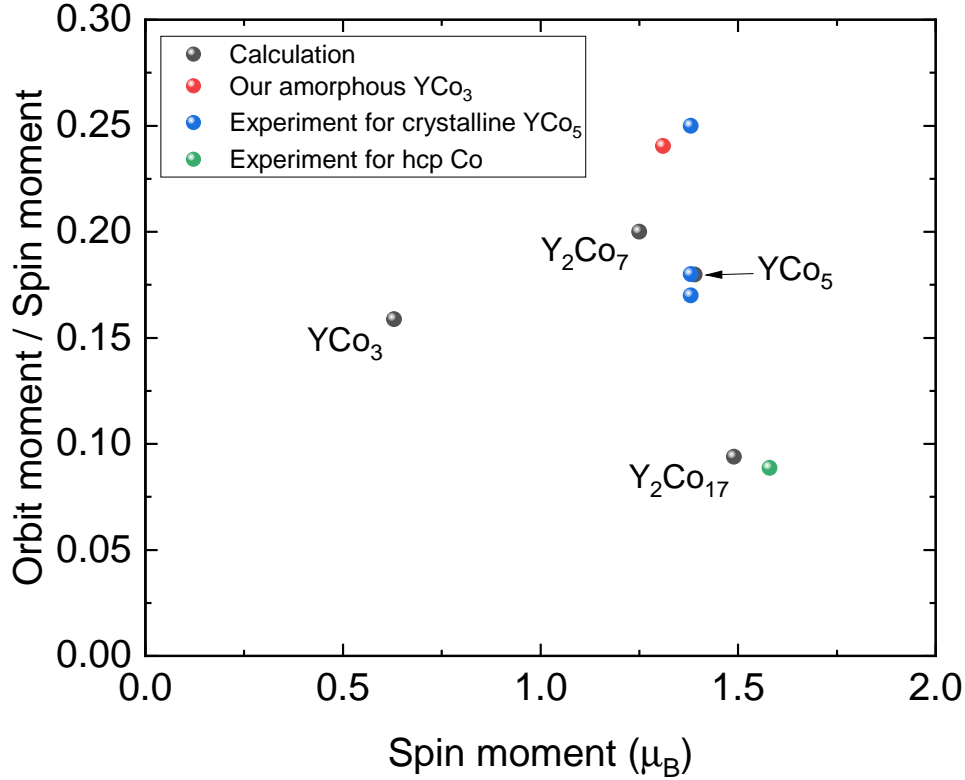


Figure 3.21: Ratio of average orbital to spin moment to spin moment plotted against spin moment in crystalline Y-Co compounds. The labels for the calculated average orbital and spin moments of the crystalline Y-Co intermetallic compounds have been assigned.

that each Co only needs 7 nearest neighbors of Co to have a magnetic moment. That is why the green curve fits the data points well at low x range. When the x value is high, the concentration of Co is low. There are a lot of Y atoms around each Co, Co atom needs more nearest neighbors of Co to have a magnetic moment. It is supported by the fact that the high x value part of data is fitted better by the blue curve. The reason is that, with varying Co ratio, the local structure is changing, as we know from the figure of density vs x as well. It was reported that very thin Co films with a thickness of approximately 0.8 nm, which is equivalent to 3 atomic layers since the atomic radius of Co is about 0.125 nm, become non-magnetic [62]. It can be explained by the Jaccarino-Walker model as well. For data points with x ranging between 0.2 and 0.45, it is anticipated that a significantly broader distribution of coordination numbers will occur, as the concentrations of Y and Co are more evenly balanced and the unequal size of Y and Co with a volume ratio 3:1 [50]. Therefore, we can say, at those concentration x , there are some fluctuation of the local structures at different sites. It means that at the same time, in some locations of the system, at least 7 nearest neighbors Co atoms are needed for Co to have a moment, some place at least 8 and some place at least 9. Basically, the ratio for those three different cases can be inferred from the experimental data.

It is noteworthy that, in the Jaccarino-Walker model, the value of Z is conventionally assumed to be 12. This might not be very appropriate when the radii of the constituting elements differ significantly [63]. As illustrated by the simulation results in Figure 3.19, the value of Z is approximately 8, owing to the volume ratio of Y to Co, which is significantly smaller than the assumed value of 12. Another point is that, at the beginning, we assume the probability of find a Co is $1-x$ without considering the heat of formation for like and unlike atoms. However, this heat of formation certainly will influence the local environment and hence the probability of finding Co [52, 64]. It was reported that segregated Gd and Fe nanometer-sized regions were

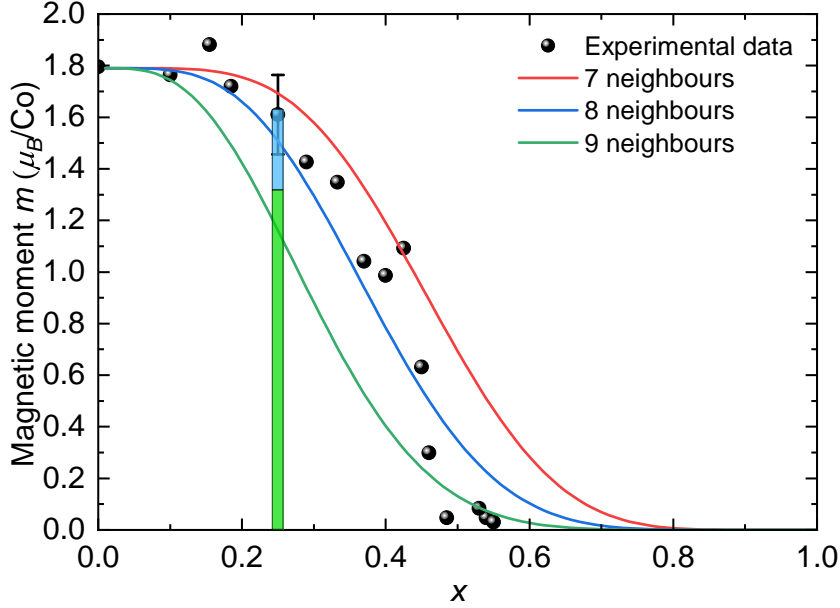


Figure 3.22: Concentration dependence of the saturation moment per Co atom in $a\text{-Y}_x\text{Co}_{1-x}$. The scattered black data points represent the experimental data of $a\text{-Y}_x\text{Co}_{1-x}$. The green, blue and red curves represent calculated curves obtained by assumption that each Co atom needs at least 9, 8 and 7 nearest neighbour Co atoms to have a magnetic moment. Another assumption is that the nearest neighbor coordination number Z is 12. The vertical bar represents the spin moment (green) and orbital moment (blue) determined by X-ray circular dichroism. The error bar at $x = 0.25$ is the standard deviation of the mean of six measurements on three samples.

confirmed in amorphous ferrimagnet GdFeCo [9]. These suggest that further investigation and simulation is needed to better elucidate the origin of magnetism.

It is helpful to compare the difference in concentration dependence of magnetic moment in crystalline and amorphous Y-Co system. As seen from Figure 3.23, the crystalline YCo_2 has a zero magnetic moment per Co atom since YCo_2 compound is an exchange-enhanced Pauli paramagnet¹¹. But when $x = 0.33$, amorphous $\text{Y}_x\text{Co}_{1-x}$ still has a moment about $1.3 \mu_B$ per Co atom. The x value at which the Co moment disappears is much higher in the amorphous alloys than in their crystalline counterparts. This might be due to that a substantial fraction of Co atoms in amorphous alloys experience a larger number of nearest-neighbor Co atoms, as compared to the corresponding crystalline alloys leading to higher threshold value of x [52].

However, it was reported that two surface layers of crystalline YCo_2 remain ferromagnetic and bulk defects are magnetic [66, 67]. It was also reported that YCo_2 was changed from paramagnetic to ferromagnetic by achieving amorphization of intermetallic compounds by a mechanical treatment such as ball-milling. It was experimentally confirmed that milled and sputtered amorphous alloys have similar structural and magnetic properties and there was a change in the coordination number and in the atomic distance of Co-Co from 6.0 and 2.55 Å to 6.7 and 2.42 Å, respectively [68]. The atomic distance in the crystalline and amorphous states are shown in Table 3.5. So the Co-Co distance becomes shorter in the amorphous state and the exchange interaction increases. Other nonmagnetic elements such as La and Zr were used to alloy with Co to perform similar studies. The experimental results are similar to what we present here [69].

¹¹ AB_2 phase is called Laves phase and it is named for Fritz Laves who first described it. Fritz Laves associated the structural properties with the bond distribution between the atoms, who extended the ideas of Goldschmidt on the importance of the radial ratios for structure determination [65]

Pair	Atomic distance (Å)	
	Crystalline	Amorphous
Co-Co	2.55	2.42
Co-Y	2.99	2.92
Y-Y	3.13	3.64

Table 3.5: Atomic distance in the crystalline and amorphous states for Co-Co, Co-Y and Y-Y in YCo_2 . Data from K.Suzuki's paper [68]

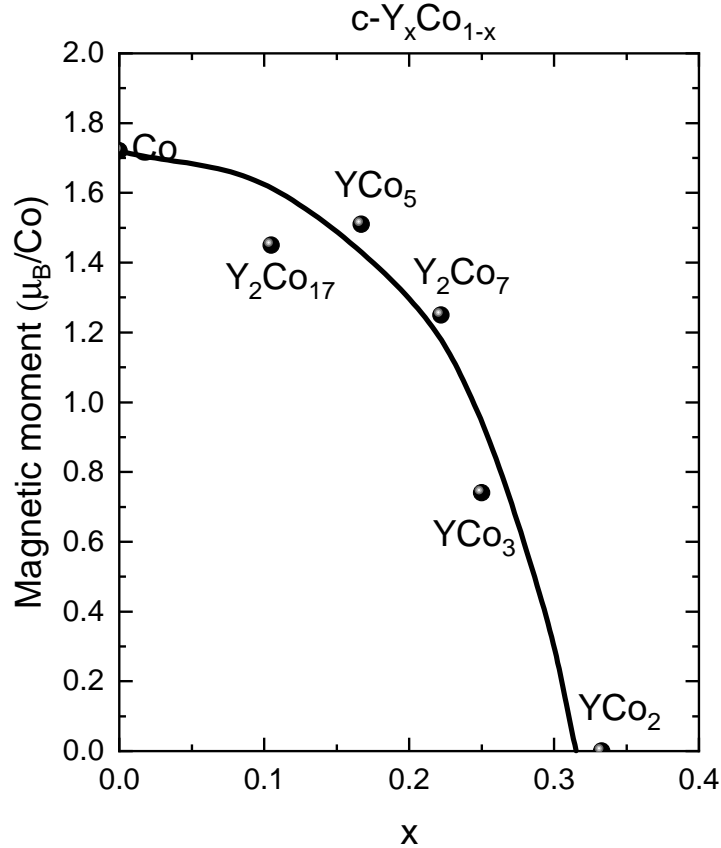


Figure 3.23: Co magnetic moment vs x for crystalline Y-Co compounds.

3.4.4 Comparison with $\text{a-Y}_x\text{Fe}_{1-x}$

Comparing the strongly ferromagnetic cobalt subnetwork in $\text{a-Y}_x\text{Co}_{1-x}$ with the $\text{a-Y}_x\text{Fe}_{1-x}$ with non-collinear magnetism due to a distribution of ferromagnetic and antiferromagnetic Fe-Fe exchange interaction [13, 70], yields intriguing insights. In $\text{a-Y}_x\text{Fe}_{1-x}$, the critical concentration for the appearance of magnetism is greater, with a value $x_0 \approx 0.6$. Notably, the magnetization curves in this system are nonlinear can't be saturated even under magnetic fields as strong as 18 T [71]. Their magnetic structure $\text{a-Y}_x\text{Fe}_{1-x}$ is asperomagnetic, where the spins are frozen in random orientations but exhibit short-range ferromagnetic correlations below a magnetic ordering temperature of 109 K. It shows the sensitivity of Fe-Fe exchange to the interatomic distance. For instance, in fcc γ iron, which has a nearest-neighbour distance of 254 pm, ferromagnetic is observed. However, for shorter interatomic distances, it is antiferromagnetic. In the case of amorphous YFe_2 , Forester *et al.* demonstrated that the broad first peak in the radial distribution function encompasses distances on both sides of 254 pm, making both signs of nearest-neighbour

exchange effects possible [72]. However, the peak of exchange distribution is primarily centered at positive values. Interestingly, a small expansion of the amorphous structure induced by hydrogen is adequate to produce collinear ferromagnetism, resulting in a full iron moment of $2.3 \mu_B$ and Curie temperature $T_c = 500$ K. This decrease in frozen spin disorder upon hydrogenation can be attributed to a shift in the exchange distribution towards more positive values, arising from an increase in the average Fe-Fe distance [73].

3.4.5 Electrical transport

The very high resistivity data of $a\text{-Y}_x\text{Co}_{1-x}$ which is much higher than normal metallic thin films and implies that the scattering in these amorphous metallic systems is very strong. Those systems with a resistivity higher than $150 \mu\Omega\cdot\text{cm}$ usually, over which the mean free path becomes comparable to the interatomic distance, show a negative temperature coefficient of resistance. It means that the resistance increases with decreasing temperature, as found by J.H. Mooij in 1973 after collecting data for bulk alloys, thin films and amorphous alloys [74]. The existence of an asymmetric peak of resistivity is very similar to that observed in the transition metals with monovalent metals such as PdAg [75].

The scaling for the ordinary and spontaneous (anomalous) Hall effect and magnetoresistance plotted in Figure 3.15 is closely related to the behavior of the average, macroscopic magnetization which rotates coherently when the field is smaller than saturation field. For fields below saturation, the antisymmetrized spontaneous Hall voltage V_{xy}^{as} is proportional to M_z and the M_z is proportional to H . The symmetrized V_{yy} is proportional to the in-plane magnetization M_y^2 , which changes as $\cos^2\left(\sin^{-1}\left(\frac{H}{2H_a}\right)\right)$ where the H_a is the anisotropy field corresponding to the anisotropy constant K_1 . When the field are bigger than saturation field, the ordinary Hall effect (linear in H) and the conventional band magnetoresistance (quadratic in H) dominate dependencies on field. Using a Gaussian distribution with a width of $\approx 18\%$, we model the microscopic distribution in magnitude and direction of the local cobalt anisotropy. The fit, as an example, is shown with with the residual, in Figure 3.15. The large magnitude of the Hall effect implies a low density of carriers with poor mobility at the Fermi level. No change of sign in the spontaneous Hall component occurs.

3.5 Conclusion

In these $a\text{-Y}_x\text{Co}_{1-x}$ thin films, Co has a strong ferromagnetism. The disappearance of Co moment occurs at $x_c = 0.5$, where the average coordination of a Co atom in the random dense-packed structure is 3.2 Y and 3.2 Co. The large orbital moments on cobalt, amounting to $0.32 \mu_B$ in $a\text{-YCo}_3$, are attributed to the low densities of the Co-rich compositions. The corresponding local anisotropy in these thin films is anticipated to be strong, comparable to that of crystalline YCo_5 . Surprisingly, a system that is extremely anisotropic at a microscopic scale behaves macroscopically like a soft ferromagnet, which is due to the exchange average of the local anisotropy. The average ferromagnetic moment on the cobalt subnetwork for in $a\text{-YCo}_3$ is $1.5 \mu_B$, and it changes little with temperature within 300 K, since the Curie temperature for this composition is 760 K. The exchange averaging associated with this high Curie temperature makes sure that deviations from collinear ferromagnetism are tiny. The films almost exhibit almost no coercivity at room temperature for both in-plane and out-of-plane magnetization measurements¹².

The magnetization of the amorphous thin films lies in-plane, but there exists an intrinsic perpendicular magnetic anisotropy, which is overcome by shape anisotropy in the series. For $x = 0.25$, the intrinsic term would be enough to induce perpendicular magnetic anisotropy in ferrimagnetic $a\text{-GdCo}_3$ alloys with smaller magnetization, which results in the shape anisotropy

¹²At 5 K, an amorphous YCo_3 thin film was measured with an out-of-plane magnetization curve with a coercivity of approximately 12 mT.

being small as well. The possible origin of perpendicular magnetic anisotropy comes from the interface of the film.

This study of the Co subnetwork in alloys with a nonmagnetic rare earth will enable a more accurate description of the noncollinear sperimagnetic structures, which arise with heavy rare earths such as Dy or Tb and show compensation near room temperature.

References

- [1] F. C. Nix and W. Shockley, “Order-disorder transformations in alloys,” *Reviews of Modern Physics*, vol. 10, no. 1, p. 1, 1938. (Cited on page: 72)
- [2] W. Rosenhain, “Solid solutions and inter-metallic compounds,” *Nature*, vol. 112, no. 2823, pp. 832–834, 1923. (Cited on page: 72)
- [3] W. Klement, R. Willens, and P. Duwez, “Non-crystalline structure in solidified gold-silicon alloys,” *Nature*, vol. 187, no. 4740, pp. 869–870, 1960. (Cited on page: 72, 73)
- [4] J. Finney, “Random packings and the structure of simple liquids. I. the geometry of random close packing,” *Proceedings of the Royal Society of London. A. Mathematical and Physical Sciences*, vol. 319, no. 1539, pp. 479–493, 1970. (Cited on page: 72)
- [5] J. Finney, “Modelling the structures of amorphous metals and alloys,” *Nature*, vol. 266, no. 5600, pp. 309–314, 1977. (Cited on page: 72)
- [6] Y. Yang, J. Zhou, F. Zhu, Y. Yuan, D. J. Chang, D. S. Kim, M. Pham, A. Rana, X. Tian, Y. Yao, *et al.*, “Determining the three-dimensional atomic structure of an amorphous solid,” *Nature*, vol. 592, no. 7852, pp. 60–64, 2021. (Cited on page: 72)
- [7] Y. Yuan, D. S. Kim, J. Zhou, D. J. Chang, F. Zhu, Y. Nagaoka, Y. Yang, M. Pham, S. J. Osher, O. Chen, *et al.*, “Three-dimensional atomic packing in amorphous solids with liquid-like structure,” *Nature materials*, vol. 21, no. 1, pp. 95–102, 2022. (Cited on page: 72)
- [8] G. Sala, V. Krizakova, E. Grimaldi, C.-H. Lambert, T. Devolder, and P. Gambardella, “Real-time hall-effect detection of current-induced magnetization dynamics in ferrimagnets,” *Nature Communications*, vol. 12, no. 1, p. 656, 2021. (Cited on page: 72)
- [9] G. Sala, C.-H. Lambert, S. Finizio, V. Raposo, V. Krizakova, G. Krishnaswamy, M. Weigand, J. Raabe, M. D. Rossell, E. Martinez, *et al.*, “Asynchronous current-induced switching of rare-earth and transition-metal sublattices in ferrimagnetic alloys,” *Nature Materials*, vol. 21, no. 6, pp. 640–646, 2022. (Cited on page: 72, 93)
- [10] I. Radu, K. Vahaplar, C. Stamm, T. Kachel, N. Pontius, H. Dürr, T. Ostler, J. Barker, R. Evans, R. Chantrell, *et al.*, “Transient ferromagnetic-like state mediating ultrafast reversal of antiferromagnetically coupled spins,” *Nature*, vol. 472, no. 7342, pp. 205–208, 2011. (Cited on page: 72)
- [11] T. Ostler, J. Barker, R. Evans, R. Chantrell, U. Atxitia, O. Chubykalo-Fesenko, S. El Mousaoui, L. Le Guyader, E. Mengotti, L. Heyderman, *et al.*, “Ultrafast heating as a sufficient stimulus for magnetization reversal in a ferrimagnet,” *Nature communications*, vol. 3, no. 1, p. 666, 2012. (Cited on page: 72)
- [12] S. Mangin, M. Gottwald, C. Lambert, D. Steil, V. Uhlř, L. Pang, M. Hehn, S. Alebrand, M. Cinchetti, G. Malinowski, *et al.*, “Engineered materials for all-optical helicity-dependent

- magnetic switching,” *Nature materials*, vol. 13, no. 3, pp. 286–292, 2014. (Cited on page: 72)
- [13] K. Moorjani and J. M. D. Coey, *Magnetic Glasses*. Elsevier, 1984. (Cited on page: 72, 88, 94)
- [14] K. Gschneider and L. Eyring, eds., *Handbook on the Physics and Chemistry of Rare Earths*, vol. 1: Metal. North Holland, 1979. (Cited on page: 73)
- [15] K. Buschow, “Intermetallic compounds of rare-earth and 3d transition metals,” *Reports on Progress in Physics*, vol. 40, no. 10, p. 1179, 1977. (Cited on page: 73)
- [16] K. Le Dang, P. Veillet, R. Krishnan, and G. Suran, “Spin echo studies in amorphous yco3 films,” *Journal of Magnetism and Magnetic Materials*, vol. 15, pp. 1399–1400, 1980. (Cited on page: 73)
- [17] K. Buschow, “Magnetic properties of amorphous rare-earth–cobalt alloys,” *Journal of Applied Physics*, vol. 51, no. 5, pp. 2795–2798, 1980. (Cited on page: 73, 79)
- [18] J. Karel, D. Bouma, C. Fuchs, S. Bennett, P. Corbae, S. Song, B. Zhang, R. Wu, and F. Hellman, “Unexpected dependence of the anomalous hall angle on the hall conductivity in amorphous transition metal thin films,” *Physical Review Materials*, vol. 4, no. 11, p. 114405, 2020. (Cited on page: 73, 79)
- [19] V. Vas’kovskiy, E. Kudyukov, A. Svalov, K. Balymov, and V. Maltseva, “Magnetic structure and macroscopic magnetic properties of $Gd_{100-x}Co_x$ films: Changing x from 0 to 100,” *Journal of Magnetism and Magnetic Materials*, vol. 565, p. 170254, 2023. (Cited on page: 74, 89)
- [20] D. Wang, U. Geyer, and S. Schneider, “Formation of amorphous Ni–Y films by physical vapor deposition,” *Journal of non-crystalline solids*, vol. 221, no. 2-3, pp. 222–227, 1997. (Cited on page: 74)
- [21] J. P. Cline, M. H. Mendenhall, D. Black, D. Windover, and A. Henins, “The optics and alignment of the divergent beam laboratory x-ray powder diffractometer and its calibration using nist standard reference materials,” *Journal of research of the National Institute of Standards and Technology*, vol. 120, p. 173, 2015. (Cited on page: 74)
- [22] B.-H. Hwang, “Calculation and measurement of all (002) multiple diffraction peaks from a (001) silicon wafer,” *Journal of Physics D: Applied Physics*, vol. 34, no. 16, p. 2469, 2001. (Cited on page: 74)
- [23] M. Lammel, K. Geishendorf, M. A. Choffel, D. M. Hamann, D. C. Johnson, K. Nielsch, and A. Thomas, “Fast fourier transform and multi-gaussian fitting of XRR data to determine the thickness of ald grown thin films within the initial growth regime,” *Applied Physics Letters*, vol. 117, no. 21, 2020. (Cited on page: 74)
- [24] J. M. Cimbala, “Fourier Transforms, DFTs, and FFTs,” *Penn State University, State College*, 2010. (Cited on page: 74)
- [25] S. L. Brunton and J. N. Kutz, *Data-driven Science and Engineering: Machine Learning, Dynamical Systems, and Control*. Cambridge University Press, 2019. (Cited on page: 74)
- [26] Q. Kong, T. Siau, and A. Bayen, *Python Programming and Numerical Methods: A Guide for Engineers and Scientists*. Academic Press, 2020. (Cited on page: 74)

- [27] J. Liu, Y. Fu, Y. Tang, X. Wang, Q. Cao, D. Zhang, and J. Jiang, “Thickness dependent structural evolution in Mg–Zn–Ca thin film metallic glasses,” *Journal of Alloys and Compounds*, vol. 742, pp. 524–535, 2018. (Cited on page: 77)
- [28] S. M. Lock, K. Lau, A. Shariff, Y. Yeong, and M. Bustam, “Computational insights on the role of film thickness on the physical properties of ultrathin polysulfone membranes,” *RSC advances*, vol. 7, no. 70, pp. 44376–44393, 2017. (Cited on page: 77)
- [29] A. Shishatskii, Y. P. Yampol’skii, and K.-V. Peinemann, “Effects of film thickness on density and gas permeation parameters of glassy polymers,” *Journal of membrane science*, vol. 112, no. 2, pp. 275–285, 1996. (Cited on page: 77)
- [30] P. Stamenov and J. M. D. Coey, “Sample size, position, and structure effects on magnetization measurements using second-order gradiometer pickup coils,” *Review of scientific instruments*, vol. 77, no. 1, p. 015106, 2006. (Cited on page: 78)
- [31] B. Ponomarev, “Magnetic properties of terbium in the paraprocess region,” *Zh. Eksp. Teor. Fiz.*, vol. 69, pp. 1352–1361, 1975. (Cited on page: 78)
- [32] J. M. D. Coey, *Magnetism and Magnetic Materials*. Cambridge university press, 2010. (Cited on page: 79, 89, 90)
- [33] T. Goto, T. Sakakibara, K. Murata, H. Komatsu, and K. Fukamichi, “Itinerant electron metamagnetism in YCo_2 and LuCo_2 ,” *Journal of magnetism and magnetic materials*, vol. 90, pp. 700–702, 1990. (Cited on page: 79)
- [34] K. Fukamichi, T. Goto, and U. Mizutani, “The crystallization temperature, electrical resistivity and magnetic properties of Co–Y amorphous alloys,” *IEEE transactions on magnetics*, vol. 23, no. 5, pp. 3590–3592, 1987. (Cited on page: 83)
- [35] T. Yonamine, A. P. B. Tufaile, J. Vogel, A. Santos, F. Vicentin, and H. Tolentino, “Magnetic characterisation and X-ray magnetic circular dichroism study of amorphous yco2 films,” *Journal of magnetism and magnetic materials*, vol. 233, no. 1-2, pp. 84–87, 2001. (Cited on page: 84)
- [36] K. Balymov, E. Kudyukov, V. Vas’kovskiy, O. Adanakova, N. Kulesh, E. Stepanova, and A. Rusalina, “Magnetism of amorphous Dy-Tb-Co-type films,” in *Journal of Physics: Conference Series*, vol. 1389, p. 012014, IOP Publishing, 2019. (Cited on page: 84)
- [37] M. Takahashi, T. Shimamori, T. Miyazaki, T. Wakiyama, and A. Yoshihara, “Perpendicular magnetic anisotropy and magnetostriction of evaporated Co-(Pr, Nd, Gd, Dy, Er) amorphous binary alloy films,” *IEEE translation journal on magnetics in Japan*, vol. 4, no. 11, pp. 666–672, 1989. (Cited on page: 87)
- [38] H. Leamy and A. Dirks, “Microstructure and magnetism in amorphous rare-earth–transition-metal thin films. II. magnetic anisotropy,” *Journal of Applied Physics*, vol. 50, no. 4, pp. 2871–2882, 1979. (Cited on page: 87)
- [39] P. Hansen, C. Clausen, G. Much, M. Rosenkranz, and K. Witter, “Magnetic and magneto-optical properties of rare-earth transition-metal alloys containing Gd, Tb, Fe, Co,” *Journal of applied physics*, vol. 66, no. 2, pp. 756–767, 1989. (Cited on page: 87)
- [40] A. El-Ghazaly, B. Tran, A. Ceballos, C.-H. Lambert, A. Pattabi, S. Salahuddin, F. Hellman, and J. Bokor, “Ultrafast magnetization switching in nanoscale magnetic dots,” *Applied Physics Letters*, vol. 114, no. 23, 2019. (Cited on page: 87)

- [41] K. Srinivasan, Y. Chen, L. Cestarollo, D. K. Dare, J. G. Wright, and A. El-Ghazaly, “Engineering large perpendicular magnetic anisotropy in amorphous ferrimagnetic gadolinium cobalt alloys,” *Journal of Materials Chemistry C*, vol. 11, no. 14, pp. 4820–4829, 2023. (Cited on page: 87)
- [42] T. Niihara, S. Takayama, K. Kaneko, and Y. Sugita, “Perpendicular magnetic anisotropy of Tb–Co amorphous films sputtered in H₂-added ar gas,” *Applied physics letters*, vol. 45, no. 8, pp. 872–874, 1984. (Cited on page: 87)
- [43] A. Ceballos, M. Charilaou, M. Molina-Ruiz, and F. Hellman, “Coexistence of soft and hard magnetic phases in single layer amorphous Tb–Co thin films,” *Journal of Applied Physics*, vol. 131, no. 3, 2022. (Cited on page: 87)
- [44] Z. Hu, J. Besbas, R. Smith, N. Teichert, G. Atcheson, K. Rode, P. Stamenov, and J. Coey, “Single-pulse all-optical partial switching in amorphous Dy_xCo_{1-x} and Tb_xCo_{1-x} with random anisotropy,” *Applied Physics Letters*, vol. 120, no. 11, 2022. (Cited on page: 87)
- [45] J. M. D. Coey, J. Chappert, J. Rebouillat, and T. Wang, “Magnetic structure of an amorphous rare-earth transition-metal alloy,” *Physical Review Letters*, vol. 36, no. 17, p. 1061, 1976. (Cited on page: 87)
- [46] G. Roberts, W. Wilson, and H. Bourne, “Magnetic properties of Ho–Co, Dy–Co, and Gd–Fe amorphous films prepared by dual-source evaporation,” *IEEE Transactions on Magnetics*, vol. 13, no. 5, pp. 1535–1537, 1977. (Cited on page: 87)
- [47] V. Vas’kovskiy, O. Adanakova, E. Kudryukov, E. Stepanova, A. Rusalina, and K. Balymov, “Magnetism of Dy–Co system amorphous films,” in *AIP Conference Proceedings*, vol. 2174, AIP Publishing, 2019. (Cited on page: 87)
- [48] M. Kim, M.-H. Jung, C. M. Kim, and S. H. Lim, “Effects of ar pressure on magnetic and magnetocaloric properties of sputtered Er–Co thin films,” *Physica B: Condensed Matter*, vol. 476, pp. 175–178, 2015. (Cited on page: 87)
- [49] Y. Cheng and E. Ma, “Atomic-level structure and structure-property relationship in metallic glasses,” *Progress in materials science*, vol. 56, no. 4, pp. 379–473, 2011. (Cited on page: 88)
- [50] A. Clarke and J. Wiley, “Numerical simulation of the dense random packing of a binary mixture of hard spheres: Amorphous metals,” *Physical Review B*, vol. 35, no. 14, p. 7350, 1987. (Cited on page: 88, 92)
- [51] Q. Zhang, C. Lian, Q. Xu, Y. Yu, and M. Skowronski, “Density of amorphous sputtered Ge₂Sb₂Te₅ thin films,” *AIP Advances*, vol. 13, no. 1, p. 015014, 2023. (Cited on page: 88)
- [52] P. Hansen, “Magnetic amorphous alloys,” *Handbook of magnetic materials*, vol. 6, pp. 289–452, 1991. (Cited on page: 88, 92, 93)
- [53] M. Yamaguchi and S. Asano, “First-principles calculations of the 3d magnetocrystalline anisotropy energy of YCo₅, Y₂Co₇, YCo₃, and Y₂Co₁₇,” *Journal of magnetism and magnetic materials*, vol. 168, no. 1-2, pp. 161–168, 1997. (Cited on page: 89)
- [54] A. Heidemann, D. Richter, and K. Buschow, “Investigation of the hyperfine fields in the compounds LaCo₁₃, LaCo₅, YCo₅ and ThCo₅ by means of inelastic neutron scattering,” *Zeitschrift für Physik B Condensed Matter*, vol. 22, no. 4, pp. 367–372, 1975. (Cited on page: 89)

- [55] R. Coehoorn, “Electronic structure calculations for rare earth-transition metal compounds,” in *Supermagnets, Hard Magnetic Materials*, pp. 133–170, Springer, 1991. (Cited on page: 89)
- [56] R. Harris, M. Plischke, and M. Zuckermann, “New model for amorphous magnetism,” *Physical Review Letters*, vol. 31, no. 3, p. 160, 1973. (Cited on page: 89)
- [57] J. M. D. Coey and S. S. Parkin, *Handbook of Magnetism and Magnetic Materials.*, vol. 1 and 2. Springer International Publishing, 2021. (Cited on page: 90)
- [58] R. Alben, J. Becker, and M. Chi, “Random anisotropy in amorphous ferromagnets,” *Journal of applied physics*, vol. 49, no. 3, pp. 1653–1658, 1978. (Cited on page: 90, 91)
- [59] S. Blundell, *Magnetism in Condensed Matter*. Oxford University Press, 2001. (Cited on page: 90)
- [60] R. O’handley, “Physics of ferromagnetic amorphous alloys,” *Journal of applied physics*, vol. 62, no. 10, pp. R15–R49, 1987. (Cited on page: 91)
- [61] V. Jaccarino and L. Walker, “Discontinuous occurrence of localized moments in metals,” *Physical Review Letters*, vol. 15, no. 6, p. 258, 1965. (Cited on page: 91)
- [62] A. Scholl, H. Ohldag, F. Nolting, J. Stöhr, and H. A. Padmore, “X-ray photoemission electron microscopy, a tool for the investigation of complex magnetic structures,” *Review of scientific instruments*, vol. 73, no. 3, pp. 1362–1366, 2002. (Cited on page: 92)
- [63] M. Mansuripur and M. Ruane, “Mean-field analysis of amorphous rare earth-transition metal alloys for thermomagnetic recording,” *IEEE transactions on magnetics*, vol. 22, no. 1, pp. 33–43, 1986. (Cited on page: 92)
- [64] J. M. Ziman, *Models of disorder: the theoretical physics of homogeneously disordered systems*. Cambridge university press, 1979. (Cited on page: 92)
- [65] K. Taylor, “Intermetallic rare-earth compounds,” *Advances in Physics*, vol. 20, no. 87, pp. 551–660, 1971. (Cited on page: 93)
- [66] S. Khmelevskiy, P. Mohn, J. Redinger, and M. Weinert, “Magnetism on the surface of the bulk paramagnetic intermetallic compound YCo_2 ,” *Physical review letters*, vol. 94, no. 14, p. 146403, 2005. (Cited on page: 93)
- [67] Z. Śniadecki, N. Pierunek, B. Idzikowski, B. Wasilewski, M. Werwiński, U. Rößler, and Y. Ivanisenko, “Influence of structural disorder on the magnetic properties and electronic structure of YCo_2 ,” *Physical Review B*, vol. 98, no. 9, p. 094418, 2018. (Cited on page: 93)
- [68] K. Fukamichi, T. Goto, T. Fukunaga, and K. Suzuki, “Magnetic properties of Co–Y amorphous alloys prepared by milling,” *Materials Science and Engineering: A*, vol. 133, pp. 245–247, 1991. (Cited on page: 93, 94)
- [69] N. Heiman and N. Kazama, “Concentration dependence of the Co moment in amorphous alloys of Co with Y, La, and Zr,” *Physical Review B*, vol. 17, no. 5, p. 2215, 1978. (Cited on page: 93)
- [70] J. M. D. Coey, D. Givord, A. Liénard, and J. Rebouillat, “Amorphous yttrium-iron alloys. I. magnetic properties,” *Journal of Physics F: Metal Physics*, vol. 11, no. 12, p. 2707, 1981. (Cited on page: 94)

- [71] J. Chappert, J. M. D. Coey, A. Lienard, and J. Rebouillat, “Amorphous yttrium-iron alloys. II. mossbauer spectra,” *Journal of Physics F: Metal Physics*, vol. 11, no. 12, p. 2727, 1981. (Cited on page: 94)
- [72] D. Forester, N. Koon, J. Schelleng, and J. Rhyne, “Amorphous YFe_2 —a concentrated spin glass,” *Journal of Applied Physics*, vol. 50, no. B11, pp. 7336–7341, 1979. (Cited on page: 95)
- [73] J. M. D. Coey, A. Lienard, J. Rebouillat, D. Ryans, W. Zhenxi, and Y. Boliang, “Amorphous yttrium-iron alloys: III. the influence of hydrogen,” *Journal of Physics F: Metal Physics*, vol. 18, no. 6, p. 1299, 1988. (Cited on page: 95)
- [74] J. Mooij, “Electrical conduction in concentrated disordered transition metal alloys,” *physica status solidi (a)*, vol. 17, no. 2, pp. 521–530, 1973. (Cited on page: 95)
- [75] J. M. Ziman, *Electrons and Phonons: the Theory of Transport Phenomena in Solids*. Oxford university press, 2001. (Cited on page: 95)

4 Magnetism of noncollinear amorphous TbCo_3 and DyCo_3 thin films.

We must know.
We shall know.

David Hilbert

4.1 Motivation and background

Amorphous ferromagnets mainly consist of a combination of transition metal elements, Fe, Co or Ni and metalloids, carbon and boron well-known as glass formers. However, yttrium and cobalt without metalloids are also able to make amorphous $\text{Y}_x\text{Co}_{1-x}$, which is an amorphous ferromagnet since Y is a non-magnetic element. Y has the same outer electron structures as the magnetic rare earths and is very close metallic radius (1.80 Å) to the trivalent magnetic rare-earths (1.75Å-1.83Å) [1, 2]. Although Y and Co atoms are randomly distributed, Co magnetic moments on each site are still collinearly ferromagnetically coupled when the composition ratio of Co is beyond a certain threshold value. It can be understood by thinking of the first nearest neighbor direct exchange interactions, which only become effective and important when each Co atom has enough Co atoms surrounding it, as noticed in amorphous $\text{Co}_x\text{Si}_{1-x}$ and $\text{Co}_x\text{Ge}_{1-x}$. Therefore, these systems are able to have a well-defined and high curie temperature T_c due to the Co subnetwork, which might be bigger or smaller than that of the corresponding crystalline compounds. Here, a- $\text{Y}_x\text{Co}_{1-x}$ ¹ is taken as a basic reference for more complex amorphous ferrimagnet where Y is replaced by the other rare earth elements, Dy and Tb which are going to be discussed next. As a reference, lanthanum can also be used [3].

When there are two magnetic atoms in the non-crystalline structures, more complex and interesting magnetic structures such as ferrimagnetism and sperimagnetism are possible due to the competition of different magnetic interactions such as exchange interaction and local random anisotropy. Rare-earth (R)-transition metal (T) alloys are one of the most famous magnetic examples with a two-subnetwork amorphous structure. Here T is fixed to Co.

When R is a light rare earth element such as Nd, the exchange coupling of T and R spins is negative, which tends to align the T and R moments parallel, but when R is a heavy rare-earth such as Gd, Tb, and Dy, the exchange interaction between T and R spins is positive, which favors that T and R moments are antiparallel. However, for non-S state elements, there is an additional factor that needs to be considered, which is the random electrostatic field by the surrounding ions and conduction electrons on the R sites. It tends to lift the degeneracy of the energy levels of partly filled f shells. The particular spatial distribution of atomic electron density stabilized by the electrostatic field is associated with a specific state of orbital angular momentum. The magnetic moment of the R atom therefore points into certain directions due to spin-orbit coupling [2]. This effect is negligible for Gd since Gd is an S-state element with a spherical symmetry of the orbits, but it is essential for Dy and Tb, with non-spherical electron density distributions.

¹The notation “a-” will be used to denote an amorphous alloy.

So, when R is Gd, a-GdCo is a ferrimagnet because the magnetic moment of Gd is coupled antiferromagnetically with that of Co. But for R is Dy or Tb, the average of magnetic moments of R is antiparallel to that of Co and there is a cone angle in the distribution of R moments due to the strong local random magnetic anisotropy [4]. Dy atoms in a-DyCo₃ were shown by ¹⁶¹Dy Mossbauer spectroscopy to adopt a noncollinear structure at low temperature related to the random local electrostatic fields acting on the incomplete 4f shell, which produces the local random magnetic anisotropy [4].

Recently, there has been a lot of interest and progress in amorphous ferrimagnets. Single-pulse all-optical thermal switching of magnetization was observed in ferrimagnetic a-GdFeCo² with Gd concentration around 25% [6] and later in binary a-Gd_{0.30}Co_{0.70} films [7]. A new type of partial single-pulse all-optical switching is demonstrated in a-TbCo and a-DyCo systems in Chapter 5 as well [8]. Besides the ultrafast optical manipulation of magnetic order, current-induced switching of magnetization excited by spin-orbit torque has been reported in a-GeFeCo and a-TbCo [9, 10]. In the asynchronous current-induced switching, transient ferromagnetic states appear in the nanosecond time scale. The same phenomenon occurs in optical switching but on a different time scale. They might have different physical origins. The observation of skyrmions in those a-R-T systems has been reported as well [11].

While so many exciting discoveries have been made for the a-RCo system, the old but important problem of anomalous Hall effect (AHE) of those systems is still not completely resolved, despite extensive research on the topic. The AHE has been traditionally attributed to the transition metal subnetwork.

In this work, we compare the magnetization and magneto-transport in a-Dy_xCo_{1-x} and a-Tb_xCo_{1-x} at different temperatures systematically, with the composition ratio x around 0.25. A big difference in the hysteresis loop between the magnetization and anomalous Hall effect (AHE) has been observed. A double hysteresis appears in the magnetization measurements, but AHE measurement only shows a pure single hysteresis loop for all temperature measurements from 10 K to 300 K. In the discussion section, we will talk about the possible explanations for the discrepancy.

During the preparation of this thesis, we noticed there are some reports showing data similar to some of our work here but almost no attention were made. The study of Ke Wang *et al.* in 2019 showed the double magnetization hysteresis loop but a single AHE loop for their 21 nm a-TbFeCo sample, but they did not provide any explanation for it since the paper was focusing on using thickness of thin films to tune the perpendicular magnetic anisotropy of the ultra-thin a-TbFeCo films [12]. The very same behavior was shown in another paper from the same authors but again without explanation [13]. Another example is CoFe/Tb multilayers where discrepancy exists between M(H) and polar MOKE loops, both measured at room temperature [14].

4.2 Methodology

To avoid possible contamination with surface impurities of the target, pre-sputtering of rare earth targets was performed for at least 15 min before each day's thin film depositions. The sample holder was rotating during deposition to ensure the thickness and composition uniformity³. All thin films were made right after the pre-sputtering of targets to make sure the rare-earth targets were kept in a good condition.

Since we are studying the magnetism and electrical transport of the thin films, the use of Pt or Ta as underlayer and overlayer is avoided. The motivation for using those heavy metals

²During the 1990s, the primary driving force was to develop media for magneto-optical data recording based on either Curie point or compensation point writing. Ferrimagnetic a-Gd_{0.25}Fe_{0.656}Co_{0.094} films were optimized in this context. Later, these materials found applications in the emerging field of all-optical switching [5].

³Recently, it has been reported that fixing the sample holder in a specific direction without rotating the holder helps to produce a well-defined in-plane anisotropy [15].

are diverse, for example, enhancing the perpendicular anisotropy, protecting the sample from oxidation and promoting the growth of amorphous materials [16, 17]. One difference between a-Dy_xCo_{1-x} and a-Tb_xCo_{1-x} samples is that the Dy films were stable in ambient conditions for more than a year, but the Tb films began to deteriorate after few weeks. This might be due to the different oxides associated with the two rare-earths. Dy forms a sesquioxide, like most other trivalent lanthanides, but Tb might forms a higher oxide Tb₄O₇ which is a mixture of phases having trivalent 4f⁸ and quadrivalent 4f⁷ terbium ions [18].

Based on a thorough review of previous research in the field, we determined that starting with a composition near $x \approx 0.25$ would be an optimal initial point. This choice was guided by the expectation that it would facilitate the development of perpendicular magnetic anisotropy, a critical factor in our investigation. Regarding the thickness, our approach was to explore various thicknesses to assess their significance for our study. Consequently, at the very beginning, we prepared amorphous alloys a-Dy_{0.25}Co_{0.75} with a thickness range spanning from 5 to 90 nm. However, it became evident that perpendicular anisotropy was only observed in films approximately 10 nm thick, as depicted in Figure 4.1. As we can see, in particular, the saturation

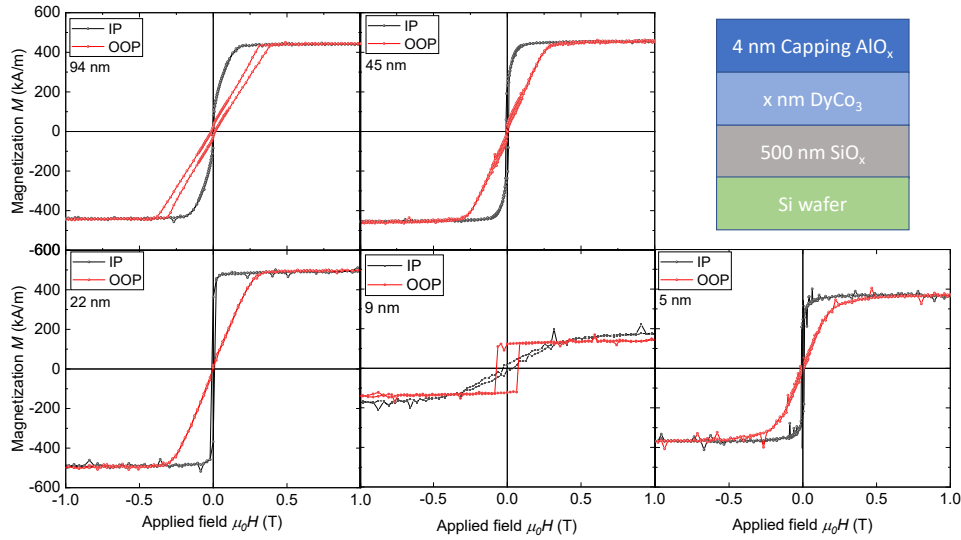


Figure 4.1: Room-temperature in-plane and out-of-plane magnetization curves of a-Dy_{0.25}Co_{0.75} with different thicknesses. The target currents for Dy and Co are fixed to 20 mA and 130 mA, respectively. The thicknesses were measured by fitting XRR data and labelled for each panel. The sample structure is illustrated in the top-right corner.

magnetization M_s of the 9 nm thin film is dramatically different from the others. For thicknesses above 20 nm, the M_s is between 400 kA/m and 450 kA/m, while for those below 20 nm, the M_s is smaller than 400 kA/m and it is even less than 200 kA/m for 9 nm a-Dy_{0.25}Co_{0.75} thin film. When growing those samples, the currents for Dy and Co targets were fixed to 20 mA and 130 mA, respectively. The thicknesses of the thin films were controlled by adjusting the deposition time. The longer deposition time, the thicker the films. There are some small variations between 20 nm to 90 nm thin films, which might be due to the slight fluctuation of target currents. This however can't explain the occurrence of big change of 9 nm thin film, which will be discussed later. The most important point for us is that 10 nm is a good thickness and composition to observe perpendicular magnetic anisotropy. After observing this, our primary focus shifted towards producing 10 nm a-Dy_{0.25}Co_{0.75} thin films. The same procedure was applied to a-Tb_{0.25}Co_{0.75}, where we determined that a thickness of 20 nm is optimal. The a-Dy_{0.25}Co_{0.75} and a-Tb_{0.25}Co_{0.75} samples of interest are outlined in Table 4.1, which also includes two a-Y_{0.25}Co_{0.75} samples for future comparisons.

Number	Sample code	Chemical formula	Main layer thickness (nm)	Main layer roughness (nm)	Main layer density (g/cm ³)	Capping layer	Capping layer thickness (nm)	Capping layer roughness (nm)	M _s (kA/m)	H _s (kA/m)	H _c (mT)
1	HZX201022B_DyCo ₃	Dy _{0.25} Co _{0.75}	10.3	1.2	9.2	SiO ₂	3.3	0.9	173.0	*	48.2
2	HZX200304A_DyCo ₃	Dy _{0.25} Co _{0.75}	8.8	1.0	9.0	Al ₂ O ₃	3.2	1.0	148.5	*	73.0
3	HZX210115A_DyCo ₃	Dy _{0.25} Co _{0.75}	10.5	1.6	8.2	SiO ₂	4.6	0.8	223.0	*	33.6
4	HZX20220514A_TbCo ₃	Tb _{0.25} Co _{0.75}	17.1/1.4	1.6/0.5	8.0/7.5	SiO ₂	4.5	1.5	106.0(H); 26.8(S)	*	295.9
5	HZX20220817A_TbCo ₃	Tb _{0.25} Co _{0.75}	20/0.6	1.7/0.4	7.2/5.5	SiO ₂	4.6	0.8	120.0(H); 50.7(S)	*	253.6
6	HZX210927A_YCo ₃	Y _{0.25} Co _{0.75}	8.8	1.0	6.5	SiO ₂	2.0	0.8	705.4	647.0	-
7	HZX210927B_YCo ₃	Y _{0.25} Co _{0.75}	19.0	1.3	6.5	SiO ₂	2.0	1.5	721.7	598.4	-

Table 4.1: Structural and magnetic data on amorphous Dy_{0.25}Co_{0.75} and Tb_{0.25}Co_{0.75} thin films.

4.3 Results

The amorphous alloys have been reported to have simple or complex hysteresis loops with an anhysteretic component in the $M(H)$ measurement [19, 20]. Simple loops are more common with Dy and complex loops are more common with Tb. Some typical data are shown in Figure 4.2. Investigations are performed for both in the following section. At both 300 K and 10

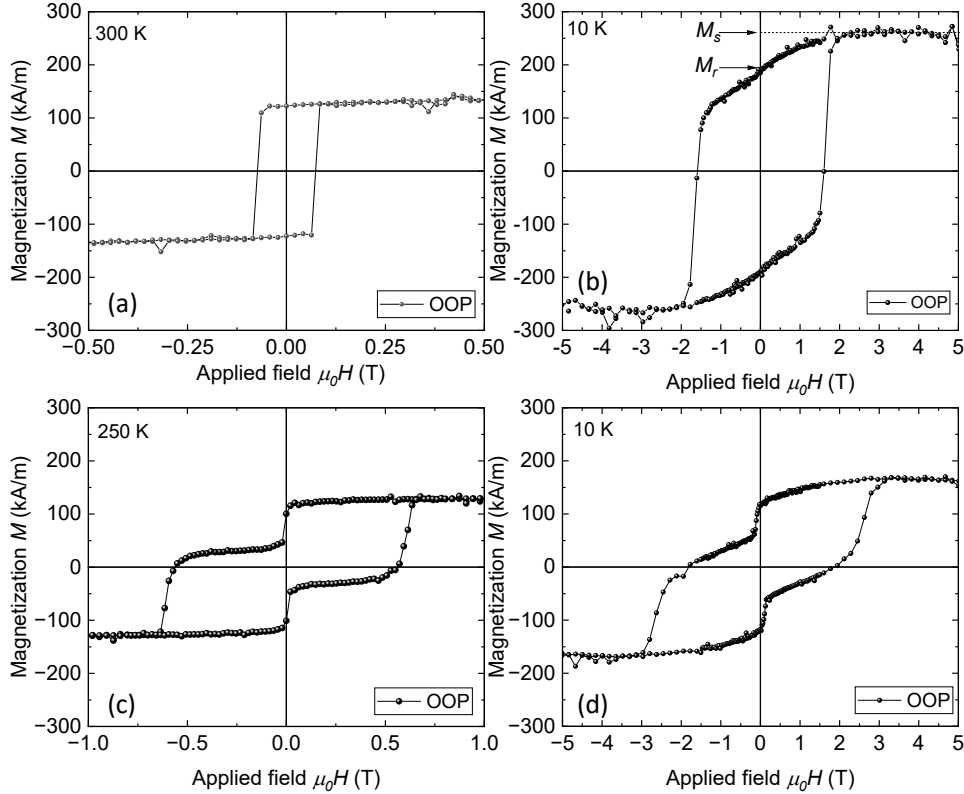


Figure 4.2: Some representative hysteresis loops of a-Dy_{0.25}Co_{0.75} (sample number 2, as labelled in the Table 4.1) and a-Tb_{0.25}Co_{0.75} (the number 5 sample) alloys. (a) DyCo at 300 K; (b) DyCo at 10 K, (c) TbCo at 250 K; and (d) TbCo at 10 K. Note that we assumed the magnetization is saturated at high fields, around 4 or 5 T, for all temperatures when processing the raw data from SQUID magnetometry. This assumption is applied to the $M(H)$ data in this chapter (Chapter 4) and the following one (Chapter 5).

K, the a-Dy_{0.25}Co_{0.75} exhibits a single hysteretic behavior indicative of a homogeneous magnetic film as seen in Figure 4.2 (a) and (b). In Figure 4.2 (b), we define two quantities which we will follow as a function of temperature. The spontaneous magnetization M_s is the magnetization extrapolated to zero field from the high field region. The remnant magnetization M_r is the

magnetization remaining when the magnetic field is 0 T⁴.

4.3.1 Dysprosium alloys

A plot shown in Figure 4.3 of the coercivity measured from both magnetization and anomalous Hall loops as a function of temperature shows a divergence at the magnetization compensation temperature T_{comp} . It is also supported by the fact that the sign of anomalous Hall effect reverses below and above T_{comp} . Like the magneto-optic Kerr effect, the anomalous Hall effect is principally due to the cobalt subnetwork. The magnetic moment $|m|$ in Bohr magnetons per DyCo₃ formula unit is measured, and the plot in Figure 4.4 considers the reversal of sign at the magnetization compensation temperature⁵. The axis on the right shows the net moment per Dy atom by assuming the contribution of the Co subnetwork remains constant at $4.9 \mu_{\text{B}}$ over the whole measured temperature range and fixing the net Dy moment to this value at the compensation temperature. There is sharp up-turn of the M_{s} below 100 K in Figure 4.4, which is due to the linear term in magnetization up to saturation which appears at low temperature as shown in Figure 4.2 (b). It implies that part of the thin film undergoes spin reorientation to in-plane below 50 K. If the remanence M_{r} is plotted, the M_{r} is almost constant below 50 K. The M_{r} and M_{s} values diverge significantly below 50 K when K_1 , the net anisotropy of the film, is unable to maintain the magnetization perpendicular to the film plane. The bulk anisotropy energy of the thin film, 28 kJ/m^3 , is deduced from the 375 mT saturation field $\mu_0 H_{\text{s}}$ in the hard-axis magnetization curve at 300 K of the film shown in Figure 4.2 (a), by using the relation $K_1 = \frac{1}{2} \mu_0 H_{\text{s}} M_{\text{s}}$

4.3.2 Terbium alloys

The films under study are about 20 nm thick and exhibit perpendicular magnetic anisotropy. Most of them show a sharp change of magnetization in their hysteresis loops close to zero field. A representative example was shown in Figure 4.2 (c) and (d). Unexpectedly, there is never any trace of this behavior in either Hall or Kerr effect measurements of the hysteresis loops, which are illustrated for the same film at 300 K in Figure 4.5.

Figure 4.6 plots the coercivity of a-Tb_{0.25}Co_{0.75} which tends to diverge at the compensation temperature of about 200 K, where a thermal scan at remanence crosses zero. The anhysteretic phase (or called soft phase) has a nearly temperature-independent magnetization behavior, as illustrated in Figure 4.7. The hysteretic phase behaves like a normal ferrimagnet with a compensation temperature about 200 K, in line with the result from the thermal magnetization. The magnetic moment $|m|$ in Bohr magnetons per TbCo₃ formula unit is measured, and the plot in Figure 4.8 considers the reversal of sign at compensation temperature. The a-Tb_{0.25}Co_{0.75} (sample number 5) behaves similarly, only with a lower T_{comp} of about 180 K.

4.4 Discussion

4.4.1 Dispersed moments induced by local anisotropy

Given the Co magnetic moment⁶ is $1.63 \mu_{\text{B}}$ in a-YCo₃ discussed in the previous chapter, this allows us to infer the magnetic moment of Dy and Tb. From both Figure 4.4 and Figure 4.8 the

⁴After obtaining the density, composition, thickness sample size, we can convert the magnetization in A/m unit into magnetic moment in μ_{B} /formula [1]. In this way, we know M_{s} and M_{r} .

⁵Because the Co-Co exchange interaction is stronger than the Dy-Co interaction, the magnetization of the rare earth subnetwork falls off more rapidly with increasing temperature than that of the Co. For a certain range of compositions, there exists a magnetization compensation temperature where those two subnetwork magnetizations cancel each other.

⁶When talking about the Co, Dy and Tb magnetic moments or the magnetic moment per formula unit, such as magnetic moment per DyCo₃, we are actually referring to their thermally averaged magnetic moments.

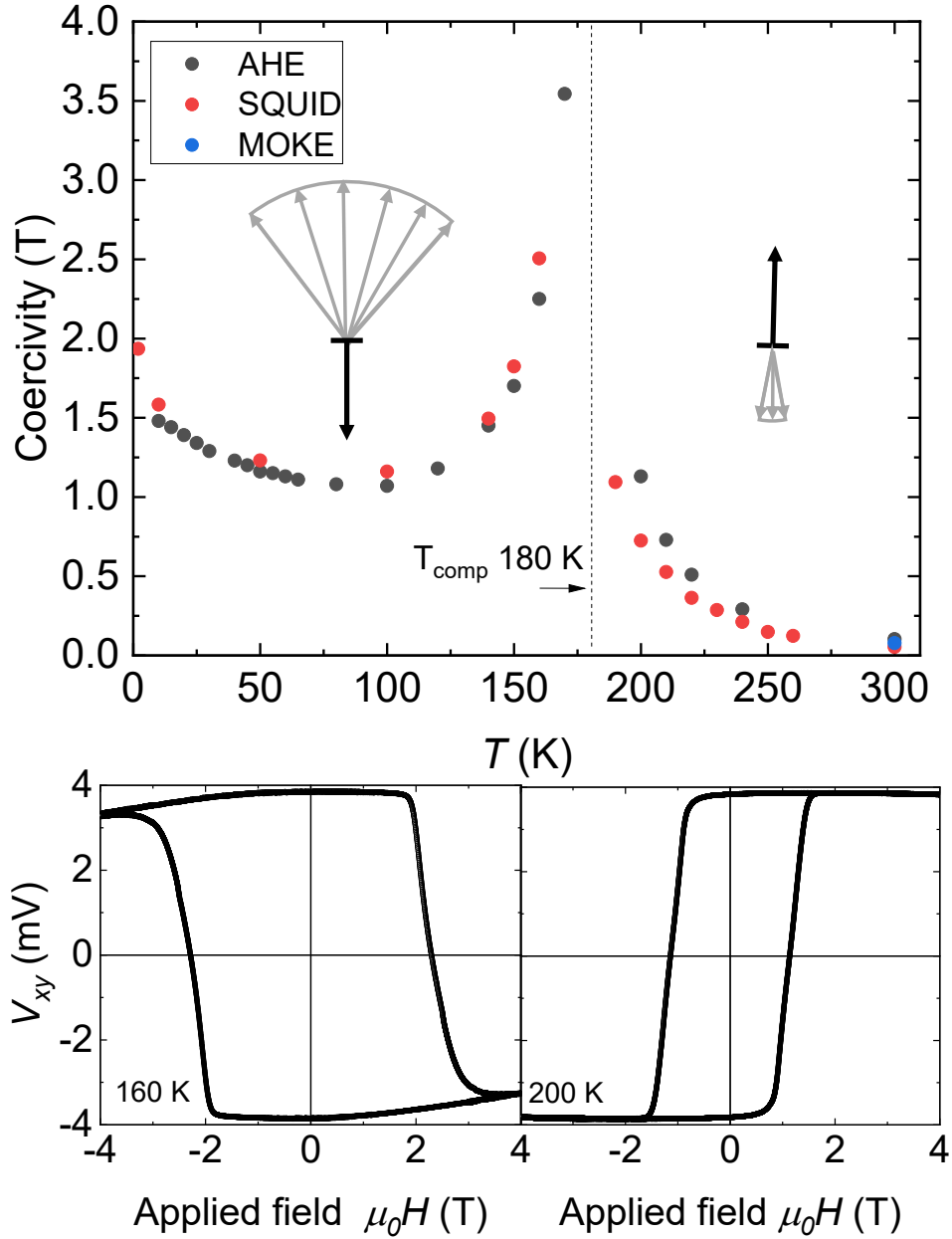


Figure 4.3: Coercivity for a-Dy_{0.25}Co_{0.75} (sample number 2) showing a divergence at the compensation temperature of 180 K. Data points at different temperature are obtained by SQUID magnetometry or anomalous Hall effect. A polar MOKE point at 300 K is included (in blue). There are two panels at the bottom, illustrating the anomalous Hall effect loops below and above compensation temperature where the current used is 1 mA (current density of $\approx 1.4 \times 10^7$ A/m²).

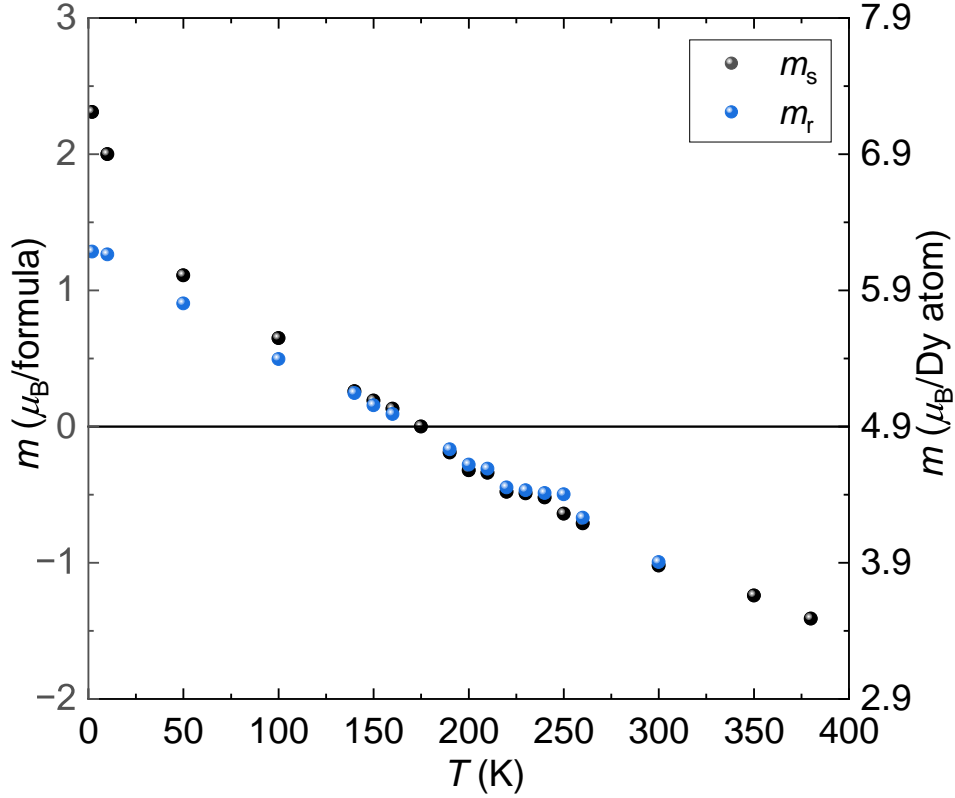


Figure 4.4: Magnetic moment per DyCo_3 formula unit in $a\text{-Dy}_{0.25}\text{Co}_{0.75}$ (sample number 2), taking account of the change of sign at T_{comp} . The thermal averaged magnetic moment $\langle m \rangle$ per dysprosium atom is marked on the right hand scale. The black points are extrapolations to zero applied field. The blue points are values at remanence.

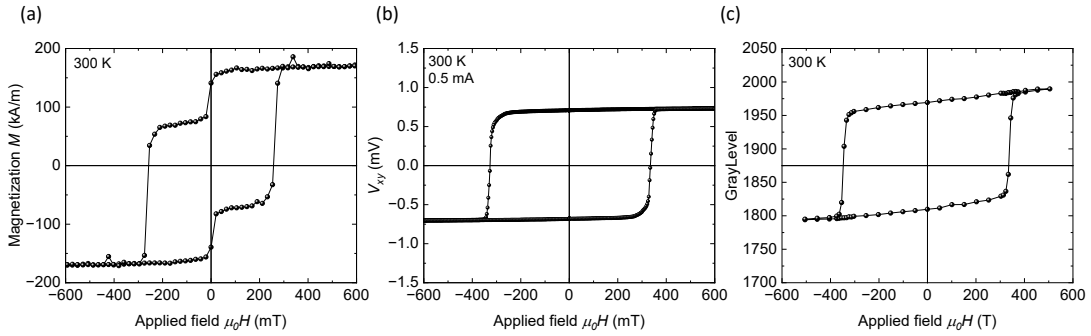


Figure 4.5: Room-temperature hysteresis loops measured (a) by SQUID magnetometry (b) by anomalous Hall effect and (c) by polar MOKE in blue light of the same sample $a\text{-Tb}_{0.25}\text{Co}_{0.75}$ (the number 5 sample) as Figure 4.2 (c) and (d). They show no sign of any sharp increase at remanence.

saturation magnetic moment per Dy (Tb) atom at low temperature in the amorphous alloy thin film has a value of $7.3 \mu_{\text{B}}$ ($7.0 \mu_{\text{B}}$). They appear smaller than that of the trivalent Dy and Tb ion values 10 and $9 \mu_{\text{B}}$ [1], respectively. The measured Dy moment of $7.3 \mu_{\text{B}}$ is comparable to literature values, which ranges from $6.7 \mu_{\text{B}}$ to $8.2 \mu_{\text{B}}$, depending on the choice of Co moment, precise composition and sample preparation conditions [3, 21, 4].

What we plotted in Figure 4.4 and Figure 4.8 is the z -component of Dy and Tb, respectively. Because $4f$ electrons responsible for magnetism are well-shielded by the $5s$ and $5p$ shells, we expect that the at atomic level, the magnetic moment of Dy and Tb should be 10 and $9 \mu_{\text{B}}$,

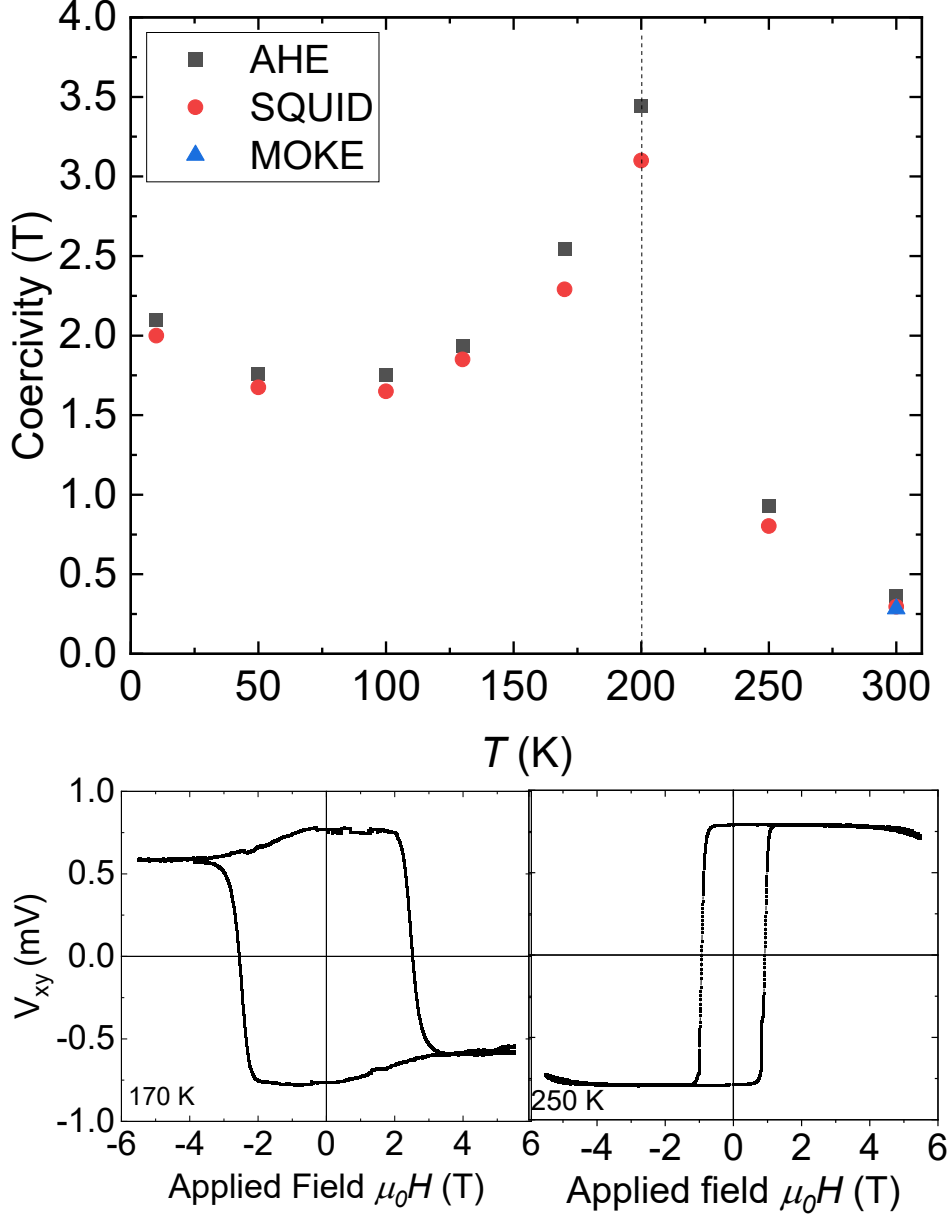


Figure 4.6: Coercivity for a-Tb_{0.25}Co_{0.75} (sample number 4) showing a divergence at the compensation temperature of 180 K. Data points are obtained by SQUID magnetometry or anomalous Hall effect. A magneto-optic Kerr effect point at 300 K is included. The current used for Hall measurements is 0.5 mA (current density of $\approx 7 \times 10^6$ A/m²).

respectively. The apparent difference is due to the random uniaxial anisotropy on the Dy and Tb sites, which leads to a cone angle in the distribution of magnetic moments for Dy and Tb. For comparison, the Gd ion moment is estimated to be $7.6 \mu_B$ in a-GdCo_{3.5} based on the magnetization value provided by the reference [22] if we assume the film density of 7.5 g/cm^3 . The spin moment of Gd contributes $7 \mu_B$ and the other $0.6 \mu_B$ comes from 5d/6s conduction electrons. Therefore, the Gd moment is antiparallel to the Co moment in the ferrimagnetic a-GdCo_{3.5} system.

The model for magnetism in amorphous materials was brought up by Harris, Plischke and Zuckermann in 1973 [23]. Essentially, it is a Heisenberg model in which each spin has the same magnitude but it is subjected to a local anisotropy field of random orientation. Using this model, Chi and Alben conducted crucial simulations by representing spins as classical unit

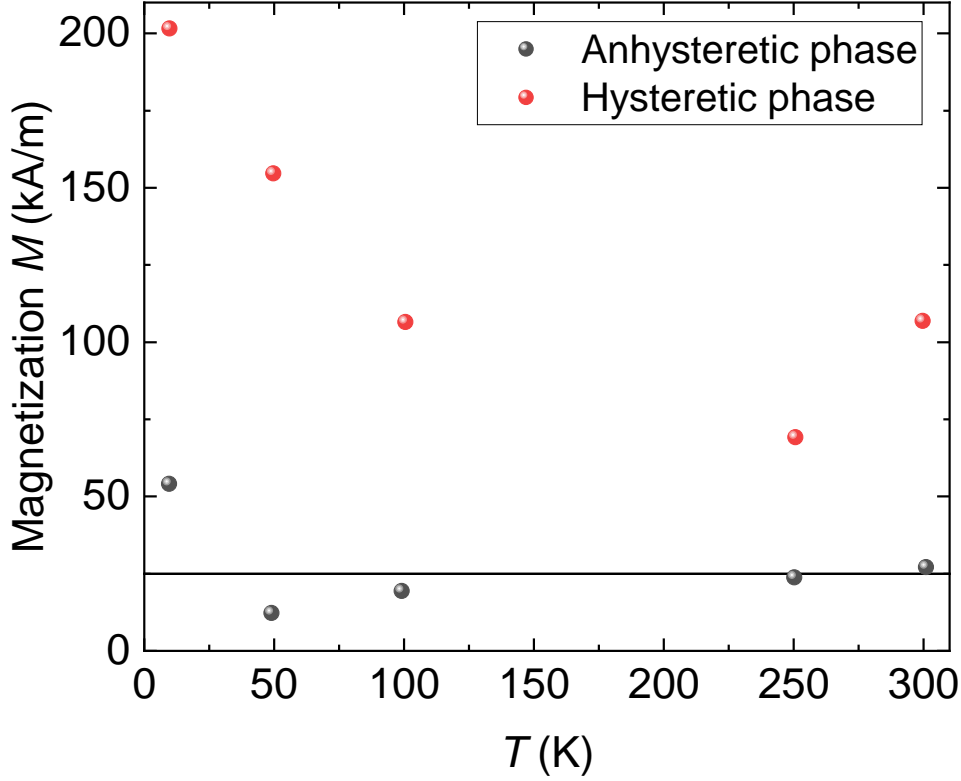


Figure 4.7: Temperature dependence of magnetization in both anhysteretic and hysteretic phases of a-Tb_{0.25}Co_{0.75} (sample number 4) with the black line as an eye guide.

vectors, in the 1970s [24, 25]. At one limit when anisotropy is negligible, each spin will lie along the exchange field from Co, and $m_s = m_0$. At the other limit, when anisotropy is infinite, each spin can only point in either of the two directions along the local easy axis. The material is amorphous, so all directions are equally likely for the local easy axis of any rare earth site⁷ and it can be shown by integration over a hemisphere that

$$\frac{m_s}{m_0} = \frac{\frac{1}{m_0} \int_0^{\pi/2} m \cos \theta 2\pi r^2 \sin \theta d\theta}{\int_0^{\pi/2} 2\pi r^2 \sin \theta d\theta} = \frac{1}{2} \Big|_{m=m_0} \quad (4.1)$$

where m_0 is the atomic magnetic moment of rare earth at 0 K and m_s is the value measured in a magnetometer at low temperature in those amorphous alloy thin films such as a-Tb_xCo_{1-x} and a-Dy_xCo_{1-x}. At intermediate value of anisotropy, the spins will on the average be pulled from their easy axes the cone is narrowed by the exchange, leading to a value of m_s , higher than 0.5 m_0 .

The complete Hamiltonian of an ion in a solid has four terms:

$$\mathcal{H} = \mathcal{H}_0 + \mathcal{H}_{so} + \mathcal{H}_{cf} + \mathcal{H}_Z. \quad (4.2)$$

\mathcal{H}_0 is responsible for the Coulomb interactions among the electrons and between the electrons and nucleus, resulting in the total spin and orbital momenta \mathbf{L} and \mathbf{S} . The remaining three terms \mathcal{H}_{so} , \mathcal{H}_{cf} , \mathcal{H}_Z are the spin-orbit interaction, crystal field and Zeeman terms [1]. In the case of 4f ions, the spin-orbit interaction dominates over the crystal field and Zeeman terms. Therefore, J is a good quantum number and the $|J, M_J\rangle$ -states forms a basis. Treat the two terms \mathcal{H}_{cf} and \mathcal{H}_Z on an equal footing, as perturbations to $\mathcal{H}_0 + \mathcal{H}_{so}$:

$$\mathcal{H}' = \mathcal{H}_{cf} + \mathcal{H}_Z. \quad (4.3)$$

⁷In principle, the local anisotropy can be calculated from a detailed structural model.

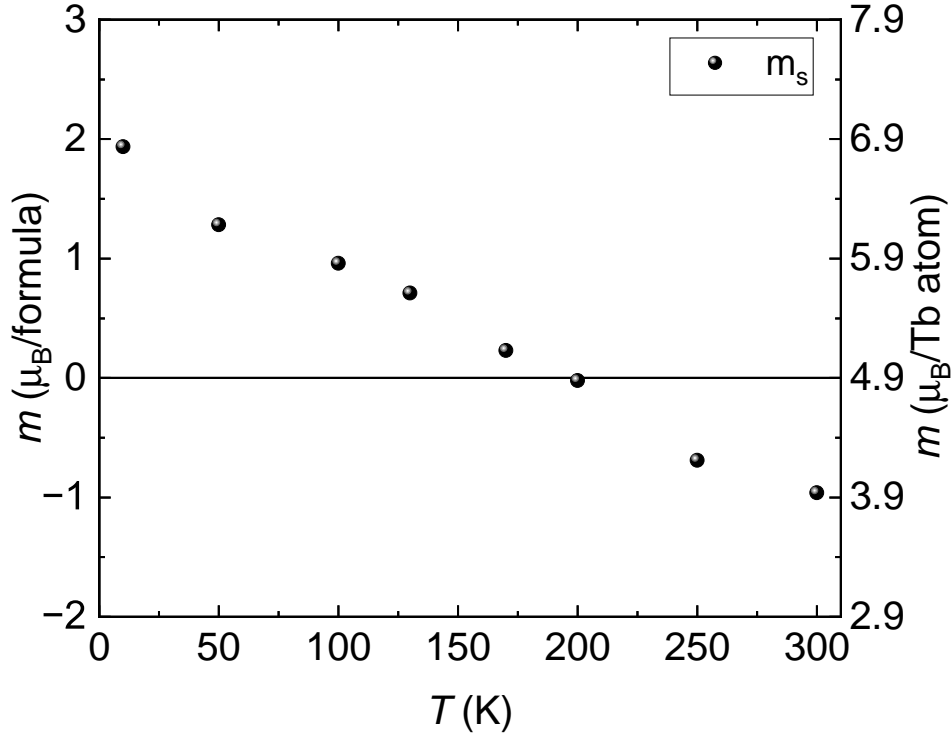


Figure 4.8: Magnetic moment per TbCo_3 formula unit in $a\text{-Tb}_{0.25}\text{Co}_{0.75}$ (sample number 4), taking account of the change of sign at T_{comp} . The thermal averaged magnetic moment $\langle m \rangle$ per terbium atom is marked on the right hand scale. Black points are extrapolations to zero applied field. Blue points are values at remanence.

The degeneracy of the crystal-field spectra is removed by the Zeeman energy term. In order to analyze the non-collinearity of Dy or Tb, we require information about both the magnitude of the random anisotropy and also the the magnitude of $\mu_0 \mathbf{H}_W^{R-Co}$, the R-Co exchange field acting on the rare earth and directed along $-z$, opposite to the Co magnetization.

Let's focus on the crystal field interaction first. The 'crystal field' is adopted here even though the rare earth atomic environment is nonperiodic, because the electrostatic field mainly come from the surrounding charges. As a first approximation, assuming the sites with uniaxial symmetry, we can take

$$\mathcal{H}_{cf} = -B_2 \hat{O}_2^0 = -B_2 (3\hat{J}_z^2 - J(J+1)) \quad (4.4)$$

where the \hat{O}_2^0 is the Steven operator equivalent for the diagonal term in the electrostatic quadrupole interaction, referred to the local easy axis z' for Dy or Tb, which makes an angle with $-z$. We neglect the off-diagonal term \hat{O}_2^2 and assume for simplicity in discussing the ground state that \mathbf{H}_W^{R-Co} and B_2 have constant magnitude at every site and are independent of temperature. A value of $B_2 = 1.0$ K was derived from the linear low-temperature specific heat in $a\text{-DyCu}$ alloy [26]. A similar value of B_2 was found in the spin ice material $\text{Dy}_2\text{Ti}_2\text{O}_7$ ⁸ [28]. Since the $J(J+1)$ is a constant, the formula 4.4 is sometimes written as $-D\hat{J}_z^2$, where $D = 3B_2$. However, the constant $J(J+1)$ is necessary to ensure zero anisotropy at high temperatures when $|J, M_J\rangle$ states are equally occupied. The uniaxial anisotropy of Dy in the ground-state doublets $|J = 15/2, M_J = 15/2\rangle$ and $|J = 15/2, M_J = -15/2\rangle$ is therefore 105 K, and that of Tb, which has a larger quadrupole moment but a lower value of J^2 is about 5% greater. At low temperature, the effect of random uniaxial anisotropy of order 100 K per rare earth atom is to reduce the possible magnetic states to just two, $|J, M_{Jz'}\rangle$ along the local easy axis z' . They become random Ising

⁸However, in the DyCo_5 compound the B_2 was found to be -1.4 K [27]. The difference in sign is most likely attributable to the distinct local environments of rare earth atoms.

moments rather than random Heisenberg moment and much easier to order magnetically. The exchange interaction with Co subnetwork at low temperature, however small, creates a uniform distribution of moments within a hemisphere, which narrows to a cone as the exchange field increases. When increasing temperature towards T_{comp} , the magnitude of thermodynamic average rare-earth moment $\langle m \rangle$ is reduced by thermal excitation to excited $|J, M_{Jz'}\rangle$ states but the anisotropy is also reduced by the occupation of excited states, which narrows the cone. The net moment becomes zero in a-RCo₃ when the component of the average rare-earth moment $\langle m \rangle$ along $-z$ falls to $4.9 \mu_B$.

The exchange field acting on the rare earth site due to Co is sufficient to increase the average moment of the rare earth $\langle m \rangle$ along the $-z$ -axis from 50% (as proved by formula 4.1) to about 70 % of its atomic saturation value at low temperatures ($7.2 \mu_B$ for Dy - Figure 4.4 and $6.8 \mu_B$ for Tb - Figure 4.8). The exchange field at the rare earth site can be considered to be composed of two contributions, the R-R and R-Co exchange interaction [27]. Based on the mean field analysis of $M(T)$ of a-DyCo₃ shown in Figure 4.5, the $\mu_0 \mathbf{H}_W^{R-R} = 16.5$ T and $\mu_0 \mathbf{H}_W^{R-Co} = 50.0$ T. Another estimate of $\mu_0 \mathbf{H}_W^{R-Co}$ is based on the difference in Curie temperature of Y₂Co₁₇ and YCo₅ and the corresponding isostructural Gd intermetallics, which are about 3 % higher [1, 29]. By assuming the same is true in a-GdCo₃ and scaling by the ratio of the rare earth spins (Gd³⁺: 7/2; Dy³⁺: 5/2), the additional exchange field acting on the Co is $848 \times 0.03 \times 5/7 = 18.2$ T, because the Heisenberg exchange interaction depends on the spin directly. The corresponding value of $\mu_0 \mathbf{H}_W^{R-Co}$ is scaled by the ratio of Co to Dy moments and the ratio of Co to Dy atoms, i.e., $\frac{2}{1} \times \frac{3}{1}$, which leads to $\mu_0 \mathbf{H}_W^{R-Co} = 18.2 \times 0.6 = 10.9$ T.

We assume that the internal magnetic field experienced by the rare-earth sites, such as Dy, due to the presence of cobalt is approximately 35 T. The direction of this field is along the z -axis direction, i.e., the normal of thin film. We assume D to be -3 K [26] (D has an energy unit, but it is commonly expressed in K⁹). At temperatures of 0 K, 100 K, 200 K, and 300 K, the thermodynamic average of Dy's m_z (magnetic moment along the z -axis) will be 10.0, 8.0, 4.9, and $3.3 \mu_B$, respectively. This qualitatively explains the temperature dependence of magnetic moment of Dy when the temperature is above 100 K. The reason for the poor fit at temperatures below 100 K is that the magnetic field generated by Co may have an angle relative to Dy's local easy axis for different sites. In that case, the coupling of the total angular momentum to the magnetic field can be written in terms of ladder operators for the single ion Hamiltonian [28]. The population of $|M_J\rangle$ -states at different temperatures can be calculated using matrix quantum mechanics, diagonalizing the matrix at each angle.

4.4.2 Effect of the underlayer

It was reported that an interfacial region of about 5 nm near the substrate in a-TbFeCo was revealed by polarized neutron reflectometry, which exhibited different magnetic properties from the rest of sample [30]. Those amorphous thin films were prepared with thickness 20 nm to 120 nm on thermally oxidized Si substrate by RF magnetron sputtering at room temperature. A 5 nm Ta capping layer was deposited on the sample to prevent oxidation. In addition, a-TbCo thin films prepared at room temperature by using DC magnetron co-sputtering, with a thin Ta underlayer and either a Ta or Pt overlayer showed evidence of both soft and hard magnetic phases [19]. The soft/hard bilayer was found to arise from a growth effect that created a low-density/high-density bilayer. The soft phase was found to be present in all thick thin films in the region closer to the underlayer. In another study, Minghong Tang *et al.* reported that for both Tb-rich and Co-rich TbCo alloy films, the perpendicular magnetic anisotropy decreased considerably with the increase of Ta underlayer thickness [31]. Inserting a 0.3 nm Cu between Ta and TbCo can significantly prevent the influence of Ta on Tb atoms. They also deposited a pure Tb or Co on various underlayers and found that the Ta underlayer seriously affected the

⁹Formally, the D should be $-3K \cdot k_B$, where k_B is the Boltzmann constant.

pure Tb magnetization but not pure Co. Based on these observations, they suspected that Tb atoms deposited on top of Ta layer tended to be partially oxidized since Ta had a good affinity to oxygen left over in the deposition chamber.

A final point to mention is that, the a-Tb_xCo_{1-x} with Ta as buffer and capping layer tends to obtain perpendicular magnetic anisotropy more easily, measured in the MOKE over a quite wide range $0.12 \leq x \leq 0.30$ as reported by Yongshan Liu *et al.* [17]. Some effects like those in Co/Pt might play an role here at the interface.

4.4.3 Anomalous Hall effect

The temperature dependence of Hall voltage of a-DyCo₃ measured at 14 T is plotted in Figure 4.9. The sign change of Hall voltage indicates the T_{comp} is about 180 K, consistent with

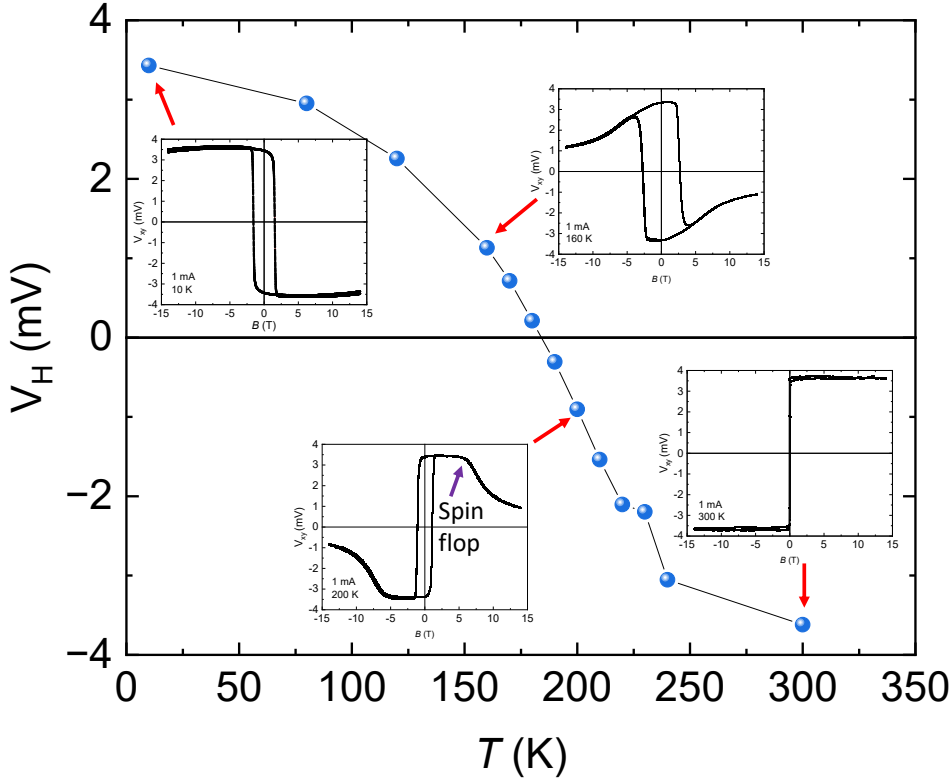


Figure 4.9: Temperature dependence of Hall voltage of a-DyCo₃ (sample number 2) measured at 14 T, with examples of the Hall loops measured at temperature below and above T_{comp} . The decrease in high fields is due to the incipient spin flops. At 200 K, the incipient spin flop for Co subnetwork is indicated by the purple arrow. Those high field measurements were performed in a 14 T PPMS system by Ajay Jha and the current used was 1 mA (current density of $\approx 1.4 \times 10^7$ A/m²).

what we see before in Figure 4.3. When the magnetic field is held at 14 T, as the temperature gets close to the T_{comp} , the magnitude of Hall voltage of a-DyCo₃ gradually decreases to zero. Conversely, if the temperature is fixed, for instance, at 200 K (the Co moment is dominant), the Hall voltage keeps decreasing after a certain field as shown in the inserted 200 K loop figure. This behavior is attributed to the spin-flop transition¹⁰ and the corresponding field is called spin-flop

¹⁰Field induced phase transitions are traditional topics for the physics of magnetic phenomena, among which, the spin flop transition (the formation of an angled structure at field strengths above a threshold value) is one of the most interesting examples. Originally, the spin-flop transition was restricted to field-driven reorientation transition in antiferromagnets. Nowadays, the spin flop was found to happen not only in antiferromagnets but also in artificial synthetic antiferromagnets and ferrimagnets [32, 33].

field H_{sf} . The Dy moments are pulled towards magnetic field direction by a small angle, and Co, being antiferromagnetically coupled to Dy, also moves away from the field direction by an angle. As we are going to discuss in the following paragraph, the Hall signal in the a-DyCo₃ system is primarily generated from Co moment. Because Hall measurement mainly probes the z -component magnetization of Co subnetwork, the decrease of z -component magnetization of the Co subnetwork due to the spin-flop, accounts for the reduction in Hall voltage. Therefore, the canted Co moment is responsible for the curvature of the Hall curve above the spin-flop field. Similar arguments can be applied when the applied field is fixed to 14 T, but the temperature is varied. When temperatures are far away from the T_{comp} , the H_{sf} is much bigger than the field available in the lab. The Co moment is simply aligned antiparallel and parallel to the applied field when temperature is far below and above T_{comp} , respectively. As temperature gets closer to the T_{comp} , the H_{sf} is getting smaller and the applied field is able to make spin-flop transition occur. The sequence of magnetic structures are found with increasing temperature up to 300 K in a-DyCo₃ under a high field such as 10 T, as illustrated in Figure 4.10. This similar tem-

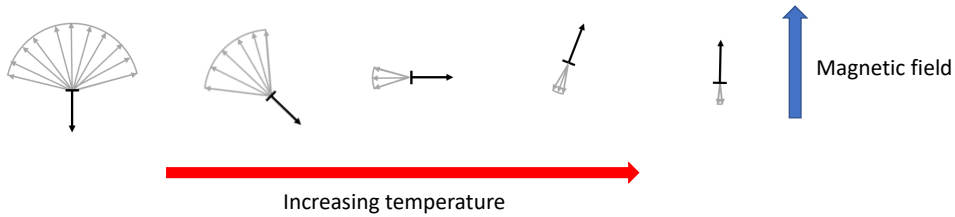


Figure 4.10: Sequence of magnetic structures are found with increasing temperature in a-DyCo₃ under a high field such as 10 T. The black arrows represents the Co moment and, while the gray ones represent the Dy moments.

perature dependence of Hall voltage at a certain field is observed in systems a-GdFeCo, as well [34, 35]. It's worth noting that the required magnetic field to observe a similar phenomenon in a-GdFeCo is significantly smaller than in a-DyCo₃, where it was reported that only 310 mT is needed to observe the former [34]. This might be due to the higher anisotropy in a-DyCo₃ than that in a-GdFeCo as the H_{sf} is given by

$$H_{\text{sf}} = \sqrt{H_{\text{a}}H_{\text{ex}}} \quad (4.5)$$

where H_{a} is an anisotropy field (corresponding to the macroscopic anisotropy) and H_{ex} is the inter-subnetwork exchange field [36]. Bigger applied fields can flop the magnetization for temperatures both below and above T_{comp} , provided the net magnetization is small in a-GdCo and in crystalline ferrimagnets with perpendicular anisotropy. A much larger field, equal to H_{ex} , is required to reach ferromagnetic saturation. Suppose M_{α} is the magnetization of either subnetwork, the perpendicular susceptibility χ_{\perp} of the antiferromagnet is

$$\chi_{\perp} = M_{\alpha}/H_{\text{ex}} \quad (4.6)$$

so the net magnetization in an applied field H is $2M_{\alpha}H/H_{\text{ex}}$.

A recent study of the anomalous Hall effect in crystalline GdCo₅ and GdCo₃ compounds claimed that the rare earth contribution to the AHE is not negligible [37]. Since the sign of the AHE of pure Gd metal is negative while that of pure Co metal is positive, it possible that 5d electrons of Gd, Tb and Dy contribute in the same sense as Co to the AHE when those rare earth moments are coupled antiparallel to the Co. But we do not think this is an essential effect in our amorphous alloys, for the following reason. The temperature dependence of Hall voltage of the same sample, extracted at zero magnetic field from loops, is illustrated in Figure 4.11. The magnetitude of the Hall voltage is quite constant below and above T_{comp} , whereas the rare earth moment falls by about 35%. Although we do not have enough data close to T_{comp} , it is

reasonable to expect that a step-like sign change should happen, as reported in other similar systems [38].

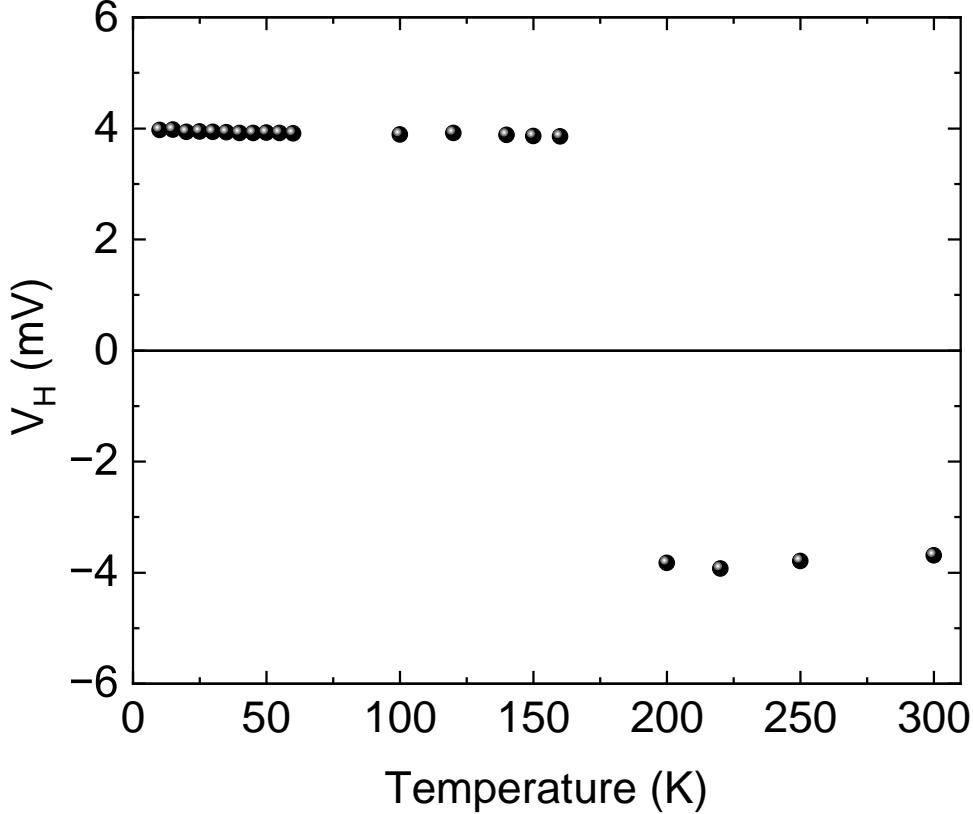


Figure 4.11: Temperature dependence of Hall voltage of a-DyCo₃ (sample number 2) extracted from the Hall loops at zero magnetic field. Those Hall effect loops were measured in the Cryo-magnet and the current used was 1 mA.

4.4.4 Divergence of coercivity

One of the characters of ferrimagnets, the coercivity H_c diverges near T_{comp} . The coercive field measures how easy it is to reverse the magnetization. For our samples with good perpendicular magnetic anisotropy, there are mainly two energy terms, anisotropy energy and Zeeman energy. The field at which the reversal of magnetization takes place relies on the competition between anisotropy energy, which prefers to keep the moment in their current direction, and the Zeeman energy of the net magnetization in the applied field, which tries to align the net magnetization along the field direction. So when the net magnetization decreases (close to the magnetization compensation point), the anisotropy energy wins and it takes a larger field to switch the magnetization. Quantitatively, as we discuss in section 1.3.3, $H_c = \frac{2K}{\mu_0 M_s}$ when the applied field is along the easy axis of uniaxial anisotropy. Since the H_c is proportional to $\frac{1}{M_s}$, the coercivity of the hysteresis loops increases as the saturation magnetization decreases near T_{comp} [39, 40]. Being ferrimagnetic, the a-R-T can possess a T_{comp} that can be brought to the vicinity of room temperature by proper choice of composition. The high coercivity field around T_{comp} protects the sample from stray magnetic field, which is useful for some applications such as magneto-optical recording [41].

Besides magnetization compensation temperature T_{comp} , we also have angular momentum compensation temperature, at which the net angular momentum disappears. The angular momentum of Dy is $7.7 \hbar$ ($7.5 \hbar$ from J and a contribution of $0.2 \hbar$ from the $5d/6s$ electrons). The

atomic moment of Co is $1.63 \mu_B$ ($1.31 \mu_B$ spin moment and $0.32 \mu_B$ orbital moment), and its angular momentum is $0.98 \hbar$ per atom. Scaling the net magnetization of Dy in μ_B by 0.77 to obtain its angular momentum in \hbar , we estimate that angular momentum compensation, where each subnetwork has $2.94 \hbar$ per DyCo_3 formula unit, is close to 270 K, neglecting temperature dependence of the cone angle. The distinct g-factors of T and R are responsible for the difference in angular momentum compensation and magnetization compensation temperatures¹¹.

4.4.5 Magnetically-ordered anhysteretic component silent in AHE and MOKE

To compare with Figure 4.5, a set of data of $\text{a-Y}_{0.25}\text{Co}_{0.75}$ is plotted in Figure 4.12. The maximum field available in the MOKE measurement setup is limited. Apart from this limitation, the behavior is similar among those three measurements, SQUID, AHE and polar MOKE, demonstrating good overall consistency¹².

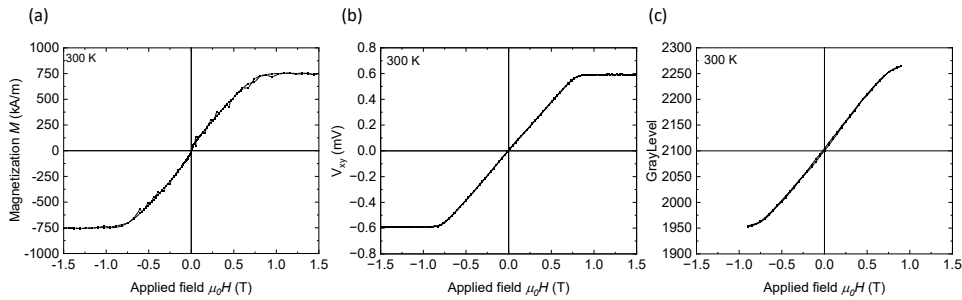


Figure 4.12: Room-temperature hysteresis loops measured (a) by SQUID magnetometry (b) by anomalous Hall effect (The current used for Hall measurements is 0.5 mA with a current density of $\approx 7 \times 10^6 \text{ A/m}^2$.) and (c) by polar MOKE in blue light of $\text{a-Y}_{0.25}\text{Co}_{0.75}$ (sample number 7).

One plausible hypothesis is that the anhysteretic phase may relate to a non-conductive layer. What could be its composition? We know EuO was the first ferromagnetic rare earth oxide to be with a $T_c = 69.3 \text{ K}$ and magnetic moment $7.0 \mu_B$ [42, 1]. Hence, one speculation is that terbium oxides will be plausible candidates. Six terbium oxides phases whose compositions range between Tb_2O_3 and TbO_2 were prepared and their magnetic properties at temperature from 1.4 K to 300 K. Except for $\text{TbO}_{1.823}$, the ordering is antiferromagnetic and there is no remanence. In the case of $\text{TbO}_{1.823}$ with a magnetic ordering temperature 6 K, remanence up to 2 % of the magnetization at 8 T was observed upon removal of the field [43]. The low magnetic ordering temperature might be responsible for the upturn of magnetization when the temperature reaches 10 K as seen in Figure 4.7. This can't explain the appearance of an anhysteretic component at the other temperatures. It was reported that vacancy mediated room temperature ferromagnetism can be introduced in the Co-doped Dy_2O_3 , where Dy_2O_3 by itself is a dielectric material [44]. Therefore, the Co-doped terbium oxides might exist, potentially accounting for the presence of the anhysteretic phase throughout the entire temperature range.

The second possible explanation is the existence of Tb in the +4 oxidation state, which then has the isoelectronic $4f^7$ like Gd^{3+} . The Gd^{3+} is an S-state ion with $L = 0$ so the single ion anisotropy is negligible. Lanthanides usually occur in the +3 oxidation state¹³ but Tb^{4+} is observed in concentrated aqueous carbonate solutions and in a few inorganic solids such as

¹¹A correlation between those two types of temperatures is demonstrated [35].

¹²The magnitude of the Hall voltage is similar for 0.5 mA in a-TbCo_3 (shown in Figure 4.5) and a-YCo_3 . However, the Hall voltage magnitude for 1.0 mA in a-DyCo_3 (shown in Figure 4.3) is more than twice that of 0.5 mA in a-YCo_3 . The probe current is applied along the diagonal of the samples, each approximately 5 by 5 mm^2 in size, using the Van der Pauw method. Making Hall bars will enable a more accurate comparison in the future.

¹³Eu and Yb are exceptions, preferring the stable closed configuration $4f^7$ and $4f^{14}$, respectively, that corresponds to divalent ionic configuration. For similar reasons, Ce prefers to adopt a Ce^{4+} . [29].

metal oxides [43, 45] or fluorides [46, 47]. By modifying the environment surrounding a rare-earth ion, and consequently altering the crystal fields that affect it, it becomes possible to excite a 4f electron into the valence shell, resulting in terbium becoming tetravalent [48].

The third one is that the sample deposited on the substrate sides, and these additional areas with their different orientations, are responsible for the anhysteretic phase. It was reported by Mandru *et al.* that a class of artifacts manifesting as soft magnetic components are evident from magnetometry measurements of a-TbFe thin films prepared by magnetron sputtering [49]. They show that this is not inherent to a-TbFe but is due to the manner in which the substrates are mounted during deposition, with a material deposited at the substrate sides giving rise to this soft material signal. They prepared three different sample configurations, i.e., mask, no mask and cut. In our case, we mount $10 \times 10 \text{ mm}^2$ or $20 \times 20 \text{ mm}^2$ substrate in the sputtering chamber and subsequently then cut smaller pieces. We then selected one of the pieces with a dimension about $5 \times 5 \text{ mm}^2$ and performed all the characterizations, such as magnetization in SQUID, MOKE and AHE. Therefore, there is a high possibility for us to choose a piece of sample with two substrate sides deposited with material, instead of four substrate sides in the no mask configuration studied in Mandru *et al.*'s work. The area of the two sides is 20 % of the flat area of the chip since the thickness of the substrate is $525 \pm 25 \text{ }\mu\text{m}$. In order to confirm this, we selected one of the samples showing the anhysteretic component, polished the substrate sides to remove all samples deposited onto the sides, and finally re-measured it in the SQUID, as shown in Figure 4.13. As we can see clearly, after polishing the substrate sides, the anhysteretic component indeed disappears. The absence of overlap between the positive and negative loops in the right panel may be attributed to sample movement. This arises as the sample size becomes smaller than the diameters of the mounting straw following the polishing of the substrate sides. A more secure fix of the sample to the straw is expected to resolve the issue of non-overlap. The saturation magnetization, measured at about 223 kA/m, remains nearly unchanged before and after polishing the sides, providing further evidence that the anhysteretic component originates from the material deposited on the sides.

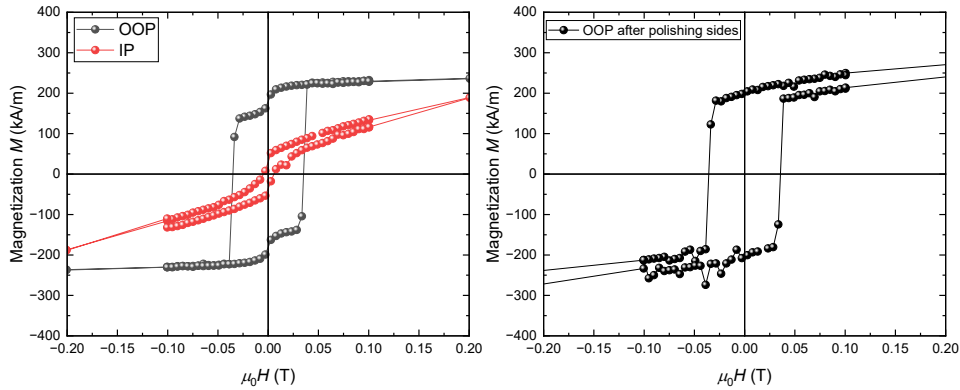


Figure 4.13: Room-temperature magnetization loops of a-Dy_{0.25}Co_{0.75} (the number 3 sample) measured by SQUID magnetometry before and after polishing the substrate sides. **Left:** In-plane (in red) and out-of-plane (in black) measurements before the substrate sides being polished. The anhysteretic soft component represent about 20 % of the magnetization; **Right:** Out-of-plane (in black) measurement after the substrate sides being polished.

SQUID magnetometry measures everything including the samples deposited on the substrate sides. But MOKE and AHE measurements do not. MOKE only probes a very small part of the top surface and the AHE probes the top surface where the anisotropy is perpendicular. In summary, the SQUID measures the top surface + sample deposited on the substrate sides, but the MOKE and AHE only probe the top surface, which provides a reasonable explanation of the discrepancy observed in our data as shown in Figure 4.5. Given that the substrate we employed

has a thickness of 0.5 mm, the area of the sample deposited on the substrate sides comprises approximately 20% of the top surface area. The ratio of anhysteretic to hysteretic part is of that order and gets bigger when temperature deviates from the T_{comp} . However, the nature of the anhysteretic material observed in the sample deposited on the substrate sides remains unclear.

4.5 Conclusions and outlook

The magnetic ground state of a-Dy_{0.25}Co_{0.75} and a-Tb_{0.25}Co_{0.75} is sperimagnetic due to the strong local random uniaxial anisotropy. More detailed quantitative analysis of the effect of the random anisotropy is required.

In some samples, magnetic hysteresis loops with anhysteretic component, which does not appear either in MOKE or AHE. A likely explanation is that this discrepancy is due to the material sputtered on the substrate sides.

It will be beneficial to fabricate Hall bars for simultaneous measurement of Hall voltage and imaging of the domains by polar MOKE. If possible, combining Hall measurement and XMCD will be even better, in which we could get a better understanding of the relation between magnetization behavior of the two subnetworks and Hall voltage. It is important to exercise caution during the deposition of thin film samples to prevent them from being over-deposited onto the substrate's sides.

References

- [1] J. M. D. Coey, *Magnetism and Magnetic Materials*. Cambridge university press, 2010. (Cited on page: 103, 107, 109, 111, 113, 117)
- [2] K. Moorjani and J. M. D. Coey, *Magnetic Glasses*. Elsevier, 1984. (Cited on page: 103)
- [3] K. Balymov, E. Kudryukov, V. Vas'kovskiy, O. Adanakova, N. Kulesh, E. Stepanova, and A. Rusalina, "Magnetism of amorphous Dy-Tb-Co-type films," in *Journal of Physics: Conference Series*, vol. 1389, p. 012014, IOP Publishing, 2019. (Cited on page: 103, 109)
- [4] J. M. D. Coey, J. Chappert, J. Rebouillat, and T. Wang, "Magnetic structure of an amorphous rare-earth transition-metal alloy," *Physical Review Letters*, vol. 36, no. 17, p. 1061, 1976. (Cited on page: 104, 109)
- [5] C. D. Stanciu, F. Hansteen, A. V. Kimel, A. Kirilyuk, A. Tsukamoto, A. Itoh, and T. Rasing, "All-optical magnetic recording with circularly polarized light," *Physical review letters*, vol. 99, no. 4, p. 047601, 2007. (Cited on page: 104)
- [6] T. Ostler, J. Barker, R. Evans, R. Chantrell, U. Atxitia, O. Chubykalo-Fesenko, S. El Mousaoui, L. Le Guyader, E. Mengotti, L. Heyderman, *et al.*, "Ultrafast heating as a sufficient stimulus for magnetization reversal in a ferrimagnet," *Nature communications*, vol. 3, no. 1, p. 666, 2012. (Cited on page: 104)
- [7] A. El-Ghazaly, B. Tran, A. Ceballos, C.-H. Lambert, A. Pattabi, S. Salahuddin, F. Hellman, and J. Bokor, "Ultrafast magnetization switching in nanoscale magnetic dots," *Applied Physics Letters*, vol. 114, no. 23, 2019. (Cited on page: 104)
- [8] Z. Hu, J. Besbas, R. Smith, N. Teichert, G. Atcheson, K. Rode, P. Stamenov, and J. Coey, "Single-pulse all-optical partial switching in amorphous $\text{Dy}_x\text{Co}_{1-x}$ and $\text{Tb}_x\text{Co}_{1-x}$ with random anisotropy," *Applied Physics Letters*, vol. 120, no. 11, p. 112401, 2022. (Cited on page: 104)
- [9] G. Sala, V. Krizakova, E. Grimaldi, C.-H. Lambert, T. Devolder, and P. Gambardella, "Real-time hall-effect detection of current-induced magnetization dynamics in ferrimagnets," *Nature Communications*, vol. 12, no. 1, p. 656, 2021. (Cited on page: 104)
- [10] G. Sala, C.-H. Lambert, S. Finizio, V. Raposo, V. Krizakova, G. Krishnaswamy, M. Weigand, J. Raabe, M. D. Rossell, E. Martinez, *et al.*, "Asynchronous current-induced switching of rare-earth and transition-metal sublattices in ferrimagnetic alloys," *Nature Materials*, vol. 21, no. 6, pp. 640–646, 2022. (Cited on page: 104)
- [11] K. Chen, D. Lott, A. Philippi-Kobs, M. Weigand, C. Luo, and F. Radu, "Observation of compact ferrimagnetic skyrmions in DyCo_3 film," *Nanoscale*, vol. 12, no. 35, pp. 18137–18143, 2020. (Cited on page: 104)
- [12] K. Wang, Z. Xu, and S. Dong, "A simple method for tuning perpendicular magnetic properties of ultra-thin TbFeCo films," *Materials Letters*, vol. 236, pp. 89–91, 2019. (Cited on page: 104)

- [13] K. Wang, Y. Huang, Z. Xu, S. Dong, and R. Chen, “Effect of sputtering power on the magnetic properties of amorphous perpendicular TbFeCo films,” *Journal of Magnetism and Magnetic Materials*, vol. 424, pp. 89–92, 2017. (Cited on page: 104)
- [14] S. Zhang, Y. Zhang, L. Zhang, Z. Li, Y. Ren, Q. Jin, and Z. Zhang, “Temperature dependence of magnetic properties in CoFe/Tb multilayers with perpendicular magnetic anisotropy,” *ACS Applied Electronic Materials*, vol. 4, no. 11, pp. 5361–5367, 2022. (Cited on page: 104)
- [15] J. Lin, M. Hehn, T. Hauet, Y. Peng, J. Igarashi, Y. L. Guen, Q. Remy, J. Gorchon, G. Malinowski, S. Mangin, *et al.*, “Single laser pulse induced magnetization switching in in-plane magnetized GdCo alloys,” *arXiv preprint arXiv:2308.10516*, 2023. (Cited on page: 104)
- [16] A. Hassdenteufel, B. Hebler, C. Schubert, A. Liebig, M. Teich, M. Helm, M. Aeschlimann, M. Albrecht, and R. Bratschitsch, “Thermally assisted all-optical helicity dependent magnetic switching in amorphous Fe_{100-x}Tb_x alloy films,” *Advanced Materials*, vol. 25, no. 22, pp. 3122–3128, 2013. (Cited on page: 105)
- [17] Y. Liu, H. Cheng, P. Vallobra, H. Wang, S. Eimer, X. Zhang, G. Malinowski, M. Hehn, Y. Xu, S. Mangin, and Z. Weisheng, “Ultrafast single-pulse switching of Tb-dominant CoTb alloy,” *Applied Physics Letters*, vol. 122, no. 2, 2023. (Cited on page: 105, 114)
- [18] G.-y. Adachi and N. Imanaka, “The binary rare earth oxides,” *Chemical reviews*, vol. 98, no. 4, pp. 1479–1514, 1998. (Cited on page: 105)
- [19] A. Ceballos, M. Charilaou, M. Molina-Ruiz, and F. Hellman, “Coexistence of soft and hard magnetic phases in single layer amorphous Tb–Co thin films,” *Journal of Applied Physics*, vol. 131, no. 3, 2022. (Cited on page: 106, 113)
- [20] K. Thórarinsdóttir, B. Thorbjarnardóttir, U. Arnalds, and F. Magnus, “Competing interface and bulk anisotropies in Co-rich TbCo amorphous thin films,” *Journal of Physics: Condensed Matter*, vol. 35, no. 20, p. 205802, 2023. (Cited on page: 106)
- [21] S. Uchiyama, “Magnetic properties of rare earth-cobalt amorphous films,” *Materials chemistry and physics*, vol. 42, no. 1, pp. 38–44, 1995. (Cited on page: 109)
- [22] A. Gangulee and R. Taylor, “Mean field analysis of the magnetic properties of vapor deposited amorphous Fe-Gd thin films,” *Journal of Applied Physics*, vol. 49, no. 3, pp. 1762–1764, 1978. (Cited on page: 110)
- [23] R. Harris, M. Plischke, and M. Zuckermann, “New model for amorphous magnetism,” *Physical Review Letters*, vol. 31, no. 3, p. 160, 1973. (Cited on page: 110)
- [24] M. C. Chi and R. Alben, “Hysteresis curves and magnetization processes in a model for an amorphous magnet with random uniaxial anisotropy,” *Journal of Applied Physics*, vol. 48, no. 7, pp. 2987–2991, 1977. (Cited on page: 111)
- [25] R. Alben, J. Becker, and M. Chi, “Random anisotropy in amorphous ferromagnets,” *Journal of applied physics*, vol. 49, no. 3, pp. 1653–1658, 1978. (Cited on page: 111)
- [26] J. M. D. Coey and S. Von Molnar, “Linear specific heat of an amorphous magnet due to single-ion excitations,” *Journal de Physique Lettres*, vol. 39, no. 18, pp. 327–330, 1978. (Cited on page: 112, 113)

- [27] J. Greedan and V. Rao, “An analysis of the rare earth contribution to the magnetic anisotropy in RCo_5 and R_2Co_{17} compounds,” *Journal of Solid State Chemistry*, vol. 6, no. 3, pp. 387–395, 1973. (Cited on page: 112, 113)
- [28] B. Tomasello, C. Castelnovo, R. Moessner, and J. Quintanilla, “Single-ion anisotropy and magnetic field response in the spin-ice materials $\text{Ho}_2\text{Ti}_2\text{O}_7$ and $\text{Dy}_2\text{Ti}_2\text{O}_7$,” *Physical Review B*, vol. 92, no. 15, p. 155120, 2015. (Cited on page: 112, 113)
- [29] J. M. D. Coey and S. S. Parkin, *Handbook of Magnetism and Magnetic Materials.*, vol. 1 and 2. Springer International Publishing, 2021. (Cited on page: 113, 117)
- [30] C. T. Ma, B. J. Kirby, X. Li, and S. J. Poon, “Thickness dependence of ferrimagnetic compensation in amorphous rare-earth transition-metal thin films,” *Applied Physics Letters*, vol. 113, no. 17, 2018. (Cited on page: 113)
- [31] M. Tang, S. Chen, X. Zhang, Z. Zhang, and Q. Jin, “Investigation and effective control of perpendicular magnetic anisotropy for TbCo films with different underlayers,” in *Spin*, vol. 6, p. 1650009, World Scientific, 2016. (Cited on page: 113)
- [32] N. Antropov, E. Kravtsov, M. Makarova, V. Proglyado, T. Keller, I. Subbotin, E. Pashaev, G. Prutskov, A. Vasiliev, Y. M. Chesnokov, *et al.*, “Tunable spin-flop transition in artificial ferrimagnets,” *Physical Review B*, vol. 104, no. 5, p. 054414, 2021. (Cited on page: 114)
- [33] A. E. Clark and E. Callen, “Néel ferrimagnets in large magnetic fields,” *Journal of Applied Physics*, vol. 39, no. 13, pp. 5972–5982, 1968. (Cited on page: 114)
- [34] J. Wang, M. Li, C. Li, R. Tang, M. Si, G. Chai, J. Yao, C. Jia, and C. Jiang, “Piezostain-controlled magnetization compensation temperature in ferrimagnetic GdFeCo alloy films,” *Physical Review B*, vol. 107, no. 18, p. 184424, 2023. (Cited on page: 115)
- [35] Y. Hirata, D.-H. Kim, T. Okuno, T. Nishimura, D.-Y. Kim, Y. Futakawa, H. Yoshikawa, A. Tsukamoto, K.-J. Kim, S.-B. Choe, *et al.*, “Correlation between compensation temperatures of magnetization and angular momentum in gdfeco ferrimagnets,” *Physical Review B*, vol. 97, no. 22, p. 220403, 2018. (Cited on page: 115, 117)
- [36] A. Zvezdin, “Field induced phase transitions in ferrimagnets,” *Handbook of Magnetic Materials*, vol. 9, pp. 405–543, 1995. (Cited on page: 115)
- [37] N. T. Hai, J.-C. Wu, J.-P. Chou, and J. Pothan, “Novel anomalous hall effect mechanism in ferrimagnetic gdco alloy,” *Journal of Applied Physics*, vol. 133, no. 23, 2023. (Cited on page: 115)
- [38] M. Davydova, P. Skirdkov, K. Zvezdin, J.-C. Wu, S.-Z. Ciou, Y.-R. Chiou, L.-X. Ye, T.-H. Wu, R. C. Bhatt, A. Kimel, *et al.*, “Unusual field dependence of the anomalous hall effect in Ta/Tb–Fe–Co,” *Physical Review Applied*, vol. 13, no. 3, p. 034053, 2020. (Cited on page: 116)
- [39] D. Webb, A. Marshall, Z. Sun, T. Geballe, and R. M. White, “Coercivity of a macroscopic ferrimagnet near a compensation point,” *IEEE transactions on magnetics*, vol. 24, no. 1, pp. 588–592, 1988. (Cited on page: 116)
- [40] S. Demirtas, M. Hossu, R. Camley, H. Mireles, and A. Koymen, “Tunable magnetic thermal hysteresis in transition metal (Fe, Co, CoNi)/rare earth (Gd) multilayers,” *Physical Review B*, vol. 72, no. 18, p. 184433, 2005. (Cited on page: 116)

- [41] M. Mansuripur and M. Ruane, “Mean-field analysis of amorphous rare earth-transition metal alloys for thermomagnetic recording,” *IEEE transactions on magnetics*, vol. 22, no. 1, pp. 33–43, 1986. (Cited on page: 116)
- [42] B. Matthias, R. Bozorth, and J. Van Vleck, “Ferromagnetic interaction in EuO,” *Physical Review Letters*, vol. 7, no. 5, p. 160, 1961. (Cited on page: 117)
- [43] J. MacChesney, H. Williams, R. Sherwood, and J. Potter, “Magnetic properties of the terbium oxides at temperatures between 1.4° and 300° k,” *Journal of Applied Physics*, vol. 37, no. 3, pp. 1435–1435, 1966. (Cited on page: 117, 118)
- [44] A. Bandyopadhyay, S. Sutradhar, B. Sarkar, A. Deb, and P. Chakrabarti, “Vacancy mediated room temperature ferromagnetism in Co-doped Dy₂O₃,” *Applied Physics Letters*, vol. 100, no. 25, 2012. (Cited on page: 117)
- [45] S. Quezel-Ambrunaz and E. Bertaut, “Structure magnetique de l’oxyde de terbium TbO₂,” *Solid State Communications*, vol. 11, no. 5, pp. 605–610, 1972. (Cited on page: 118)
- [46] Y. Tratsiak, M. Korzhik, A. Fedorov, G. Dosovitsky, O. Akimova, S. Belus, M. Fasoli, A. Vedda, V. Mechinsky, and E. Trusova, “On the stabilization of Ce, Tb, and Eu ions with different oxidation states in silica-based glasses,” *Journal of Alloys and Compounds*, vol. 797, pp. 302–308, 2019. (Cited on page: 118)
- [47] D. Avignant, E. Largeau, V. Gaumet, P. Dugat, and M. El-Ghozzi, “Recent progress in tetravalent terbium chemistry,” *Journal of alloys and compounds*, vol. 275, pp. 1–5, 1998. (Cited on page: 118)
- [48] K. Gschneider and L. Eyring, eds., *Handbook on the Physics and Chemistry of Rare Earths*, vol. 1: Metal. North Holland, 1979. (Cited on page: 118)
- [49] A.-O. Mandru, O. Yildirim, M. A. Marioni, H. Rohrmann, M. Heigl, O.-T. Ciubotariu, M. Penedo, X. Zhao, M. Albrecht, and H. J. Hug, “Pervasive artifacts revealed from magnetometry measurements of rare earth-transition metal thin films,” *Journal of Vacuum Science & Technology A*, vol. 38, no. 2, 2020. (Cited on page: 118)

5 Single pulse all-optical partial switching in amorphous $\text{Tb}_x\text{Co}_{1-x}$ and $\text{Dy}_x\text{Co}_{1-x}$

When you do some mountaineering ... you sometimes ... want to climb some peak but there is fog everywhere ... you have your map or some other indication where you probably have to go and still you are completely lost in the fog. Then ... all of a sudden you see, quite vaguely in the fog, just a few minute things from which you say, "Oh, this is the rock I want."

Werner Heisenberg

5.1 Background and motivation

In spin electronics, over the last decade, the manipulation of magnetization in thin films without the need for an external magnetic field has garnered significant interest. Traditional approaches rely on external directional stimuli like pulsed magnetic fields or spin-polarized currents, but these methods are limited to timescales of approximately 100 ps [1]. However, the groundbreaking work by Beaupaire *et al.* demonstrated that single ultrafast laser pulses with durations on the order of 100 fs can demagnetize a nickel film in about a picosecond [2]. Building upon this, Ostler *et al.* demonstrated that single-pulse all-optical thermal switching (SP-AOS) in ferrimagnetic amorphous GdFeCo films with an atomic Gd concentration of approximately 25% [3], whereby the magnetization toggles between two oppositely oriented states following each single shot of a femtosecond laser pulse. Subsequent studies extended the observation of SP-AOS to other Gd-based thin film systems [4, 5]. Crystalline $\text{Mn}_2\text{Ru}_x\text{Ga}$ was the first non-Gd based ferrimagnetic films to show this effect [6, 7], where Banerjee *et al.* have shown that re-switching is possible after only 10 ps [8].

Gd^{3+} has 7 4f electrons and is a spherically symmetric ion. a-GdFeCo is ferrimagnetic because of the negative rare-earth (R) transition-metal (T) exchange interaction¹. However, for a-R-T alloys with non-spherical R ions, such as a-TbCo and a-DyCo, the random local electrostatic field created by the environment acts on the non-spherical 4f charge distributions, which creates random local anisotropy. It influences the orientation of R moments. At low temperature, the contribution of R to the ferrimagnetic magnetization is much reduced because the Dy or Tb subnetwork moments are distributed at random in a cone [9].

After the discovery of SP-AOS in a-GdFeCo, a lot of efforts were made to look for this effect in other systems with a different rare earth element, with very little success. Films of a-TbCo were shown to have multi-pulse helicity-dependent AOS when the atomic ration of Tb is about 25% [10, 11, 12]. It was claimed that film thickness and the size of laser spot in relation to domain size are necessary conditions for the effect to occur [11]. A series of a-Gd_{0.22-x}Tb_xCo_{0.78} alloys, from $x = 0$ to 0.18, were demonstrated to exhibit SP-AOS [13]. A study by Liu *et al.* utilized two-wire gold nanoantennas placed on a-Tb_{0.17}Fe_{0.72}Co_{0.11} thin films in order to enhance the near-field of the laser pulse, which helps to reversibly switch single 50 nm domains [14]. Besides,

¹It is worth noting that the prefix 'a-' denotes an amorphous alloy.

SP-AOS in Tb/Co multilayers electrodes in a magnetic tunnel junction was established, but the system studied was not an amorphous alloy [15].

Based on these works, we decided to examine a-Tb_xCo_{1-x} and a-Dy_xCo_{1-x} alloys with x about 0.25 for the appearance of SP-AOS and hints of the effects of local random anisotropy, looking for a better understanding of this phenomenon.

5.2 Methodology

Thin films samples a-Tb_xCo_{1-x} and a-Dy_xCo_{1-x} were made by using the co-sputtering method as described previously. X-ray diffraction was performed to confirm they are amorphous as usual. X-ray reflectivity was used to measure the thickness, roughness and density of main layer and capping layer. The SQUID magnetometer was used to measure magnetization and hysteresis. Both types of films studied here show perpendicular anisotropy. Hysteresis was also measured in our Evico MagneticsTM magneto-optical Kerr (MOKE) microscope in blue light and by anomalous Hall effect. Structural and magnetic information on five representative samples is listed in Table 5.1.

Number	Sample Code	Thickness (nm)	Roughness (nm)	Capping layer	T_{comp} (K)	M_c @ RT (kA/m)	H_c @ RT (mT)
1	HZX210520A_TbCo ₃	20	0.8	Al ₂ O ₃ (1.7 nm)	< RT	240	44.3
2	HZX210520C_TbCo ₄	19.5	0.7	Al ₂ O ₃ (1.7 nm)	20	389	49.6
3	HZX200304A_DyCo ₃	8.8	0.9	Al ₂ O ₃ (3.1 nm)	180	161	52.5
4	HZX201022B_DyCo ₃	10.3	1.2	SiO ₂ (3.3 nm)	180	175	35.0
5	HZX201020A_DyCo ₃	11.6	1.0	SiO ₂ (2.7 nm)	> 320	86.6	90.0

Table 5.1: Characteristics of the representative a-Tb_xCo_{1-x} and a-Dy_xCo_{1-x} samples. Magnetic values are at 296 K except that the number 5 sample was measured at 320 K. Up to 320 K, no magnetization compensation was observed since the Dy target current for this sample is higher than that used for the number 3 and 4 samples. The number 5 sample might have a high compensation temperature or may not be compensated.

For the single-pulse all-optical switching experiments, we used a Ti-sapphire laser seeding a 1 kHz amplifier with a Q-switched cavity. Their central wavelength was 800 nm and the pulse duration was about 200 fs. The laser can be operated in single pulse or pulse train mode at a repetition rate of 1 kHz. We selected samples with reasonable coercivity fields (easily saturated by a hard magnet with a 0.5 T field on the surface) and good perpendicular magnetic anisotropy. Initially, the samples were saturated by a cubic magnet with 0.5 T field on the surface. Subsequently, the sample was mounted onto an XYZ linear translation stage, and the magnet was placed in a safe location away from the sample. Throughout the all-optical switching experiment, no external magnetic field was applied. Finally, laser pulses were emitted. We systematically irradiated different regions of the samples with sequences of one to ten pulses, as depicted in the top figure of Figure 5.1. Additionally, we performed another type of optical experiment by sweeping 1 kHz laser pulses across the sample surface, as illustrated in the bottom figure. The other steps are the same as what described for single-pulse all-optical switching experiment. The experimental set-up is discussed in 5.3.3.

Absolute calibration of the laser fluence is essential for quantitative studies of the light interaction with materials. In this work, a technique known as the Liu method was used to calibrate the laser beam spot size [16]. It is very convenient and accurate to use *in situ*.

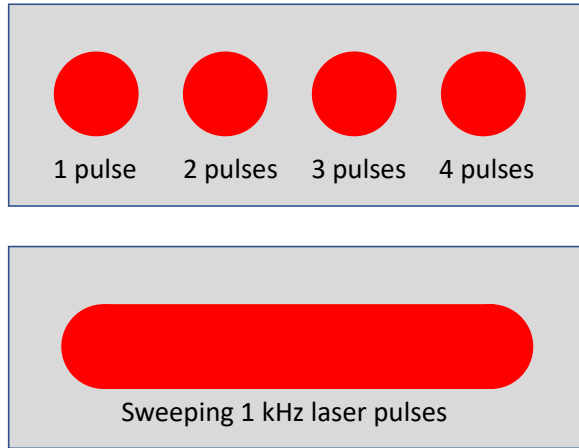


Figure 5.1: Two types of optical switching experiments. Top: single pulse all-optical switching where different regions are shot with different numbers of pulses. Bottom: sweeping the 1 kHz laser pulses across the sample surface.

The main procedure for this is described below:

1. A series of single pulses with increasing pulse fluence was shot onto the saturated thin films. Record the laser fluence for each pulse. The initial sample preparation follows the previously described procedure.
2. Image the switched domains by polar-MOKE. Note that some regions might not show any indication of switching if the laser pulse fluence was lower than the threshold fluence value.
3. Measure the total area within the contour of switched domains. It can be measured either manually using software ImageJ software or by utilizing a Python-based detection program written by myself.
4. Make a table with two columns, the first one for the fluence of the single pulse and the second one for the measured total area.

An example is shown in Figure 5.2. The fluence of single pulse increased from 0.096 μJ to 0.614 μJ and the corresponding total area increased.

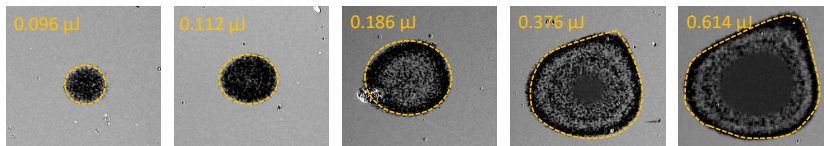


Figure 5.2: Polar MOKE images of switched domains of the a-Dy_{0.25}Co_{0.75} (the number 4 sample) film with increasing pulse fluence from the left to right. The fluences are noted at the top left of each image. The total area is measured manually by using ImageJ within the contour (yellow dashed line).

The data of pulse fluence and the total area within the contour of switched domains is tabulated in the Table 5.2.

The formula used to fit the data is shown below

$$A = A_0 \cdot \ln\left(\frac{E}{E_t}\right) \quad (5.1)$$

where A represents the total area within the contour of switched domains, A_0 is the laser beam spot size within 1/e intensity profile, E refers to the fluence of each single pulse and E_0 is the

Pulse energy (μJ)	Total area (μm^2)
0.096	593
0.112	1074
0.186	2544
0.376	4537
0.614	6309

Table 5.2: Pulse fluence vs total area within the contour of switched domains.

threshold fluence where switched domains become visible. There are two parameters to be fitted, A_0 and E_0 . An example of this is plotted in Figure 5.3 using the data from a-Tb_{0.25}Co_{0.75} (the number 1 sample) thin film. Having the fluence of each pulse and the fitted laser spot size A_0

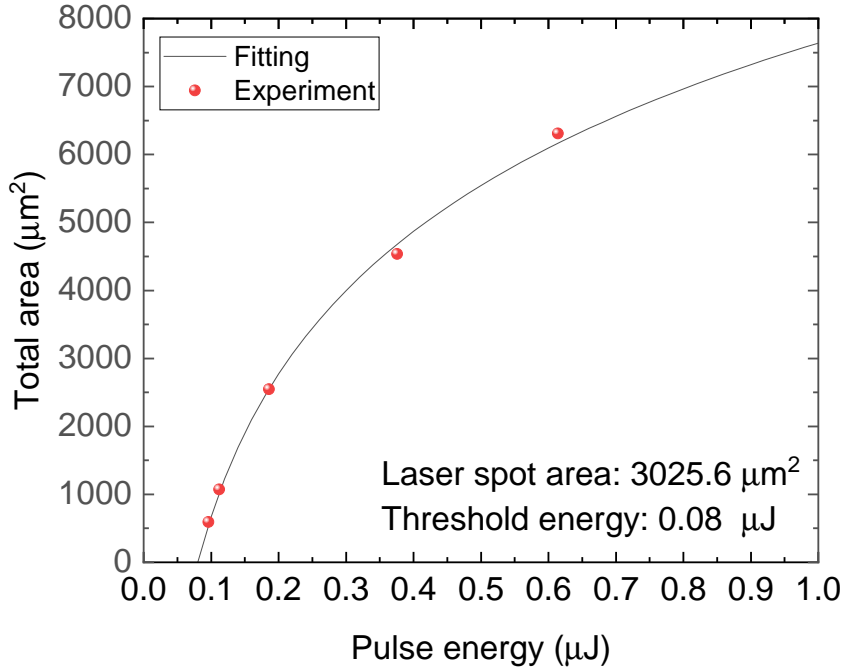


Figure 5.3: Liu method used for calibrating the laser beam spot size. The measured data are depicted in red, following the description provided in the main text. The fitting curve is represented by the black line. The two fitted parameters A_0 and E_0 have values of $3025.6 \mu\text{m}^2$ and $0.08 \mu\text{J}$, respectively.

enables us to know the fluence of each single pulse. Further discussions are given in the following sections.

The X-ray magnetic circular dichroism photoemission electron microscopy (XMCD-XPEEM) experiment was performed at UE49 PGM SPEEM beamline at BESSY II Synchrotron facility in Helmholtz-Zentrum Berlin by Katarzyna Siewierska. At typical working conditions of the microscope the field of view is about 3-10 μm . The spectral range covers extends from 80 to 1800 eV. The absorption of the X-ray beam results in the emission of photoelectrons from the sample which is under the influence of an accelerating voltage of 10 keV between the sample and the objective lens. After passing through a series of projective lenses and a hemi-spherical energy analyzer with an energy resolution less than 0.2 eV, the lateral distribution of secondary electrons is imaged on a screen. Magnetic images are recorded at Co L_3 absorption edge, utilizing the XMCD for left and right circularly polarized X-rays. The resulting contrast is proportional to the scalar product of the local magnetization and the incoming X-ray wave vector, that is, the more parallel the magnetization is to the X-ray wave vector, the brighter the contrast. Since the X-ray

is incident at 16° with respect to the surface, the in-plane components of magnetization has a stronger contrast compared with the out-of-plane component of magnetization. The sample was excited by laser pulses from a Femtolasers Scientific XL Ti:sapphire oscillator set to about 100 fs temporal width. The laser can be operated in single pulse or pulse-train mode at a repetition rate up to 1.25 MHz. A Femtolasers Pulsfinder was used to deliver single laser pulses to the sample. The linearly laser pulses with a central wavelength of 800 nm were sent onto the sample. The laser spot size was $290 \mu\text{m}^2$, with an elliptical shape due to the laser beam's incident angle of about 10° with respect to the surface. The X-ray beam was continuously used for imaging during the delivery of the single laser pulses.

5.3 Results

5.3.1 XRD, XRR and AFM

Figure 5.4 displays the X-ray diffraction measurements, revealing distinct peaks attributed to the silicon substrate, including a broad (002) peak resulting from stacking faults in the Si. By analyzing small angle X-ray reflection, the film thickness and density values were determined.

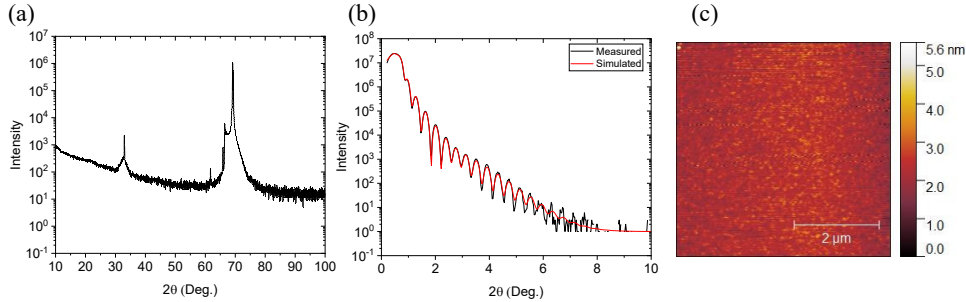


Figure 5.4: (a) X-ray diffraction, (b) x-ray reflectivity, and (c) AFM characterization of the $\text{Tb}_{0.25}\text{Co}_{0.75}$ (sample number 1) film. The area in (c) is $5 \times 5 \mu\text{m}^2$.

5.3.2 MOKE and AHE

The samples used for all-optical switching, preferably exhibit perpendicular magnetic anisotropy. This was checked by using room-temperature hysteresis measured by polar MOKE and anomalous Hall effect as presented in Figure 5.5. They have a coercive field around 50 mT and are easily saturated by a hard magnet. The square loops ensures that the remnant magnetization is close to the saturation magnetization. Those are all desired properties for single pulse all-optical switching experiments.

5.3.3 Single pulse all-optical switching

There are main 4 types of behavior based on the response to different laser fluences as shown in Figure 5.6.

When the fluence is too low, no magnetic contrast could be detected by MOKE. When the fluence was increased to $3.2 \text{ mJ}/\text{cm}^2$, the single-pulse partial all-optical switching occurs as shown in Figure 5.7. A significant portion of the central region did not exhibit switching based on the polar MOKE imaging. However, since the polar MOKE imaging was conducted after the SP-AOS experiment, which typically took more than 10 minutes due to the need to transport the sample to another lab for the polar MOKE measurement, it remains unclear whether these regions might have initially switched but subsequently switched back, or if switching simply did not occur in those regions. Now, after further increasing the fluence of laser pulse to 7.0

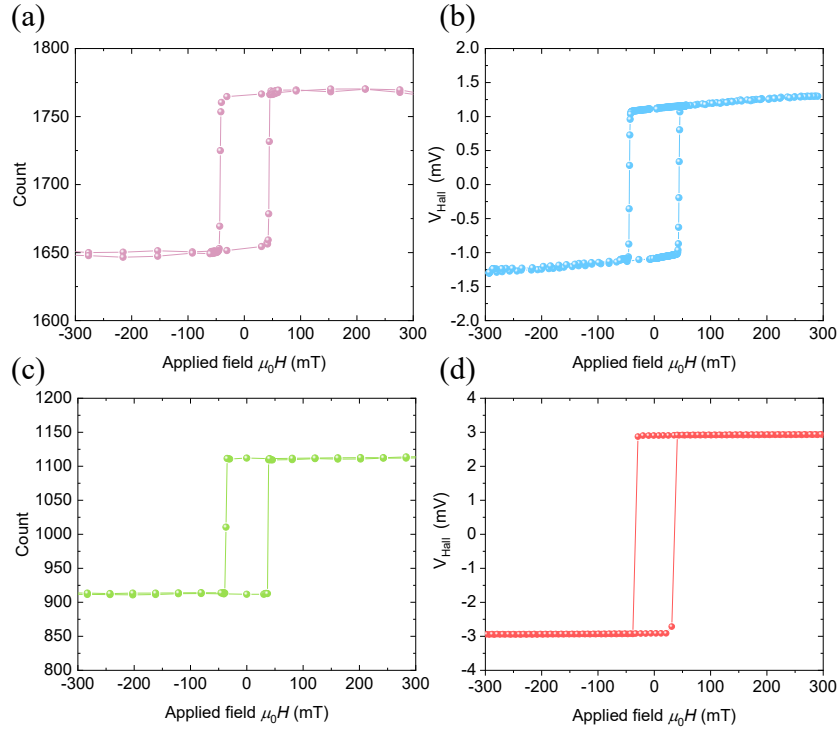


Figure 5.5: Room-temperature hysteresis loops measured for a-Tb_{0.25}Co_{0.75} (the number 1 sample) by polar MOKE in blue light (a) and anomalous Hall effect (b) and for Dy_{0.25}Co_{0.75} (the number 4 sample) (c) and (d).

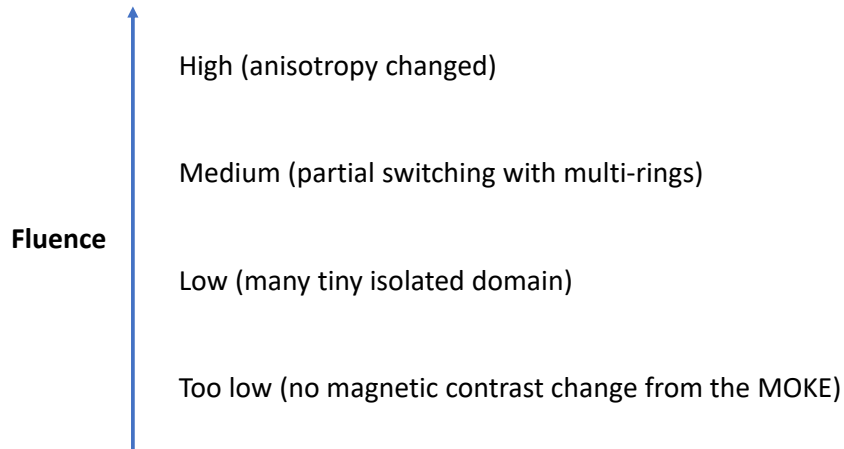


Figure 5.6: Four responses to different laser pulse fluences.

mJ/cm², a new phenomenon occurred, a ringlike domain patterns appeared which can be seen clearly in the first pulse image in Figure 5.8. When the fluence reached 9.3 mJ/cm², the very center part of the laser spot got a different contrast under polar MOKE as shown in Figure 5.9. At first sight, it seemed that it was in demagnetized state since the high fluence might have heated the system up to the Curie temperature. But as will be shown in the discussion section, this is not the case. The anisotropy of that region indeed changed from perpendicular magnetic anisotropy to in-plane anisotropy as proved by combining polar MOKE and pure longitudinal MOKE together. A natural thing to do was to increase the laser fluence further, seeing whether the region of changing anisotropy got bigger or not. It was indeed confirmed to be as expected, as presented in Figure 5.10. From 7.0 mJ/cm² to 14.6 mJ/cm², the region where the change of anisotropy happens gets bigger. This change is permanent, which means that once it occurs, it

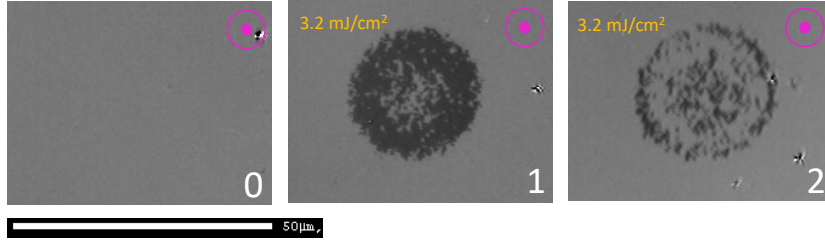


Figure 5.7: Polar MOKE images of films of $\text{Dy}_{0.25}\text{Co}_{0.75}$ after a sequence of 200 fs laser pulses with a fluence of $3.2 \text{ mJ}/\text{cm}^2$. The number of pulses is indicated on the figures. The scale bar is $50 \mu\text{m}$.

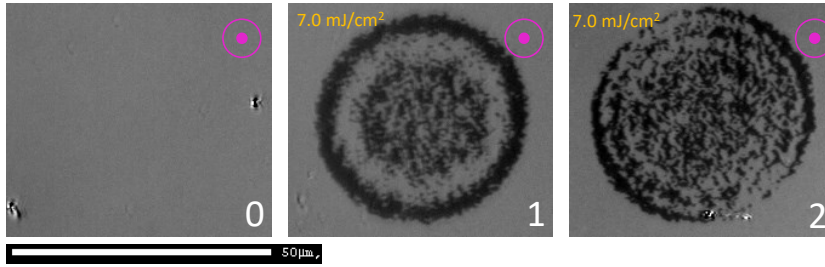


Figure 5.8: Polar MOKE images of films of $\text{Dy}_{0.25}\text{Co}_{0.75}$ (the number 5 sample) after a sequence of 200 fs laser pulses with a fluence of $7.0 \text{ mJ}/\text{cm}^2$. The number of pulses is indicated on the panels. The scale bar is $50 \mu\text{m}$.

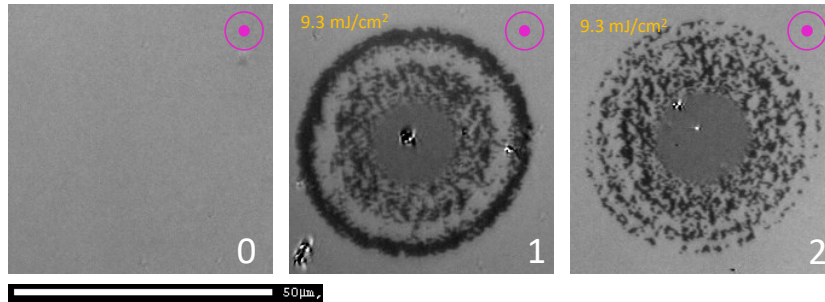


Figure 5.9: Polar MOKE images of films of $\text{Dy}_{0.25}\text{Co}_{0.75}$ (the number 5 sample) after a sequence of 200 fs laser pulses with a fluence of $9.3 \text{ mJ}/\text{cm}^2$. The number of pulses is indicated on the panels. The scale bar is $50 \mu\text{m}$.

is unable to recover back to initial state where anisotropy is along the normal direction of thin film. In a word, it seems that there exist 3 different threshold fluence values for the switching behaviors, appearance of switching, appearance of ringlike domains pattern and appearance of permanent change of anisotropy.

Having talked about the fluence dependence of the ring-like switching behavior, it is helpful to look into switched domains at the low fluence, where no ringlike domain appears, as depicted in Figure 5.11. Those regions were systematically irradiated with with sequences of one to six pulses and then measured in the polar MOKE microscope. After an initial, nearly complete switch with the first pulse, the contrast between subsequent pulse pairs is reduced. The toggle switching was still evident after six pulses, but the differential diminishes with successive shots. A detailed analysis of higher-magnification (12-bit greyscale) images were recorded as shown in Figure 5.12. A biquadratic polynomial is used to flatten the background away from the region of interest. The normalization is performed based on the remnant state of the initial outwardly magnetized film, with an accuracy within 5 %. Histogram distributions of the local normalized

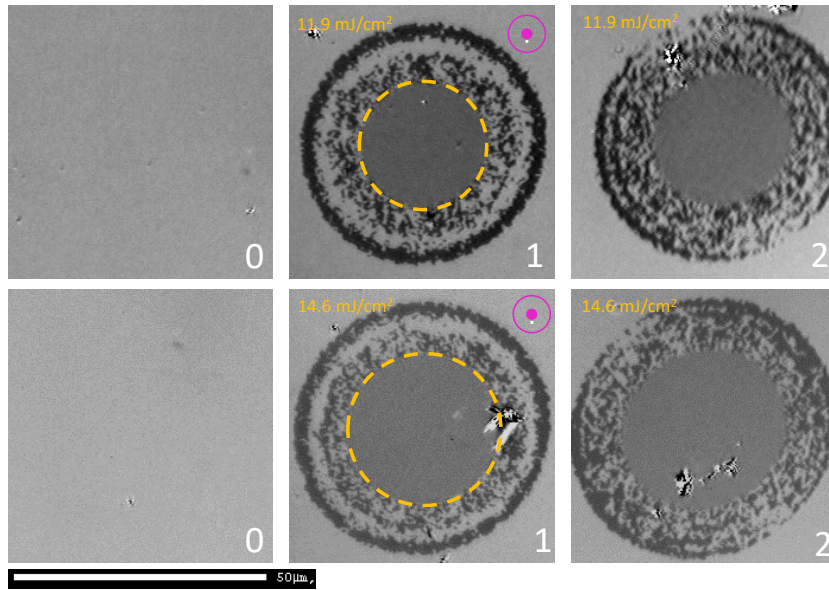


Figure 5.10: Polar MOKE images of films of $\text{Dy}_{0.25}\text{Co}_{0.75}$ (the number 5 sample) after a sequence of 200 fs laser pulses with fluences of 11.9 and 14.6 mJ/cm^2 . The number of pulses is indicated on the panels. The scale bar is 50 μm . The region where anisotropy changes from out-of-plane to in-plane is indicated by a yellow circle.

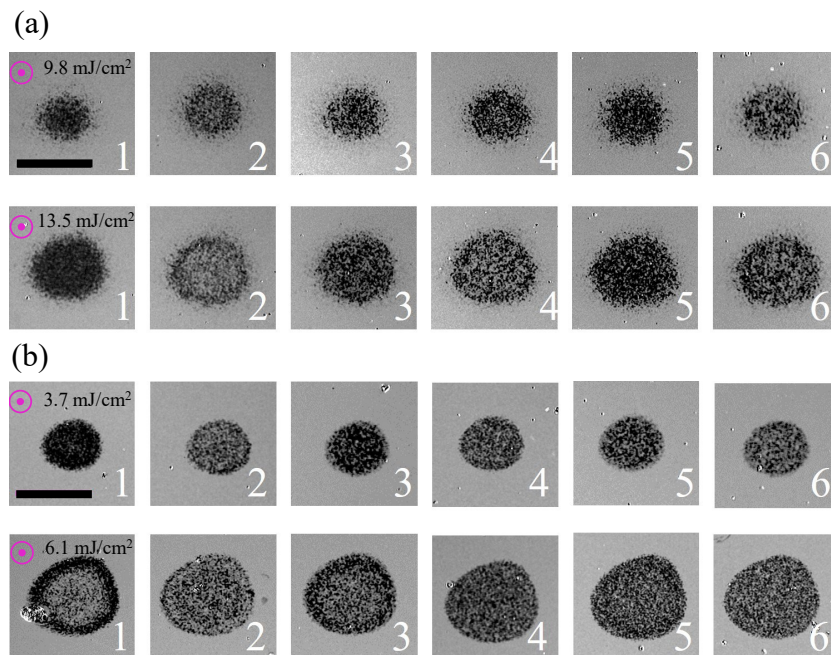


Figure 5.11: Polar MOKE images of films of (a) $\text{a-Tb}_{0.25}\text{Co}_{0.75}$ (the number 1 sample) and (b) $\text{Dy}_{0.25}\text{Co}_{0.75}$ (the number 4 sample) after a sequence of 200 fs laser pulses. The number of pulses is indicated on the panels. The fluences are noted at the beginning of each sequence. The scale bar is 50 μm .

m_z data are constructed from the greyscale distributions within elliptical regions of interest that are fully located within the irradiated spots. Figure 5.12 (b) illustrates the distributions for the undisturbed region (0 shot) and after the first 1-3 shots. The peak of magnetization distribution is shown in Figure 5.12 (c), where the error bars denote the positive and negative half widths

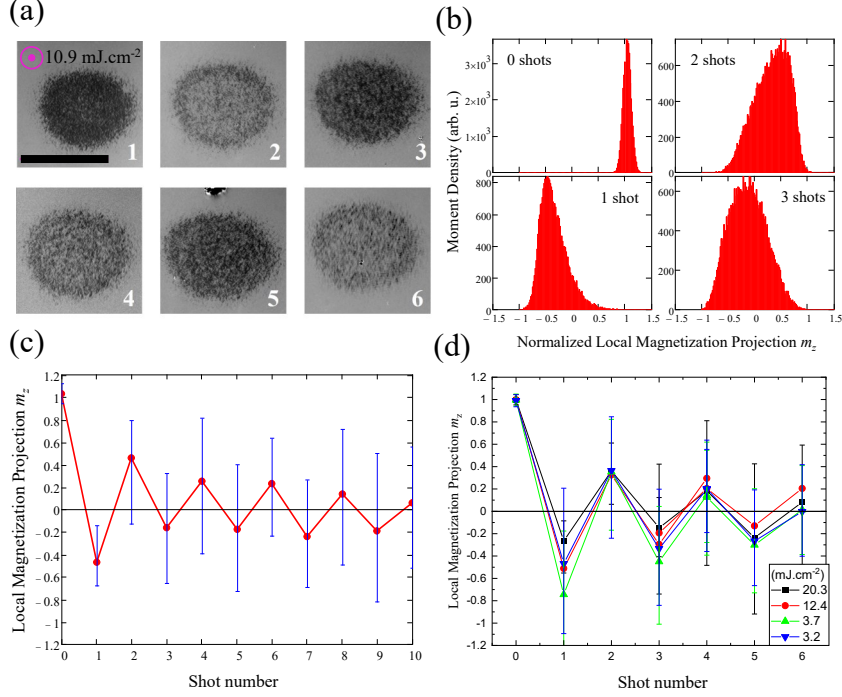


Figure 5.12: (a) MOKE images of a-Tb_{0.25}Co_{0.75} (the number 1 sample) film obtained after a sequence of 200 fs laser pulses. The scale bar is 50 μm . (b) The domain size distribution of the a-Tb_{0.25}Co_{0.75} magnetized film, and after 0–3 pulses (c) The normalized fractions of outwardly or inwardly magnetized domains of a-Tb_{0.25}Co_{0.75} after 0–10 pulses. (d) Switching measured for a-Dy_{0.25}Co_{0.75} (the number 4 sample) film irradiated with different laser fluences.

at half maximum of the distributions. 75 % of the domains are switched by the first pulse and only 10 % is being reversed after ten pulses. The average isolated domain size is $0.7 \pm 0.3 \mu\text{m}$. In Figure 5.12 (d), the switching of a-Dy_{0.25}Co_{0.75} sample with 4 various fluences. In each case, the outmost contour of the switched domains are analyzed, as indicated by yellow dash lines in the Figure 5.2.

5.3.4 XMCD-PEEM

The X-ray absorption spectroscopy (XAS) of a-Dy_{0.25}Co_{0.75} around Co L_{2,3} edge (2p-3d) and Dy M_{4,5} edge (3d-4f) was measured respectively, as plotted in Figure 5.13. For the Co L_{2,3} edge

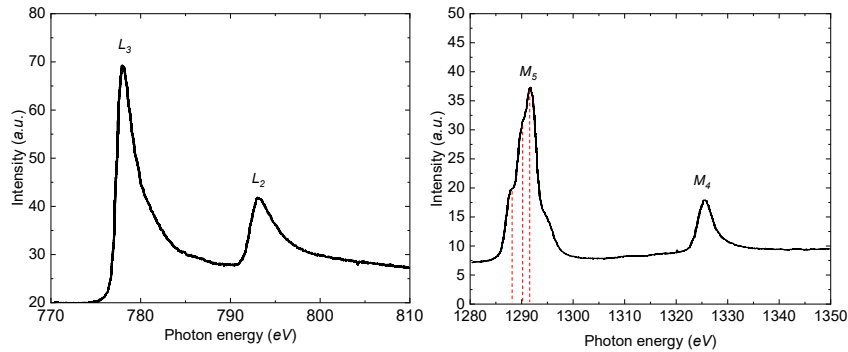


Figure 5.13: Room temperature X-ray absorption spectroscopy (XAS) of a-Dy_{0.25}Co_{0.75} recorded at the Co L_{2,3} edge (left) and Dy M_{4,5} (right) edge respectively. The peaks from the left, marked in red dash lines, correspond to transitions with $\Delta J = +1, 0, -1$, respectively [17, 18, 19].

XAS spectra, the spin-orbit split L_2 and L_3 features are separated by an energy of 15.2 eV. The L_3 main peak occurs at an incident photon energy of 777.9 eV and L_2 main peak is observed at an incident photon energy of 793.1 eV. Regarding the Dy $M_{4,5}$ edge XAS spectra, the spin-orbit split M_4 and M_5 levels are separated by about 33.8 eV. The M_5 main peak is observed at an incident photon energy of 1291.7 eV with additional features at 1287.9 and 1290.1 eV. The M_4 main peak occurs at an incident photon energy of 1325.5 eV. Although XAS spectra contain chemical state information, in our case, it is not possible for us to ascertain whether the Dy rare earth element is oxidized or not in our sample structure. The Dy edges are not affected by oxidation and the oxygen K edges can not be used to distinguish between oxidized Dy and capping layer Al_2O_3 [20].

Figure 5.14 (a)-(c) present the XMCD-PEEM images after 0-2 laser pulses (35.9 mJ/cm^2) at 300 K, respectively². For the 0 pulse, i.e., without any irradiation, the non-uniform contrast is

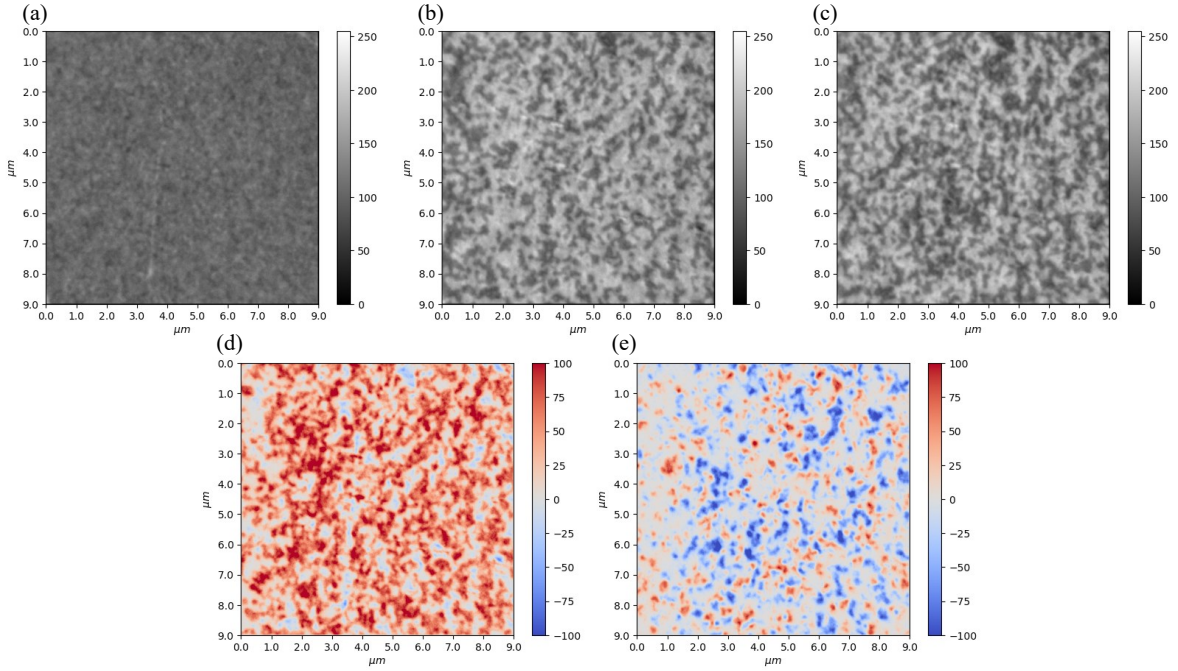


Figure 5.14: XMCD-PEEM image of a-Dy_{0.25}Co_{0.75} (the number 3 sample) film showing single pulse partial all-optical switching at 300 K. (a)-(c) correspond to states after 0-2 pulses with a fluence 35.9 mJ/cm^2 , respectively. (d) displays the difference image obtained by subtracting the image captured after pulse 1 from the image after pulse 0. Similarly, (e) shows the difference image obtained by subtracting the image after pulse 2 from the image after pulse 1. The magnetic images were recorded at Co $L_{2,3}$ absorption edge, exploiting the XMCD for x circularly polarized X-ray. The scale bar is provided in the axis ticks.

attributed to the fact that remnant magnetization is smaller than saturation magnetization after the out-of-plane saturation field is removed. The magnetization loop is shown in Figure 5.15.

A single laser pulse switches most of the magnetic domains, which is consistent with what we observed in the data of last section by blue polar MOKE. Before we discuss the difference images, it is good to clarify the meaning of colorbar first. We assume that the local magnetization pointing up has a higher greylevel in the XMCD-PEEM images such as Figure 5.14 (b), while those pointing down have a lower greylevel. In total, there are four different switching possibilities as listed in Table 5.3. For instance, if the magnetization of a domain points down after $(N - 1)$

²Here, the fluence is much higher than that used in our own lab experiments because of the different reflectivity due to the different incident angles of laser pulses. In our own lab, the incident laser pulse is perpendicular to the sample surface, but in the XMCD-PEEM experiment, the incident angle is only 10° with respect to the surface.

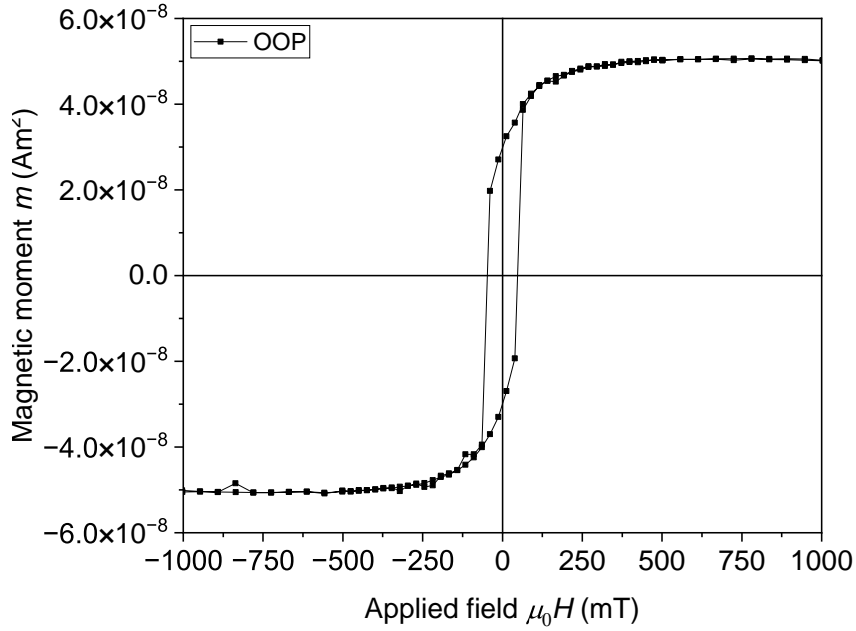


Figure 5.15: Room-temperature magnetization hysteresis measured for the a-Dy_{0.25}Co_{0.75} (the number 3 sample) film used for XMCD-PEEM experiment.

pulses, it can either be switched or unswitched in the N^{th} pulse. If it is switched to point up, it will have a red color in the difference image. If it remained the same, it will have a light red or blue color. Some variation of X-ray intensity or vibration of samples might contribute to the light red or blue even some domains remain unchanged.

Local \mathbf{M} @ (N-1) pulses	Local \mathbf{M} @ N pulses	Change of \mathbf{M}
↓	↑	Deep Red
↑	↓	Deep Blue
↑	↑	Light red or blue
↓	↓	Light red or blue

Table 5.3: Meaning of colorbar in the difference images. Assume that the local magnetization pointing up has a higher greylevel in the XMCD-PEEM images. Switching from down (up) to up (down) will have a deep red (blue) color in the difference image. For those domains with no or little change of magnetization, they will show a light red or blue color in the difference image. Here the symbols \uparrow and \downarrow represent that the local magnetization of domains points up and down in respect to the sample surface, respectively.

Figure 5.14 (d) and (e) further confirm that the observed phenomenon corresponds to single pulse partial switching. Those switched domains are almost connected with each other in the first pulse as seen in Figure 5.14 (d). A second laser pulse is sent to the same sample region³ and the switching pattern changes. By comparing (d) and (e), it can be noticed that some switched regions in the first pulse do not go on switching while other switched regions do switch back in the second pulse. Similarly, some unswitched regions in the first pulse switch while the other unswitched regions remain unswitched in the second pulse. It shows that the switching occurs randomly in the a-Dy_{0.25}Co_{0.75} at 300 K.

The same experiment is executed at a lower temperature of 180 K, close to the magnetization compensation temperature, as shown in Figure 5.16. The laser beam size is 290 μm^2 , much

³In the XMCD-PEEM experiment, the same region of the sample was utilized for a sequence of laser pulses at each temperature. It is different from what we did in our own lab for SP-AOS experiment, as shown in Figure 5.1.

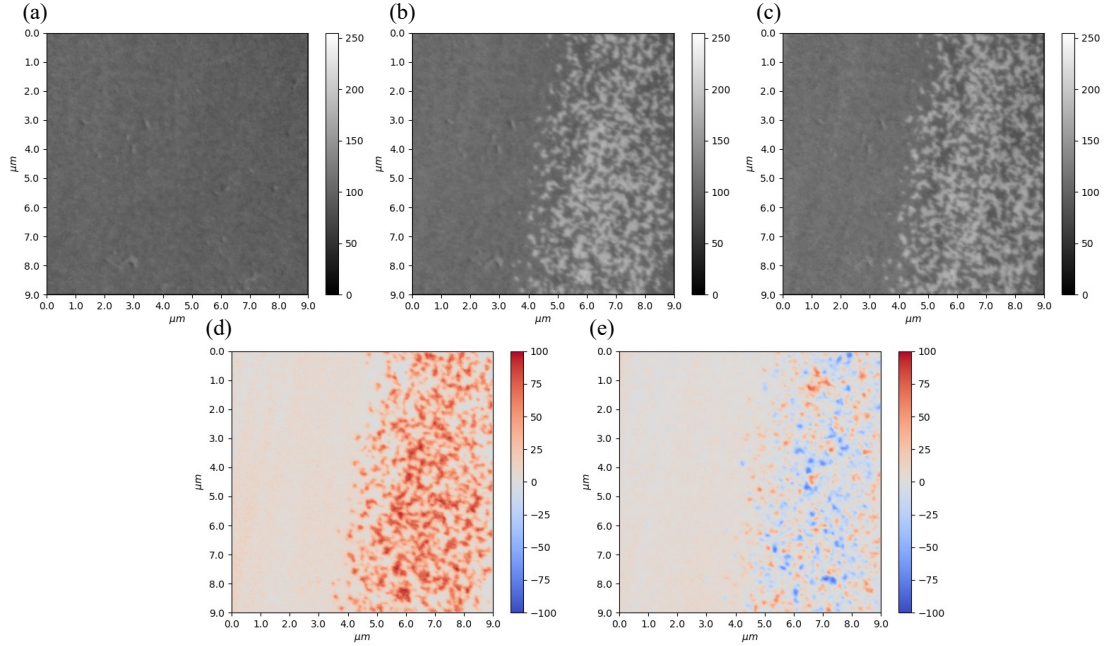


Figure 5.16: XMCD-PEEM image of a-Dy_{0.25}Co_{0.75} (the number 3 sample) film showing single pulse partial all-optical switching at 180 K. (a)-(c) correspond to states after 0-2 pulses with a fluence 35.9 mJ/cm², respectively. (d) displays the difference image obtained by subtracting the image captured after pulse 1 from the image after pulse 0 (no irradiation). Similarly, (e) shows the difference image obtained by subtracting the image after pulse 2 from the image after pulse 1. Magnetic images were recorded at Co L_{2,3} absorption edge, exploiting the XMCD for *x* circularly polarized X-ray. The scale bar is provided in the axis ticks.

bigger than the size of field view about 3 – 10 μm . The XMCD-PEEM is taken around the edge threshold fluence, which accounts for why less than half of the regions experience effective irradiation. Similar behavior is observed.

When the temperature is lowered down to 120 K, almost double the fluence is needed to achieve a similar switching behavior, as illustrated in Figure 5.17. It proves that the single pulse partial switching is possible both above and below the compensation temperature of about 180 K.

5.3.5 Growth of magnetic domains with a swept pulsed laser beam

The phenomenon to be discussed was initially observed due to an accident. The sample was prepared as described previously, firstly being saturated by a cube magnet with a projected field of 0.5 T. After being mounted onto the translation stage, the train of 1 kHz laser pulses was swept across the sample surface along the yellow dash line in order to make a marking point before the SP-APS experiment was done⁴. To our surprise, several very interesting things happened, as illustrated in Figure 5.18. The laser fluence used for this was estimated to be about 8 mJ/cm². The irregular shapes observed in the sample were a direct consequence of manually operating the translation stage to move the sample. As we can see, there are many tiny domains nucleated with size about 1 μm around the yellow dashed line swept path. At the three turning points, denoted by red dashed ellipses, there was a significantly higher number of laser pulse shots since the time spent there was longer. The domains began to grow bigger, with

⁴Just to clarify, while the laser remained fixed, we moved the sample, which was mounted on a translation stage, to achieve a sweeping motion of the laser pulses across the surface. The term 'sweeping train of laser pulses' is used for convenience to describe this process.

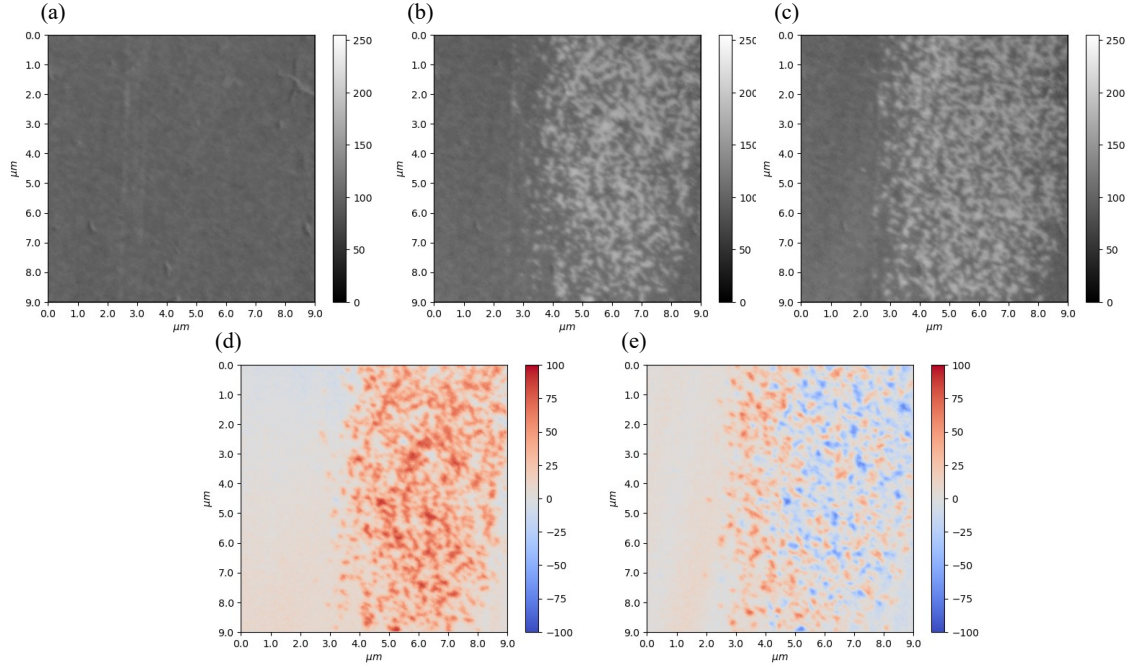


Figure 5.17: XMCD-PEEM image of a-Dy_{0.25}Co_{0.75} (the number 3 sample) film showing single pulse partial all-optical switching at 120 K. (a)-(c) correspond to states after 0-2 pulses with a fluence 69.0 mJ/cm², respectively. (d) displays the difference image obtained by subtracting the image captured after pulse 1 from the image after pulse 0 (no irradiation). Similarly, (e) shows the difference image obtained by subtracting the image after pulse 2 from the image after pulse 1. Magnetic images were recorded at Co L_{2,3} absorption edge, exploiting the XMCD for *x* circularly polarized X-ray. The scale bar is provided in the axis ticks.

size up to about 7 μ m. All linear polarized, right circularly polarized and left circularly polarized 1 kHz laser pulses were executed and the same phenomena were observed, which means that the phenomenon was independent of the polarization of the laser beam. Regarding the outermost left red ellipse region, initial nucleation of tiny domains occurred during the sweeping of the pulsed laser beam. Subsequently, these tiny domains began to grow larger after the laser beam remained there for 2 seconds before being turned off. One might question why the domains closer to the center of the pulsed laser did not exhibit similar behavior. The reason is that they were continuously undergoing switching, as the fluence at that location reached the threshold of SP-AOS. The 200 fs laser pulse did not allow these domains to grow sufficiently.

In order to obtain more details about the sweeping speed effect on magnetic domain growth and size distribution, the same sample, whose result has been shown in Figure 5.18, was mounted onto a programmable translation stage in order to control the sweeping speed accurately. Figure 5.19 shows that a domain size distribution in the lateral direction. Visually, it can be seen that closer to the middle of pulsed laser beam, the domain size appears to be smaller. Additionally, due to the higher fluence of 14.6 mJ/cm², the anisotropy in the middle part of the laser pulsed beam was changed towards to in-plane, as previously mentioned in the SP-AOS results. Since the track is symmetric, it is safe to focus on the top part to do this analysis. Therefore, a detailed image analysis of the region inside the blue box is performed in order to obtain a quantitative investigation on the domain size distribution, as illustrated in Figure 5.20. The image in grey scale was first converted to black-white image (binary image). Fourier analysis is executed to analyze the switched domain sizes at the different locations indicated by the green lines. The bottom two figures are the analysis results corresponding to the top two figures, respectively. It can be seen that, the spatial frequency of the peak in the bottom left figure is smaller than

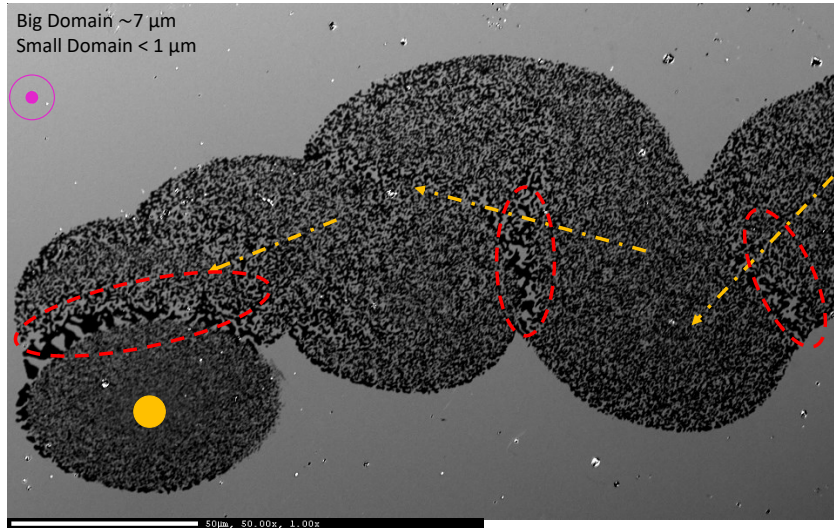


Figure 5.18: The nucleation and growth of magnetic domains was observed by sweeping a 1 kHz pulsed laser beam along the yellow dash line across the surface of the $\text{Dy}_{0.33}\text{Co}_{0.66}$ (the number 5 sample) thin film, which exhibits a magnetization compensation temperature of approximately 350 K, a coercivity of 90 mT at room temperature, and an easy axis of magnetic anisotropy perpendicular to the surface. The laser beam finally stopped at the yellow circle and the time spent there was about 2 seconds. The turning points, where a significantly higher number of laser pulses were concentrated, are indicated by red dashed ellipses. The laser fluence used was estimated to be about $8 \text{ mJ}/\text{cm}^2$.

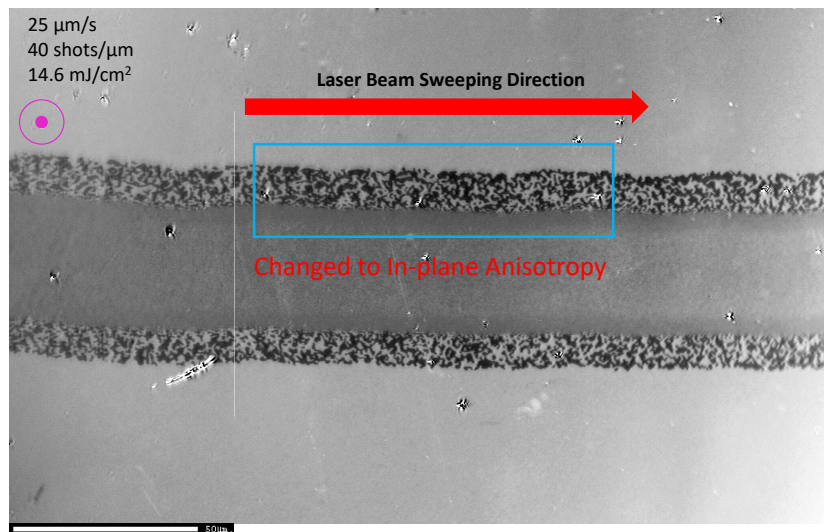


Figure 5.19: A 1 kHz pulsed laser beam with a fluence of $14.6 \text{ mJ}/\text{cm}^2$ was scanned from left to right of the $\text{Dy}_{0.33}\text{Co}_{0.66}$ (the number 5 sample) thin film. The initial magnetization was saturated out of plane, represented by the purple symbol at the top left. The sweeping speed was $25 \text{ μm}/\text{s}$, which is equivalent to 40 laser pulse shots over a distance of 1 μm .

that in the bottom right figure. The smaller the spatial frequency, the bigger the domain size. It means that the region farther away from the pulsed laser beam has bigger magnetic domains. However, the domains were being continuously switched at the region closer to the pulsed laser beam, as explained earlier.

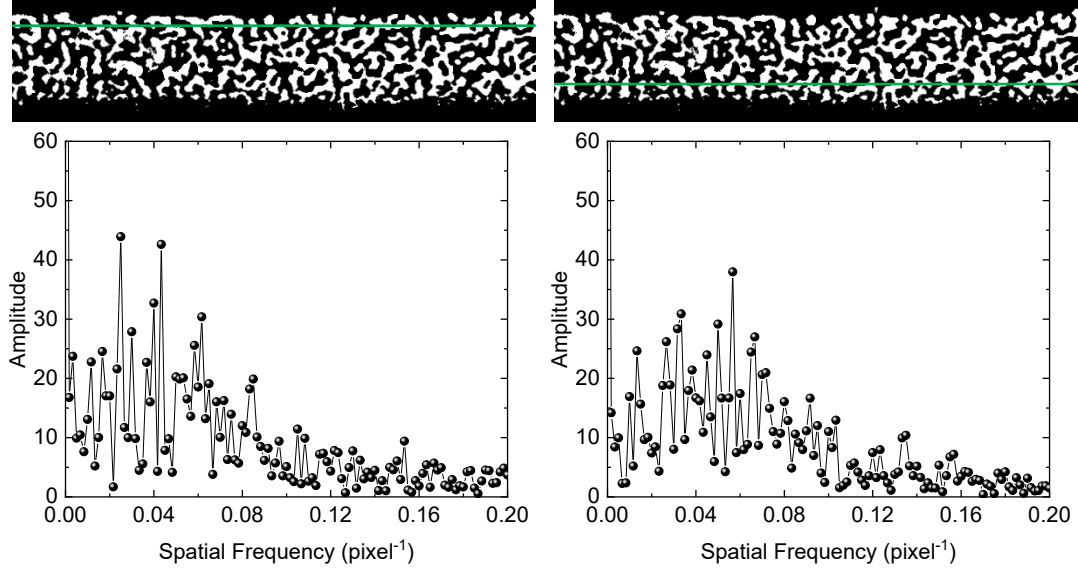


Figure 5.20: Fourier analysis of the binary magnetic domain images of the $\text{Dy}_{0.33}\text{Co}_{0.66}$ (the number 5 sample) thin film. The green lines indicates the locations, where the Fourier analysis is performed. The bottom left image shows the analysis result of the region (further away the sweeping pulsed laser beam) denoted in the top left image, while the bottom right image displays the analysis result of the region (closer to the sweeping pulsed laser beam) denoted in the top right image.

5.4 Discussion

5.4.1 Anisotropy

It is well known that amorphous R-T thin films show a strong perpendicular anisotropy for a certain range of compositions [10]. However, since its discovery in sputtered GdCo films, many different ideas were brought up. One of them is related to the columnar microstructures [21]. But this seems unlikely to be the main reason here since we noticed that many thin films samples $a\text{-Tb}_x\text{Co}_{1-x}$ capped with a layer of Al_2O_3 or SiO_2 about 3 nm thick lost their perpendicular magnetic anisotropy within one or two weeks. The samples were stored at room temperature under normal atmospheric conditions. If the formation of columnar microstructures during thin film deposition is the primary factor, it would not be anticipated that these microstructures would undergo significant changes or relaxation within such a short time scale. In contrast to the microstructure mechanism, a generic source of perpendicular magnetic anisotropy is shown that the magnetic dipolar energy of antiparallel dipoles in the surface layers contributes to the intrinsic uniaxial perpendicular anisotropy [22]. Its idea is very elegant as shown in Figure 5.21. An amorphous R-T film consists of two different kinds of magnetic ions. The exchange integrals are positive for R-R and T-T pairs and negative for R-T pairs. It results in a parallel alignment for the same type of dipoles and an antiparallel alignment for the different types of dipoles. Let us consider the magnetic dipolar energy of antiparallel pairs first, i.e., the R-T pairs, as shown in Figure 5.21 (a) and (b). In Figure 5.21 (a) the dipoles are perpendicular to the bond connecting the atomic centers while in Figure 5.21 (b) the dipoles are parallel or antiparallel the bond. The dipolar interaction energy of two magnetic dipoles \mathbf{m}_i and \mathbf{m}_j separated by \mathbf{r}_{ij} is given by

$$E_{ij} = 1/r_{ij}^3 [\mathbf{m}_i \cdot \mathbf{m}_j - 3/r_{ij}^2 (\mathbf{m}_i \cdot \mathbf{r}_{ij})(\mathbf{m}_j \cdot \mathbf{r}_{ij})] \quad (5.2)$$

The dipolar energy $E_{\perp,ap} = -m_R m_T / (r_R + r_T)^3$ for the case in Figure 5.21 (a) and $E_{\parallel,ap} = 2m_R m_T / (r_R + r_T)^3$ for the case in Figure 5.21 (b), where m_R and m_T are the magnitudes of

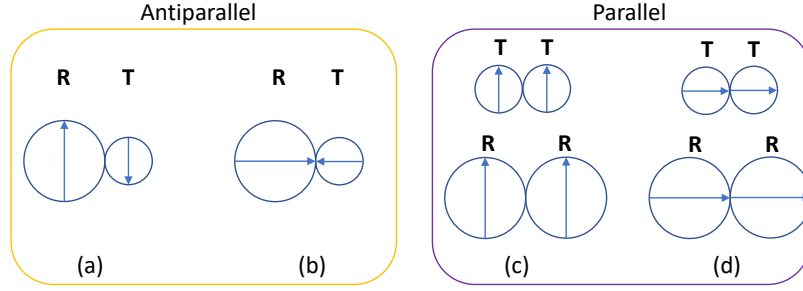


Figure 5.21: Typical magnetic arrangements of dipoles. (a) the two antiparallel dipoles are perpendicular to the bond connecting the atomic centers, (b) the antiparallel dipoles are parallel or antiparallel the bond, (c) the two parallel dipoles are perpendicular to the bond, (d) the two parallel dipoles are parallel or antiparallel the bond. In each case, the direction of dipoles can be reversed together, but this will not change the interaction energy between them.

magnetic moment of R and T respectively. This indicates that antiparallel dipoles prefer the orientation perpendicular to the bond. At the interface between the capping layer and main layer $a\text{-Tb}_x\text{Co}_{1-x}$ or $a\text{-Dy}_x\text{Co}_{1-x}$, there are more in-plane bonds at the surface. Because of this, the antiparallel pairs at the interface tend to orient perpendicularly to the film plane. For the cases in Figure 5.21 (c) and (d), the dipole interaction energies are $E_{\perp,p} = m_i^2/r_i^3$ and $E_{\parallel,p} = -2m_i^2/r_i^3$ where $i = R, T$. They tend to orient in the plane, giving a negative contributions to perpendicular anisotropy. However, we should expect that R and T should tend to mix with each other since there a lot of compounds in their binary phase diagrams such as Tb-Co and Dy-Co. The number of R-R and T-T pairs should be much fewer than that of R-T pairs. The contribution from R-T should play a dominant role, which helps to build up the perpendicular magnetic anisotropy.

Another fact helps to support this idea is illustrated in Figure 5.22. This image was taken by a normal optical microscope with unpolarized light, which means there is no magneto-optics effects like Kerr effect here. The green regions were the marking points, over which the laser beam was swept with 1 kHz frequency. The time interval is about 1 s so about few thousand pulses landed there. A huge amount of heat was produced there. The rare earth elements are very sensitive to oxygen and can easily be oxidized.

Therefore, one possible explanation for the green color is the oxidation of the rare earth element Dy. If looking at it closely and carefully, contrast can be seen for the spots indicated by red arrows. Those spots were shot by laser pulses with increasing numbers from the left to right. The contrast increases with increasing pulse numbers but still much weaker than that in the marking region, since the pulse numbers are much smaller. The contrast is attributed to the change of reflectivity of those irradiated spots. The oxidation of Dy is again one possible reason. In a previous study, it was reported that the oxygen K-edge was detected in the region where a single pulse of about 120 mJ/cm^2 was applied deliberately [23]. In that work, Ta(1nm)/Ru(1nm) were used as a capping layer. They speculated that the oxygen peak originated mainly from oxidized capping layers. Besides, they also checked the region after 1,000,000 pulses of $10\text{-}25 \text{ mJ/cm}^2$ but no change in the electronic states of oxygen was found. In our case, Al_2O_3 or SiO_2 were used, the capping layer seems to play an important role for the different behavior. A further comprehensive investigation is needed.

The oxidation of the rare earth element in the top layer can reduce the pair number of R-T, therefore the perpendicular magnetic anisotropy is much reduced or even disappears based on the argument given above. It was reported that the perpendicular anisotropy was destroyed by 1 – 2 at. % oxygen [24]. The reduction of perpendicular anisotropy in regions under irradiation was indeed confirmed by measuring the hysteresis loops from longitudinal and polar MOKE

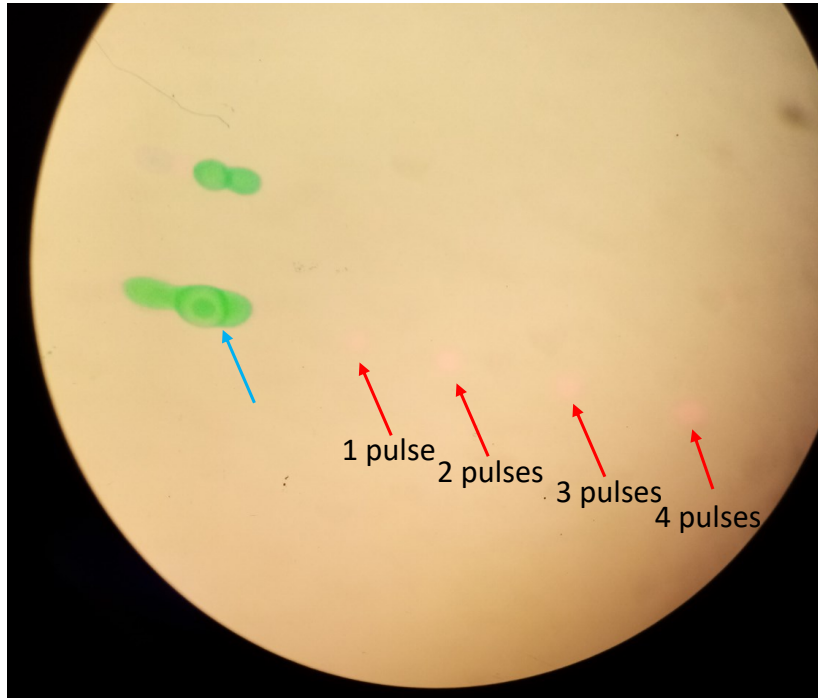


Figure 5.22: Optical microscope images of $a\text{-Dy}_{0.25}\text{Co}_{0.75}$ (sample number 3) thin film after SP-AOS experiment. The blue arrow indicates the marking points, representing the beginning of the SP-AOS experiment. The four red arrows indicate the 4 different spots after being shot with increasing number of laser pulses from the left to right.

magnetometry, as presented in Figure 5.23. The figure on the left shows a hysteresis loop measured by polar MOKE of an unirradiated region. The squareness of the loop clearly shows the perpendicular magnetic anisotropy of this thin film sample. For a region after irradiation of a single pulse, the anisotropy is clearly changed towards to in-plane as shown by the middle and right figures, measured by polar MOKE and pure longitudinal MOKE respectively.

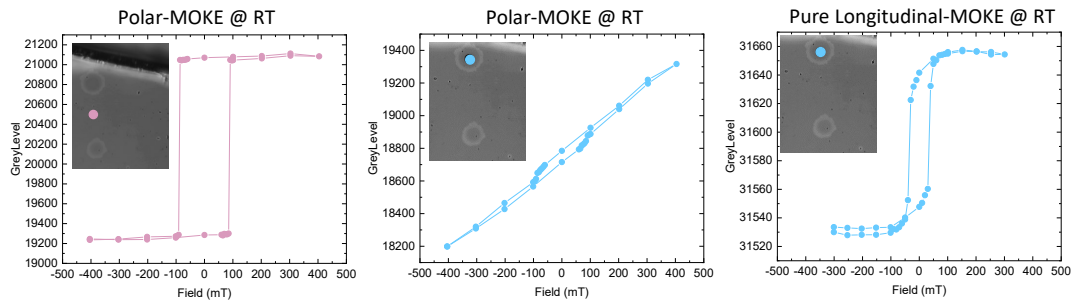


Figure 5.23: Room-temperature hysteresis loops measured by MOKE for the unirradiated and irradiated regions of the $a\text{-DyCo}_3$ (the number 5 sample) thin film sample. **Left:** polar MOKE hysteresis loop of an unirradiated region. **Middle:** polar MOKE hysteresis loop of the irradiated region after a single laser pulse. **Right:** pure longitudinal MOKE hysteresis loop of the same region measured by the middle figure. The inserted pictures show the locations where each hysteresis loop was measured, indicated by the small colored circles.

5.4.2 Optical control of coercivity

As we described previously, above a certain fluence threshold, the anisotropy changes towards in-plane. Besides that, the femtosecond laser pulses also modify the coercivity field locally as seen from the difference longitudinal MOKE images in Figure 5.24. The central irradiated part has a smaller coercivity field than that of the middle irradiated part, which is why the central part undergoes a change in contrast first during the field sweeping. This can be observed

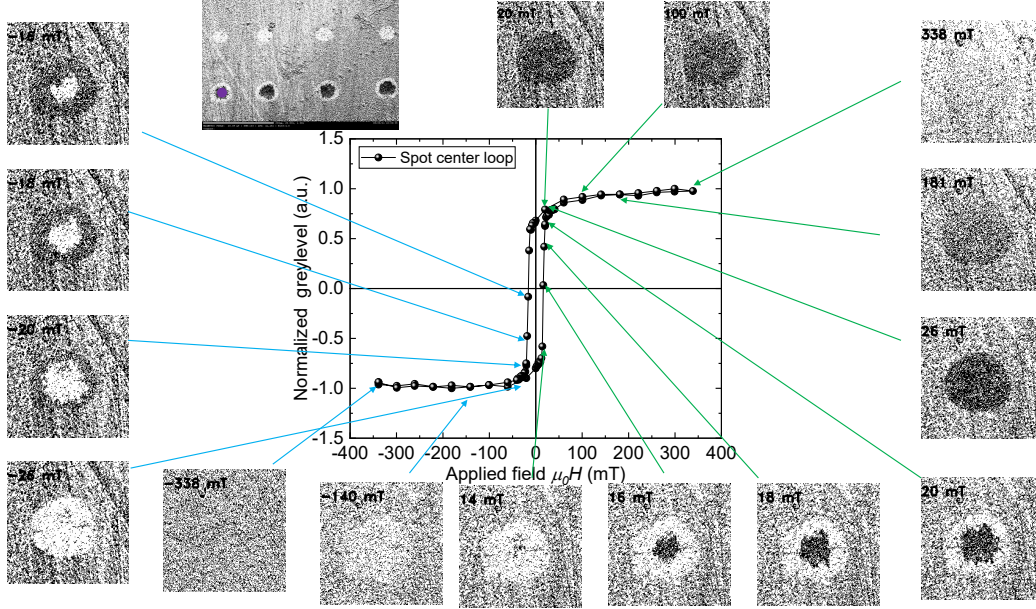


Figure 5.24: Room-temperature longitudinal MOKE hysteresis loop of irradiated spot center (indicated by the purple circle on the top left figure) of the a-DyCo₃ (the number 3 sample) thin film along with simultaneous recordings of magnetic domain structure evolution during the hysteresis loop. Blue and green arrows are referring to the magnetic states when fields are negative and positive, respectively.

more clearly by plotting the longitudinal MOKE hysteresis loop at different portions of the irradiated region after the first pulse, as illustrated in Figure 5.25. The difference in H_c between the irradiated spot center and irradiated spot middle region is 6 mT. The difference increases slightly to 7.5 mT for the 3-pulse spot, whose data is not shown here. We also swept the laser beam across the sample surface, like we did in Figure 5.19 and managed to create a strip with in-plane anisotropy within a surroundings that still exhibits perpendicular magnetic anisotropy as shown in Figure 5.26. Based on our preliminary study, it appears that the modification of H_c , following the femtosecond laser pulse with lower fluence, also occurs in the sample that still exhibits perpendicular magnetic anisotropy. More work is needed to explore the optical control of coercivity field locally by using different features of the femtosecond laser pulse, such as the helicity, fluence and number of pulses. Compared to electron or ion irradiation, using femtosecond laser pulses to modify magnetic properties offers the advantage of being achievable at ambient pressure and room temperature, with a promising application in magnetic logic [25]. Recently, a work on patterning nucleation area in exchange-coupled systems was published [26], where they managed to change the exchange bias field by femtosecond laser pulses.

5.4.3 Single pulse partial switching

The single pulse all-optical switching that we observe in low fluence as shown in Figure 5.7, Figure 5.11 and Figure 5.12, differs from that in a-GdFeCo and crystalline Mn₂Ru_xGa, where switched regions are uniform and well-defined. The nanoscale granularity of the switched areas

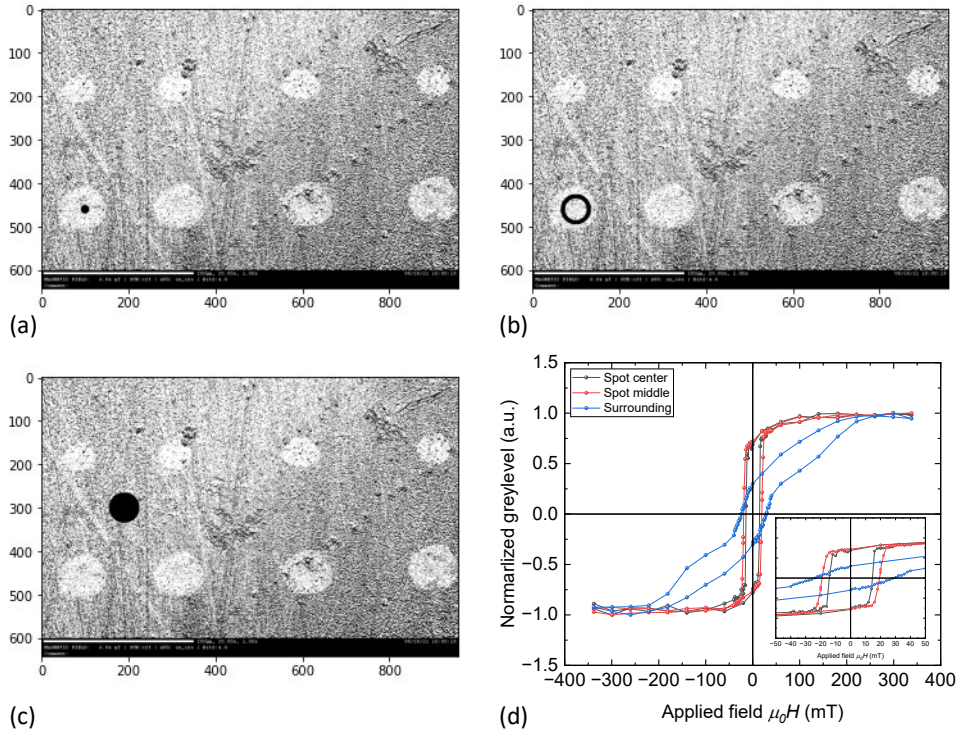


Figure 5.25: Comparison of room-temperature longitudinal MOKE hysteresis loops between irradiated and unirradiated regions after the first pulse of the a -DyCo₃ (the number 3 sample) thin film. (a) corresponds to the region for plotting the irradiated spot center loop. (b) corresponds to the region for plotting the irradiated spot middle loop. (c) corresponds to the region for plotting the unirradiated surrounding region loop. (d) displays room-temperature longitudinal MOKE hysteresis loops of the regions indicated by (a)-(c) with a inserted zoom-in plot.

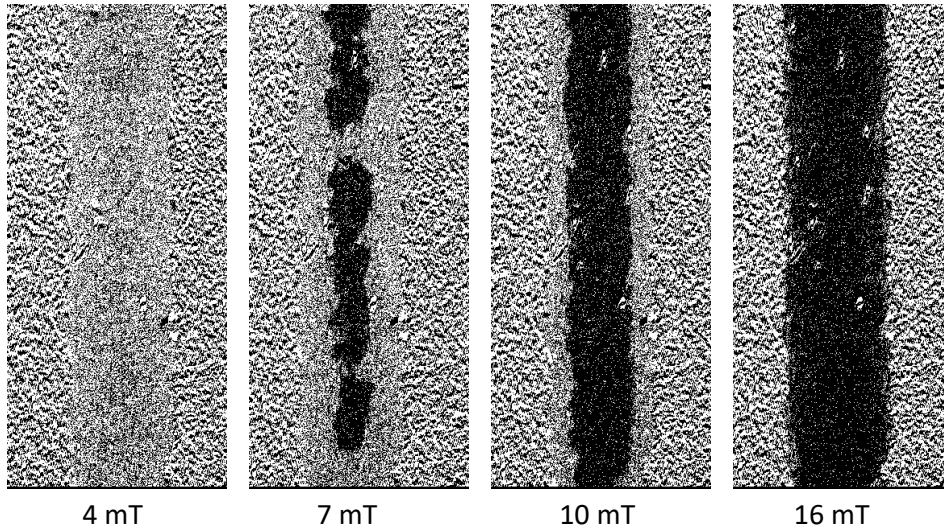


Figure 5.26: A strip with in-plane anisotropy within a surroundings that still exhibits perpendicular magnetic anisotropy in the a -DyCo₃ (the number 4 sample) thin film. MOKE images were recorded in the longitudinal configuration.

in a -Dy_{0.25}Co_{0.75} and a -Tb_{0.25}Co_{0.75} is very evident around the boundaries of the spot, where the fluence is close to the threshold and the smallest switched domain size is about 100 – 200 nm, found in the XMCD-PEEM images. Only one study performed by Liu *et al.* using

nanoscale antennas reported that SP-AOS of a 50 nm single domains, smaller than what we found, is possible. Regarding the XMCD-PEEM images, there is one thing that needs mentioning here. Since the incident angle of X-ray beam is 16° with respect to the surface, both in-plane and out-of-plane components of magnetization are probed at the same time, but with different contributions. As explained in the methodology part, the in-plane one has a bigger contribution. Ideally, a sample with well-defined perpendicular magnetic anisotropy should be used for the XMCD-PEEM experiments. But at that time, the best available sample was the one shown in Figure 5.15, having a non-square magnetic hysteresis loop. It simply means that the sample used has an in-plane component at its remnant magnetization state, at which the single pulse all-optical switching and XMCD-PEEM experiments are done. The in-plane component of remnant magnetization is about 30 %. At the same time, the in-plane component of magnetization has a bigger contribution to XMCD-PEEM signal, about 80 %. It was demonstrated that arrays of 2 μm diameter disks of $\text{Gd}_{0.25}\text{Fe}_{0.656}\text{Co}_{0.094}$, with magnetization lying either in-plane or out-of-plane, were able to show single pulse all-optical switching [3]. Thus, it is reasonable to infer that something similar happens in our system. In the difference images of XMCD-PEEM data, the strong contrasts in deep blue and red corresponds to either the switching of perpendicular magnetization or that of magnetization pointing in-plane.

We take the established mechanism for SP-AOS in a-GdFeCo as a basis for the discussion of a-TbCo and a-DyCo. Radu *et al.* performed ultrafast spin dynamic measurements in magnetic alloys containing Fe, Co, Ni, Gd, and Dy and found the change in demagnetization time with atomic magnetic moment was $90 \pm 10 \text{ fs}/\mu_B$ [27]. Therefore, the small atomic moment of Co is destroyed in less than 200 fs, but Dy or Tb will take much longer to demagnetize. It means that when Co loses its magnetic moment completely, the rare earth element still has some momentum left. The angular momentum of the RE could be transferred to Co, which helps Co re-order parallel to the average rare earth moment. This produces, in the regions where the z -projection (along the normal to the sample surface) of rare earth moment is high enough, the transient ferromagnetic alignment that is crucial for SP-AOS⁵. The restored Co subnetwork can now exert an exchange interaction on the disordered, but strongly correlated rare earth atomic moments and favor the switching of rare earth atomic moments. At some points, before the accomplishment of the switching process, the rare-earth anisotropy imposes a new wandering axis on the switched ferrimagnetism at some point.

Finally, there is one final point. It seems that although the spot center where the anisotropy changes toward to in-plane, the the z -component switching of magnetization is still going on to some extent, as shown in Figure 5.27 measured by polar MOKE in blue light. It is almost invisible by eye directly. We plot the histogram of intensity of the spot centers of 1 pulse and 2 pulses individually and then compare them. The shift of the peak intensity is clearly observed. We checked this to a maximal pulse number of 10 and this behavior shows up very stably. Does it mean in these system that the sample with in-plane anisotropy has a more stable SP-AOS? We cannot confidently assert this conclusion at this time. All previous experimental work focused on samples exhibiting strong perpendicular magnetic anisotropy, except few studies performed on in-plane magnetized samples. In 2012, as demonstrated by Ostler *et al.* an a-GdFeCo with in-plane anisotropy is able to be switched by a single laser pulse [3]. Very recently, a pre-print manuscript on single laser pulse induced magnetization switching in in-plane magnetized a-GdCo alloys has appeared [28]. The samples they used have a well-defined in-plane anisotropy by fixing the sample holder in a specific direction without rotating the holder during deposition. There exist in-plane easy axis and in-plane hard axis directions that are perpendicular to each other. They demonstrate deterministic all-optical helicity-independent switching across a wider concentration range 10% to 25% of Gd and a thickness up to 30 nm, compared with the perpendicularly magnetized a-GdCo. The absence of a perpendicular demagnetization field,

⁵In the a-TbCo and a-DyCo systems, there is a cone angle between the distribution of magnetic moments of Dy or Tb. If the z -projection of rare earth moment is not big enough, the SP-AOS will not occur.

which tends to break the magnetization into multi-domains, is thought to be responsible for this phenomenon. In contrast, an in-plane magnetized thin film does not experience a strong demagnetized field that would induce a multi-domains state. In our case, the conditions were different. First, there is no easy axis direction for the in-plane anisotropy since it is induced by laser pulse with cylindrical symmetry. Second, we are measuring the out-of-plane component of the magnetization. Further work is needed to clarify the laser-induced switching mechanism for those samples with in-plane anisotropy, either created during deposition or indeed, induced by the laser pulse.

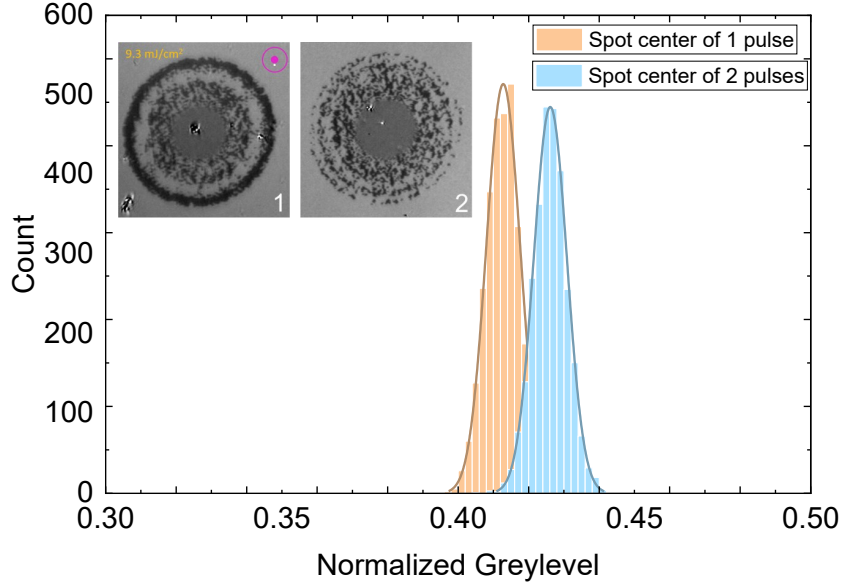


Figure 5.27: Histogram of intensity of the spot center of 1 and 2 pulses, measured by polar MOKE in blue light. The greylevel is normalized.

5.4.4 Ringlike-domain patterns

The appearance of ringlike-domain patterns is clearly observed, especially for the first pulse with a fluence $7.0 - 14.6 \text{ mJ/cm}^2$. It becomes less obvious with increasing pulse numbers, which is attributed to the fact that at the same time, the single pulse partial switching is happening. The biggest difference between the first and other other pulses is the different magnetic state. Before the first pulse is shot, the sample is in remnant magnetization state, where magnetization is almost along out-of-plane direction. The whole sample can be seen at a single magnetic domain state. But after the first pulse, many isolated domains are present and scattered throughout. As we see from the XMCD-PEEM data, they switch randomly. The randomness of this makes the ringlike-domain pattern less obvious when the number of pulses becomes bigger. The phenomenon of ringlike-domains is interesting by itself. We give some thoughts here on the possible mechanisms. The magnetization precession is one possibility. To be clear at the start, we did not apply any external field, in-plane or out-of-plane, during the experiment. The experimental condition was different from those in previous work on ferrites [29]. So for this explanation to be possible, we need to find a source for the dominant effective in-plane field, which helps to enable magnetization precession. There are two main ingredients at play here. First, the dominance of an effective in-plane field, which requires a decrease of the original perpendicular magnetic anisotropy and a increase of the effective in-plane anisotropy in a certain way. Second, the magnetization should still be non-zero.

The high fluence seems to be a key for the formation of ringlike-domain. Therefore, we

mainly focus on the heating effect, since most of the laser pulse energy is absorbed by the metallic thin film system. The temperature will increase locally at the beginning and then dissipate. Both magnetization and anisotropy will decrease since the experiment is performed at room temperature and the magnetization compensation temperature is smaller than 200 K. However, the a-R-T thin films have different temperature dependence of magnetization and anisotropy, as reported by Hansen *et al.* [30], which shows that when x is about 0.3, the decrease of anisotropy is more rapid than that of magnetization in the temperature heats up from 300 K to 400 K. This provides the possibility that the heating due to laser pulses might destroy the perpendicular magnetic anisotropy but some non-zero magnetization may remain. One particular and interesting point is that, they compared a-Gd_{0.24}Tb_{0.04}Fe_{0.72} with a-Tb_{0.30}Fe_{0.70} and found that the former one has a much smaller slope in the temperature dependence of anisotropy⁶. Now we only need to find a source for the in-plane anisotropy, which acts like a in-plane magnetic field to help to achieve magnetization precession. This idea is inspired by a work done by Shinya *et al.* in 2016 [31]. They sputtered 6 nm a-TbFeCo alloy thin film with a 4 nm Pt underlayer and a 4 nm Pt capping layer onto a flexible substrate, a 50 μm thick Polyethylene naphthalate. A in-plane uniaxial tensile strain was reversibly applied up to 2 % and the magnetic anisotropy was reversibly switched between in-plane and out-of-plane. We think something similar is happening in our case. The laser pulse has a Gaussian beam profile. Around the boundary of laser spot, there is a region between the very hot center and the surroundings with little or no irradiation. The thermal gradient helps to build a tension, which induces a in-plane anisotropy⁷. It acts like an effective in-plane field, around which the magnetization precesses. After sufficient thermal dissipation, the tension disappears and hence the in-plane \mathbf{H}_{in} disappears as well. At the same time, the perpendicular magnetic anisotropy recovers since the temperature cools back to 300 K. If the magnetization has precessed for an odd (even) number of half-periods, the domains are switched (unswitched). The whole process is illustrated in Figure 5.28. At a higher fluence, oxidation is very likely and the properties of the thin films change dramatically, as we showed previously. Hence switching becomes impossible. At lower fluence but still above switching threshold, not enough energy is deposited there and no tension is built, the magnetization precession is not possible and only single pulse partial switching occurs. After we presented our ringlike-domains works to others at the international conferences, more attention was given to this phenomenon although still more attention is given to single pulse all-optical switching [33, 34]. In their cases, the samples are synthetic multilayers. A study done by A.Kirilyuk's group discusses the different switching behavior in Tb/Co multilayers and amorphous TbCo alloy thin films [35]. In addition, they also observed ringlike-domain but it is a transient phenomenon, which collapsed to a homogeneously reversed state after about 100 ps. They gave a possible explanation of the origin of the effective in-plane field, different from ours. They measured the temperature dependence of the in-plane and out-of-plane magnetic components from 300 K to 375 K and noticed that in-plane hysteresis loops became squarer in shape and out-of-plane hysteresis became less squar. The appearance of in-plane anisotropy provided the in-plane effective magnetic field about which the magnetization precessed. Very recently, a study on [Tb/Fe]₄ and [Tb/Co]₅ multilayers showed concentric ring domain structures in single pulse switching experiments and the authors claimed that a precessional reversal mechanism could explain [36]. Interestingly, another work on quad-layer Co/Gd/Co/Gd synthetic ferrimagnetic thin film confirms the resilience of this material system against the in-plane strain in the order of 0.1% [37]. It will be interesting to see whether externally applied in-plane strain can change

⁶The reason why we mention this is the following. At the 2022 5th Ultrafast Magnetism Conference in Nancy, this kind of ringlike-domains were not observed in a-GdFeCo or a-GdCo systems, which were both studied a lot in the last decade. Based on our idea about the possible mechanism, the slower decrease of anisotropy in a-GdCo and a-GdFeCo as a function of temperature might be the reason for the absence of ringlike-domains switching.

⁷It was reported that, in the ferromagnetic ErFeO₃ system, the magnetization flip does not occur around the peak of THz excitation at the spot center but rather occurs at approximately the peak of the intensity gradient profile [32].

the switching patterns even in the multi-layer synthetic ferrimagnetic thin films.

The understanding of the ringlike-domain pattern in our alloy thin films remains incomplete. Some future work could be done in order to look for a complete explanation for the ringlike-domains.

- Apply in-plane field during single pulse all-optical experiment to see how the in-plane field will influence the switched ringlike-domains or not.
- Grow the a-TbCo and a-DyCo on some flexible substrates such as polyethylene naphthalate and apply stress to see whether it will influence the switching patterns or not. Alternatively, ultra-thin Si substrates may be bent, since the Si substrate is more widely used.
- Perform single-shot time-resolved imaging to see the switching dynamics not only the final state.

5.4.5 Growth of magnetic domains

Similar to the results shown in section 5.3.5, the nucleation and growth of magnetic domains are promoted by the 1 kHz femtosecond laser pulses. By comparing with the earlier experimental results of a-TbCo system in helicity-dependent magnetic switching [38], some differences can be spotted, as listed in Table 5.4. Those distinguishing characteristics can be identified by comparing those two sets of data side by side. Two points need to be emphasized here. First, we use different substrates and buffers, and cappings layers. In reference [38], the sample structure is glass/Ta(4nm)/DyCo/Ta(4nm), instead of Si/SiO₂(500 nm)/DyCo/SiO₂(3nm) in our case. Notably, the metallic Ta layer is known to possess superior properties for absorbing and dissipating heat compared to SiO₂. Second, in the case of the citation [38], the laser beam is swept at a constant rate 3 – 20 $\mu\text{m}\cdot\text{s}^{-1}$ with laser spot size about 80 μm but the fluence value is not explicitly provided. In our case, we have a sweeping rate 25 $\mu\text{m}\cdot\text{s}^{-1}$, similar spot size and a fluence 14.6 mJ/cm^2 . Initially, We did attempt to repeat the helicity-dependent magnetic switching by adjusting laser fluence and sweeping speed, but we were unable to achieve the same results, possibly due to the differences in sample structure, as previously mentioned.

	Our result	Reference [38]
Alternating Domains	Yes	No
Domain boundary plays a role	Yes	No
Helicity independent	Yes	No
Heat accumulation	Yes	No

Table 5.4: Comparisons between our results and those in the case of the citation [38] on the a-TbCo system.

5.4.6 Aging effects on the magnetic properties

For some of a-Tb_xCo_{1-x} thin films we fabricated, over the course of few months, the magnetic properties and characterizations, such as magnetization loops, change significantly. For the a-Dy_xCo_{1-x} thin films, their magnetic properties could survive for more than one year. The aging problem for the amorphous rare-earth transition metal alloy thin films is generic. A wealth of valuable references regarding the aging problem in these systems can be found in a recent publication *et al.* [39]. Several factors are thought to give rise to changing magnetic properties over time, like the capping layer, compositional inhomogenetites at the nanoscale, and thermodynamically driven intermixing. In the same paper, the authors extensively discuss the aging effects in synthetic bilayer Co/Gd ferrimagnets. In summary, aging effects should be

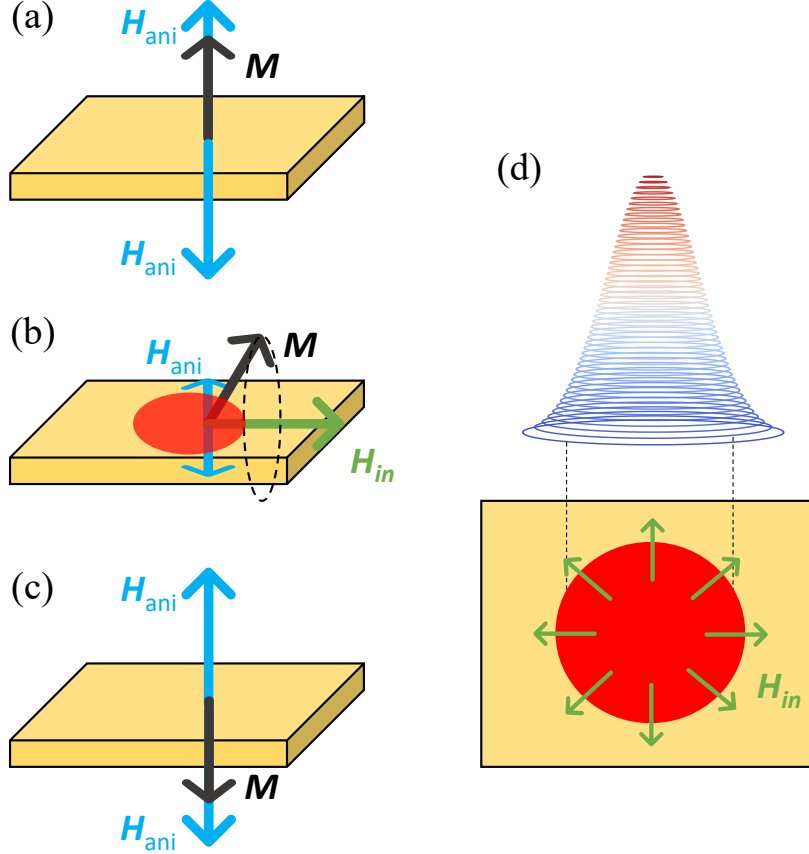


Figure 5.28: Schematics for explaining of ringlike-domain patterns. (a) magnetization \mathbf{M} (represented by blue arrow) lies parallel to the normal of surface in the remnant magnetization state. The perpendicular magnetic anisotropy can be thought as a field \mathbf{H}_{ani} , which is represented by blue arrow. (b) The anisotropy field \mathbf{H}_{ani} is temporarily reduced by the thermal load of the laser pulse (represented by a red circle), which triggers the magnetization precession about the dominant in-plane effective anisotropy field \mathbf{H}_{in} (represented by a green arrow). The \mathbf{H}_{in} is induced radially and locally by the strain caused by the nonuniform thermal expansion around the boundary. (c) After sufficient thermal dissipation, the strain disappears and hence the in-plane \mathbf{H}_{in} disappears as well. At the same time, the perpendicular magnetic anisotropy recovers since the temperature cools back to 300 K. If the magnetization has precessed for an odd (even) number of half-periods, the domains are switched (unswitched). (d) The tension is induced radially and locally by the nonuniform thermal expansion around the boundary, which further helps to develop an in-plane anisotropy field (represented by green arrows). This is the in-plane field, which helps to achieve magnetization precession in (b).

taken into consideration in potential spintronic applications. Improving the long-term stability is one the important challenges that will need to be addressed in the future study.

5.5 Conclusions

In conclusion, the single-pulse all-optical partial switching, non-uniform on a length scale of about 150 nm that we observe in a-Dy_{0.25}Co_{0.75} and a-Tb_{0.25}Co_{0.75}, is quite distinct from that in a-Gd_xCo_{1-x} or crystalline Mn₂Ru_xGa where the toggle switching is indefinitely repeatable and uniform. Random atomic-scale anisotropy on the rare-earth subnetwork of Dy and Tb alloys distinguishes them from their ferrimagnetic Gd counterpart. The demagnetization rate of the high-moment atoms Dy and Tb is expected to be at least as slow as that of Gd. For both Dy and

Tb, the formation of the transient aligned state and the re-magnetization process are influenced by the local random anisotropy. The challenge for future experimental and theoretical work is to understand and describe in detail the effect of the non-collinear magnetic moments of Dy or Tb on the all-optical switching, where the influence of local random anisotropy is of particular interest.

At higher fluence, on top of the single pulse all-optical switching behavior, the ringlike-domains imply that magnetization precession might play a role. The decrease of perpendicular magnetic anisotropy and thermally-induced in-plane effective field, both make magnetization precession possible. The detailed understanding of the underlying mechanism of ringlike domains remains incomplete. Future work on dynamics is eagerly anticipated.

References

- [1] A. Kirilyuk, A. V. Kimel, and T. Rasing, “Ultrafast optical manipulation of magnetic order,” *Reviews of Modern Physics*, vol. 82, no. 3, p. 2731, 2010. (Cited on page: 124)
- [2] E. Beaurepaire, J.-C. Merle, A. Daunois, and J.-Y. Bigot, “Ultrafast spin dynamics in ferromagnetic nickel,” *Physical review letters*, vol. 76, no. 22, p. 4250, 1996. (Cited on page: 124)
- [3] T. Ostler, J. Barker, R. Evans, R. Chantrell, U. Atxitia, O. Chubykalo-Fesenko, S. El Mousaoui, L. Le Guyader, E. Mengotti, L. Heyderman, *et al.*, “Ultrafast heating as a sufficient stimulus for magnetization reversal in a ferrimagnet,” *Nature communications*, vol. 3, no. 1, p. 666, 2012. (Cited on page: 124, 143)
- [4] M. Lalieu, M. Peeters, S. Haenen, R. Lavrijsen, and B. Koopmans, “Deterministic all-optical switching of synthetic ferrimagnets using single femtosecond laser pulses,” *Physical review B*, vol. 96, no. 22, p. 220411, 2017. (Cited on page: 124)
- [5] M. L. Lalieu, R. Lavrijsen, and B. Koopmans, “Integrating all-optical switching with spintronics,” *Nature communications*, vol. 10, no. 1, p. 110, 2019. (Cited on page: 124)
- [6] C. Banerjee, N. Teichert, K. Siewierska, Z. Gercsi, G. Atcheson, P. Stamenov, K. Rode, J. Coey, and J. Besbas, “Single pulse all-optical toggle switching of magnetization without gadolinium in the ferrimagnet $\text{Mn}_2\text{Ru}_x\text{Ga}$,” *Nature communications*, vol. 11, no. 1, p. 4444, 2020. (Cited on page: 124)
- [7] C. Davies, G. Bonfiglio, K. Rode, J. Besbas, C. Banerjee, P. Stamenov, J. Coey, A. Kimel, and A. Kirilyuk, “Exchange-driven all-optical magnetic switching in compensated 3d ferrimagnets,” *Physical Review Research*, vol. 2, no. 3, p. 032044, 2020. (Cited on page: 124)
- [8] C. Banerjee, K. Rode, G. Atcheson, S. Lenne, P. Stamenov, J. Coey, and J. Besbas, “Ultrafast double pulse all-optical reswitching of a ferrimagnet,” *Physical Review Letters*, vol. 126, no. 17, p. 177202, 2021. (Cited on page: 124)
- [9] J. M. D. Coey, *Magnetism and Magnetic Materials*. Cambridge university press, 2010. (Cited on page: 124)
- [10] S. Mangin, M. Gottwald, C. Lambert, D. Steil, V. Uhlíř, L. Pang, M. Hehn, S. Alebrand, M. Cinchetti, G. Malinowski, *et al.*, “Engineered materials for all-optical helicity-dependent magnetic switching,” *Nature materials*, vol. 13, no. 3, pp. 286–292, 2014. (Cited on page: 124, 138)
- [11] M. S. El Hadri, M. Hehn, P. Pirro, C.-H. Lambert, G. Malinowski, E. E. Fullerton, and S. Mangin, “Domain size criterion for the observation of all-optical helicity-dependent switching in magnetic thin films,” *Physical review B*, vol. 94, no. 6, p. 064419, 2016. (Cited on page: 124)

- [12] A. Ciuciulkaite, K. Mishra, M. V. Moro, I.-A. Chioar, R. M. Rowan-Robinson, S. Parchenko, A. Kleibert, B. Lindgren, G. Andersson, C. S. Davies, *et al.*, “Magnetic and all-optical switching properties of amorphous $\text{tb}_x\text{co}_{100-x}$ alloys,” *Physical Review Materials*, vol. 4, no. 10, p. 104418, 2020. (Cited on page: 124)
- [13] A. Ceballos, A. Pattabi, A. El-Ghazaly, S. Ruta, C. P. Simon, R. F. Evans, T. Ostler, R. W. Chantrell, E. Kennedy, M. Scott, *et al.*, “Role of element-specific damping in ultrafast, helicity-independent, all-optical switching dynamics in amorphous (Gd,Tb)Co thin films,” *Physical Review B*, vol. 103, no. 2, p. 024438, 2021. (Cited on page: 124)
- [14] T.-M. Liu, T. Wang, A. H. Reid, M. Savoini, X. Wu, B. Koene, P. Granitzka, C. E. Graves, D. J. Higley, Z. Chen, *et al.*, “Nanoscale confinement of all-optical magnetic switching in tb/co -competition with nanoscale heterogeneity,” *Nano letters*, vol. 15, no. 10, pp. 6862–6868, 2015. (Cited on page: 124)
- [15] L. Avilés-Félix, A. Olivier, G. Li, C. S. Davies, L. Álvaro-Gómez, M. Rubio-Roy, S. Auffret, A. Kirilyuk, A. Kimel, T. Rasing, *et al.*, “Single-shot all-optical switching of magnetization in tb/co multilayer-based electrodes,” *Scientific reports*, vol. 10, no. 1, p. 5211, 2020. (Cited on page: 125)
- [16] J.-M. Liu, “Simple technique for measurements of pulsed gaussian-beam spot sizes,” *Optics letters*, vol. 7, no. 5, pp. 196–198, 1982. (Cited on page: 125)
- [17] K. Chen, D. Lott, F. Radu, F. Choueikani, E. Otero, and P. Ohresser, “Temperature-dependent magnetic properties of ferrimagnetic DyCo_3 alloy films,” *Physical Review B*, vol. 91, no. 2, p. 024409, 2015. (Cited on page: 132)
- [18] B. Thole, G. Van der Laan, J. Fuggle, G. Sawatzky, R. Karnatak, and J.-M. Esteve, “3d x-ray-absorption lines and the $3d^94f^{m+1}$ multiplets of the lanthanides,” *Physical Review B*, vol. 32, no. 8, p. 5107, 1985. (Cited on page: 132)
- [19] S. Pizzini and X.-r. M. C. Dichroism, “basic concepts and theory for rare earths and 3d metals,” *Ecole Franco-Roumaine: Magnétisme des systèmes nanoscopiques et structures hybrides*, 2003. (Cited on page: 132)
- [20] D. H. Suzuki, M. Valvidares, P. Gargiani, M. Huang, A. E. Kossak, and G. S. Beach, “Thickness and composition effects on atomic moments and magnetic compensation point in rare-earth transition-metal thin films,” *Physical Review B*, vol. 107, no. 13, p. 134430, 2023. (Cited on page: 133)
- [21] T. Mizoguchi and G. Cargill III, “Magnetic anisotropy from dipolar interactions in amorphous ferrimagnetic alloys,” *Journal of Applied Physics*, vol. 50, no. 5, pp. 3570–3582, 1979. (Cited on page: 138)
- [22] H. Fu, M. Mansuripur, and P. Meystre, “Generic source of perpendicular anisotropy in amorphous rare-earth–transition-metal films,” *Physical review letters*, vol. 66, no. 8, p. 1086, 1991. (Cited on page: 138)
- [23] T. Ohkochi, H. Fujiwara, M. Kotsugi, A. Tsukamoto, K. Arai, S. Isogami, A. Sekiyama, J. Yamaguchi, K. Fukushima, R. Adam, *et al.*, “Microscopic and spectroscopic studies of light-induced magnetization switching of GdFeCo facilitated by photoemission electron microscopy,” *Japanese journal of applied physics*, vol. 51, no. 7R, p. 073001, 2012. (Cited on page: 139)
- [24] D. Mergel, H. Heitmann, and P. Hansen, “Pseudocrystalline model of the magnetic anisotropy in amorphous rare-earth–transition-metal thin films,” *Physical Review B*, vol. 47, no. 2, p. 882, 1993. (Cited on page: 139)

- [25] R. Cowburn and M. Welland, “Room temperature magnetic quantum cellular automata,” *Science*, vol. 287, no. 5457, pp. 1466–1468, 2000. (Cited on page: 141)
- [26] P. Vallobra, Y. Xu, H. Wang, G. Malinowski, M. Hehn, J.-C. Rojas-Sánchez, and S. Mangin, “Patterning nucleation area by femtosecond laser in exchange-coupled systems,” *Applied Physics Letters*, vol. 123, no. 11, 2023. (Cited on page: 141)
- [27] I. Radu, K. Vahaplar, C. Stamm, T. Kachel, N. Pontius, H. Dürr, T. Ostler, J. Barker, R. Evans, R. Chantrell, *et al.*, “Transient ferromagnetic-like state mediating ultrafast reversal of antiferromagnetically coupled spins,” *Nature*, vol. 472, no. 7342, pp. 205–208, 2011. (Cited on page: 143)
- [28] J. Lin, M. Hehn, T. Hauet, Y. Peng, J. Igarashi, Y. L. Guen, Q. Remy, J. Gorchon, G. Malinowski, S. Mangin, *et al.*, “Single laser pulse induced magnetization switching in in-plane magnetized GdCo alloys,” *arXiv preprint arXiv:2308.10516*, 2023. (Cited on page: 143)
- [29] C. Davies, K. Prabhakara, M. Davydova, K. Zvezdin, T. Shapaeva, S. Wang, A. Zvezdin, A. Kirilyuk, T. Rasing, and A. Kimel, “Anomalously damped heat-assisted route for precessional magnetization reversal in an iron garnet,” *Physical review letters*, vol. 122, no. 2, p. 027202, 2019. (Cited on page: 144)
- [30] P. Hansen, C. Clausen, G. Much, M. Rosenkranz, and K. Witter, “Magnetic and magneto-optical properties of rare-earth transition-metal alloys containing Gd, Tb, Fe, Co,” *Journal of applied physics*, vol. 66, no. 2, pp. 756–767, 1989. (Cited on page: 145)
- [31] S. Ota, Y. Hibino, D. Bang, H. Awano, T. Kozeki, H. Akamine, T. Fujii, T. Namazu, T. Takenobu, T. Koyama, *et al.*, “Strain-induced reversible modulation of the magnetic anisotropy in perpendicularly magnetized metals deposited on a flexible substrate,” *Applied Physics Express*, vol. 9, no. 4, p. 043004, 2016. (Cited on page: 145)
- [32] T. Kurihara, K. Hirota, H. Qiu, K. T. N. Phan, K. Kato, G. Isoyama, and M. Nakajima, “Reconfiguration of magnetic domain structures of ErFeO₃ by intense terahertz free electron laser pulses,” *Scientific Reports*, vol. 10, no. 1, p. 7321, 2020. (Cited on page: 145)
- [33] Y. Peng, D. Salomoni, G. Malinowski, W. Zhang, J. Hohlfeld, L. Buda-Prejbeanu, J. Gorchon, M. Vergès, J. Lin, R. Sousa, *et al.*, “In plane reorientation induced single laser pulse magnetization reversal in rare-earth based multilayer,” *arXiv preprint arXiv:2212.13279*, 2022. (Cited on page: 145)
- [34] D. Salomoni, Y. Peng, L. Farcis, S. Auffret, M. Hehn, G. Malinowski, S. Mangin, B. Dieny, L. Buda-Prejbeanu, R. Sousa, and I. L. Prejbeanu, “Field-free all-optical switching and electrical read-out of Tb/Co-based magnetic tunnel junctions,” *arXiv preprint arXiv:2305.15135*, 2023. (Cited on page: 145)
- [35] K. Mishra, T. G. Blank, C. Davies, L. Avilés-Félix, D. Salomoni, L. Buda-Prejbeanu, R. Sousa, I. Prejbeanu, B. Koopmans, T. Rasing, A. V. Kimel, and A. Kirilyuk, “Dynamics of all-optical single-shot switching of magnetization in Tb/Co multilayers,” *Physical Review Research*, vol. 5, no. 2, p. 023163, 2023. (Cited on page: 145)
- [36] Y. Peng, D. Salomoni, G. Malinowski, W. Zhang, J. Hohlfeld, L. Buda-Prejbeanu, J. Gorchon, M. Vergès, J. Lin, D. Lacour, R. C. Sousa, I. L. Prejbeanu, S. Mangin, and M. Hehn, “In-plane reorientation induced single laser pulse magnetization reversal,” *Nature Communications*, vol. 14, no. 1, p. 5000, 2023. (Cited on page: 145)

- [37] G. Masciocchi, T. J. Kools, P. Li, A. A. Petrillo, B. Koopmans, R. Lavrijsen, A. Kehlberger, and M. Kläui, “Strain effects on magnetic compensation and spin reorientation transition of Co/Gd synthetic ferrimagnets,” *Journal of Applied Physics*, vol. 134, no. 1, 2023. (Cited on page: 145)
- [38] S. Mangin, M. Gottwald, C. Lambert, D. Steil, V. Uhlíř, L. Pang, M. Hehn, S. Alebrand, M. Cinchetti, G. Malinowski, *et al.*, “Engineered materials for all-optical helicity-dependent magnetic switching,” *Nature materials*, vol. 13, no. 3, pp. 286–292, 2014. (Cited on page: viii, 146)
- [39] T. J. Kools, Y. L. van Hees, K. Poissonnier, P. Li, B. Barcones Campo, M. A. Verheijen, B. Koopmans, and R. Lavrijsen, “Aging and passivation of magnetic properties in Co/Gd bilayers,” *Applied Physics Letters*, vol. 123, no. 4, 2023. (Cited on page: 146)

6 Conclusions and outlook

6.1 Conclusions

The conclusions of our systematic study of the magnetic properties of amorphous rare-earth cobalt alloys (YCo, DyCo and TbCo) in thin film form with thicknesses from 10 to 20 nm, by means of SQUID magnetometry, MOKE, magneto-transport measurements and SP-AOS experiments, are the following:

In chapter 3, the work on a- Y_xCo_{1-x} with $0 \leq x \leq 0.54$ and thickness ≈ 15 nm provides a basis for the understanding the ferromagnetism of cobalt in amorphous rare-earth cobalt alloys since Y is non-magnetic. All compositions with $x < 0.5$ are soft ferromagnets with no coercivity measured with a field step of 24 mT. When $x \leq 0.2$, the Co moment is $\geq 1.75 \mu_B$, the Co moment in crystalline Co thin films. When $x > 0.2$, the Co moment starts to decrease and disappears at $x_c = 0.5$, where an average Co atom in a random close-packed of hard sphere model is coordinated by about 3 Y and 3 Co atoms. 3 Y neighbours destroy a Co moment both in a- Y_xCo_{1-x} and in crystalline YCo₂. In the vicinity of x_c , there is a large susceptibility (paraprocess) where the magnetic moment is switched on by the externally applied magnetic field, similar to that in Laves phase crystalline YCo₂. In thin films, the magnetic easy axis is in-plane due to shape anisotropy, which overcomes weaker intrinsic perpendicular magnetic anisotropy with a value 24 kJ/m³ when the saturation magnetization is 500 kA/m³. This implies that perpendicular magnetic anisotropy can dominate in thin films with heavy rare earths like Dy or Tb, because of the reduction in shape anisotropy, as the net magnetization decreases due to the antiparallel coupling between rare earth and Co moments. For a-YCo₃, the spin and orbital moment of Co is 1.31 and 0.32 μ_B , respectively, based on XMCD measurements. Strong local anisotropy is associated with the large cobalt orbital moment, but there is little influence of anisotropy on the ferromagnetic order because of exchange averaging. Below 350 K, a-YCo₃ has a nearly temperature independent magnetic moment 1.63 μ_B from the XMCD, which agrees with 1.61 μ_B from SQUID magnetometry. This becomes the basis of deducing the other rare earth moments in a-Dy_{0.25}Co_{0.75} and a-Tb_{0.25}Co_{0.75}, in the following chapter.

In chapter 4, the study of sputtered thin films of a-DyCo and a-TbCo focuses on the non-collinear magnetism. The magnetic ground state of a-Dy_{0.25}Co_{0.75} and a-Tb_{0.25}Co_{0.75} is sperimagnetic with a averaged magnetic moment of Dy (7.3 μ_B) and Tb (7.0 μ_B), due to the strong random local magnetic anisotropy on the rare earth sites. This is due to the topological disorder of the random close-packed structure, which is characteristic of amorphous metals. The temperature dependence of Dy and Tb moment in the range 4 – 300 K is deduced based on the Co moment in a- Y_xCo_{1-x} . Exchange averaging of the rare-earth anisotropy is negligible, unlike the exchange averaging of the cobalt anisotropy, which ensures that the Co subnetworks remains practically collinear. A spin-flop transition near the compensation temperature $T_{comp} = 180$ K, with a spin-flop field of approximately 2 T, was observed in the anomalous Hall effect measurement of a-DyCo₃ in 14 T magnetic fields. The estimated value of spin-flop field, based on the formula for an antiferromagnet well below the magnetic ordering temperature, $H_{sf} = \sqrt{H_a H_{ex}}$ with $H_a = 0.22$ T and $H_{ex} = 18.3$ T, is in agreement with the measured value near compensation. From the Hall voltage vs temperature of a-DyCo₃ at remanence, it is inferred that the anomalous Hall voltage comes from Co subnetwork, not from the rare earth subnetwork.

In chapter 5, the investigation concentrates on the all-optical switching in amorphous $\text{a-Dy}_x\text{Co}_{1-x}$ and $\text{a-Tb}_x\text{Co}_{1-x}$ with $x \approx 0.25$ irradiated with single 200 fs pulses of 800 nm laser light. A new type of single pulse partial all-optical switching, non-uniform on a length scale of about 150 nm, as measured by XMCD-PEEM, is found in $\text{a-Dy}_x\text{Co}_{1-x}$ and $\text{a-Tb}_x\text{Co}_{1-x}$ with $x = 0.25$ for temperature both below and above T_{comp} . After the first pulse, many switched domains appear and subsequent pulses lead to partial re-switching. This random and partial single pulse all-optical switching is attributed to the noncollinear magnetic structure on the rare earth sites. The noncollinear magnetic structure of rare earth sites leads to a varying z -component of magnetic moments of rare earth at various positions. Only the region, with a big enough z -component of the magnetic moments of rare earth, is able to be switched. This explains why the switching is partial. Before the accomplishment of the switching process, the rare-earth anisotropy imposes a new wandering axis on the switched region at some point, which explains the reason for being random. Ringlike domain patterns appear at higher fluence but below the fluence at which the anisotropy begins to change toward in-plane. One possible explanation for the appearance of ringlike switched domains is the Larmor precession of magnetization around the effective in-plane field induced by the thermal strain, following the laser pulse. The optical control of coercivity is demonstrated with potential applications in magnetic logic. The nucleation and growth of magnetic domains with a swept 1 kHz train of 200 fs laser pulses were observed, independent of the polarization of laser pulses. Domain size is governed by the time spent at elevated temperature.

6.2 Outlook

The study of $\text{a-Y}_x\text{Co}_{1-x}$ series could be extended to look for even bigger orbital Co moments with other non-magnetic rare earths (such as La, Sc, or Lu) or with smaller x . Sc has a smaller metallic radius, approximately 9 % smaller. This will enable more Co within the same sample volume, potentially leading to larger orbital Co moments. It is valuable to investigate the threshold value of x for an amorphous structure in these binary metallic systems. A value of x , smaller than 0.1, the minimum value in this $\text{a-Y}_x\text{Co}_{1-x}$ work, allows obtaining more Co in the amorphous state, with the potential for larger orbital and spin Co moments.

Modeling of local electrostatic field at each rare earth site will be useful to get more insights of the local random electrostatic field gradients and anisotropy in these amorphous rare-earth transition-metal systems.

The ringlike domain patterns observed in $\text{a-Dy}_x\text{Co}_{1-x}$ and $\text{a-Tb}_x\text{Co}_{1-x}$ require a more systematic work to understand the dynamics and the underlying mechanism. A comparison with stroboscopy on concentric ring domain structures in $[\text{Tb}/\text{Co}]$ and $[\text{Tb}/\text{Fe}]$ magnetic multilayers will be interesting. Further research is also required to systematically investigate the local optical control of coercivity using various characteristics of femtosecond laser pulses, including helicity, fluence, and number of pulses.

Among the rare earth transition-metal systems, the Gd-based system shows the best single pulse all-optical switching behavior. By considering the energy levels of triply ionized rare earths, Gd has the largest splitting of the J-multiplets close to the ground state, of approximately 4 eV. However, Tb and Dy have only 0.25 eV and 0.50 eV, respectively. The wavelength of the laser we used is 800 nm, which is equivalent to 1.55 eV, higher than splitting of the J-multiplets of Tb and Dy close to the ground but smaller than that of Gd. Based on this fact, it is worthwhile to perform a systematic study of the magnetization and the single pulse all-optical switching of the $\text{a-Er}_x\text{Co}_{1-x}$ system using a laser with a longer wavelength since Er has a 0.9 eV splitting of the J-multiplets close to the ground. A free electron laser might be employed for generating deep infrared energy photons.

Practical applications of the $\text{a-R}_x\text{Co}_{1-x}$ systems may be sought in the areas of magnetic domain-wall logic and magneto-optical recording.

7 Appendix

7.1 B , H and M for a magnet

If we assume the cube hard magnet has a uniform magnetization \mathbf{M} , pointing vertically up. Then the \mathbf{H} and \mathbf{B} fields are in the xz plane, as shown in Figure 7.1. It meets the relation

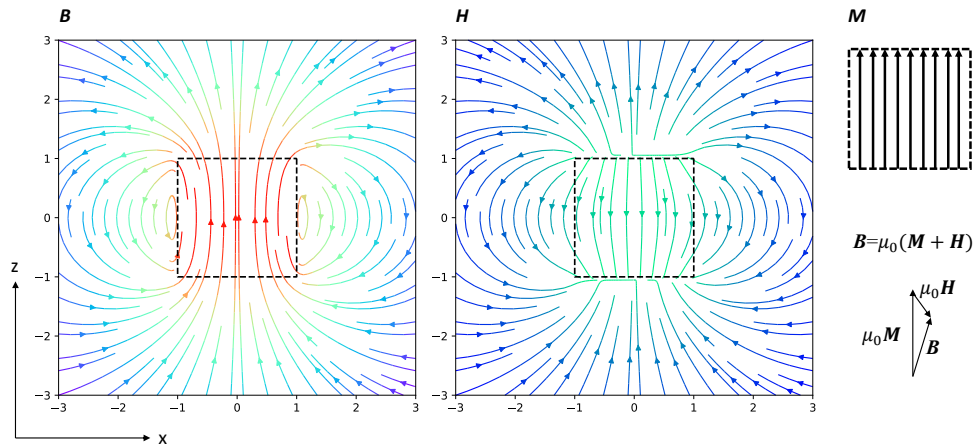


Figure 7.1: \mathbf{B} , \mathbf{H} and \mathbf{M} for a cube magnet. Those two plots for \mathbf{B} and \mathbf{H} are produced by using Magpylib [1], a Python package for calculating 3D static magnetic fields of permanent magnets.

$\mathbf{B} = \mu_0(\mathbf{M} + \mathbf{H})$. Outside the magnet, there is no difference for \mathbf{B} and \mathbf{H} direction apart from the constant μ_0 . Inside the cube, they are quite different. \mathbf{H} is directed oppositely to \mathbf{M} (hence the name 'demagnetizing field' for \mathbf{H} inside the magnet) and discontinuous at top and bottom surfaces, which are very easy to understand from the magnetic charge picture. But for \mathbf{B} , it is in the same direction as \mathbf{M} roughly and continuous at those surfaces, which is equivalent to four current sheets on the lateral surface from the Ampèrian molecular current model [2].

7.2 Self-energy

The Zeeman energy of a magnetic moment \mathbf{m} in the external field \mathbf{B} is given

$$E = -\mathbf{m} \cdot \mathbf{B} \quad (7.1)$$

From a basic point of view, there is no difference between an external field provided by electric current and the field created by all the other magnetic dipoles in the solids. The field from the moment is

$$\mathbf{H} = \frac{\mu_0}{4\pi} \left[3 \frac{(\mathbf{m} \cdot \mathbf{r})\mathbf{r}}{r^5} - \frac{\mathbf{m}}{r^3} \right] \quad (7.2)$$

In reality, the solids consist of atoms and we have the ability to probe the magnetic fields at the atomic nuclei experimentally via the hyperfine interactions. The question then arises: 'What is the value of the local magnetic field $\mathbf{H}_{loc}(\mathbf{x}_i)$ at a point in a solid?' Lorentz gave an argument

to simplify the calculation. The sample was divided into two regions as illustrated in Figure 7.2: region 1 which can be treated as a continuum since the moments are far from \mathbf{x}_i and the region

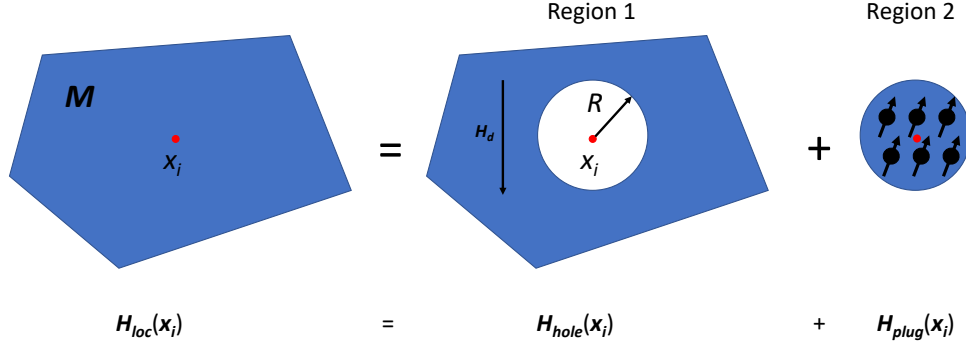


Figure 7.2: Calculation of magnetic field inside a solid: the field at point \mathbf{x}_i in magnetic materials can be considered as the sum of the field in a spherical hole plus the field due to a spherical plug.

2 where the field is calculated as a dipole sum because the moments are located within a small sphere with radius R around \mathbf{x}_i . Therefore, the local field at position \mathbf{x}_i can be split into two parts

$$\mathbf{H}_{loc}(\mathbf{x}_i) = \mathbf{H}_{hole}(\mathbf{x}_i) + \mathbf{H}_{plug}(\mathbf{x}_i) \quad (7.3)$$

where the $\mathbf{H}_{hole}(\mathbf{x}_i)$ is the field at the position \mathbf{x}_i due to all the moments in the region 1 and the $\mathbf{H}_{plug}(\mathbf{x}_i)$ is the field at the position \mathbf{x}_i due to the moments in the region 2. It can be shown that

$$\mathbf{H}_{hole}(\mathbf{x}_i) = \mathbf{H}_d(\mathbf{x}_i) + \frac{\mathbf{M}}{3} \quad (7.4)$$

where $\mathbf{H}_d(\mathbf{x}_i)$ is the demagnetizing field inside the material and the second part $\frac{\mathbf{M}}{3}$ is known as the Lorentz cavity field [3]. The field $\mathbf{H}_{plug}(\mathbf{x}_i)$ produced by the moments contained within the spherical plug region 2 is evaluated as a sum:

$$\mathbf{H}_{plug}(\mathbf{x}_i) = \sum_j \frac{1}{4\pi} \left[3 \frac{(\mathbf{m}_j \cdot \mathbf{r}_{ij}) \mathbf{r}_{ij}}{r_{ij}^5} - \frac{\mathbf{m}_j}{r_{ij}^3} \right] \quad (7.5)$$

where the vector $\mathbf{r}_{ij} = \mathbf{x}_i - \mathbf{x}_j$ and $r_{ij} = |\mathbf{r}_{ij}|$.

The energy required to bring the small moment in position is $\delta m = -\mu_0 \delta m \cdot \mathbf{H}_{loc}$. We neglect the \mathbf{H}_{plug} in the mesoscopic approximation, where

$$\mathbf{H}_{loc}(\mathbf{x}_i) = \mathbf{H}_d(\mathbf{x}_i) + \frac{\mathbf{M}}{3} \quad (7.6)$$

The integration over the whole sample gives

$$E = -\frac{1}{2} \int_V \mu_0 \mathbf{H}_d \cdot \mathbf{M} d^3r - \frac{1}{6} \int_V \mu_0 M^2 d^3r. \quad (7.7)$$

where the factor $\frac{1}{2}$ is needed to avoid double counting because each element δm contributes as a field source and as a moment. The first term $-\frac{1}{2} \int_V \mu_0 \mathbf{H}_d \cdot \mathbf{M} d^3r$ is conventionally defined as the magnetostatic self-energy since the second term is unimportant and much smaller than exchange energy, a term dependent on M^2 as well but with a coefficient larger by more than three orders of magnitude. The magnetostatic self-energy can be written in the equivalent form $\frac{1}{2} \int_V \mu_0 \mathbf{H}_d^2 d^3r$ where the integral is now calculated over all space. This equivalence follows from $\nabla \times \mathbf{H}_d = 0$ and $\nabla \cdot \mathbf{B}_d = 0$ where $\mathbf{B}_d = \mu_0(\mathbf{H}_d + \mathbf{M})$ [4].

7.3 Adiabatic approximation

At each instant t , the time-independent Schrödinger equation is

$$H(t)|\phi_n(t)\rangle = E_n(t)|\phi_n(t)\rangle \quad (7.8)$$

with $E_1(t) < E_2(t) < E_3(t) < \dots$ so that there are no degeneracies. Note that at any time t , the instantaneous eigenstates ($|\phi_1(t)\rangle, |\phi_2(t)\rangle, |\phi_3(t)\rangle, \dots$) and instantaneous eigenvalues ($E_1(t), E_2(t), E_3(t), \dots$) may change [5]. If we now look for the general solutions to the time-dependent Schrödinger equation:

$$i\hbar \frac{\partial}{\partial t} |\Phi(t)\rangle = H(t)|\Phi(t)\rangle \quad (7.9)$$

We can write

$$|\Phi(t)\rangle = \sum_n c_n(t) |\phi_n(t)\rangle \quad (7.10)$$

which is a good approximation. Substituting equation 7.10 into time-dependent Schrödinger equation 7.9, we get

$$i\hbar \sum_n (\dot{c}_n(t) |\phi_n(t)\rangle + c_n(t) \dot{|\phi_n(t)\rangle}) = \sum_n c_n(t) E_n(t) |\phi_n(t)\rangle \quad (7.11)$$

Not taking the inner product with $\langle \phi_k(t) |$ and invoking orthonormality of the eigenstates, we arrive

$$i\hbar \dot{c}_k = E_k c_k - i\hbar \sum_n \langle \phi_k | \dot{\phi}_n \rangle c_n = E_k c_k - i\hbar \langle \phi_k | \dot{\phi}_k \rangle c_k - i\hbar \sum_{n \neq k} \langle \phi_k | \dot{\phi}_n \rangle c_n \quad (7.12)$$

We can calculate the $\langle \phi_k | \dot{\phi}_k \rangle$ in the space of instantaneous eigenstates. Take the time derivatives of both sides of equation 7.8:

$$\dot{H}(t)|\phi_n(t)\rangle + H(t)|\dot{\phi}_n(t)\rangle = \dot{E}_n(t)|\phi_n(t)\rangle + E_n(t)|\dot{\phi}_n(t)\rangle \quad (7.13)$$

and then multiply by $\langle \phi_k(t) |$ with $k \neq n$:

$$\langle \phi_k(t) | \dot{H}(t) | \phi_n(t) \rangle + E_k(t) \langle \phi_k(t) | \dot{\phi}_n(t) \rangle = E_n \langle \phi_k(t) | \dot{\phi}_n(t) \rangle \quad (7.14)$$

hence

$$\langle \phi_k(t) | \dot{\phi}_n(t) \rangle = \frac{\langle \phi_k(t) | \dot{H}(t) | \phi_n(t) \rangle}{E_n(t) - E_k(t)} = \frac{\dot{H}_{kn}}{E_n(t) - E_k(t)} \quad (7.15)$$

Now, we can plug it back in equation 7.12 and get

$$i\hbar \dot{c}_k = E_k c_k - i\hbar \langle \phi_k | \dot{\phi}_k \rangle c_k - i\hbar \sum_{n \neq k} \frac{\dot{H}_{kn}}{E_n(t) - E_k(t)} c_n \quad (7.16)$$

Notice that if the term proportional to $\frac{\dot{H}_{kn}}{E_n(t) - E_k(t)}$ vanishes, then $|c_k| = 1$. It means that if the system starts in $|\phi_k\rangle$ and then it remains $|\phi_k\rangle$ up to a calculable phase. If we neglect the third term in equation 7.16, we obtain

$$c_k(t) = c_k(0) e^{i\theta_k(t)} e^{i\gamma_k(t)} \quad (7.17)$$

where

$$\theta_k(t) = -\frac{1}{\hbar} \int_0^t E_k(t') dt' \quad (7.18)$$

$$\gamma_k(t) = \int_0^t i \langle \phi_k(t') | \dot{\phi}_k(t') \rangle dt' \quad (7.19)$$

Finally we know find

$$|\Phi(t)\rangle = e^{i\theta_k(t)} e^{i\gamma_k(t)} |\phi_k(t)\rangle \quad (7.20)$$

In summary, the adiabatic approximation says that: if at $t = 0$, $|\Phi(0)\rangle = |\phi_k(0)\rangle$ for some k , then if $H(t)$ is slowly changing for $0 \leq t' \leq t$ then at $t' = t$ we have $|\Phi(t)\rangle = e^{i\theta_k(t)} e^{i\gamma_k(t)} |\phi_k(t)\rangle$ where $\theta_k(t)$ is called dynamical phase and $\gamma_k(t)$ is called a Berry phase or a geometric phase [6].

7.4 Deposition rate calculation

The critical step in the fabrication process is to ensure that the produced samples closely match the desired specifications. To achieve this, a simple program has been developed. The underlying principle is straightforward. For binary systems, the first step involves determining the growth rate of one of the elements by calibrating the pure element target, such as a Co target. This can be calculated by dividing the thickness of the pure Co thin film by the corresponding growth time. The former is obtained from X-ray reflectivity (XRR) data, while the latter is typically a fixed deposition time, such as 10 minutes. Once the composition ratio is determined, for example, DyCo₃ with a Dy to Co atomic ratio of 1:3, combining the densities and molar masses of the two elements allows for the calculation of the required growth rate for the other element. There is a relation between those two growth rates. The derivation of this formula, which forms the basis of the entire study, involves the introduction of various symbols, as listed in the Table 7.1. During the deposition time t , a StG_1d_1/M_1 is the number of moles of element 1

Symbol	Definition	Unit
S	Area of the substrate	m ²
t	Deposition time	s
G ₁	Growth rate of element 1	m/s
G ₂	Growth rate of element 2	m/s
d ₁	Density of element 1	kg/m ³
d ₂	Density of element 2	kg/m ³
M ₁	Molar mass of element 1	kg/mol
M ₂	Molar mass of element 2	kg/mol

Table 7.1: Symbol definitions for deposition rate calculation using the International system of units. Practically, more convenient units can be used, such as Å/s for growth rate.

deposited onto the substrata with area S. Similarly, the number of moles of element 2 deposited onto the substrate is StG_2d_2/M_2 . Assume the formula is $a-Dy_xCo_{1-x}$. Here, Dy is the element 1 and Co is the element 2. In order to make a sample with specific atomic percentage of x. The ratio of growth rate of element 1 to that of element 2 should equate to the ratio $\frac{x}{1-x}$. Therefore, the relation between those two elements growth rate is the following:

$$G_1 = G_2 \frac{d_2}{d_1} \frac{x}{1-x} \frac{M_1}{M_2} \quad (7.21)$$

It means that, if one of the growth rate is known, the required growth rate for the other element can be determined from the aforementioned formula. then the objective is to closely match the calculated value by employing different target currents during thin film depositions. For studies involving compositional dependence, a series of various compositions are needed. A recommended approach is to begin with calibrating at least three growth rates for different target currents. When plotted on a graph, with the target current on the x -axis and the growth rate on the y -axis, a linear relationship can often be observed. This linear relationship can be used to determine the appropriate target current for other compositions. After obtaining the samples, there are few checks that can be performed to quickly know whether those samples are desired or not. First, the thickness of samples should be close to expected value based on a predetermined co-sputtering time and alloy growth rate which is the sum of growth rate of two targets, i.e., G_1 and G_2 . The difference should be within 20 %; in most cases it is about 2.5 % in my whole PhD work. The second aspect to consider is the comparison between the fitted density obtained from the XRR measurements and the calculated density. For the calculated density, there is a good approximate formula can be employed for calculating the density. The first one is quite straightforward, it $xd_1 + (1-x)d_2$.

7.5 Fast Fourier transform

In the early 1800s, French mathematician Jean-Baptiste Joseph Fourier introduced the concept of sine and cosine functions of increasing frequency as an orthogonal basis for the space of solution functions, during his investigations of heat [7]. The analytical Fourier series and Fourier transform are defined for continuous functions. However, when working with the real data, it is necessary to approximate the Fourier transform on discrete vectors of data, resulting in discrete Fourier transform (DFT). It is essentially a discretized version of Fourier series for vectors of data $\mathbf{f} = [f_1 \ f_2 \ f_3 \ \dots \ f_n]$ obtained by discretizing the function $f(x)$ at a regular spacing. DFT is an extremely useful method but it does not scale well to large $n \gg 1$ since the multiplication of an $n \times n$ matrix requires $O(n^2)$. In 1965, James W. Cooley and John W. Tukey developed the fast Fourier transform (FFT) algorithm which scales as $O(n \log(n))$. At the large value of n , the FFT algorithm approaches a linear scaling. Essentially, it allows an n -dimensional DFT to be solved with a number of lower dimensional DFT computations [8].

Consider the domain $x \in [-L/2, L/2)$. On this domain, the Fourier series is

$$f(x) = \sum_{n=-\infty}^{\infty} c_n e^{in\frac{2\pi}{L}x} \quad (7.22)$$

with the coefficients

$$c_n = \frac{1}{L} \int_{-\frac{L}{2}}^{\frac{L}{2}} f(x) e^{-in\frac{2\pi}{L}x} dx \quad (7.23)$$

based on the orthogonal property of functions $e^{-in\frac{2\pi}{L}x}$ for integer n and the factor $\frac{1}{L}$ is used for normalization.

Now, we need to make an approximation to evaluate the c_n [8]:

$$\begin{aligned} c_n &= \frac{1}{L} \int_{-\frac{L}{2}}^{\frac{L}{2}} f(x) e^{-in\frac{2\pi}{L}x} dx \\ &\approx \frac{1}{L} \sum_{k=0}^{N-1} f(x_k) e^{-in\frac{2\pi}{L}x_k} \Delta x_k \\ &= \frac{1}{L} \sum_{k=0}^{N-1} f(x_k) e^{-in\frac{2\pi}{L} \frac{kL}{N}} \frac{L}{N} \\ &= \frac{1}{N} \sum_{k=0}^{N-1} f(x_k) e^{i\frac{2\pi}{N}nk} \end{aligned} \quad (7.24)$$

where $\Delta x_k = \Delta = \frac{L}{N}$ and $x_k = k \times \Delta = \frac{Lk}{N}$ since the data points x_k are evenly distributed. We can set $c_n = \alpha F_n$ where α is a constant. For aesthetic reasons of symmetry, α is set to $\frac{1}{\sqrt{N}}$ so we obtain

$$F_n = \frac{1}{\sqrt{N}} \sum_{k=0}^{N-1} f(x_k) e^{i\frac{2\pi}{N}nk} \quad (7.25)$$

and the inverse discrete Fourier transform (iDFT) is given by

$$f(x_k) = \frac{1}{\sqrt{N}} \sum_{n=0}^{N-1} F_n e^{-i\frac{2\pi}{N}nk} \quad (7.26)$$

Therefore, the DFT is a linear operator, mapping the data points $\mathbf{f} = [f_1 \ f_2 \ f_3 \ \dots \ f_n]^T$ to the frequency domain $\mathbf{F} = [F_1 \ F_2 \ F_3 \ \dots \ F_n]^T$ where $f_n = f(x_n) = f(n\Delta x)$ and $F_n = F(n\Delta f) = F(n\frac{1}{L})$. The meaning of f_n is quite straightforward; it represents the measured data points. The meaning of F_n and Δf require some clarifications. The Δf is called the frequency increment or frequency resolution of the output of DFT and is defined as $\frac{1}{L}$. The DFT provides information about the relative contribution of harmonics of Δf [9]:

- For $n = 1$, $F_1 = F(1\Delta f)$ is the DFT at the first harmonic frequency Δf .
- For $n = 2$, $F_2 = F(2\Delta f)$ is the DFT at the second harmonic frequency Δf and so on.

Finally if we define $\omega = e^{2i\pi/N}$, the relation between \mathbf{f} and \mathbf{F} can be compactly expressed in matrix form:

$$\begin{bmatrix} F_1 \\ F_2 \\ F_3 \\ \vdots \\ F_n \end{bmatrix} = \begin{bmatrix} 1 & 1 & 1 & \dots & 1 \\ 1 & \omega & \omega^2 & \dots & \omega^{n-1} \\ 1 & \omega^2 & \omega^4 & \dots & \omega^{2(n-1)} \\ \vdots & \vdots & \vdots & \ddots & \vdots \\ 1 & \omega^{n-1} & \omega^{2(n-1)} & \dots & \omega^{(n-1)(n-1)} \end{bmatrix} \begin{bmatrix} f_1 \\ f_2 \\ f_3 \\ \vdots \\ f_n \end{bmatrix} \quad (7.27)$$

7.6 Resistivity and conductivity tensor

How to measure the resistivity and conductivity tensor experimentally is attached here as it is frequently used for experimental physicists. The geometry of Hall bar is shown in Figure 7.3. The x -axis is along the direction of long edge L . The y -axis is along that of width W . Based on

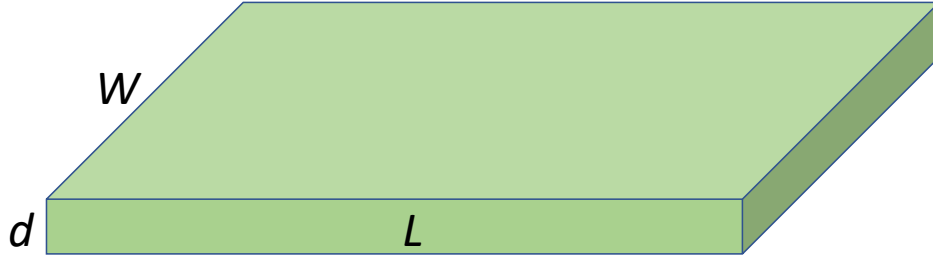


Figure 7.3: Sketch of Hall bar layout with width W , length L and thin film sample thickness d .

the material equation, there is a general equation between electric field \mathbf{E} and current density \mathbf{J} , i.e. $\mathbf{E} = \tilde{\rho}\mathbf{J}$ where $\tilde{\rho}$ is the resistivity tensor. Since we are talking about thin film sample, we assume the z component of current is 0, which simply the resistivity and conductivity tensors to 2 by 2 matrix as shown in equation 7.28. In experiment, current is sent along a certain direction. Here the x direction is chosen as current direction, so x component j_x of \mathbf{j} is not zero, which means $j_x = J$ where J is the magnitude of \mathbf{j} . It is equal to current I divided by area Wd by using the notation defined.

$$\begin{bmatrix} E_x \\ E_y \end{bmatrix} = \begin{bmatrix} \rho_{xx} & \rho_{xy} \\ \rho_{yx} & \rho_{yy} \end{bmatrix} \begin{bmatrix} J_x \\ J_y \end{bmatrix} \quad (7.28)$$

From current density and voltage definition, the following formulas in equation 7.29 are available.

$$\begin{aligned} I &= J_x W d \\ V_x &= E_x L \\ V_H &= E_y W \end{aligned} \quad (7.29)$$

The definition of ρ_{xx} and ρ_{yx} follow from the basic matrix operation as indicated in equation 7.30. Those are the foundation for experimental measurements of ρ_{xx} and ρ_{yx} .

$$\begin{aligned} \rho_{xx} &= \frac{E_x}{J_x} = \frac{V_x/L}{I/(Wd)} = \frac{V_x W d}{L I} \\ \rho_{yx} &= \frac{E_y}{J_x} = \frac{V_H/W}{I/Wd} = \frac{V_H W d}{W I} = \frac{V_H d}{I} \end{aligned} \quad (7.30)$$

A very helpful dimensionless quantity called Hall angle θ_{Hall} is frequently seen in literatures and defined as $\frac{E_y}{E_x} \frac{J_x}{J_y}$ [10]. From equation 7.29, it is equal to $\frac{\rho_{yx}}{\rho_{xx}}$. Finally, it is helpful to find the expressions that will allow to switch between different entities of resistivity and conductivity tensor. There is a material equation $\mathbf{J} = \tilde{\sigma} \mathbf{E}$ where $\tilde{\sigma}$ is the conductivity tensor.

$$\begin{bmatrix} J_x \\ J_y \end{bmatrix} = \begin{bmatrix} \sigma_{xx} & \sigma_{xy} \\ \sigma_{yx} & \sigma_{yy} \end{bmatrix} \begin{bmatrix} E_x \\ E_y \end{bmatrix} \quad (7.31)$$

If I do the inverse, I will get the following:

$$\begin{bmatrix} J_x \\ J_y \end{bmatrix} = \begin{bmatrix} \rho_{xx} & \rho_{xy} \\ \rho_{yx} & \rho_{yy} \end{bmatrix}^{-1} \begin{bmatrix} E_x \\ E_y \end{bmatrix} = \frac{1}{\rho_{xx}\rho_{yy} - \rho_{xy}\rho_{yx}} \begin{bmatrix} \rho_{yy} & -\rho_{xy} \\ -\rho_{yx} & \rho_{xx} \end{bmatrix} \begin{bmatrix} E_x \\ E_y \end{bmatrix} \quad (7.32)$$

If we compare 7.31 and 7.32, and also noticed we have $\rho_{xy} = -\rho_{yx}$ which can be seen from the transport equation for a system in both an electric and a magnetic field, we get

$$\begin{aligned} \sigma_{xx} &= \frac{\rho_{yy}}{\rho_{xx}\rho_{yy} - \rho_{xy}\rho_{yx}} = \frac{\rho_{yy}}{\rho_{xx}\rho_{yy} + \rho_{xy}\rho_{xy}} \\ \sigma_{xy} &= \frac{-\rho_{xy}}{\rho_{xx}\rho_{yy} - \rho_{xy}\rho_{yx}} = \frac{-\rho_{xy}}{\rho_{xx}\rho_{yy} + \rho_{xy}\rho_{xy}} \end{aligned} \quad (7.33)$$

and for isotropic materials such as amorphous materials, the diagonal components should be equal, which means $\rho_{xx} = \rho_{yy}$, the above formula can be further simplified to the following:

$$\begin{aligned} \sigma_{xx} &= \frac{\rho_{yy}}{\rho_{xx}^2 + \rho_{xy}^2} \\ \sigma_{xy} &= \frac{-\rho_{xy}}{\rho_{xx}^2 + \rho_{xy}^2} \end{aligned} \quad (7.34)$$

The relation $\rho_{xy} = -\rho_{yx}$ can also be seen from the symmetry consideration. We have $\mathbf{E} = \tilde{\rho} \mathbf{J}$. After rotating the sample by 90 °, we should have

$$R\mathbf{E} = \tilde{\rho}^R R\mathbf{J} \quad (7.35)$$

where the R represents the rotation operation which rotates the current and electric field \mathbf{E} by 90 ° and the $\tilde{\rho}^R$ denotes the resistivity tensor connecting the those two rotated quantities $R\mathbf{E}$ and $R\mathbf{J}$. From the equation 7.35, we know $\mathbf{E} = R^{-1}\tilde{\rho}^R R\mathbf{J} = \tilde{\rho} \mathbf{J}$. So we have $\tilde{\rho}^R = R\tilde{\rho}R^{-1}$. Rotating the amorphous sample by 90 ° should not change any physics here. So it must have the relation that $\tilde{\rho}^R = \tilde{\rho}$. Remember the matrix of rotation by 90 ° is

$$\begin{bmatrix} 0 & -1 \\ 1 & 0 \end{bmatrix} \quad (7.36)$$

and its inverse is

$$\begin{bmatrix} 0 & 1 \\ -1 & 0 \end{bmatrix} \quad (7.37)$$

After substituting those two matrices into $\tilde{\rho}^R = \tilde{\rho}$, we will have $\rho_{xx} = \rho_{yy}$ and $\rho_{xy} = -\rho_{yx}$.

It is highly valuable to establish a bridge between the experimental and theoretical fields concerning the data of Hall effect or anomalous Hall effect. The resistance R_{xy} is defined as

$$R_{xy} = \frac{V_{xy}}{I} \quad (7.38)$$

From the formula 7.30, we know

$$R_{xy} = \frac{\rho_{xy}}{d} \quad (7.39)$$

R_{xy} and ρ_{xy} are the commonly used quantities for experimental physicists. But from a theoretical viewpoint, it is helpful to convert them to the conductivity σ_{xy} , through which the underlying mechanism of anomalous Hall effect might be demonstrated by employing Berry curvature within the first Brillouin zone. As shown in formula 7.34, we have

$$\sigma_{xy} = \frac{-\rho_{xy}}{\rho_{xx}^2 + \rho_{xy}^2} \approx \frac{-\rho_{xy}}{\rho_{xx}^2} \quad (7.40)$$

This approximation is made by considering the fact that $\rho_{xy}^2 \ll \rho_{xx}^2$. It is clear now that the signal represented by V_{xy} , R_{xy} , ρ_{xy} , σ_{xy} as a function of magnetic are identical, except that there is a minus sign for σ_{xy} [11].

7.7 Make Hall bar

Before entering the cleaning room, there are 2 things needed to be done.

- Use MgO as the capping layer (SiO₂ is not suitable for the adhesion of photoresist to the sample).
- Bring the pipette into the cleaning room.

After being in the cleaning room, two immediate things should be done:

- Set the exposure time to 8 seconds.
- Turn on the two heating machines at 150°C and 115°C, respectively.

Now, it is ready to begin making Hall bar pattern. The following steps are used for lift-off process by using negative photoresist.

1. Begin by cleaning the sample with Acetone and then IPA.
2. Set up the spinning machine, use the chunk shown in (a) in Figure 7.4, place a test sample onto it, and turn on the pump for the machine. Ensure the spinning process is working correctly.
3. Once the temperature of the heating machine stabilizes, place the sample onto the 150°C hot plate for 2 minutes. Then remove it and let it cool down. This step removes any residual chemical substances, such as the IPA from the first step.
4. After the cooling is complete, load the sample into the spinning machine, load the recipe for 5000RPM, press center to ensure it is centered, and then pipette 2 drops of S1813 positive photoresist onto the sample surface. Press spin to turn on the spinning machine.
5. Once the spinning process is complete, put the sample onto the plate of the 115°C heating machine for 90 seconds for the softbake, which is crucial and strict.
6. The sample preparation is complete at this point.
7. Now, onto the mask part. Choose the mask and mask holder, mount the mask in the holder, and connect the pump system as shown in (b) in Figure 7.4. Select the right face (the side with the ring-trace should face the sample surface) and the correct mask (the one used for the Hall bar patterning is different from that used for the connecting patterning).
8. Go to the Main menu → manual test → mask vacuum → check system vacuum. Once the contact vacuum is good, mount it on the aligner.

9. Ensure that the exposure time is correct, which is 8 seconds.
10. Place the sample on the vacuum chuck, press substrate vacuum button on the screen, and then check the vacuum.
11. Push them gently forward. Once they reach the correct position, press level.
12. Focus on the green LED (an indication of the gap between the mask and the sample). Find the critical height where the LED light is on. Once the light is on, move the sample down using the black knob (at least 1/2 turn) to ensure the x and y direction movement is free.
13. Align the sample correctly using rotation and x , y movement.
14. Once the alignment is complete, move the sample up to contact the mask (make the LED green again) and move it 1/4 turn down.
15. Press the move contact position, and then contact vacuum, check the contact vacuum in the meter.
16. Move the microscopes out of the way and press cycle (2 points here, as indicated by the blue arrows in (c) of Figure 7.4). The patterning process will now begin. Do not look at the UV light.
17. Press the substrate vacuum and remove sample.
18. Once finishing the exposure step, that is it! No hardbake! No hardbake! No hardbake!
19. Use the public developer and the develop time 40 s
20. Wash the sample in DI water and dry it with nitrogen gas.
21. Ensure that the hotplate is closed, the vacuum for the spin machine is off, and only the system vacuum for the Mask aligner is on. All other vacuums should be off.
22. Dispose of the used acetone and IPA in the red container.
23. Fill out the notebook.

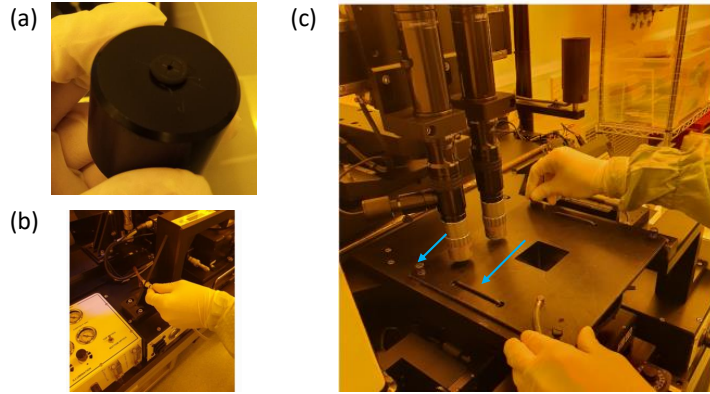


Figure 7.4: Three images showing key steps in the fabrication Hall bars in the cleanroom.

Now, the silicon wafer with Hall bar pattern can be loaded into the Shamrock to deposit the amorphous RE-Co. Once the deposition is finished, using acetone and IPA to remove the unnecessary photoresist. Now, it is ready to do magneto-transport measurement.

7.8 XMCD-PEEM image process

The RGB images of XMCD-PEEM have a dimension 2965 by 2965 with a 24 bit depth (8 bit per channel). Because the values for R, G and B are equal at each pixel, we can convert the images to greylevel, more convenient for image process. In order to obtain more details about the partial switching behaviors, we need to get difference image by subtracting the images taken sequentially. It means that the resulting pixel values might become negative. But in Python, some popular libraries, such as Numpy, OpenCV and Matplotlib, will automatically use an appropriate data type based on the input data. To ensure that the resulting image can store negative values, it is helpful to explicitly use a floating-point data type.

7.9 Phase diagram of Y-Co, Tb-Co and Dy-Co

The rare earths easily alloy with most of the other metals in the periodic table [12]. The phase diagrams for Y-Co, Tb-Co and Dy-Co are shown in Figure 7.5, Figure 7.6 and Figure 7.7, respectively. The intermetallic compounds are represented as vertical lines on the phase diagram [13]. Those three phase diagrams show many similarities, especially for Dy-Co and Tb-Co ones. Here, we take the Dy-Co as an example. DyCo_3 melts congruently with no compositional alternations. So it is quite easy to make polycrystalline DyCo_3 and TbCo_3 by arc-melting method. When atomic ratio of Dy is about 7% and the temperature is 1365 °C, there is a eutectic point, where upon cooling a liquid phase is converted to two solid phases. Upon cooling DyCo_5 , at 1130 °C, decomposes to two compounds $\text{Dy}_2\text{Co}_{17}$ and Dy_2Co_7 by the eutectoid reaction. When the atomic percent Dy is 75% and upon cooling, at 875 °C, liquid phase with 73% atomic percent Dy and solid phase Dy are converted to Dy_3Co by the peritectic reaction. All the three reactions, eutectic reaction, eutectoid reaction and peritectic reaction are invariant reactions involving three different phases in binary systems¹. Based on the Gibbs phase rule, there are no degrees of freedom, which means the compositions of all three phases and temperature are fixed [14].

¹For binary phase diagrams, a horizontal line is always associated with an invariant reaction.

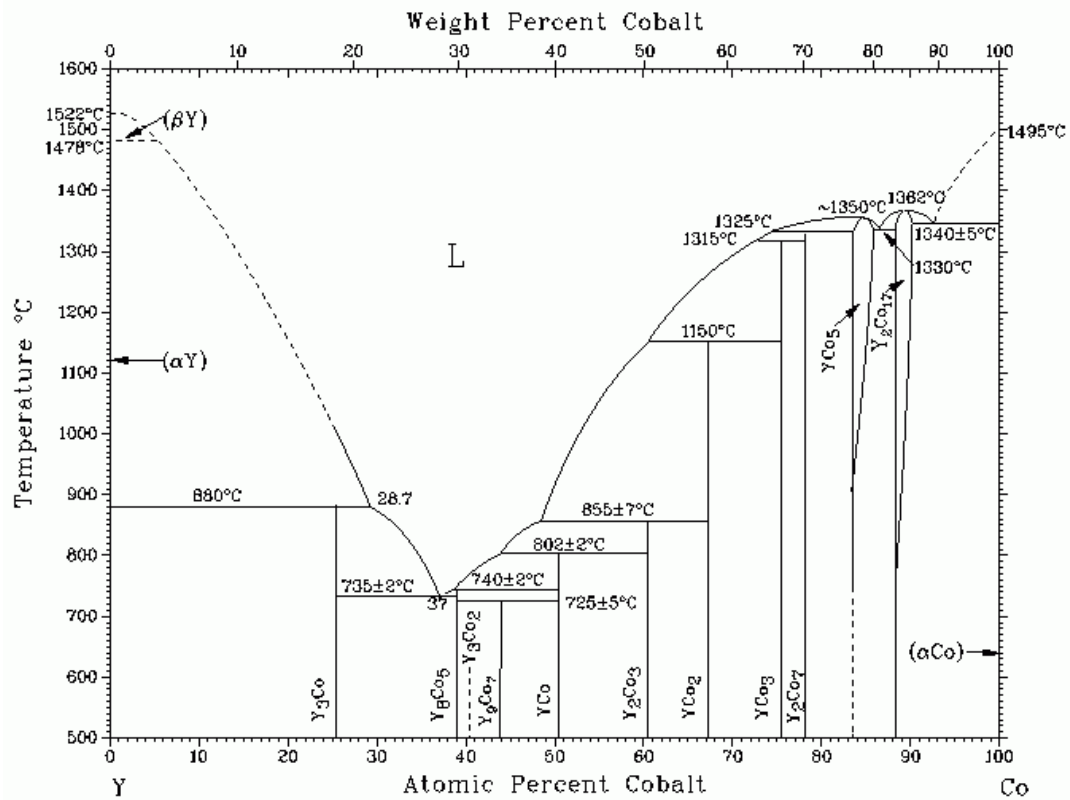


Figure 7.5: Phase diagram of Y-Co [15].

7.10 Additional data for Chapter 5

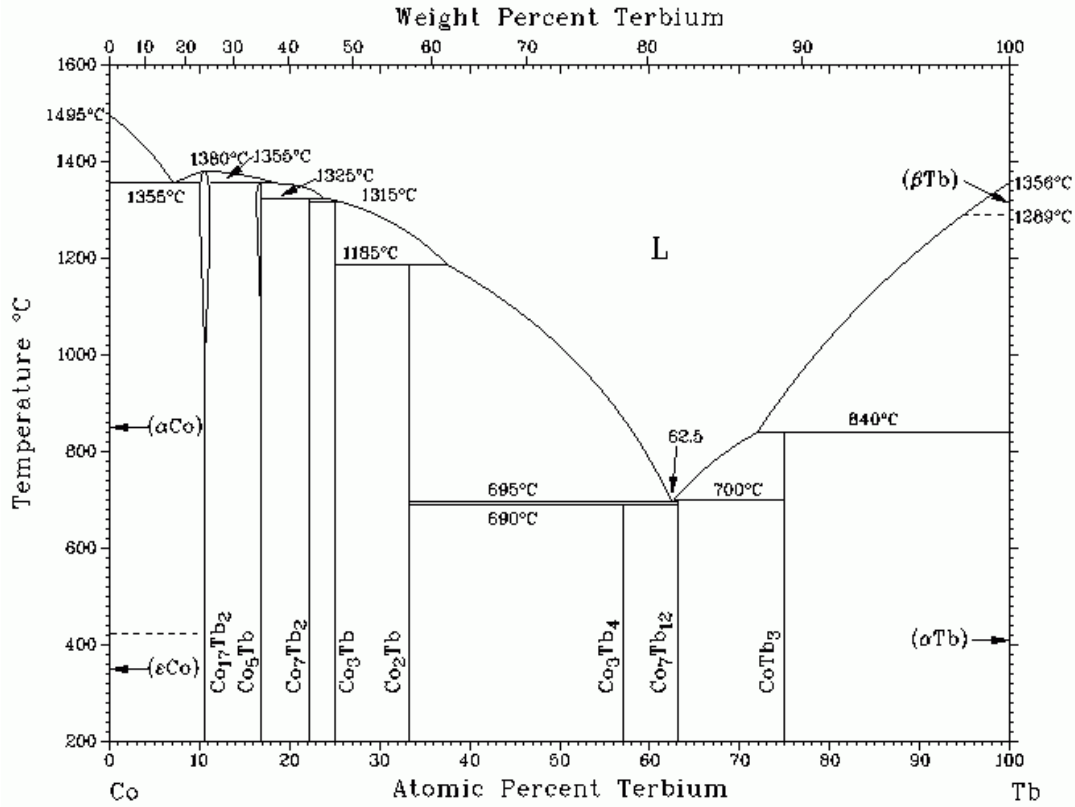


Figure 7.6: Phase diagram of Tb-Co [15].

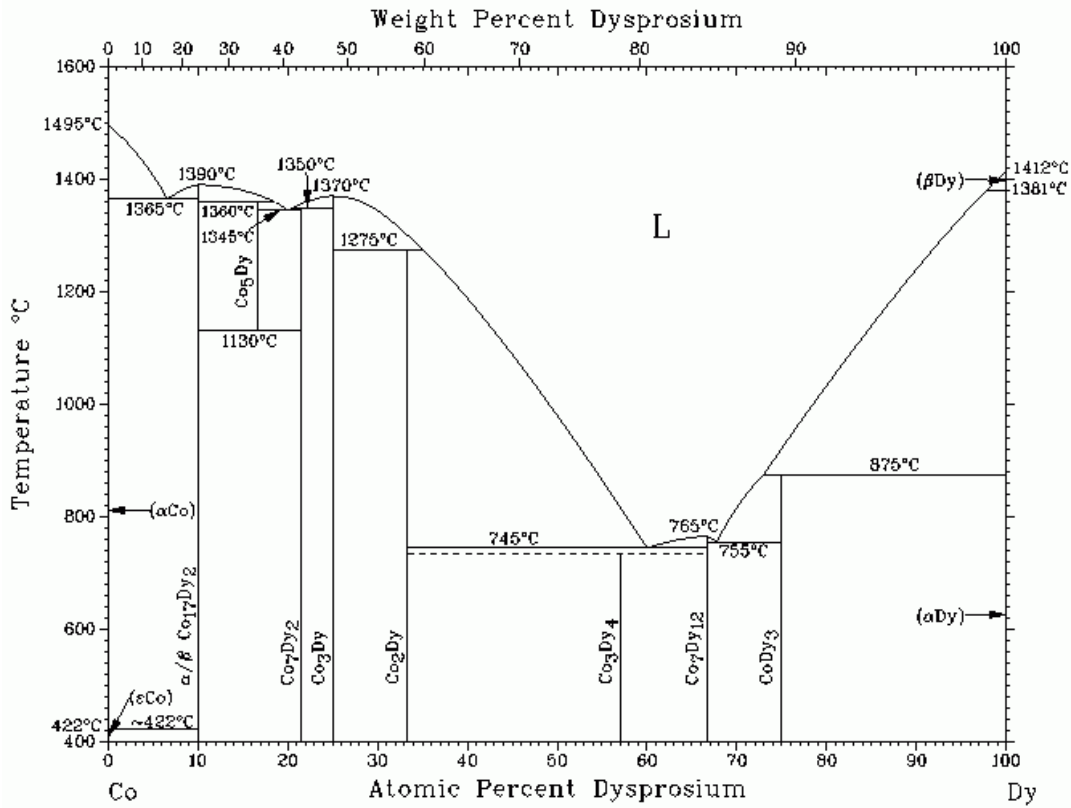


Figure 7.7: Phase diagram of Dy-Co [15].

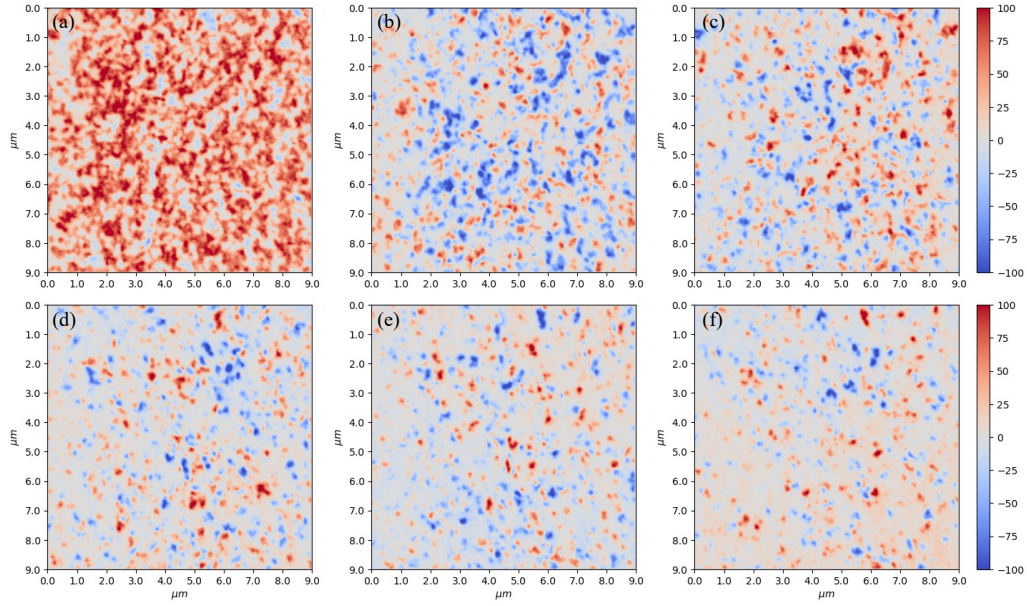


Figure 7.8: Difference XMCD-PEEM images of a-Dy_{0.25}Co_{0.75} (the number 3 sample in Chapter 5) film were generated by subtracting the image captured after pulse N-1 from the image after pulse N, with the XMCD-PEEM images collected at 300 K. The fluence of each pulse is 35.9 mJ/cm². The resulting difference images are as follows: (a) Pulse 1 image minus Pulse 0 image; (b) Pulse 2 image minus Pulse 1 image; (c) Pulse 3 image minus Pulse 2 image; (d) Pulse 4 image minus Pulse 3 image; (e) Pulse 5 image minus Pulse 4 image; (f) Pulse 6 image minus Pulse 5 image.

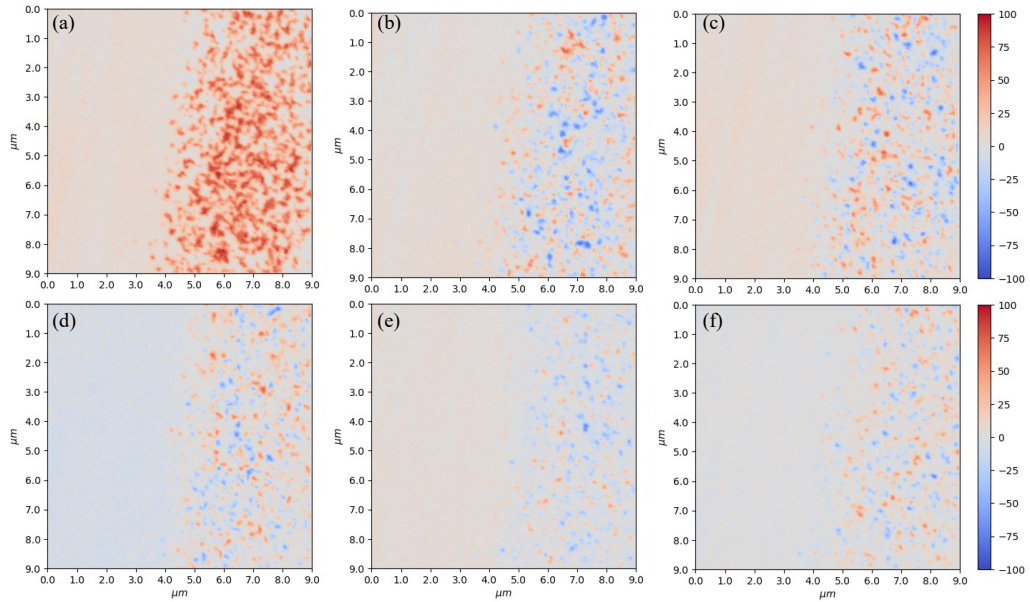


Figure 7.9: Difference XMCD-PEEM images of a-Dy_{0.25}Co_{0.75} (the number 3 sample in Chapter 5) film were generated by subtracting the image captured after pulse N-1 from the image after pulse N, with the XMCD-PEEM images collected at 180 K. The fluence of each pulse is 35.9 mJ/cm². The resulting difference images are as follows: (a) Pulse 1 image minus Pulse 0 image; (b) Pulse 2 image minus Pulse 1 image; (c) Pulse 3 image minus Pulse 2 image; (d) Pulse 4 image minus Pulse 3 image; (e) Pulse 5 image minus Pulse 4 image; (f) Pulse 6 image minus Pulse 5 image.

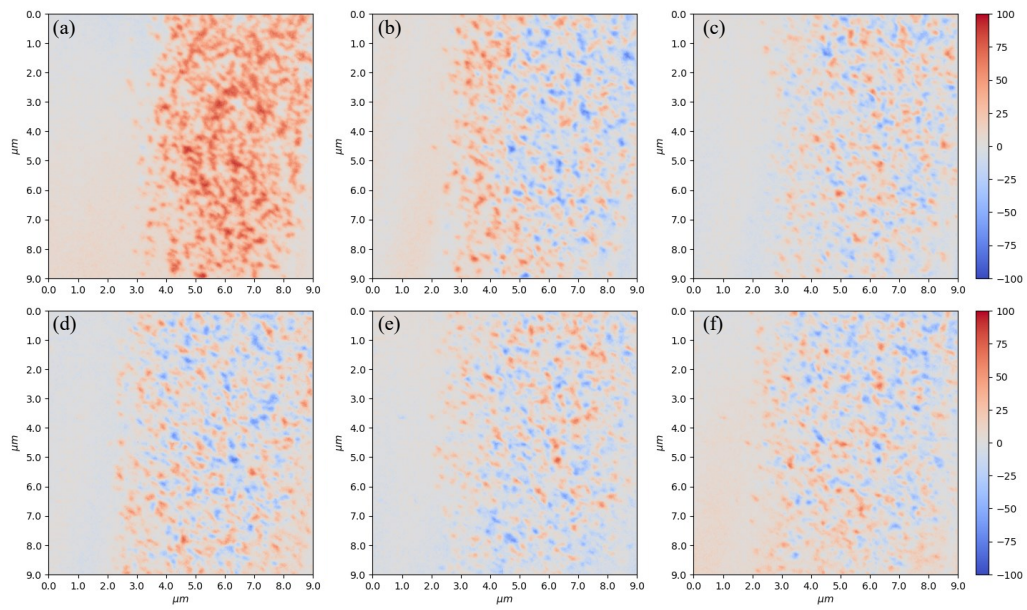


Figure 7.10: Difference XMCD-PEEM images of $a\text{-Dy}_{0.25}\text{Co}_{0.75}$ (the number 3 sample in Chapter 5) film were generated by subtracting the image captured after pulse N-1 from the image after pulse N, with the XMCD-PEEM images collected at 120 K. The fluence of each pulse is 69.0 mJ/cm^2 . The resulting difference images are as follows: (a) Pulse 1 image minus Pulse 0 image; (b) Pulse 2 image minus Pulse 1 image; (c) Pulse 3 image minus Pulse 2 image; (d) Pulse 4 image minus Pulse 3 image; (e) Pulse 5 image minus Pulse 4 image; (f) Pulse 6 image minus Pulse 5 image.

References

- [1] M. Ortner and L. G. Coliado Bandeira, “Magpylib: A free python package for magnetic field computation,” *SoftwareX*, 2020. (Cited on page: 155)
- [2] V. Ziemann, “Closed-form expressions for the magnetic field of permanent magnets in three dimensions,” *arXiv preprint arXiv:2106.04153*, 2021. (Cited on page: 155)
- [3] R. P. Feynman, R. B. Leighton, and M. Sands, *The Feynman Lectures on Physics; New millennium ed.* New York, NY: Basic Books, 2010. Originally published 1963-1965. (Cited on page: 156)
- [4] G. Bertotti, *Hysteresis in magnetism: for physicists, materials scientists, and engineers.* Academic Press, 1998. (Cited on page: 156)
- [5] J. J. Sakurai and J. Napolitano, *Modern Quantum Mechanics.* Cambridge University Press, 3 ed., 2020. (Cited on page: 157)
- [6] B. Zwiebach, *Mastering Quantum Mechanics: Essentials, Theory, and Applications.* MIT Press, 2022. (Cited on page: 157)
- [7] J. B. J. Fourier, *The Analytical Theory of Heat.* Cambridge University Press, 2009. (Cited on page: 159)
- [8] S. L. Brunton and J. N. Kutz, *Data-driven Science and Engineering: Machine Learning, Dynamical Systems, and Control.* Cambridge University Press, 2019. (Cited on page: 159)
- [9] J. M. Cimbala, “Fourier Transforms, DFTs, and FFTs,” *Penn State University, State College*, 2010. (Cited on page: 159)
- [10] J. M. D. Coey and S. S. Parkin, *Handbook of Magnetism and Magnetic Materials.*, vol. 1 and 2. Springer International Publishing, 2021. (Cited on page: 161)
- [11] N. T. Hai, J.-C. Wu, J.-P. Chou, and J. Pothan, “Novel anomalous hall effect mechanism in ferrimagnetic gdco alloy,” *Journal of Applied Physics*, vol. 133, no. 23, 2023. (Cited on page: 162)
- [12] K. Gschneider and L. Eyring, eds., *Handbook on the Physics and Chemistry of Rare Earths*, vol. 1: Metal. North Holland, 1979. (Cited on page: 164)
- [13] W. D. Callister Jr and D. G. Rethwisch, *Materials science and engineering: an introduction.* John Wiley & Sons, 2020. (Cited on page: 164)
- [14] F. C. Campbell, *Phase diagrams: understanding the basics.* ASM international, 2012. (Cited on page: 164)
- [15] H. Okamoto, T. Massalski, *et al.*, *Binary Alloy Phase Diagrams.* 1990. (Cited on page: 165, 166)